Energy Education and Research Collaboration **EERC**

Fourth Quarterly Report
Phase II
May 1, 2010

Prepared by

Prof. Nariman Farvardin, Provost
Principal Investigator and EERC Project Director

Prof. Avram Bar-Cohen, Chair
EERC Project Deputy Director

Dr. Azar Nazeri
EERC Research Manager

THE UNIVERSITY OF MARYLAND AND THE PETROLEUM INSTITUTE OF ABU DHABI, UAE

EERC Key Contributors

University of Maryland – College Park, MD, USA

Shapour Azarm
Balakumar Balachandran
David Bigio
Hugh A. Bruck
Nikil Chopra
Avram Bar-Cohen
Serguei Dessiatoun
Bryan Eichhorn
Ashwani K. Gupta
Satyandra K. Gupta
Yunho Hwang
Greg Jackson
P.K. Kannan
Mohammad Modarres
Reinhard Radermacher
Amir Shooshtari

Petroleum Institute – Abu Dhabi, UAE

Youssef Abdel-Majid
Ahmed Al Shoaibi
Saleh Al Hashimi
Ebrahim Al-Hajri, Returning ADNOC Scholar
Ali Almansoori
Mohamed Alshehhi
Sai Cheong Fok
Afshin Goharzadeh
Didarul Islam
Hamad Karki
Isoroku Kubo
Ahmed Nafees
Michael Ohadi
Peter Rodgers
Abdennour Seibi

Table of Contents

Executive Summary

The following is a summary of the major project activities that have taken place over the completed quarter. For more detail, see the individual reports in the last section of this report.

Thrust 1: Energy Recovery and Conversion

Sulfur Recovery from Gas Stream using Flameless and Flame Combustion Reactor

A.K. Gupta, A. Al Shoaibi

- Conducted non-reactive simulations to investigate the mixing characteristics of hydrogen sulfide and hot products (produced of CH_4/O_2 reaction). Five mixing configurations were examined where CH_4/O_2 products of combustions were assumed to be only H_2O and CO_2.
- Conducted reactive CFD simulations to examine the diffusion effect on the H_2S/O_2 reaction. The simulations were primarily used for simulating perfectly mixed H_2S/O_2 mixture with different equivalence ratios using Fluent software and comparing it with our Chemkin simulations. The results revealed very good agreement between the Chemkin and Fluent simulations.
- Examined diffusion effect using counter-flow flame of H_2S/O_2. The results highlighted the presence of different localized reaction spots where the reaction has different directions corresponding to the mixture at each spot. On the other hand, the results revealed that hydrogen sulfide dissociates significantly inside the injector into hydrogen and sulfur.
- Conducted an experimental examination for configuration 4, presented in the non-reactive mixing investigation, to identify the mixing uniformity using two different sets of reactant flow rates. The results showed promising mixing uniform characteristics where the change of oxygen mole fraction throughout the mixing chamber axial distance did not exceed 13% of the asymptotic value of oxygen mole fraction.

Solid Oxide Fuel Cell Systems for Operation on Petroleum Off-Gases with Contaminants

G. Jackson, B. Eichhorn, A. Almansoori, A. Nafees

- Re-ran durability tests for Ni/YSZ operating continuously on a direct C_4H_{10} feed to provide baseline comparison with more advanced $Ni/CeO_2/YSZ$ cells. This work was done in order to complete some holes in the data for a joint UMD-PI publication with the UMD team (Patel, Wang, and Jackson) and PI's Almansoori as co-authors.
- Enhanced MEA models by combining the distributed electrochemistry and the non-isothermal models for better coupling of electrochemistry and internal reforming predictions in down-the-channel models.
- Developed a basic SOFC model in Aspen Plus, which is being expanded to include the previous SOFC physics-based model through a FORTRAN sub-model utilizing previously presented physics. This model will be used as the basis for two summer intern projects from the PI, who will study plant-level system models relevant to petroleum processing.

Separate Sensible and Latent Cooling with Solar Energy

R. Radermacher, Y. Hwang, I. Kubo

- Ordered main components of equipment and instruments. The data acquisition system has been received, which will allow us to calibrate the instruments in the near future.
- Started building the experiment.
- Modeled the evaporator using CoilDesigner, which was also used to find the pressure drops in the refrigerant- and air-sides. The main purpose of this simulation is to ensure that under the current test conditions, no condensation will occur at the evaporator.

Waste Heat Utilization in the Petroleum Industry

R. Radermacher, Y. Hwang, S. Al Hashimi, P. Rodgers

The following were modeled using HYSYS:

- CO_2 capturing plant from a power plant
- Gas turbine steam and absorption-chiller combined cycle

Thrust 2: Energy-Efficient Transport Process Projects

Multidisciplinary Design and Characterization of Polymer Composite Seawater Heat Exchanger Module

P. Rodgers, A. Bar-Cohen, S.K. Gupta, D. Bigio, H.A. Bruck

- Hygrothermally aged specimens in 25°C freshwater and saltwater to determine if mechanical property degradation is result of moisture diffusion or aging temperature. The combined effects of both moisture absorption and elevated temperatures lead to the change in mechanical properties seen in specimens aged in water temperatures of 40, 50 and 60°C.
- Developed finite element analysis (FEA) model using hygrothermally aged mechanical properties to determine feasibility of replacing metallic heat exchangers at the Das Island liquefied natural gas facility with polymer composite heat exchangers.
- Designed series of experiments to study mechanical properties of carbon-filled nylon polymers subjected to hygrothermal aging in dynamic stress environment at a variety of temperatures in order to investigate effect of stress applied during aging of material upon mechanical properties of material.
- Constructed a dynamic chamber to conduct tensile testing of hygrothermally aged polymer samples in an aqueous saline environment.
- Designed apparatus for application of tensile stress to carbon-filled nylon samples undergoing hygrothermal aging in aqueous saline environment.
- Evaluated the thermofluid performance of different PHX concepts using several figures of merit to understand their advantages and disadvantages.
- Split the plate-fin heat exchanger module design space to improve mold-filling meta-model. Performed Moldflow® analyses with representative geometries from each design region to determine the failure mode of each design region.
- Used model simplification techniques to develop a volume scaling mold-filling model applicable to portions of the PHX module design space.
- Performed finned-plate and volume-scaled flat-plate analyses in Moldflow® and compared the results to determine applicable design regions. Mesh convergence analyses confirmed that the meshing tolerance was suitable and the results accurate.

- A poster presentation entitled "Saltwater Hygrothermal Aging Studies of Short Carbon Fiber Reinforced Polyamide 12," co-authored by Frank Robinson, Prof. Hugh Bruck, Prof. S.K. Gupta, and Prof. Avram Bar-Cohen, was accepted for presentation at the ASME International Mechanical Engineering Congress & Exposition.

Study on Microchannel-Based Absorber/Stripper and Electrostatic Precipitators for CO_2 Separation from Flue Gas

S. Dessiatoun, A. Shooshtari, M. Ohadi, A. Goharzadeh

- Performed literature review on separation techniques and the kinetics between CO_2 and alkanolamines in aqueous solutions, and investigated their reaction rate.
- Identified the alkanolamine suitable for experimental study.
- Designed test section and experimental setup.
- Performed flow visualization of the EHD induced flow.

Microreactors for Oil and Gas Processes Using Microchannel Technologies

S. Dessiatoun, A. Shooshtari, M. Ohadi, A. Goharzadeh, E. Al-Hairi

- Identified target reaction.

Thrust 3: Energy System Management

Integration of Engineering and Business Decisions for Robust Optimization of Petrochemical Systems

S. Azarm, P.K. Kannan, A. Almansoori, S. Al Hashimi

- Continued the research on the integration of business and engineering decisions based on an oil refinery case study:
  - Proposed an Approximation Assisted Multi-objective collaborative Robust Optimization (AA-McRO) approach for the integration framework.
  - Continued our research on the dashboard development for the integration framework.
  - Continued progress on recent joint publications.

Dynamics and Control of Drill Strings

B. Balachandran, H. Karki, Y. Abdelmagid

- Focused on torsion vibration of the drill string and studied the effects of mass imbalance for different rotation speeds. It was shown that the current model captures the different features of the contact and non-contact dynamics better than those reported in the literature.

Studies on Mobile Sensor Platforms

B. Balachandran, N. Chopra, H. Karki, S.C. Fok

- Studied localization of a static source by using a mobile sensor platform.
- Examined noise robustness of a previously proposed localization algorithm. Using Lyapunov analysis, it was found that if noise uncertainty is constant and bounded, the adaptive localization algorithm results in bounded localization errors.

- Used adaptive control techniques to make certain that the mobile agents track the desired trajectory and drive the tracking error to zero. Simulation results are also presented for two agents.
- Carried out preliminary experimental work to build a mobile agent that is to be used to verify algorithms.

Development of a Probabilistic Model for Degradation Effects of Corrosion-Fatigue Cracking in Oil and Gas Pipelines

M. Modarres, A. Seibi

- Performed literature review on creep deformation model
- Developed mechanistic model for creep deformation
- Prepared samples for experimental work: aluminum 7075 dog-bone and X70 carbon steel (ASTM-standardized)

Introduction

The EERC enjoyed a busy and fruitful fourth quarter of Phase II of the collaboration. In addition to continued progress on individual research projects, visits between the two institutions furthered collaboration. During this quarter, Professors Cornelis Peters and Clarence Rodrigues visited UMD from PI. In May, Dr. Ashwani Gupta and Dr. Azar Nazeri, from UMD, visited PI and made significant inroads with the operating companies of ADNOC. In addition, PI's Arzanah campus students visited UMD, where they interacted with professors and students involved in WIE/WISE and explored laboratories and cultural sites in Washington DC, Baltimore and Alexandria. These visits are described in more detail below.

UMD-PI Visits

Prof. Cornelis Peters Visits UMD, March 10-12, 2010
Petroleum Institute, Chemical Engineering Department, *Chairman & Distinguished Professor*

Dr. Cornelis Peters visited UMD and gave a seminar jointly sponsored by the Mechanical Engineering and Chemical and Biomolecular Engineering departments, titled: "Carbon Dioxide, a Nuisance or a Blessing?" His talk was a part of the Distinguished Seminar Series of the Mechanical Engineering Department at UMD.
Dr. Peters met with several CBE and ME during his stay at UMD, and he also became an Adjunct professor at the CBE department at UMD.

Dr. Clarence Rodrigues Visits UMD March 22-24, 2010
Manager – Health, Safety and Environment (HSE) - Council Chair
Petroleum Institute, Mechanical Engineering Department, *Associate Professor of Mechanical Engineering*

Dr. Rodrigues visited UMD in March and met with Professor Ali Mosleh of the Reliability Engineering Program; Prof. Ali Haghani, Chair of the Civil and Environmental Engineering department; Professor Marino Di Marzo, Professor and Chair of the Fire Protection Engineering department; Professor and Chair of the Mechanical Engineering department, Avram Bar-Cohen; and Dr. George Syrmos, the Executive Director of Advanced Engineering Education. Dr. Rodrigues is planning a graduate program in Health Safety and Environment for the Petroleum Institute and is exploring the capabilities of the University of Maryland in this area and how the EERC can support and help this development at PI.

Dr. Rodrigues also met with Mr. Scott Lupin, the Director of Sustainability at UMD.

Professor Ashwani Gupta and Dr. Azar Nazeri Visit PI and OpCos, May 1-6, 2010

Professor A. K. Gupta and Dr. Nazeri visited three operating companies of ADNOC—TAKREER, ADGAS, and GASCO—and presented talks on the EERC and "Sulfur Recovery from Gas Stream Using Flameless Combustion Reactor." Dr. Ahmed Al Shoaibi, of Chemical Engineering, who is a PI collaborator on this project with Dr. Gupta, accompanied them on their visit to TAKREER, and Dr. Binay Dutta from PI was present at the GASCO meeting. The presentations were well received by all three companies and, as was anticipated, the companies reiterated their interest in this topic. At the meeting with ADGAS, Dr. Ahmad Abbas, the Integrity and Quality Manager at GASCO, was very interested in the prospects of decreasing the size of the equipment, reducing the number of catalylic stages, and increasing capacity. In the TAKREER meeting, Dr. Abdulkarim Koudil led a good discussion on the possibility of H_2 recovery from H_2S as well as

the sulfur chemistry (COS, CS_2, CS). The meeting with Mr. Salem Sayegh at GASCO went very well, and he showed great interest in receiving Professor Gupta's publications based on this project. He also asked Professor Gupta to send him a proposal on two areas of H_2 separation and cleaning of H_2S from the existing plants.

The visits to the operating companies were followed by meetings with Dr. Ahmed Al Shoaibi, on the progress of the "Sulfur Recovery" project, and other visits with several PI faculty and administration members, including Dr. Karl Bertussen and Provost Mike Ohadi.

At the GASCO meeting, from left: Dr. Nazeri, Mr. Sayegh from GASCO, and Dr. Gupta

Arzanah Students Visit UMD: A Journey of Discovery

Dr. Nadia Alhasani and Arzanah students with Dr. Nazeri on the "Journey of Discovery" Trip.

They called it a "Journey of Discovery": 14 selected junior and senior Petroleum Institute (PI) students participated in the first WISE Program at PI, a trip to the United States. The trip was co-organized by the WISE Program and Arzanah Campus Director **Dr. Nadia Alhasani and Dr. Azar Nazeri,** Research Manager of the University of Maryland's Energy Education and Research Collaboration (EERC). One of the objectives of the trip was to provide an opportunity for female PI students to visit WISE programs at partner institutions and interact with their female engineering students. The trip was also intended to expose these students to cutting-edge research and technology and to inspire and enhance their commitment to science and technology.

The major component of the itinerary was the visit to the University of Maryland, College Park campus, touring state-of-the-art research laboratories and attending presentations and workshops mostly conducted by female professors at University of Maryland. Among the laboratories visited were the Microelectronics Interconnects Laboratory, Micro-Robotics Laboratory, Virtual Reality Laboratory, Combustion Laboratory, Nano-Fabrication Laboratory and the University Nuclear Reactor. The party attended several lectures given by leading scientists in the field of MEMS and nano-engineering. For example, they attended a lecture given by **Dr. Moustafa Al-Bassyiouni** on microelectronics and one given by **Dr. Sarah Bergbreiter**, who spoke on the subject of micro-robotics.

Dr. Sarah Bergbreiter in her microelectronics laboratory

Pictured above, from top to bottom: the visit to the Combustion Lab; the visit to the UMD Nuclear Reactor.

The Arzanah students were invited to attend an interim capstone presentations class, where the student groups presented their projects in their interim states. The students also attended a workshop conducted by **Professor Linda Schmidt** on collaboration and "Kolb learning." During this workshop they took the Kolb learning test, which determined their individual styles of learning.

Shown above, Professor Linda Schmidt and the Arzanah students determine their styles of learning.

The students attended a workshop organized by Women In Engineering (WIE) at UMD and EERC. **Dr. Nadia Al Hassani** first presented a short presentation on the WISE program, its inception, and activities at PI. This was followed by an informal discussion with **Dr. Paige Smith**, Director of the WIE at UMD, and **Alana Johnson,** Assistant Director of Outreach and Recruitment, and a group of undergraduate as well as graduate engineering female students who were invited to this workshop.

WISE/WIE Workshop

Dr. Paige and Alana Johnson with some of the attendees

Dr. Paige receiving a gift from the Arzanah students.

The busy itinerary did allow for visits to Washington DC, Baltimore (Maryland) and Alexandria (Virginia). Included in the trip were opportunities for students to visit several renowned museums such as the Smithsonian Center (the Castle), the Natural History Museum, the National Air and Space Museum, and the National Art Gallery – East Wing.

The WISE program hosted a farewell luncheon at the UAE Embassy in Washington DC, in which all University of Maryland participants (faculty, staff and students) were invited to share a traditional Emirati lunch.

The Arzanah students at the UAE Embassy.

Graduate Research Assistants (GRAs)

The following table lists the GRAs working on the Phase II EERC projects.

Student	UM Professor	PI Professor	Degree	Funding Source
Mohamed Chooka (Graduated) Mohammad Nuhi	Modarres	Seibi	Ph.D. Ph.D	Graduated Aug 2009 EERC
Mohamed Alshehhi (Graduated) Paul Breuninger Toni Pfennig	Dessiatoun	Ohadi, Goharzadeh,	Ph.D.	Dec 2009
Ebrahim Al-Hajri (Graduated) Pradeep Kumar Singh	Dessiatoun	Ohadi, Goharzadeh	Ph.D.	Graduated June 2009
Weiwei Hu Naveen Al Qasas	Azarm	Al Hashimi, Almansoori	Ph.D.	EERC
Hatem Selim	Gupta	Al Shoaibi	Ph.D.	EERC
Juan Cevallos Tim Hall Frank Robinson William Pappas	Bar-Cohen, SK Gupta SK Gupta, Bar-Cohen Bar-Cohen, SK Gupta, Bruck Bigio	Rodgers, Abdala	Ph.D MS BS/MS MS	EERC(partial) EERC UMD Foundation UMD Foundation

Chien-Min Liao	Balachandran,	Karki Abdelmagid	Ph.D.	EERC
Hesham Ismail Rubyca Jaai	Balachandran Chopra	Karki Abdelmagid	Ph.D	ADNOC
Ali Al-Alili	Radermacher	Al Hashimi, Rodgers,	Ph.D.	ADNOC
Amir Mortazavi Chris Sommers (Graduated) Abdullah Alabdulkarem	Radermacher	Al Hashemi. Rodgers	MS MS Ph.D	EERC Graduated Aug 2009 EERC
Siddharth Patel (Graduated)	Jackson	Almansoori	MS	Graduated Oct 2009
Lei Wang	Jackson	Almansoori	Ph.D	EERC

Individual Project Reports

Thrust 1
Energy Recovery and Conversion

Sulfur Recovery from Gas Stream using Flameless and Flame Combustion Reactor

UMD Investigators: Ashwani K. Gupta
GRA: Hatem Selim
PI Investigators: Ahmed Al Shoaibi
Student: Nahla Al-Amoodi
Start Date: October 2006

1. Objectives / Abstract

The main objective is to obtain fundamental information on thermal process of sulfur recovery from sour gas by conventional flame combustion as well as flameless combustion, using numerical and experimental studies. Our ultimate goal is to determine optimal operating conditions for enhanced sulfur conversion. Therefore, an experimental study of the flameless combustion processes of the Claus furnace is proposed and the results are compared with the normal flame process in order to determine the improved performance. In this study we will explore different operating conditions and perform exhaust gas analyses of both flame and flameless modes of reactor operation to attain enhanced sulfur recovery.

Specific objectives are to provide:

- A comprehensive literature review of the existing flame combustion process for sulfur removal with special reference to sulfur chemistry
- Near isothermal reactor conditions and how such conditions assist in the enhanced sulfur recovery process
- CFD simulation of the flame and flameless combustion in the furnace.
- Determination of the chemical kinetics and the major reaction pathways to obtain high performance
- Design of a flameless combustion furnace for experimental verification of the numerical results
- Measurements and characterization of the flameless combustion furnace using high temperature air combustion principles that aid in flameless combustion conditions to provide uniform thermal field in the entire furnace zone
- Experiments with simulated sulfur stream to determine the mixedness under non-reactive conditions without simultaneous sulfur reactions
- Development of safe and reliable working facility using H_2S gas steream
- Experiments with different sulfur content gas streams using the flame and flameless combustion furnace modes of operation. This will require determination of the best mixers so as to rapidly mix reactant streams in a very short residence time.
- Installation of the appropriate diagnostics for quantification of stable sulfur compounds in the process
- Flow and thermal field characteristics in the reactor
- Product gas stream characteristics in the reactor and at the reactor exit for providing an evaluation of sulfur recovery and process performance.

2. Deliverables

- Further non-reactive examination for different mixing chambers configurations using nitrogen and oxygen has been performed. Five different configurations are presented here, whereas the first three geometries were presented in the previous quarter. However, in this quarter a thorough comparison between the flow field characteristics of each configuration (turbulence intensity and vorticity magnitude) was evaluated and the results are presented here. On the other hand, particle path lines analysis has also been conducted in order to identify the high mixing zone of each mixing chambers as well as the kind of mixing regime (shear layer mixing or recirculation zone mixing).

- Reactive CFD simulations for H_2S/O_2 reaction have been conducted using Fluent 6.3.26 software for different equivalence ratios. Our 19-reaction reduced mechanism has been successfully incorporated in the code to provide simulations on the outcome of sulfur in the reactor. The equivalence ratio was changed from fuel-rich, stoichiometric, to fuel-lean with values of 3, 1, and 0.5 respectively. The reactor temperature was kept constant at 1600K. Premixed as well as diffusion flames were investigated in this study. The diffusion flame was chosen to be counter flow flame for all the simulations.

- Experimental examination has been carried out to evaluate the mixing characteristics of the most promising geometry for the non-reactive simulations mentioned above. Oxygen and nitrogen have been used to simulate the Claus process reactants. These gases are chosen to best simulate the H_2S gas behavior in the reactor. The choice was based on the molecular weight and diffusivity of the gases. Momentum flux ratio is kept constant between the Claus conditions and non-reactive experiment.

3. Executive Summary

During the reported quarter, progress continued in the areas of investigation of non-reactive mixing characteristics of Claus process reactants. Non-reactive simulations were conducted to investigate the mixing characteristics of hydrogen sulfide and hot products (produced of CH_4/O_2 reaction). Five mixing configurations were examined where CH_4/O_2 products of combustions were assumed to be only H_2O and CO_2. The results showed promising mixing characteristics for geometries 2, 4, and 5 and poor mixing characteristics for geometries 1 and 3. However, configuration 2 is not favored for mixing reacting flows where high thermal stresses for the injectors are expected. On the other hand, configurations 4 and 5 give the most superior performance amongst all the configurations where mixing is significantly limited by a recirculation zone rather than weak shear layer. Although configuration 5 has better performance in terms of vorticity magnitude and turbulence intensity, configuration 4 gives better mixing characteristics. This is attributed to the better distribution of the recirculation zone of configuration 4 compared to the recirculation zone of geometry 5.

Furthermore, reactive CFD simulations were conducted to examine the diffusion effect on the H_2S/O_2 reaction. The simulations were primarily used for simulating perfectly mixed H_2S/O_2 mixture with different equivalence ratios using Fluent software and comparing it with our Chemkin simulations. Reactor temperature was maintained at an arbitrarily chosen temperature of 1600K. The results revealed very good agreement between the Chemkin and Fluent simulations. Diffusion effect was examined using counter-flow flame of H_2S/O_2. The results highlighted the presence of different localized reaction spots where the reaction has different direction corresponding to the mixture at each spot. On the other hand, the results revealed that hydrogen sulfide dissociates significantly inside the injector into hydrogen and sulfur. Moreover, the results showed the need of having a longer distance downstream in order to achieve the reaction completion compared to the perfectly premixed conditions. Finally, an experimental examination for configuration 4, presented in the non-reactive mixing investigation, was conducted to identify the mixing uniformity using two different sets of reactant flow rates. The results showed promising

mixing uniform characteristics where the change of oxygen mole fraction throughout the mixing chamber axial distance did not exceed 13% of the asymptotic value of oxygen mole fraction.

4. Progress

4.1 Investigation for Claus process reactants mixing characteristics using non-reactive simulations

In order to achieve such a high conversion efficiency, the Claus process must take place under fairly constant reactor temperature. This requires very uniform mixing characteristics for the reactants in order to have uniform temperature rise along the reactor during the thermal transformation. Claus reactions are very slow, which is attributed to the slow reaction between H_2S and SO_2 to form S_2. This means that if we are able to achieve a high degree of mixedness in a short distance of the reactor, the temperature rise due to combustion process will be very uniform along the reactor. Five mixing configurations are examined where CH_4/O_2 products of combustion are assumed to be only H_2O and CO_2. Flow rates of combustion products in numerical simulations are chosen according to the experimental results reported in the quarterly report of September 2009 to achieve uniform reactor temperature of 1600K in the reactor.

Figure 1 shows the examined configurations. For all the configurations, the mixing chamber dimensions were 1x1x2 inch, and the diameter of discharge tube into isothermal reactor was 0.25 inch. For configurations 1, 2, and 3 the inlet diameter of hot products was 0.5 inch. The inlet diameter of hydrogen sulfide was 1/8 inch. For configurations 4 and 5 the hot products inlet diameter was 0.25 inch. Also, for the last two configurations the hot products stream was split into two streams. Configurations 1 and 2 were the same in terms of the flow inlets and outlets. The only difference is that configuration 1 had H_2S inlets flush-mounted with the mixing chamber, while configuration 2 had hydrogen sulfide inlets 0.5 inch inside the mixing chamber. In other words, the length of H_2S inlets was inside the mixing chamber for configuration 2. Configuration 3 had a wall inside the mixing chamber to prevent hot products from escaping into the isothermal Claus reactor before mixing with H_2S. Configurations 4 and 5 had two exits into isothermal reactor. Fluent 6.2 software was used for the numerical simulations. The turbulence model used was the standard K-ε viscous model with buoyancy effects.

Table 1 shows the test matrix of this investigation. The same flow rates were used for all the different configurations. It is to be noted that for configuration 4 and 5 the hot products velocity was increased due to the reduction in inlet tube diameter. Only mixing between H_2S and the hot products (CO_2 and H_2O) took place under 1600K. In other words, not all of the chemical reactions between the gases are included in this investigation.

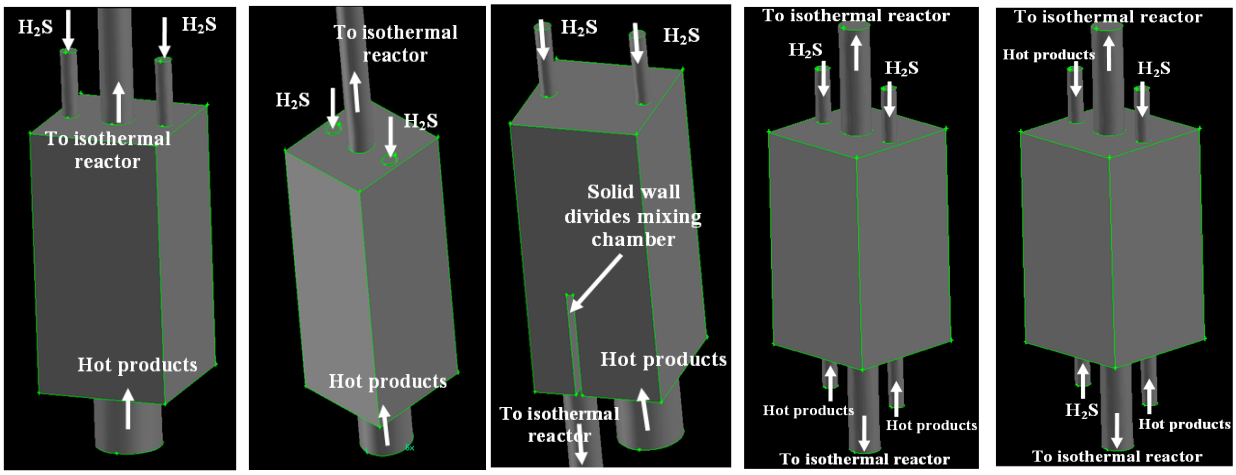

Figure 1. Different mixing configurations examined in this report.

Table 1. Test matrix

	Conf. 1	Conf. 2	Conf. 3	Conf. 4	Conf. 5
Hot products velocity (m/s)	8.95	8.95	8.95	71.1	71.1
Hydrogen sulfide velocity (m/s)	0.21	0.21	0.21	0.21	0.21

Different parameters will be discussed in order to compare the mixing characteristics of each mixing configuration. First, a comparison of hydrogen sulfide mass fraction contours obtained from each configuration will be presented. A comparison between the vorticity magnitudes contours obtained from different configuration will also be discussed in order to estimate the rate of mixing between the hot products and hydrogen sulfide based on the magnitude of vorticity. Furthermore, a comparison between the area-weighted average vorticity magnitude as well as average turbulence intensity is presented in order to evaluate the performance of every configuration compared to others. Finally, a comparison between particle path lines will be displayed in order to monitor the effect of the change in configuration geometry on the behavior of hydrogen sulfide and hot gases particles.

Figure 2 shows the mass fraction contours of H_2S for all configurations. The comparison between configurations 1 and 2 reveals that injection of hydrogen sulfide inside the mixing chamber in configuration 2 has a significant effect on enhancing mixing between H_2S and hot products. The calculation of the mixing length assures this fact. Mixing length was measured from the point where H_2S is introduced into mixing chamber (the end of injection tube) up to the point where the asymptotic H_2S mass fraction is obtained. The mixing length of configuration 1 was 1.437 inch and for configuration 2 was 0.381 inch, which is almost 4 times improvement. It is also important to note that in reacting flow, configuration 2 is challenging to implement where the injection tube will be exposed to high thermal stresses. Configuration 3 shows poorer mixing performance compared to configuration 2 and a better performance compared to configuration 1. Mixing length is found to be 1.07 inch. For a reacting flow this configuration will also be unreliable because of the presence of the wall inside the mixing chamber. Configurations 4 and 5 show better performance compared to any other configuration. The mixing length of configuration 4 is 0.307 inch and for configuration 5 it is 0.346. It is noticeable that mixing starts inside H_2S injector in both configurations. However, in configuration 4 mixing inside H_2S injector is more prominent because all the hot products flow in the direction opposite to H_2S flow injection. In configuration 5 hot-products flow creates a swirl effect inside the mixing chamber because of having the two hot products injectors diagonally opposite from each other. It is important to note that the bottom exit

tube to the isothermal reactor in configuration 4 does not have any significant effect, as the hot products momentum drifts all the flow to the upper exit tube.

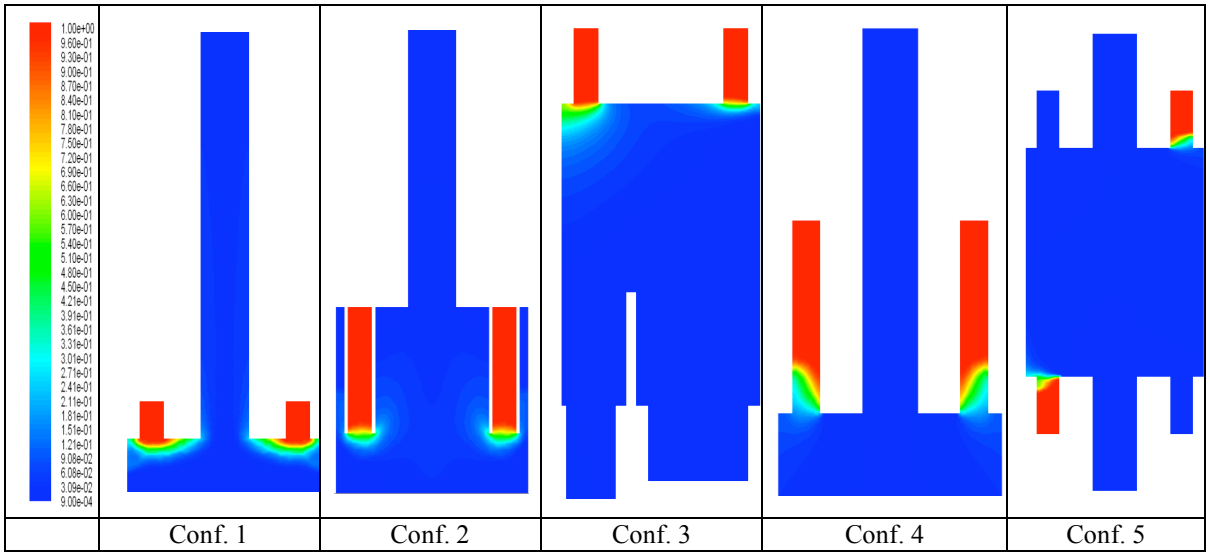

Figure 2. Hydrogen sulfide mass fraction for different mixing configurations.

Figure 3 shows the vorticity magnitude for all mixing configurations. One can see that, comparing configurations 1 and 2, the vorticity magnitude is higher in configuration 2 in the middle of the mixing chamber, where H_2S is injected. This improves mixing of H_2S and hot products. It is important to note that the vorticity magnitude has different scale for each configuration. For configuration 3 the vorticity starts to be significant inside the exit tube into the isothermal reactor. This explains why the mixing characteristics are poor for this configuration. For configurations 4 and 5 one can see better vorticity magnitude contours compared to previous configurations. For configuration 4 the hot products high velocity creates two confined regions of vorticity that extend up to H_2S injectors. For configuration 5, however, high vorticity regions are concentrated in places where no H_2S is injected. This explains the superiority of configuration 4 over configuration 5 in terms of mixing characteristics.

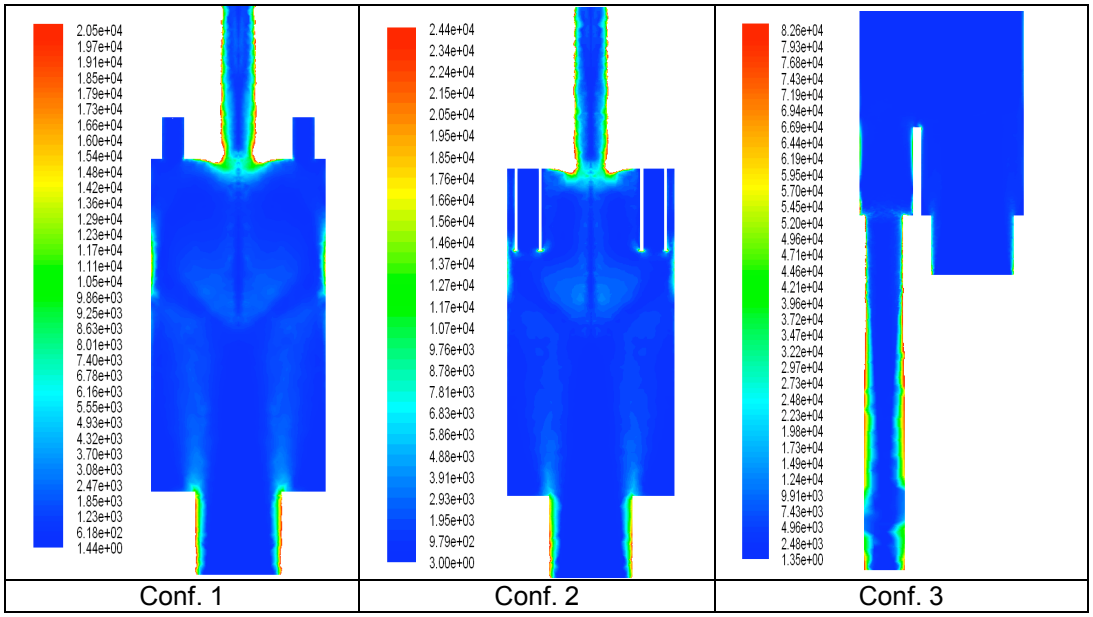

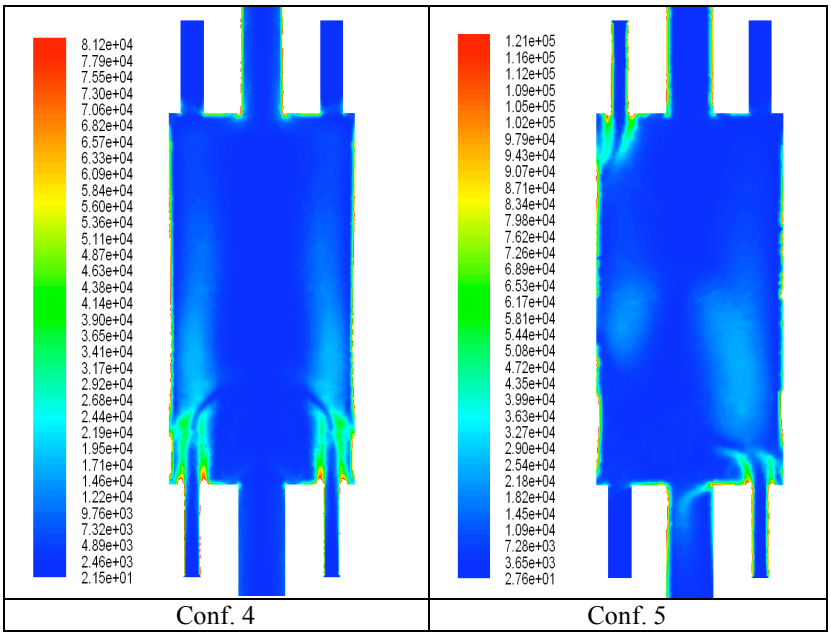

Figure 3. Vorticity magnitude contours for different configurations (1/s).

Figures 4 and 5 show average vorticity magnitude and average turbulence intensity for all configurations. One can notice that for the first three configurations both turbulence intensity and vorticity magnitude are almost constant. However, a considerable increase in both values was noticed in the last two configurations. This explains the improvement in mixing characteristics of the last two configurations. Although configuration 2 does not have high values of turbulence intensity or vorticity magnitude, mixing length is much better compared to configurations 1 and 3. Indeed, the mixing length of configuration 2 is rather comparable to the mixing length of configuration 4 and 5. This is because H_2S injection takes place at the region where the vorticity magnitude region exists. In spite of having less average vorticity magnitude and turbulence intensity, configuration 4 has a better performance the configuration 5. This is attributed to the same reason, that H_2S is injected in a better place, where vorticity and turbulence intensity are considerably high.

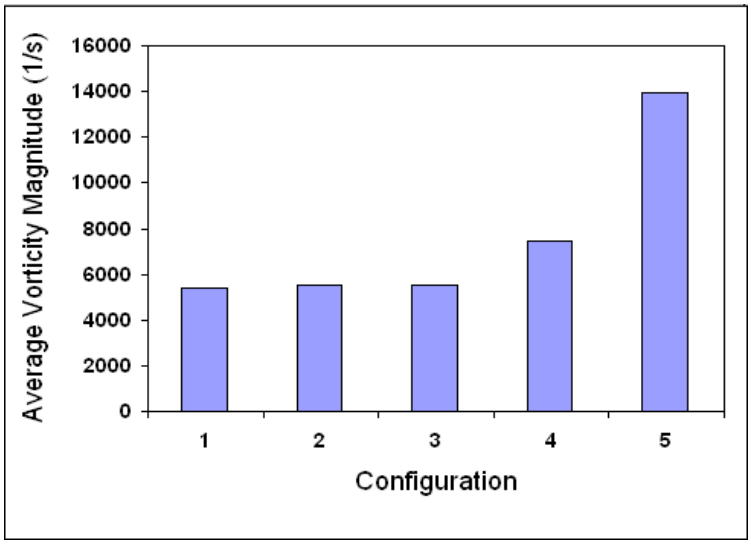

Figure 4. Average vorticity magnitude for different configurations.

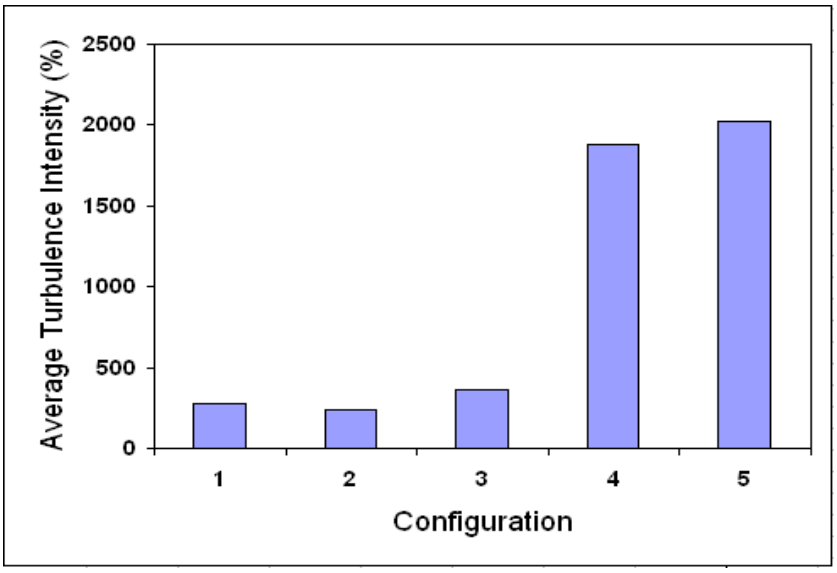

Figure 5. Average turbulence intensity for different configurations.

Figure 6 shows the particle path lines for configuration 1. Twenty-eight particles are tracked, where 10 particles represent H_2S injection stream. One can notice that the two groups of particles slide into the exit tube where mixing takes place due to the presence of a weak shear layer between the two streams.

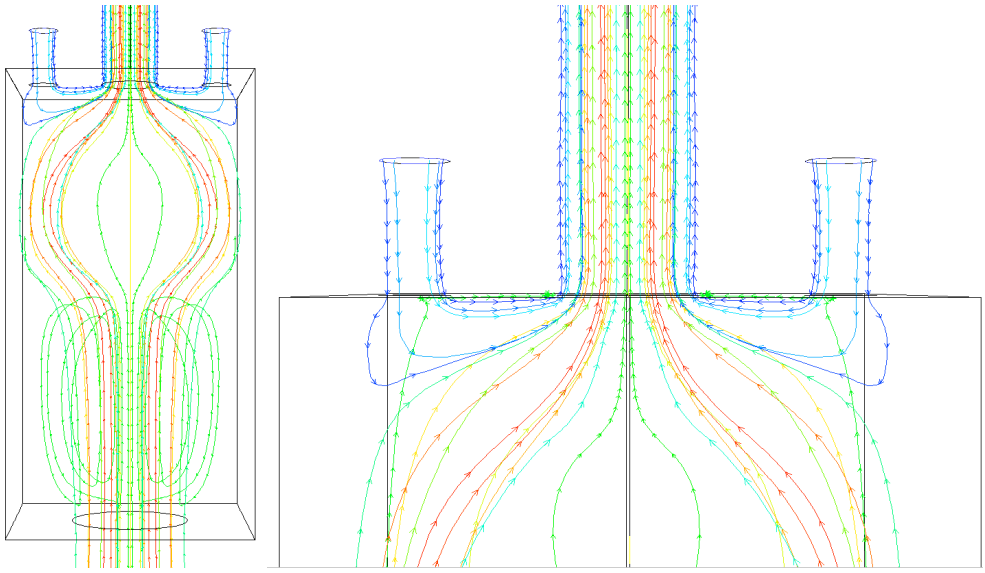

Figure 6. Particle path lines for configuration 1 (10 particles of H_2S stream and 18 particles of hot products stream).

Figure 7 shows the particle path lines for configuration 2. Thirty-six particles are tracked, where 26 particles represent H_2S injection stream. One can see that the hot products stream creates a recirculation zone where H_2S is injected. This recirculation zone vastly improves mixing between the two streams compared to configuration 1.

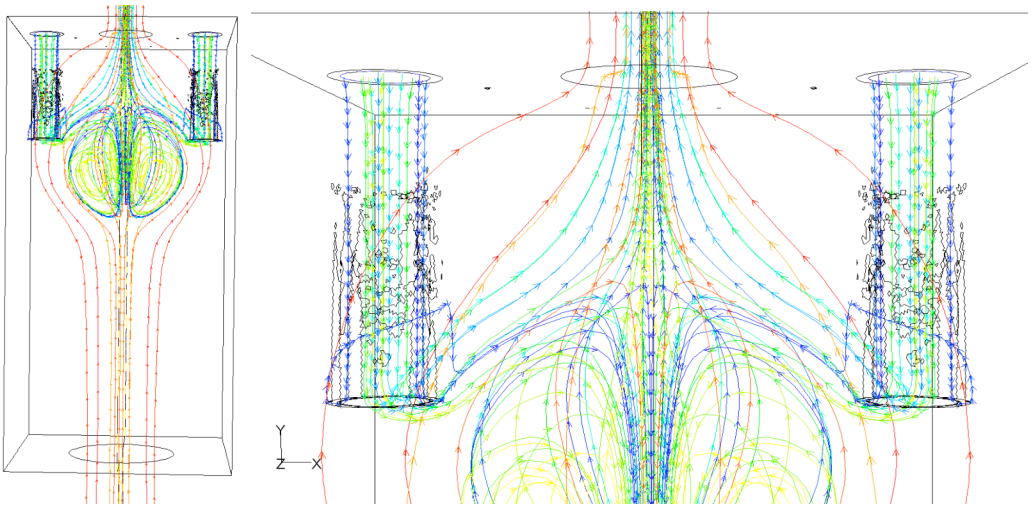

Figure 7. Particle path lines for configuration 2 (26 particles of H_2S stream and 10 particles of hot products stream).

Figure 8 shows the particle path lines for configuration 3. Figure 8.a depicts the particle path lines for hot products particles solely. Figure 8.b shows the particle path lines for the two streams combined. Thirty-two particles are tracked, where only 2 particles represent H_2S injection stream. Similar to configuration 1 mixing is due to the presence of a weak shear layer.

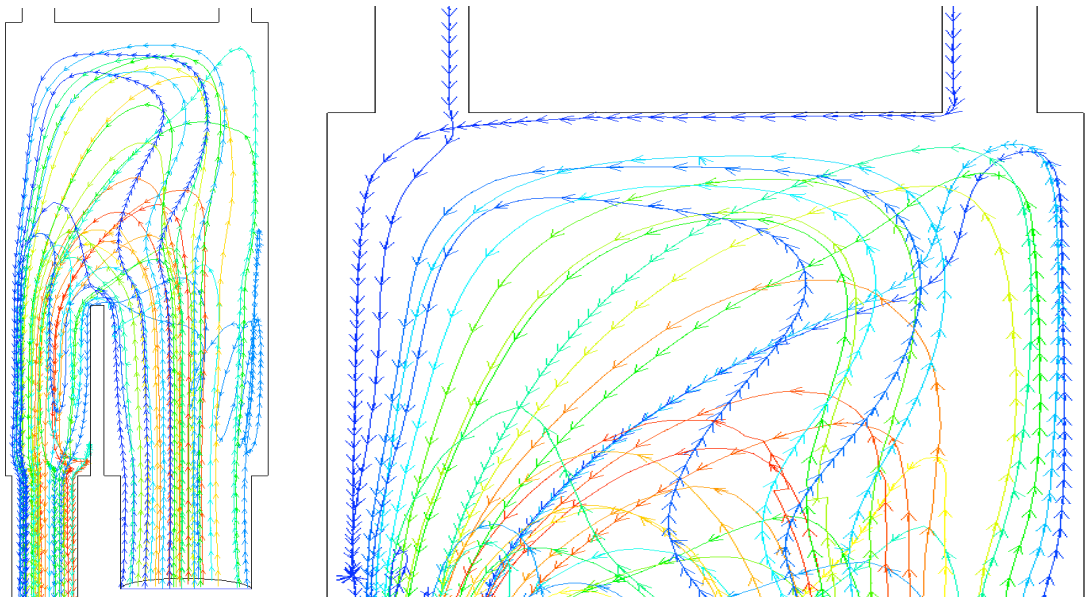

Figure 8. Particle path lines for configuration 3 (2 particles of H_2S stream and 30 particles of hot products stream).

Figure 9 shows the particle path lines for configuration 4. Figure 9.a shows the particle path lines for 8 particles of the hot products stream. A strong recirculation zone is generated by these particles. This recirculation zone entrains injected H_2S stream. Figure 9.b shows particle path lines of 8 particles of the H_2S stream. One can notice that the recirculation zone generated by the hot products stream entrains the H_2S particles into where H_2S forms its own recirculation zone. Figure 9.c shows the particle path lines of the two streams combined. A strong recirculation zone exists by the two streams where mixing takes place very efficiently.

Figure 10 shows the particle path lines for configuration 5. Similar to configuration 4, a recirculation zone is generated by the two streams. Although this recirculation zone is stronger in terms of vorticity magnitude and turbulence intensity, it does not have the effect the recirculation zone in configuration 4 has. This is attributed to the fact that this recirculation zone is concentrated in a smaller area of the reactor. This illustrates why there is better mixing performance in configuration 4.

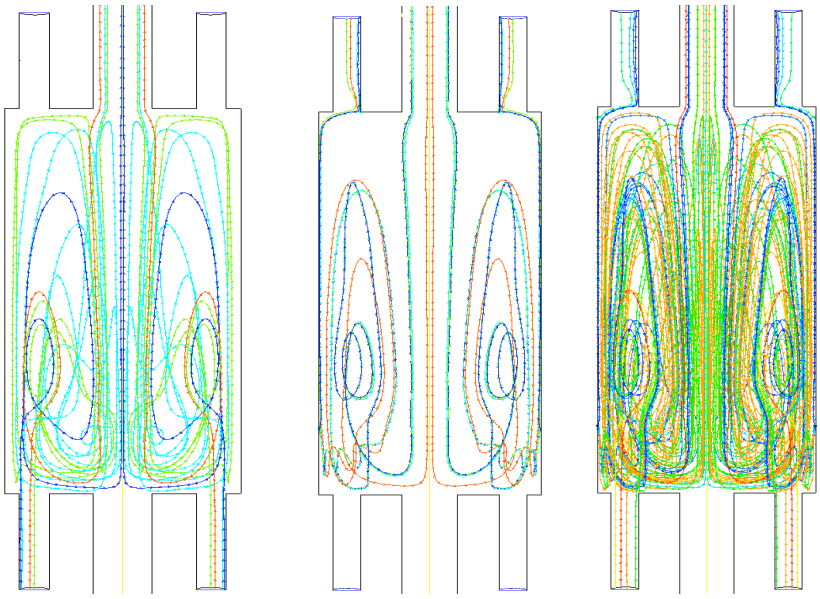

Figure 9. Particle path lines for configuration 4 (8 particles of H_2S stream and 8 particles of hot products stream).

Figure 10. Particle path lines for configuration 5 (2 particles of H_2S stream and 2 particles of hot products stream).

4.2 Reactive CFD simulations for H_2S/O_2 reaction

In this investigation a comparison is demonstrated between combustion of perfectly mixed Claus reactants and combustion of non-mixed Claus reactants. Since we aim to achieve uniform mixture combustion in the Claus process, it is important to identify the effect of having non-premixed combustion of Claus reactants. It is important to note that Chemkin software does not incorporate sound diffusion flame modeling. Therefore, Fluent 6.2 software has been used for this purpose using species transport diffusion modeling and the EDC turbulence-chemistry interaction model. Our 19-reaction reduced mechanism has been used in this examination as representation for the H_2S/O_2 reaction.

First, perfectly premixed mixture of H_2S and O_2 was simulated using 0.125 in diameter plug flow reactor of 0.254 length. The reactor temperature was arbitrarily chosen to be 1600 K. Three equivalence ratios (3, 1, and 0.5) were used to cover the fuel-rich to fuel-lean regimes. The results obtained from the Fluent simulations were compared with corresponding Chemkin simulation for the same equivalence ratio. Figures 11 to 16 show the comparison between the results obtained from Fluent simulations and Chemkin simulation for all equivalence ratios. The data obtained from Chemkin simulations are based on the detailed mechanism by Leeds University[1]. The results reveal very good agreement between the Fluent and Chemkin simulations. The maximum error was observed in the hydrogen mole fraction, which agrees with the results presented in previous quarterly reports.

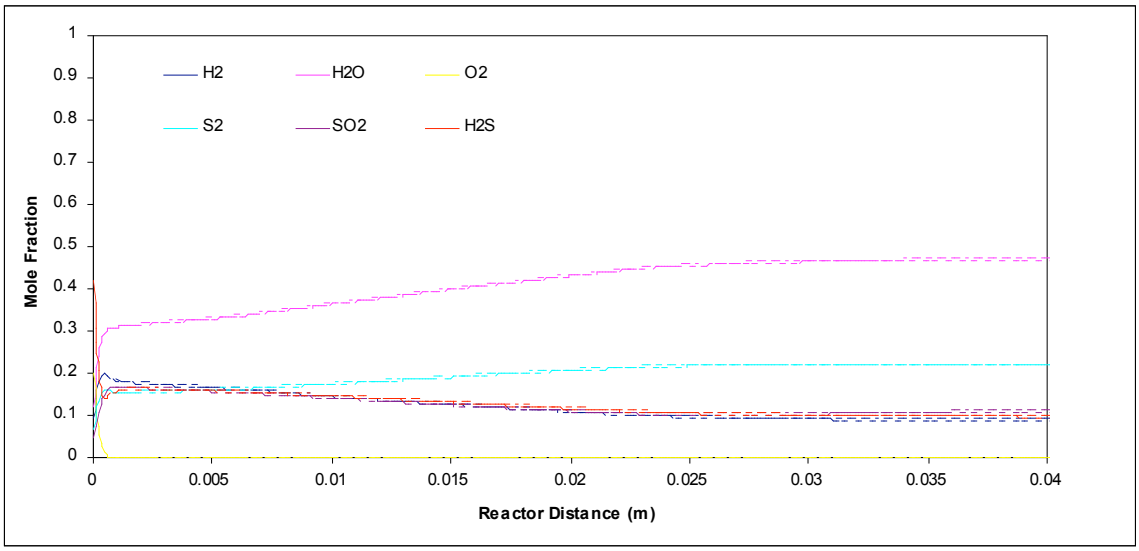

Figure 11. Fluent simulation for perfectly mixed H_2S/O_2 mixture with equivalence ratio of 3.

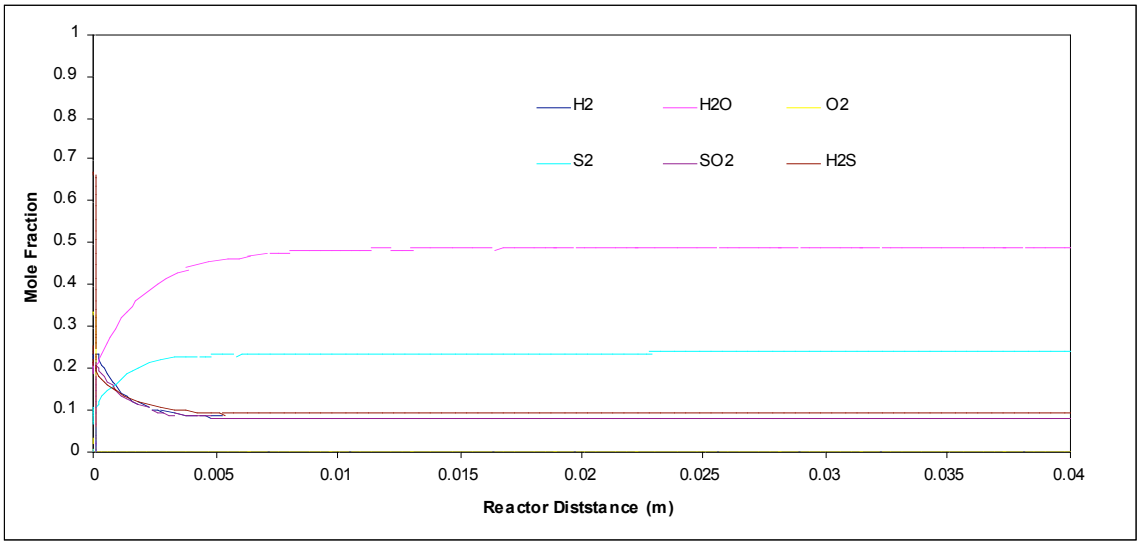

Figure 12. Chemkin simulation for perfectly mixed H_2S/O_2 mixture with equivalence ratio of 3.

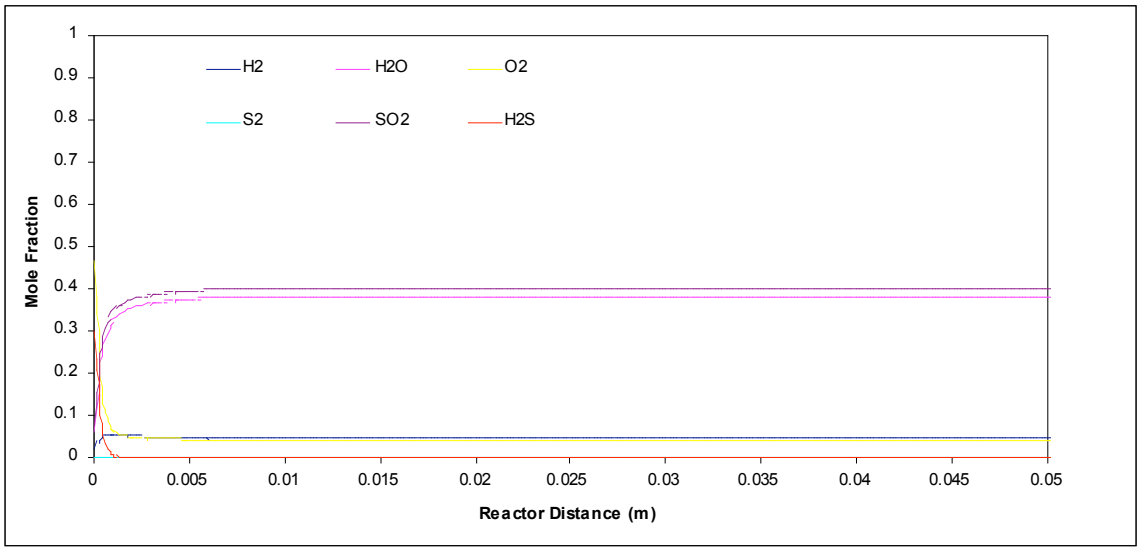

Figure 13. Fluent simulation for perfectly mixed H_2S/O_2 mixture with equivalence ratio of 1.

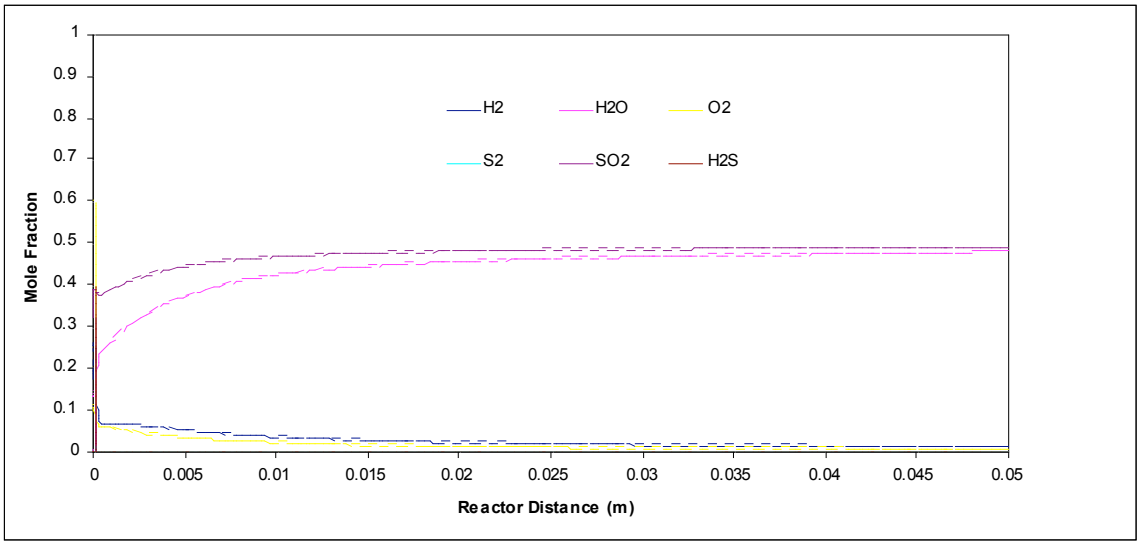

Figure 14. Chemkin simulation for perfectly mixed H_2S/O_2 mixture with equivalence ratio of 1.

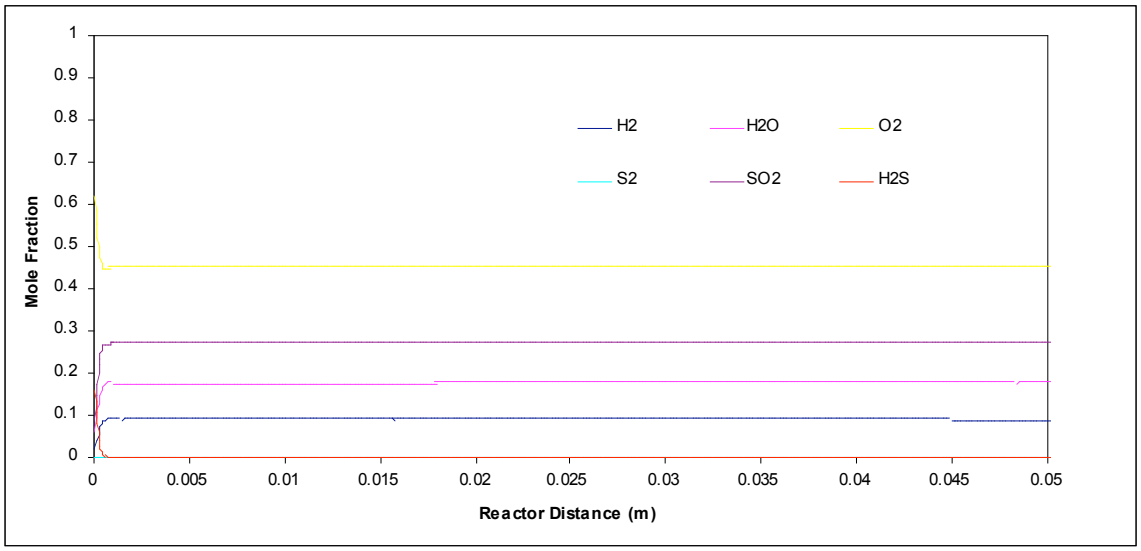

Figure 15. Fluent simulation for perfectly mixed H_2S/O_2 mixture with equivalence ratio of 0.5.

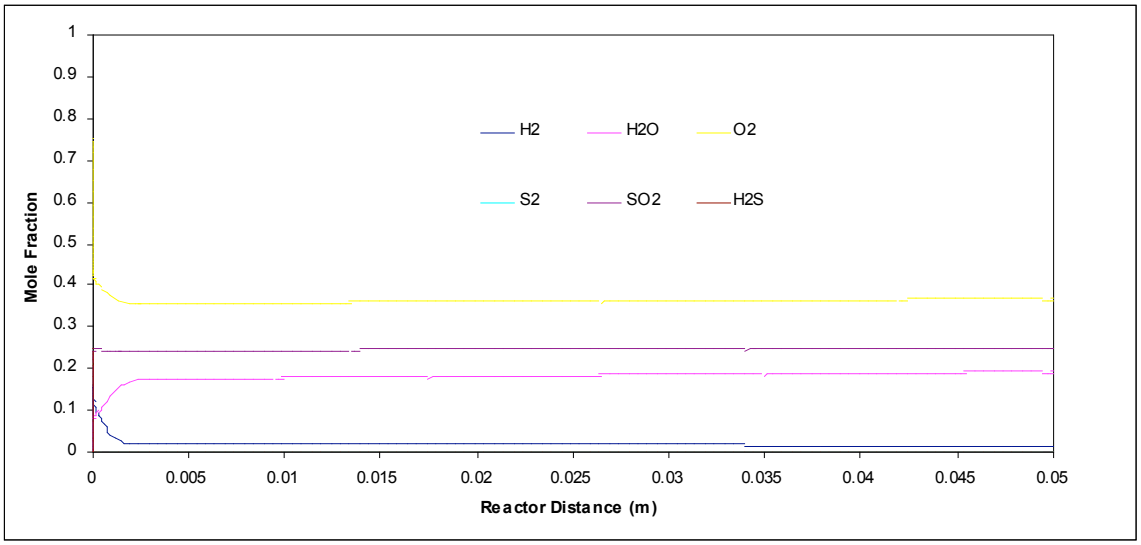

Figure 16. Chemkin simulation for perfectly mixed H_2S/O_2 mixture with equivalence ratio of 0.5.

The effect of diffusion on the H_2S/O_2 reaction was examined using counter flow flame of H_2S and O_2. The simulations started with cold flow mixing of oxygen and hydrogen sulfide. Afterwards, the temperature of the entire reactor was set constant at 1600K for the reaction to take place. Figure 17 shows the comparison between three cold flow cases of H_2S/O_2 counter-flow mixing. One can see the increase in oxygen momentum flux with the decrease of equivalence ratio, which is attributed to the increase of oxygen flow velocity.

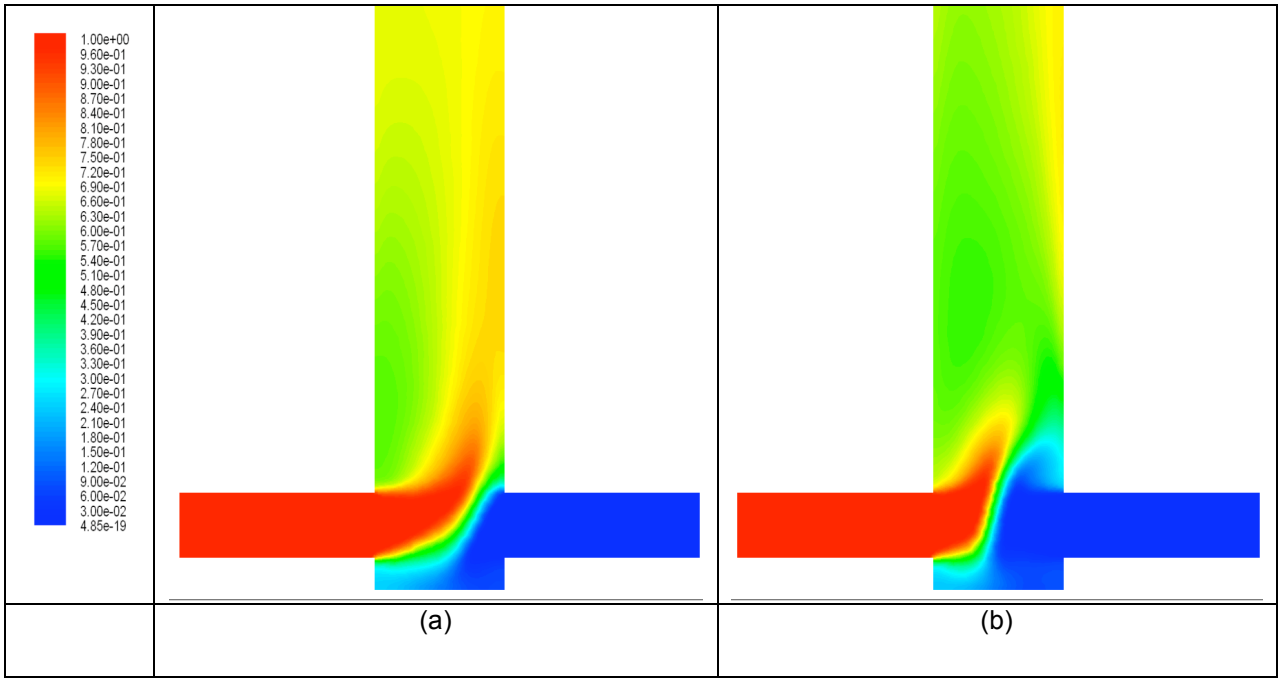

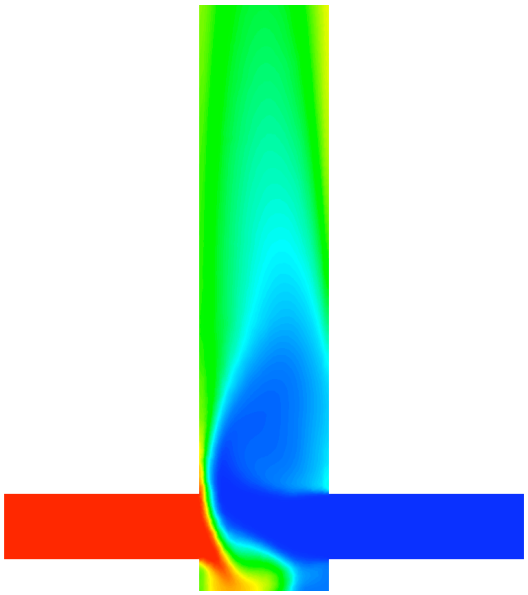

(c)

Figure 17. Hydrogen sulfide mole fraction for cold flow mixing conditions, (a) Φ=3, (b) Φ=1, and (c) Φ=0.5.

Figure 18 shows the hydrogen sulfide mole fraction contours after the reactor temperature was set at 1600 K and the chemical reaction took place. The results prove the conclusions we got from the Chemkin simulations regarding the slowness of H_2S/SO_2 reaction in Claus process. It is noticeable that for Claus conditions, H_2S does not react as rapidly it does in the stoichiometric and the lean cases. This is attributed to the lack of an extremely fast H_2S/O_2 reaction in Claus process where only one third of the required amount of oxygen is introduced. On the other hand, one can notice decomposition of H_2S mole fraction inside its injector, even though no oxygen is present inside this injector. This is attributed to the dissociation effect of the high reactor temperature where H_2S dissociates majorly to H_2 and S_2.

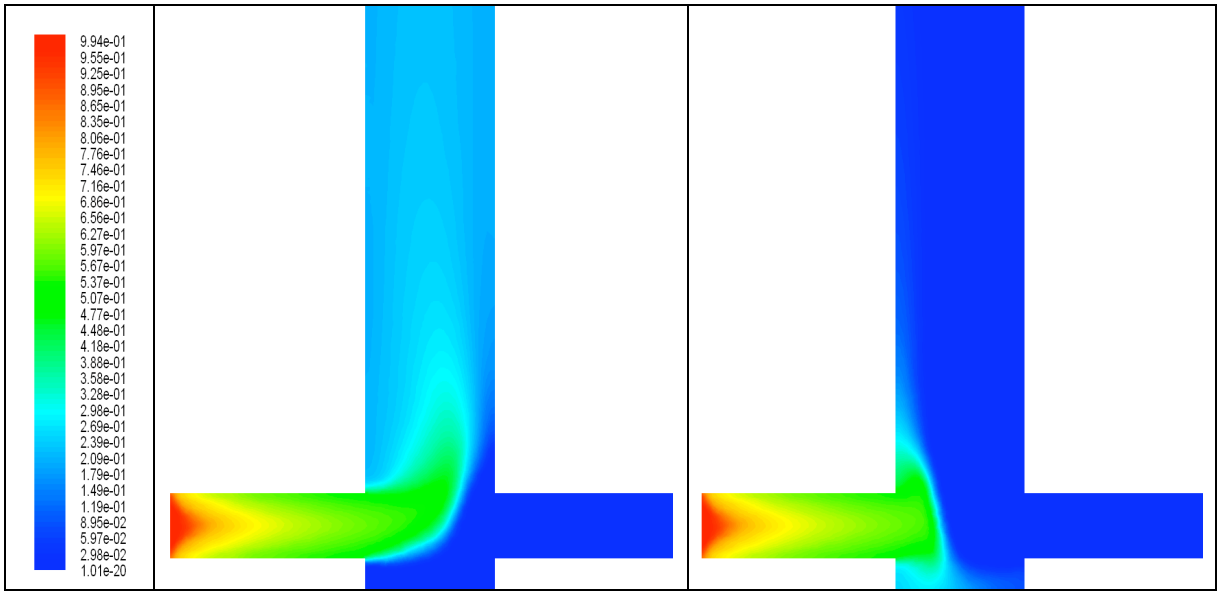

	(a)	(b)

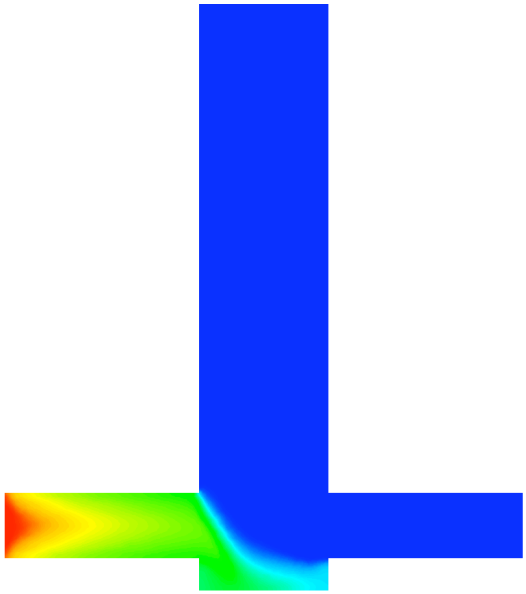

(c)

Figure 18. Hydrogen sulfide mole fraction during combustion at T= 1600 K, (a) Φ=3, (b) Φ=1, and (c) Φ=0.5.

Figure 19 shows sulfur dioxide mole fraction contours. For the Claus conditions case, the SO_2 mole fraction reaches the maximum value in the vicinity of the O_2 injector inlet. This is attributed to the higher momentum of H_2S injector, which drifts the reaction towards the lower momentum injector. A thin layer between the two jets has the maximum mole fraction of sulfur dioxide. This is attributed to the presence of localized O_2/H_2S mixture along this thin layer. On the other hand, the sulfur dioxide mole fraction is reduced downstream because of the continuation of the reaction between H_2S and SO_2 in the absence of oxygen to produce sulfur. For both stoichiometric and lean cases, the hydrogen sulfide starts with minimal mole fraction values and increases downstream. This is attributed to the presence of sufficient oxygen for the reaction of H_2S to continue in the direction of forming SO_2.

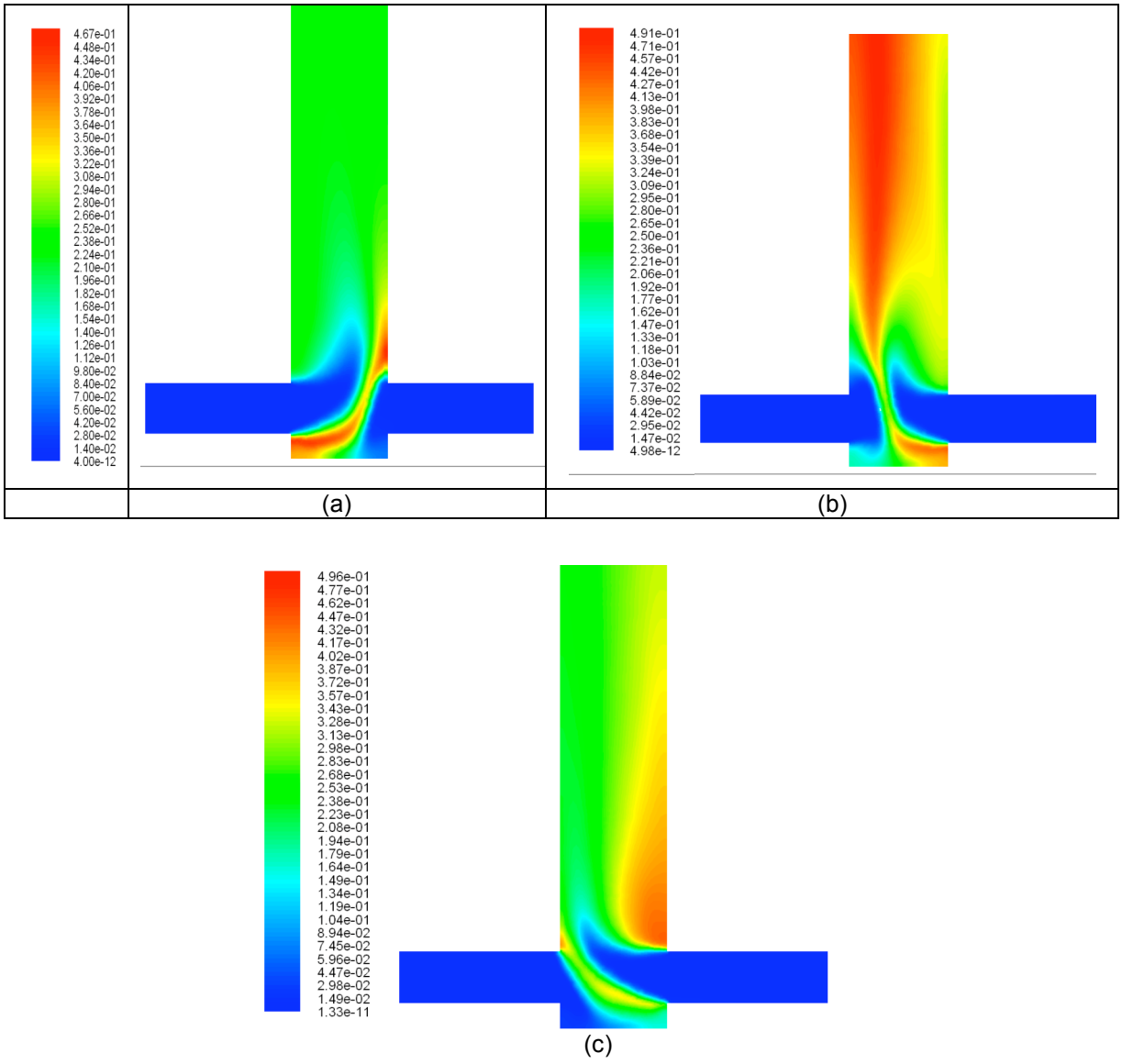

Figure 19. Sulfur dioxide mole fraction during combustion at T= 1600 K, (a) Φ=3, (b) Φ=1, and (c) Φ=0.5.

Figure 20 shows the sulfur mole fraction contours. For all the equivalence ratios, sulfur is formed inside H_2S injector because of hydrogen sulfide dissociation at high temperatures. However, the progression of the reaction differs according to the equivalence ratio. For Claus conditions, the S_2

mole fraction increases as expected. On the other hand, the S_2 mole fraction decreases to almost zero for both stoichiometric and lean conditions.

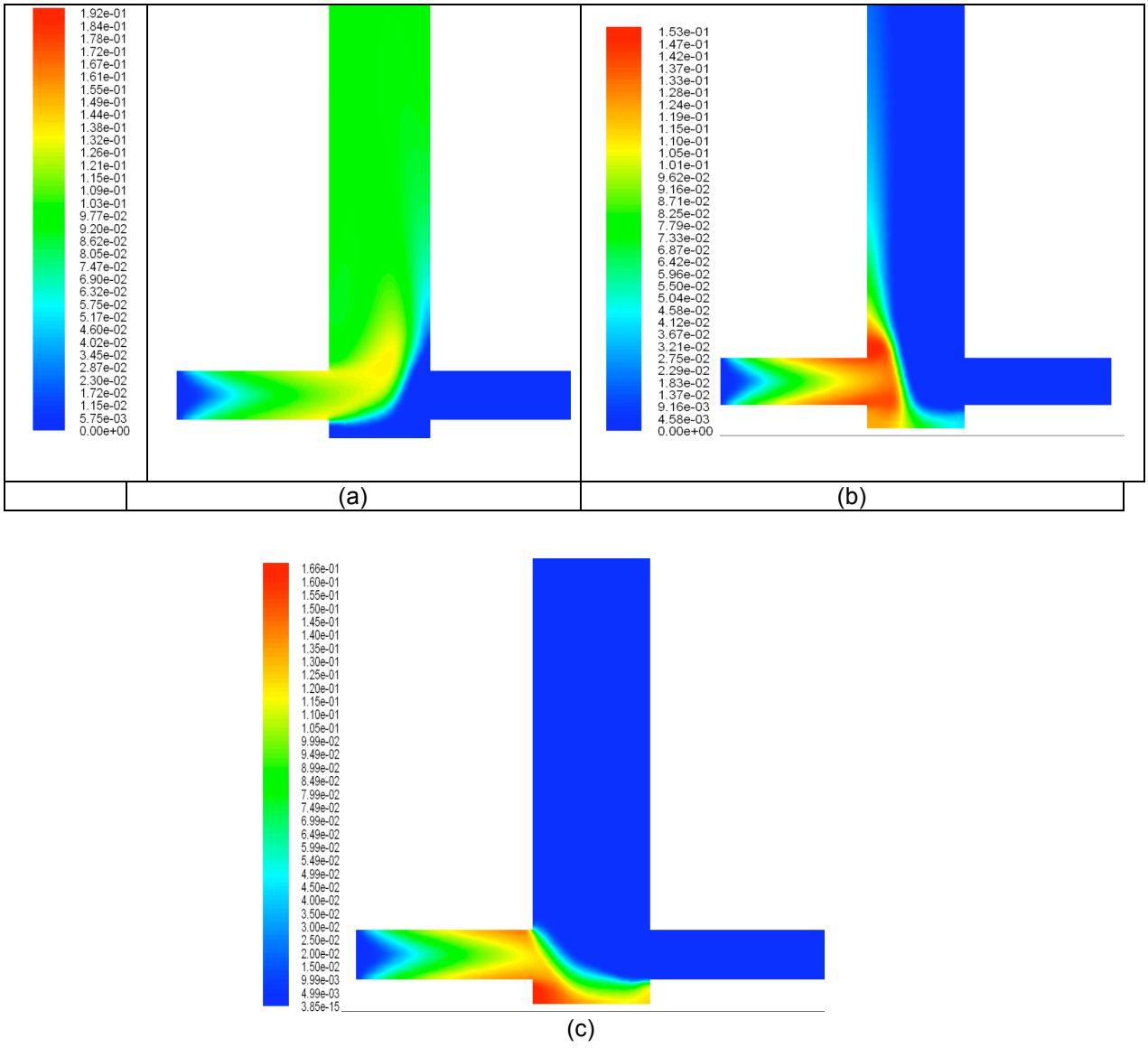

Figure 20. Sulfur mole fraction during combustion at T= 1600 K, (a) Φ=3, (b) Φ=1, and (c) Φ=0.5.

Figure 21 shows hydrogen mole fraction contours. In agreement with the aforementioned results, hydrogen production starts inside the H_2S injector where H_2S dissociates. However, the H_2 mole fraction is decreased for stoichiometric and lean conditions where oxygen is present in the reaction pool downstream.

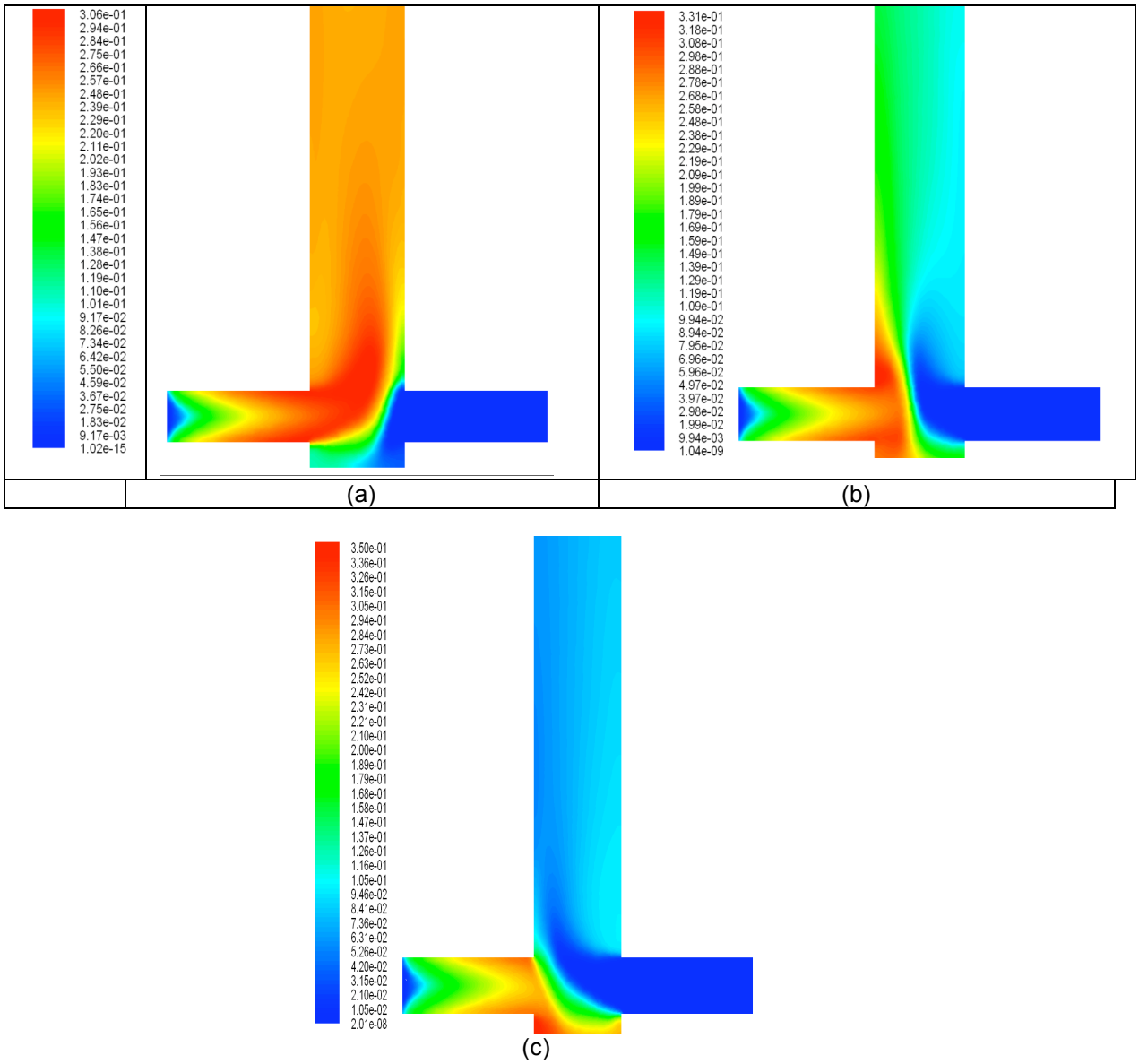

Figure 21. Hydrogen mole fraction during combustion at T= 1600 K, (a) Φ=3, (b) Φ=1, and (c) Φ=0.5.

4.3 Experimental non-reactive examination for Claus reactants mixing chamber

Based on the non-reactive simulations discussed above, configuration 4, which has the best performance amongst all the configurations, was developed in order to experimentally examine the mixing characteristics of the Claus reactants inside it. Nitrogen was used to simulate hydrogen sulfide while density correction was performed using the momentum flux ratio. Oxygen was used as the oxidizer. Figure 22 shows the experimental setup for configuration 4, where the dimensions of the mixing chambers are 4x2x1 inch.

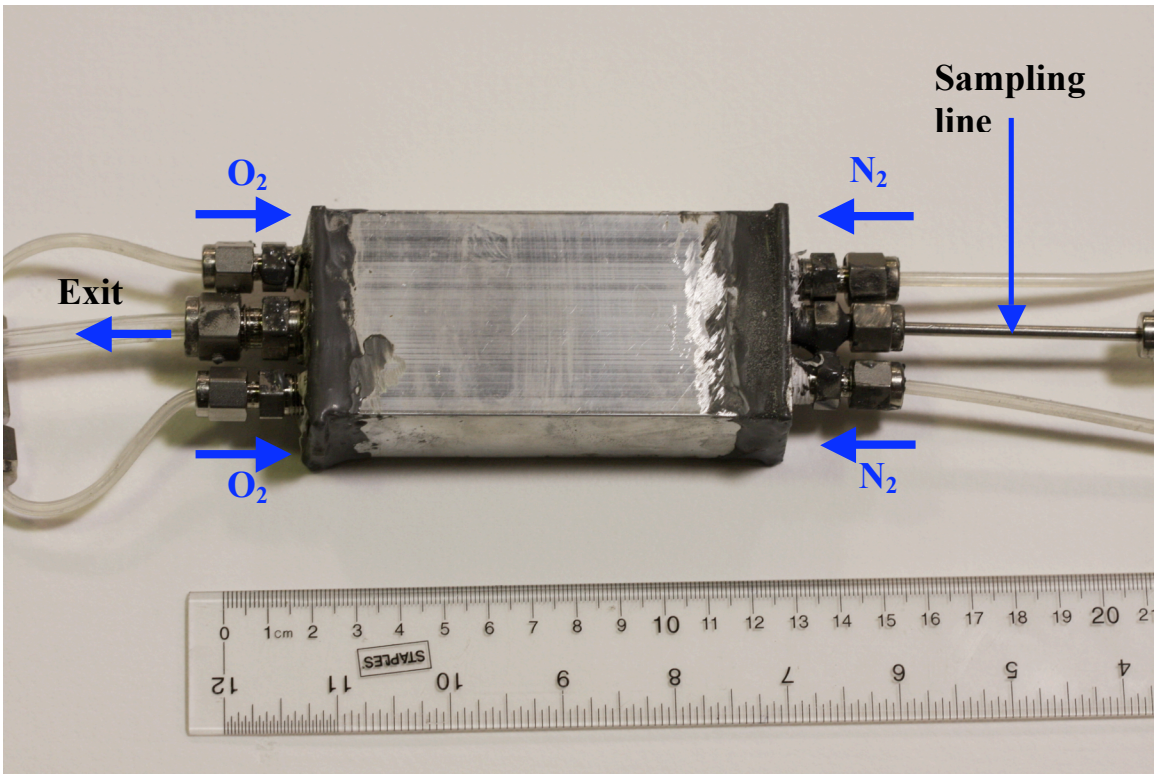

Figure 22. Mixing chamber for Claus reactants.

Figures 23 and 24 show the mole fraction of oxygen along the axial distance for two different runs. The two runs have different nitrogen and oxygen flow rates, but the ratio was maintained at Claus conditions. The results show very good mixing properties for this specific configuration. The oxygen mole fraction varies along the centerline by only 13% of the asymptotic oxygen mole fraction. The zero-centimeter axial value represents the exit side of the mixing chamber and 10-centimeter axial distance is at the sampling line side.

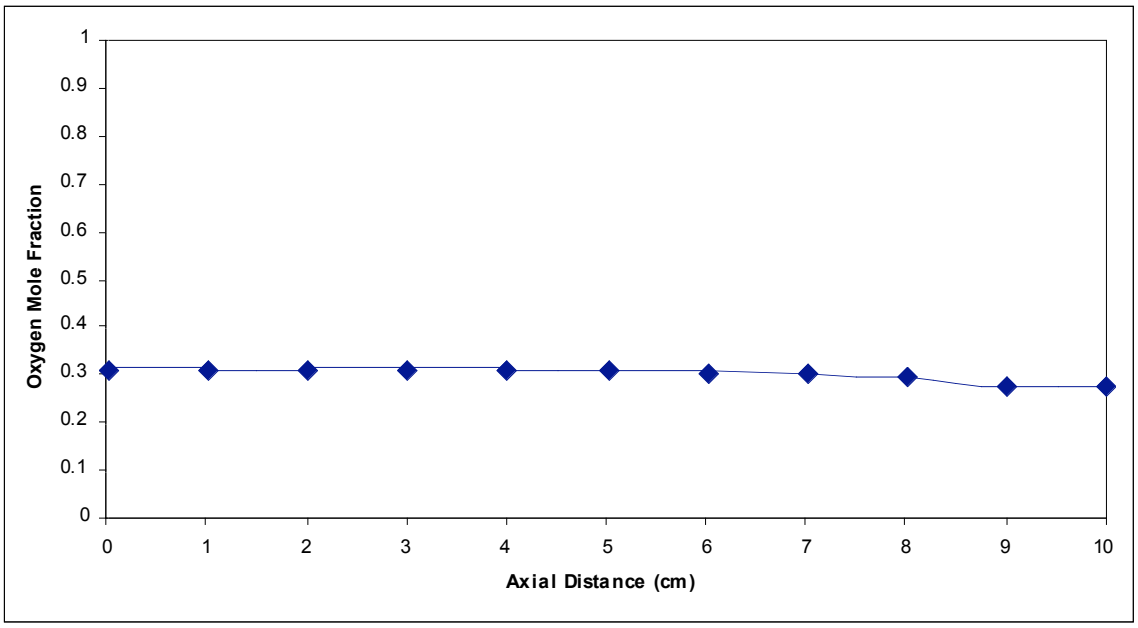

Figure 23. Oxygen mole fraction. Oxygen flow rate is 1.95 lit/min, nitrogen flow rate is 4.27 lit/min.

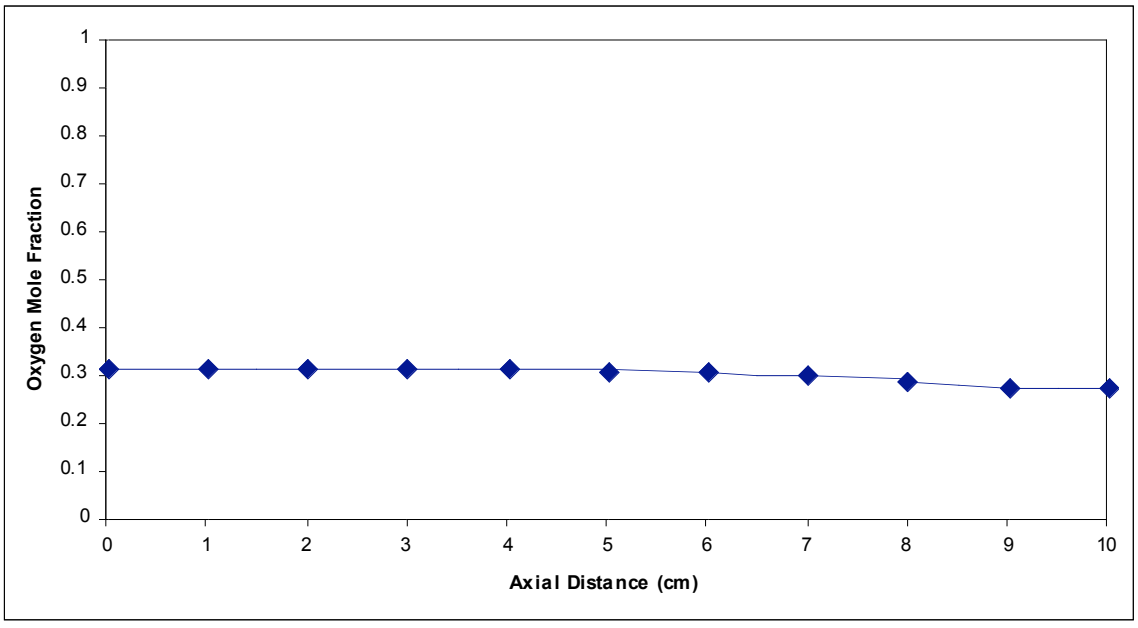

Figure 24. Oxygen mole fraction, oxygen flow rate is 1.3 lit/min, nitrogen flow rate is 2.846 lit/min.

5. Summary

Non-reactive simulations were conducted to continue the investigation of Claus reactants mixing enhancement. Five mixing chamber configurations were simulated to determine the best mixing characteristics between H_2S and hot combustions products. Configurations 1 and 3 were found to have the worse mixing characteristics, in which the mixing took place through a weak shear layer created between the two streams. Despite having equal average vorticity magnitude and turbulence intensities, configuration 2 gave much better mixing characteristics compared to configurations 1 and 3. This is attributed to the presence of a recirculation zone generated in the middle of the mixing chamber. Meanwhile, hydrogen sulfide was injected into the region where the recirculation zone was present. In other words, the injected hydrogen sulfide was injected to a recirculation zone of the combustion hot products, which improved the mixing significantly. Configurations 4 and 5 showed a prominent performance in terms of average vorticity magnitude and turbulence intensity. However, configuration 4 showed a better mixing performance, in which a strong recirculation zone is generated and well distributed along the mixing chamber. Contrary to configuration 2, the recirculation zone of configuration 4 entrains the injected hydrogen sulfide into it. This improves the mixing significantly compared to any other configuration. On the other hand, the recirculation zone of configuration 5 was more concentrated in a smaller portion of the mixing chamber.

Moreover, reactive CFD simulations were performed to identify the effect of reactants diffusion on chemical reactions. In the beginning, a comparison using Chemkin and Fluent software was performed on a perfectly premixed reactant mixture. Our 19-reaction reduced mechanism was used as the chemical reaction mechanism for Fluent simulations. The results showed good agreement between the Chemkin and Fluent simulations. The effect of reactant diffusion was examined for different equivalence ratios which vary between fuel-rich and fuel-lean regimes. Counter-flow flame was used as diffusion flame where the temperature was maintained constant throughout all the simulations at 1600 K. The results highlighted the presence of different localized reaction spots where the reaction has different directions corresponding to the mixture at each spot. On the other hand, the results revealed that hydrogen sulfide dissociates significantly inside the injector to hydrogen and sulfur. Moreover, the results showed the need to have a longer distance downstream in order to achieve the reaction completion compared to the perfectly premixed conditions. Finally, an experimental examination for configuration 4, presented in the non-reactive mixing investigation, was conducted in order to identify the mixing uniformity using two different sets of reactants flow rates. The results showed promising mixing uniform characteristics where the change of oxygen mole fraction throughout the mixing chamber axial distance did not exceed 13% of the asymptotic value of oxygen mole fraction.

7. Difficulties Encountered/Overcome

A fume hood is being installed for running hydrogen sulfide experiment in order to provide the required environmental safety for running reactive hydrogen sulfide experiments.

8. Deliverables for the Next Quarter

- Further numerical/experimental examination for the most promising mixing chamber configurations will be demonstrated in order to improve mixing characteristics. Meanwhile, the flow parameters responsible for mixing enhancement for this geometry will be identified.
- A safe working space for hydrogen sulfide experiments will be prepared.
- Our 19-reaction reduced mechanism will be validated with experimental results available in the literature.

- Reactive CFD simulations for the chosen mixing simulations will be performed as a last step before preparing the safe working facility for hydrogen sulfide use.

9. Publications

1. Gupta, A. K. and Sassi, M. "Sulfur Recovery from Acid Gas Using the Claus Process and High Temperature Air Combustion Technology," American J. of Environmental Sciences, Vol. 4, No. 5, 2008, pp. 502-511.
2. Selim, H., Gupta, A. K. and Sassi, M. "Variation of Optimum Claus Reactor temperature with Acid Gas Composition," IECEC Conference, Cleveland, OH, July 28-30, 2008, Paper No. AIAA-2008-5797.
3. Selim, H., Gupta, A. K. and Sassi, M. "Reduced Mechanism for Hydrogen Sulfide Oxidation," 47th AIAA Aerospace Sciences Conference, Orlando, FL, January 5-8, 2009, Paper No. AIAA-2009-1392.
4. Selim, H. and Gupta, A. K. "Nonreactive Study for the Reactants Mixing in Claus Reactions," 7th Intl. Energy Conversion Engineering Conference (7th IECEC), Denver, CO, August 2-5, 2009, Paper No. AIAA-2009-4506.
5. Selim, H and Gupta, A. K. and Sassi, M. "Reduction and Validation of Detailed Kinetic Reactions in Thermal Stage of Claus Process," 48th AIAA Aerospace Sciences Conference, Orlando, FL, January 3-7, 2010, Paper AIAA-2010-1356.
6. Al Amoodi, N., Selim, H., Gupta, A. K., Sassi, M. and Al Shoaibi, A. "Numerical Simulations of the Thermal Stage in Claus Process: Equilibrium and Kinetic Investigation," 48th AIAA Aerospace Sciences Conference, Orlando, FL, January 3-7, 2010, AIAA-2010-1355.

Appendix

Justification and Background

Hydrogen sulfide is present in numerous gaseous waste streams from natural gas plants, oil refineries, and wastewater treatment plants, among other processes. These streams usually also contain carbon dioxide, water vapor, trace quantities of hydrocarbons, sulfur, and ammonia. Waste gases with ammonia are called sour gases, while those without ammonia are called acid gases. Sulfur must be recovered from these waste streams before flaring them. Sulfur recovery from sour or acid gas typically involves application of the well-known Claus process, using the reaction between hydrogen sulfide and sulfur dioxide (produced at the Claus process furnace from the combustion of H_2S with air and/or oxygen), yielding elemental sulfur and water vapor: $2H_2S(g) + SO_2(g) = (3/n)\ S_n(g) + 2H_2O(g)$ with ΔH_r= -108 kJ/mol. Therefore, higher conversions for this exothermic, equilibrium-limited reaction call for low temperatures, which lead to low reaction rates that dictate the use of a catalyst. The catalytic conversion is usually carried out in a multistage, fixed-bed, adsorptive reactor process, which counteracts the severe equilibrium limitations at high conversions. This technology process can convert about 96% to 97% of the influent sulfur in H_2S to S. However, higher removal requires critical examination of the process and use of a near isothermal reactor, since the conversion is critically dependent upon the exothermic and endothermic conditions of the reactions.

Flameless combustion has been shown to provide uniform thermal field in the reactor so that the reactor temperature is near uniform. Reactor size can also be reduced and combustion-generated pollutants emissions can be reduced by up to 50%. Energy efficiency can be increased by up to 30%. The application of this technology appears to offer great advantages for the processes under consideration. The UAE, which pumps about 2.4 million bpd of crude oil, is also home to the world's fifth biggest gas reserves at about 200 trillion cubic feet. Abu Dhabi Gas Industries (GASCO), an operating company of the Abu Dhabi National Oil Company (ADNOC), is leading a drive to boost gas production in the UAE from five to seven billion cubic feet per day. This calls for sulfur recovery capacity of over 3,000 metric tons per day with the associated SOx and NOx emissions. Therefore, the adoption and further development of flameless combustion technology for sulfur recovery among other commercial and industrial heating processes is expected to be crucial and beneficial, both economically and environmentally.

The conventional sulfur recovery process is based upon the withdrawal of sulfur by in situ condensation within the reactor. The selective removal of water should, however, be a far more effective technique, as its effect on the equilibrium composition in the mass action equation is much greater. The in situ combination of the heterogeneously catalyzed Claus reaction and an adsorptive water separation seems especially promising, as both reaction and adsorption exhibit similar kinetics, and pressure can be adapted to the needs of the adsorptive separation. Such an adsorptive reactor will lead to almost complete conversion as long as the adsorption capacity is not exhausted. There are numerous possibilities for implementing these two functions, ranging from fixed-beds with homogeneous catalyst/adsorbent mixtures to spatially structured distributions or even fluidized beds. Most of the previous studies have concentrated on the Claus catalytic conversion reactors and the TGTU. However, some previous studies have identified the Claus furnace as one of the most important yet least understood parts of the modified Claus process. The furnace is where the combustion reaction and the initial sulfur conversion (through an endothermic gaseous reaction) take place. It is also where the SO_2 required by the downstream catalytic stages is produced and the contaminants (such as ammonia and BTX (benzene, toluene, xylene) are supposedly destroyed. The main two reactions in the Claus furnace are: $H_2S + 3/2\ O_2 = SO_2 + H_2O$, with ΔH_r= -518 kJ/mol, and $2H_2S + SO_2 = 3/2\ S_2 + 2H_2O$, with ΔH_r= +47 kJ/mol. This last endothermic reaction is responsible for up to 67% conversion of the sulfur at about 1200 °C. Moreover, many side reactions take place in the furnace; these side reactions reduce sulfur recovery and/or produce unwanted components that end up as ambient

pollutant emissions. Therefore, it would be useful to combine the endothermic and exothermic process using an isothermal reactor offered by flameless oxidation combustion.

Approach

Critical review

We propose to conduct a critical review of the various approaches used for sulfur removal from the sour gas. The emphasis here will be on sulfur chemistry with due consideration to the fate of ammonia. Following the review, an experimental and a CFD numerical study of the flameless oxidation of the fuel will be conducted as follows:

CFD simulation

A numerical simulation study of the flame under normal and flameless oxidation of fuels in the furnace will be conducted using the available codes. Global features of the flow and thermal behavior will be obtained using the Fluent CFD and Chemkin computer codes. These codes provide detailed simulation of the flow, thermal and chemical behaviors (i.e., detailed chemistry) in the reactor flow using gas-phase reactants. The sulfur in the fuel is in gas phase, so we will be able to simulate and monitor the fate of sulfur during various stages of endothermic and exothermic reactions and over a range of temperature regimes, including those covered in the Claus furnace process. The simulation results will also guide the final design of the flameless furnace. The simulations will also help assist in the experimental program for data validation with the eventual goal of implementing the process for sulfur removal.

Experimental study

An experimental study of the flameless vs. normal flame combustion process for the conditions examined in the theoretical study, including that of Claus furnace, will be conducted. We will explore the operating conditions and the exhaust gas analysis under conditions of both flame and flameless modes to determine the extent of sulfur conversion under the two conditions over the temperatures that can simulate endothermic and exothermic conditions in the Claus furnace. The goal is to seek conditions that yield the highest sulfur recovery from a process. To some extent, these conditions will be based on the composition of the acid/sour gas, from sulfur-rich (> 50% H_2S) to lean (< 20% H_2S). It is expected that our fundamental information will contribute to the eventual design guidelines of an advanced sulfur recovery process furnace operating under flameless combustion mode.

References

[1] http://www.chem.leeds.ac.uk/combustion/sox.htm

Evaluating Solid Oxide Fuel Cell Systems for Operation on Petroleum Off-Gases with Contaminants

UMD Investigators: Greg Jackson, Bryan Eichhorn
UMD GRAs: Siddarth Patel, Lei Wang
PI Investigators: Ali Almansoori, Ahmed Nafees
Start Date: October 2006

1. Objective/Abstract

In this program, UMD and PI will build on the established collaboration from earlier work – both experimental and modeling – to explore the impact of petroleum off-gas composition including effects of contaminants (H_2S and HCl) on SOFC performance/design. Single-cell SOFC experiments will be used to enhance and validate existing single-cell SOFC models to incorporate the effects of hydrocarbon composition and H_2S on SOFC performance. These single cell models will then be translated to full stack evaluations in higher dimensions and these models will then be incorporated into process-level plant models to evaluate the effectiveness of SOFCs for capturing energy from petroleum gases and for providing a means for possible CO_2 capture within a plant context. This Phase II testing and development effort will also seek to bring an industrial collaborator to work with the team to explore design and implementation challenges for a future SOFC demonstration operating on relevant petroleum gas streams.

2. Deliverables for the Completed Quarter

Task 1: Establishing experimental facilities for MEA testing with trace contaminants
- No experimental modifications were done during this quarter.

Task 2: Long-term testing MEAs for selected fuels and syngas with trace H_2S and HCl
- UMD has redone durability tests for Ni/YSZ operating continuously on a direct C_4H_{10} feed to provide baseline comparison with more advanced Ni/CeO_2/YSZ cells. This work has been done in order to complete some holes in the data for a joint UMD-PI publication with the UMD team (Patel, Wang, and Jackson) and PI's Almansoori as co-authors.

Task 3: Enhancing MEA models to evaluate contaminant-tolerant designs
- UMD began to enhance MEA models by combining the distributed electrochemistry and the non-isothermal models for better coupling of electrochemistry and internal reforming predictions in down-the-channel models.

Task 4: Performing system level analysis of integrated SOFC / off-gas processing plant
- UMD developed a basic SOFC model in Aspen Plus and is expanding it to include the previous SOFC physics-based model through a FORTRAN sub-model utilizing previously presented physics. This model will be used as the basis for two summer intern projects from the PI, who will study plant level system models relevant to petroleum processing.

Task 5: Establishing SOFC-industry partner for future demonstration
- No activities were pursued for this task during this quarter.

3. Summary of UMD Project Activities for the Completed Quarter

The fourth quarter of this Phase II effort included the following:

- Two discussions between UMD and PI team members about the implementation of codes in Aspen Plus with a decision to hire interns to come from PI to UMD this summer to work on the system development.
- Final durability testing of Ni/YSZ cells without CeO_2 on butane to provide the data for finalizing a joint publication;
- Establishment of simple SOFC model in Aspen Plus and initial development of more complicated model for integration into larger-scale petroleum processing plant.
  .

This quarter's progress has relied upon work at the UMD, as Mr. Nafees had an increased teaching load and was unavailable to work on the project during this quarter at the PI. Thus, the UMD team took back up the initiation of the Aspen Plus model implementation. This, combined with Mr. Wang at UMD learning new aspects of SOFC testing, meant a stronger focus on model development during this quarter than progress on experiments. Mr. Wang has now begun to get consistent cell performance, and more experimental results will be presented at the end of the upcoming quarter.

Task1: Establishing experimental facilities for MEA testing with trace contaminants
No additional changes to the experimental facility were pursued during the past quarter.

Task 2: Long-term testing MEAs for selected fuels and syngas with trace H_2S and HCl
In addition to more tests on Ni/YSZ and Ni/CeO_2/YSZ anodes operating directly on butane, additional cell characterization was undertaken by collaborating with Prof. Robert Walker's group (now at Montana State) to utilize *ex situ* Raman spectroscopy to explore the nature of cell degradation during hydrocarbon operation. The purpose of the Raman characterization was to identify decay mechanisms which began to show up in continuous testing with direct C_4H_{10} anode feeds with steam-to-carbon ratio (S/C) of 1.5 and T_{cell} = 800 ºC after six days of testing. Figure 1 shows sample Raman spectra as provided by Bryan Eigenbrodt and Prof. Rob Walker from Montana State. It is relatively clear from the Raman spectra that there is some degree of Ni oxidation throughout the anode, but in particular, the anode functional layer is impacted by the formation of various Ni oxide species that show up in the Raman signals. In addition, the results show that the anode is not overwhelmed with strong graphite peaks as observed in previous Ni/YSZ anode studies (1), but all the same, some graphite is observed particularly at the top surface of the support layer of the Ni/CeO_2/YSZ anode. However, these results nonetheless do confirm the ability for the CeO_2 addition to suppress graphite, which, as reported last time, is linked to increased stability and high power performance with direct hydrocarbon feeds.

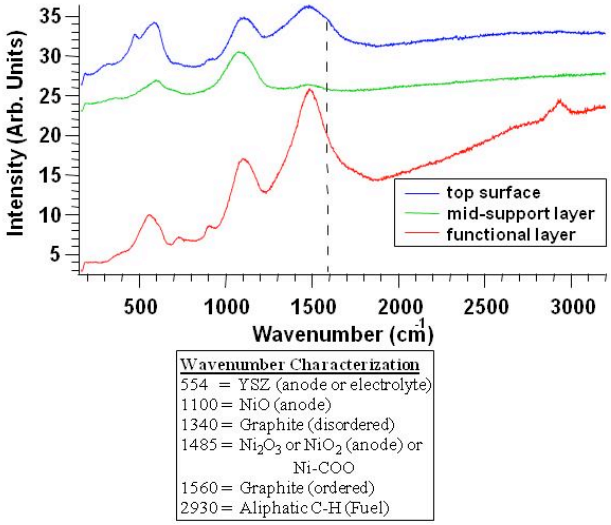

Figure 1. *Ex situ* Raman characterization of Ni/CeO2/YSZ anodes after testing during oxidation of C_4H_{10} feed with a steam-to-carbon ratio (S/C) of 1.5 and T_{cell} = 800 ºC. Raman spectra are taken at the top anode surface, at a mid-point in the anode support layer, and in the anode functional layer. The results show strong Ni oxidation in the functional layer and on the surface, and also indicate graphite most notably on the top surface.

Long-term testing results with the Ni/YSZ anodes with direct C_4H_{10} feed with a steam-to-carbon ratio (S/C) of 1.5 and T_{cell} = 800 ºC continued. Some failures in the rig slowed these tests, which were necessary to finish a joint publication entitled "Effects of ceria addition on Ni/YSZ SOFC anodes operating with syngas and n-butane." This paper is an extension of a conference paper presented last year at ASME's 7th Intl. Fuel Cell Science, Engineering, and Technology meeting (2). These tests, which are ongoing now to compare with long-term tests of the Ni/CeO_2/YSZ anodes on similar operating conditions, are near completion. Tests with H_2S and the impact of ceria on mitigating sulfur poisoning will be the focus of tests for the upcoming quarter.

Task 3: Enhancing MEA models to evaluate contaminant-tolerant designs
The detailed MEA models for non-isothermal conditions are now being combined with distributed electrochemistry as first presented in the Ph.D. dissertation of Steven DeCaluwe (3). The distributed electrochemistry models, while slower from a computational standpoint, will allow for better look-up tables for local performance based on local composition and temperature. The distributed electrochemistry model removes the artificial utilization thickness parameter in the through-the-membrane models as originally presented in an earlier SOFC modeling reference by the UMD team (4). These detailed models with microkinetic surface chemistry models are still being adapted to include hydrocarbon reforming chemistry and then being used to develop look up tables for the Aspen Plus model discussed in the following task.

Task 4: Performing system level analysis of integrated SOFC / off-gas processing plant
UMD established the equations for a simplified down-the-channel SOFC model for integration into Aspen/Hisys. Aspen Plus is currently being used by the UMD team to establish the SOFC model for larger petroleum processing plant simulation. Aspen Plus is a useful process simulator for process analysis with temperature- and pressure-dependent thermodynamic and physical property databases for relevant chemical species. While it has numerous process components, SOFCs is not one of them. Thus, the UMD team has been building a simple first-generation SOFC model for the Aspen Plus plant mode.

A challenge in modeling the SOFC in Aspen Plus is that the stream mixing and transfer functions do not accommodate the ion transport across the SOFC membrane. Others have solved this by developing custom process simulators using Aspen Plus's internal language compilers (FORTRAN, Visual Basic, or C++). The UMD team (Wang and Jackson) is now working on implementing the previously reported SOFC model into a FORTRAN code for implementation in Aspen Plus. As a predecessor to this more complete model and to a distributed electrochemistry model, a simpler process model using a combination of Aspen Plus modules has been created as illustrated in Figure 2. In this simplified model, the amount of O^{2-} flux is set as an O_2 flux which is calculated based on chemical potential driving forces across the membrane. For the model, the following assumptions are made:

- All components of the SOFC model are at uniform temperature.
- Reforming and water gas shift reactions are at equilibrium in the anode.
- Electrochemical oxidation of CO is minimal compared to H_2 oxidation.

In the Aspen Plus model, fuel and steam are mixed in a mixer and then fed to the anode after being mixed with recycled anode exhaust. Recycling anode gases is simulated by a splitter at the anode exhaust, which is sent to back to mix with the inlet fuel in the upstream pre-reformer, which is used to convert a portion of the butane to syngas. The pre-reformer is modeled as a Gibbs equilibrium reactor in which the product is determined by water-gas-shift equilibrium. For the anode model, only H_2 is oxidized as stated above, and CO is consumed in the water-gas-shift equilibration process. In the cathode model, the air stream is heated by the heat from the electrochemical reactions using a heater module. The O_2 flux from the cathode to the anode is calculated using a user-defined function based on the chemical potential driving force based on O_2 effective partial pressures in the cathode and anode. The oxide flux is modeled with a separator used to simulate the process of splitting oxygen into oxide ions by the cathode.

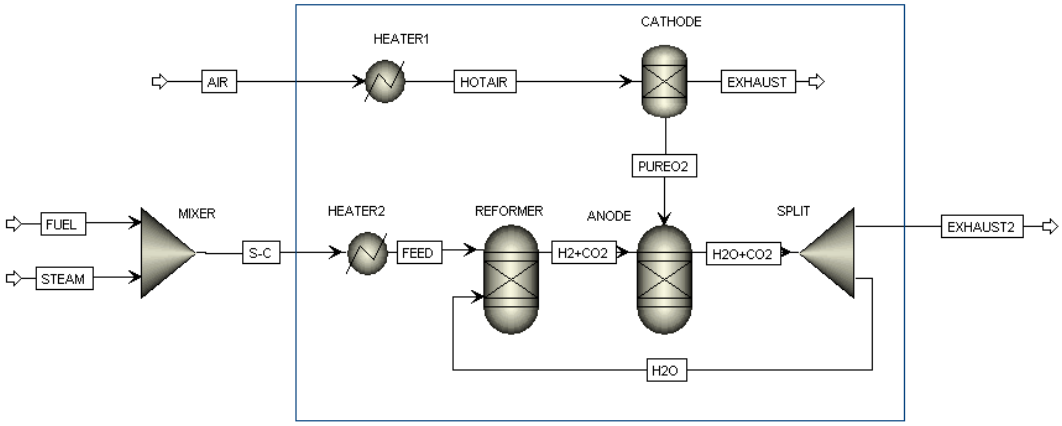

Figure 2. Aspen Plus simulation flow sheet of simplified first-generation SOFC to be integrated into larger plant model.

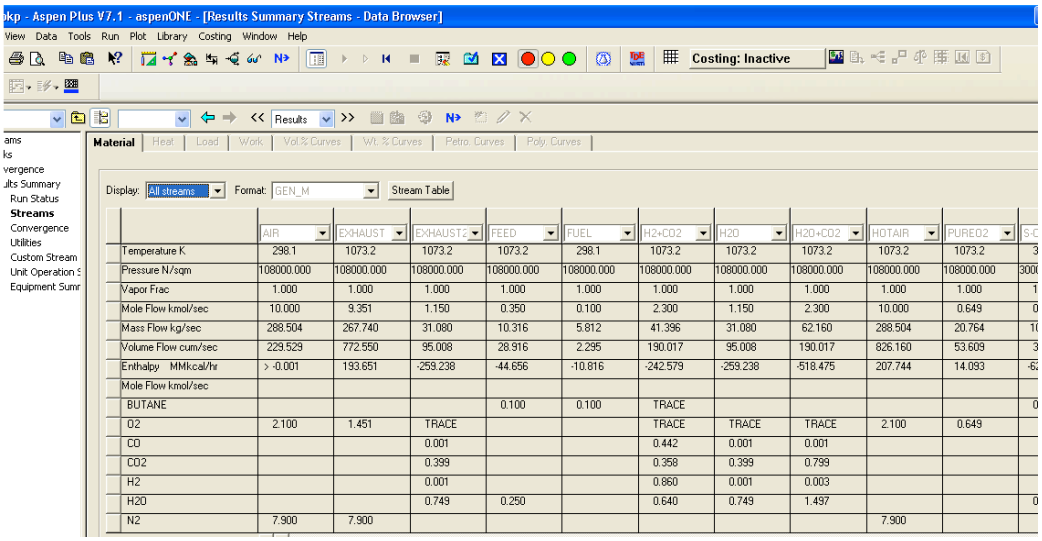

	AIR	EXHAUST	EXHAUST2	FEED	FUEL	H2+CO2	H2O	H2O+CO2	HOTAIR	PUREO2
Temperature K	298.1	1073.2	1073.2	1073.2	298.1	1073.2	1073.2	1073.2	1073.2	1073.2
Pressure N/sqm	108000.000	108000.000	108000.000	108000.000	108000.000	108000.000	108000.000	108000.000	108000.000	108000.000
Vapor Frac	1.000	1.000	1.000	1.000	1.000	1.000	1.000	1.000	1.000	1.000
Mole Flow kmol/sec	10.000	9.351	1.150	0.350	0.100	2.300	1.150	2.300	10.000	0.649
Mass Flow kg/sec	288.504	267.740	31.080	10.316	5.812	41.396	31.080	62.160	288.504	20.764
Volume Flow cum/sec	229.529	772.550	95.008	28.916	2.295	190.017	95.008	190.017	826.160	53.609
Enthalpy MMkcal/hr	> -0.001	193.651	-259.238	-44.656	-10.816	-242.579	-259.238	-518.475	207.744	14.093
Mole Flow kmol/sec										
BUTANE				0.100	0.100	TRACE				
O2	2.100	1.451	TRACE			TRACE	TRACE	TRACE	2.100	0.649
CO			0.001			0.442	0.001	0.001		
CO2			0.399			0.358	0.399	0.799		
H2			0.001			0.860	0.001	0.003		
H2O			0.749	0.250		0.640	0.749	1.497		
N2	7.900	7.900							7.900	

Figure 3. Simulation results of reforming and electrochemical reactions at anode.

Simulation results of the combined pre-reformer and SOFC at anode are shown in the Table in Figure 3. The results show that the H_2 in the feed gas from the reformer is converted in the cell to product H_2O (through electrochemical oxidation), and 45% of CO is converted into CO_2 by water gas shift reaction. This first generation model will use overpotential and curve obtained by interpolation of experimental data or from the detailed through-the-MEA model as presented in the previous report.

Task 5: Establishing SOFC-industry partner for future demonstration
Currently UMD and PI are not working on this task. The task may be pursued more fully in the second year of this program.

4. Difficulties Encountered/Overcome

Difficulties in finishing the Ni/YSZ durability testing were encountered. Some of these arose because of Mr. Wang's inexperience and some due to unexpected material issues, which have now been resolved.

The switching of the Aspen modeling effort from PI to UMD also reduced UMD's time for experimental testing, but a balance of time on both sides of the effort has now been established as the Aspen modeling is now progressing more smoothly.

5. Planned Project Activities for the Next Quarter

The following activities are planned at UMD for this upcoming quarter.

- Begin testing the Ni/CeO_2/YSZ anodes with syngas and trace H_2S for long-term sulfur-tolerance.
- Work with 2 undergraduate interns.
- Continue expanding Aspen Plus modeling of SOFC power plant and work with visiting interns from PI to do fuller plant model for petroleum process applications.

Appendix

Justification and Background

There has been a movement for petroleum processing facilities to move to zero-flaring of off gases. These gases, derived from the petroleum extraction as well as downstream processing, can contain various hydrocarbons, some H_2S, and depending on the process, HCl (derived from processes for well stimulation). These gases can be returned to an oil well to maintain well pressure. However, it is also possible to extract useful power from these gases employing SOFCs, which can provide high energy conversion efficiencies (> 50% based on fuel heating value) while maintaining separation of fuel oxidation products from N_2 dilution that comes with conventional combustion processes. If SOFC architectures can be designed to operate effectively on such off-gases, then they can produce not only useful power but also concentrated CO_2 and H_2O streams which can be readily pumped to high pressure for oil-well re-injection. This provides a potential carbon footprint reduction of the petroleum processing both by producing power from waste streams and by providing an efficient means for re-injection of C-containing gases back into the well for sequestration. System level modeling in this program will show that such potential can be realized if stable SOFC systems are successfully developed.

Approach

This effort will extend earlier single membrane electrode assembly (MEA) testing and modeling at UMD and PI by looking at new gas compositions and the impact of trace H_2S and HCl contaminants on SOFC with potentially contaminant-tolerant materials and micro-architectures. UMD will employ additional MEA experiments with Raman spectroscopy to evaluate surface chemistry on selected SOFC materials (1). Functionally graded anode micro-architectures and material systems will be investigated for high power density and sulfur tolerance. These efforts will build on the earlier work exploring ceria/metal composite anodes and on recent work of others (5) showing the effectiveness of ceria nanoparticles for high-sulfur-tolerant SOFC anodes. The benefits of integrating an SOFC with an external steam or autothermal reformer will be explored by comparing SOFC performance with syngas vs. light hydrocarbon streams, where both are impacted by trace H_2S.

This work will rely on the progress made from integrating ceria (doped and/or un-doped with appropriate metal electrocatalysts for MEA designs tolerant of hydrocarbons. The testing will be done on selected fuels (CH_4, C_3H_8, C_4H_{10}) and on syngas contaminated with trace amounts of H_2S and separately trace amounts of HCl. Durability tests will be explored for preferred MEA designs. Modeling efforts will be expanded on both the micro-scale MEA level and on the large process scale to assess how contaminants handling will influence both SOFC design as well as overall process feasibility.

The simultaneous modeling effort in this program will also extend ongoing modeling efforts which will have explored both MEA models for micro-architecture design as well as higher level process models for assessing the potential for integrating SOFC systems into oil well operations. The micro-architecture MEA modeling will expand on Phase I efforts by developing the semi-empirical kinetic models for internal reforming of hydrocarbons and of H_2S decomposition. The engineering viability of an SOFC integrated into a petroleum facility for energy recovery and possible CO_2 capture (6) will be investigated via system modeling within the context of petroleum processes by combining the SOFC models with process simulation in ASPEN/Hisys available at PI and UMD. The process models will rely on full stack SOFC models derived from the MEA models to explore overall balance of plant, adequacy of fuel supplies, and power requirements for CO_2 capture. If possible, process simulation will be done in consultation with ADNOC experts to explore how SOFCs might be integrated into petroleum processing facilities.

Specific tasks for the program are summarized in the proposed schedule below. The testing and model development effort will also seek to bring an industrial collaborator to work with the team to

explore the possibility of a future demonstration SOFC system operating on petroleum processing offgases.

Task list: The overall approach can be summarized into 5 overarching tasks.

1) Establishing experimental facilities for MEA testing with trace contaminants
2) Long-term testing MEAs for selected fuels and syngas with trace H_2S and HCl
3) Enhancing MEA models to evaluate contaminant-tolerant designs
4) System level analysis of integrated SOFC / off-gas processing plant
5) Establishing industrial partner

Anticipated Deliverables: The following deliverables will be provided on this project:

1) Summary of MEA test results for preferred SOFC material and micro-architectures for high power density operation with syngas and hydrocarbons laden with selected contaminants,
2) MEA modeling results illustrating preferred micro-architectures with metal/ceria systems for contaminant-tolerant operation
3) System-level modeling tool with process evaluation for integration of SOFC into petroleum off-gas processing

Two-Year Schedule

Year 1:

- Upgrade SOFC MEA-testing facilities at UMD for handling trace contaminants
- Further development of SOFC experimental facilities at PI
- Perform post-testing material characterization for evaluation of long-term exposure to carbonaceous fuels
- Testing MEAs for selected fuels and syngas with trace H_2S and HCl
- Adopt SOFC models at UMD for hydrocarbon studies.
- Develop system level analysis of integrated SOFC / off-gas processing plant with analysis of contaminant flow

Year 2:

- Perform experiments with preferred material systems for typical off-gas compositions (with varying team loadings) for long-term durability with trace contaminants
- Enhance MEA models to evaluate micro-architectures for contaminant-tolerant operation
- Establish industrial partner in SOFC industry and ADNOC companies for development of demonstration project

References

[1] 1. M.B. Pomfret, J. Marda, G.S. Jackson, B.W. Eichhorn, A.M. Dean, and R.A. Walker, *Journal Of Physical Chemistry C*, **112**(13), 5232 (2008).

[2] 2. S. Patel, P.F. Jawlik, and G.S. Jackson. *Effects of Ceria Addition on Ni/YSZ Anodes for SOFCs Operating with Syngas and Hydrocarbons*. in *FUEL CELL 2009*. 2009. Newport Beach, CA: ASME.

[3] 3. S.C. DeCaluwe, *Quantifying the Role of Cerium Oxide as a Catalyst in Solid Oxide Fuel Cell Anodes*, in *Mechanical Engineering*. 2009, University of Maryland: College Park, MD.

[4] 4. S.C. DeCaluwe, H. Zhu, R.J. Kee, and G.S. Jackson, *Journal Of The Electrochemical Society*, **155**(6), B538 (2008).

[5] 5. H. Kurokawa, T.Z. Sholklapper, C.P. Jacobson, L.C. De Jonghe, and S.J. Visco, *Electrochemical And Solid State Letters*, **10**(9), B135 (2007).

[6] 6. B.F. Moller, J. Arriagada, M. Assadi, and I. Potts, *Journal of Power Sources*, **131**(1-2), 320 (2004).

Separate Sensible and Latent Cooling with Solar Energy

UMD Investigators: Reinhard Radermacher, Yunho Hwang
GRA: Ali Al-Alili
PI Investigator: Isoroku Kubo
Start Date: August 2007

1. Objective/Abstract

The main objective of this project is to design, fabricate and test a solar cooling system with the highest possible cooling COP measured to date. The approach involves combining a very efficient concentrating PV-T collector with separate sensible and latent cooling approach developed at CEEE. This solar cooling system is expected to operate under the UAE's harsh climate conditions.

2. Deliverables for the Completed Quarter

These are the accomplished tasks:

- Order the equipment and the instruments
- Start building the experiment
- Model the evaporator using CoilDesigner

3. Summary of Project Activities for the Completed Quarter

The orders for the main components and instruments needed were placed. The frame and the duct construction are ongoing. The data acquisition system has been received which will allow us to calibrate the instruments in the near future.

CoilDesigner was used to find the capacity of an available evaporator. It was also used to find the pressure drops in the refrigerant- and air-sides. The main purpose of this simulation is to ensure that under the current test conditions, no condensation will occur at the evaporator.

3.1 Results of the Experimental Work

The schematic of the experiment is shown in Figure 1. The frame, which is used to support the duct, is under construction. The duct materials have been recently received and its construction is going to be started in the near future. In addition, the data acquisition system has been received and compared to available ones to ensure that it is operating appropriately.

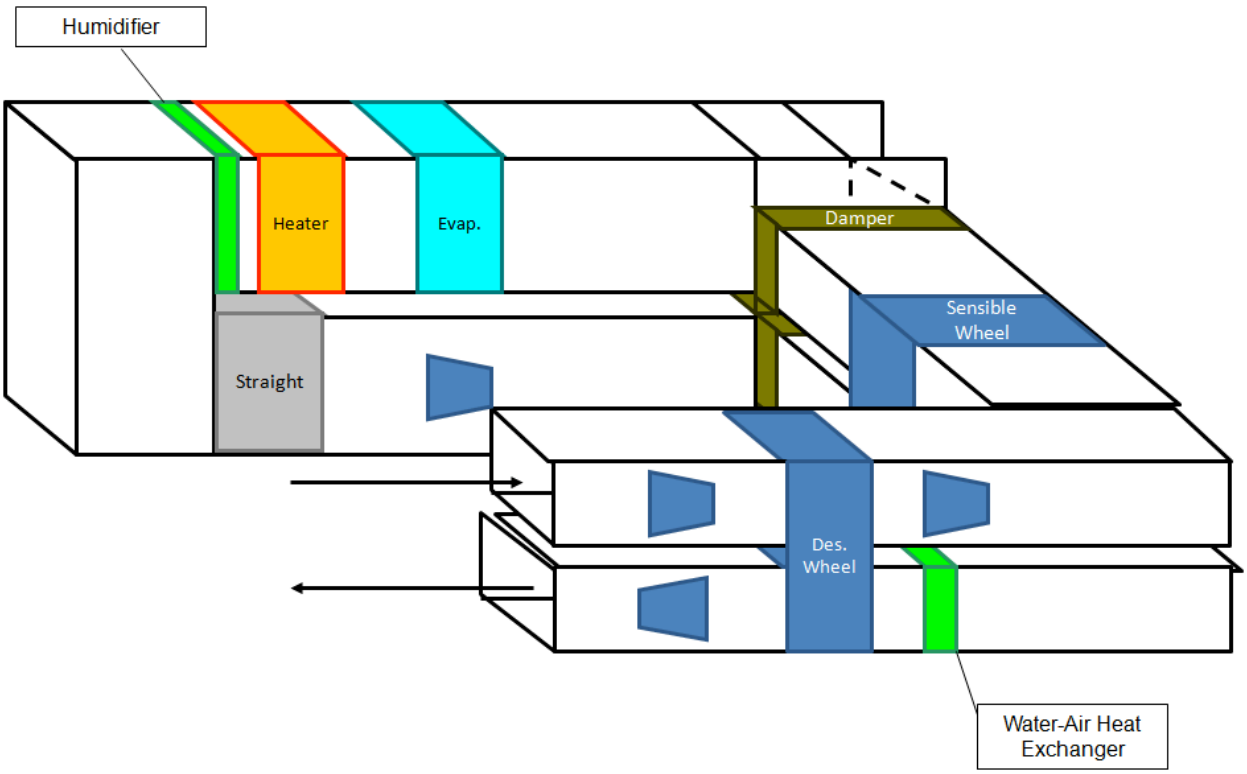

Figure 1. Schematic of the air conditioner experiment.

3.2 Results of the Evaporator Simulation

CoilDesigner was used to find the capacity of an available evaporator. All the tube dimensions were measured and inputted into the program, Figure 2. The program also requires information about the fin types and numbers, Figure 3.

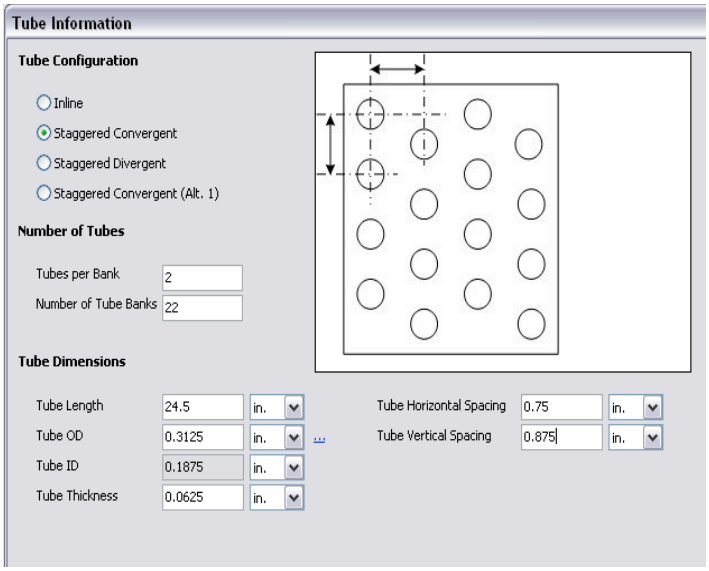

Figure 2. Tube configuration.

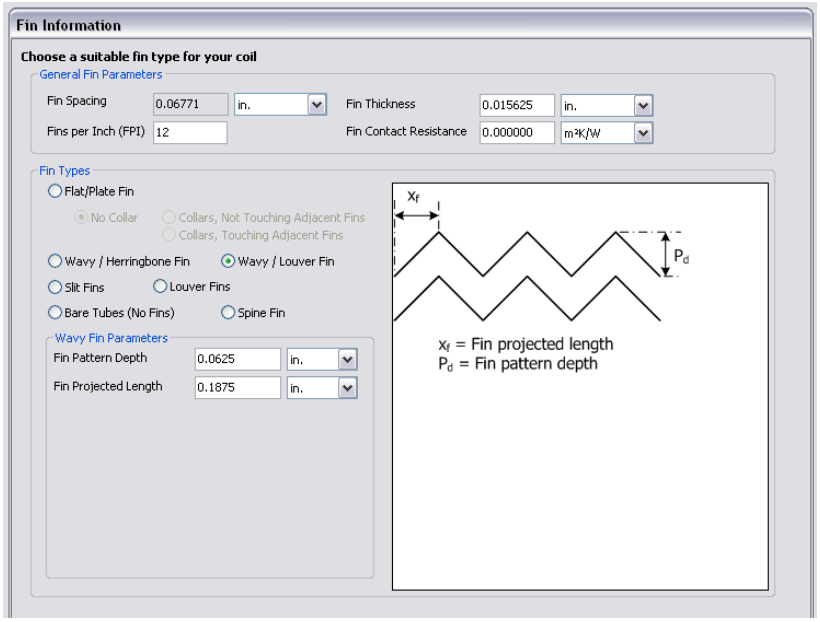

Figure 2. Fin configuration.

The inlet conditions for the refrigerant- and air-side were provided to the program. The vapor compression cycle (VCC) is required to provide about 3500 kW (1 ton of cooling). This VCC is used to accommodate only the sensible load, so condensation in the air-side is not permitted. The results of the air-side are shown in Table 1.

Table 1. Air-side inlet and outlet conditions

Air inlet Temperature	300/27	K/°C
Average Air Outlet Temperature	297/23.4	K/°C
Air inlet RH	44	%
Average Air Outlet RH	54	%

Based on these inlet conditions, the capacity of the evaporator was found to be about 1 ton of sensible cooling, as shown in Table 2.

Table 2. Evaporator capacity

Total Heat Load	3555	W
Sensible Heat Load	3555	W
Latent Heat Load	0	W

The effect of the volumetric air flow rate on the sensible capacity is shown in Figure 5. The figure shows that if the volumetric flow rate is lowered below 0.5 m^3/s condensation of water, vapor will occur. Therefore, any flow rate above the mentioned value can be used.

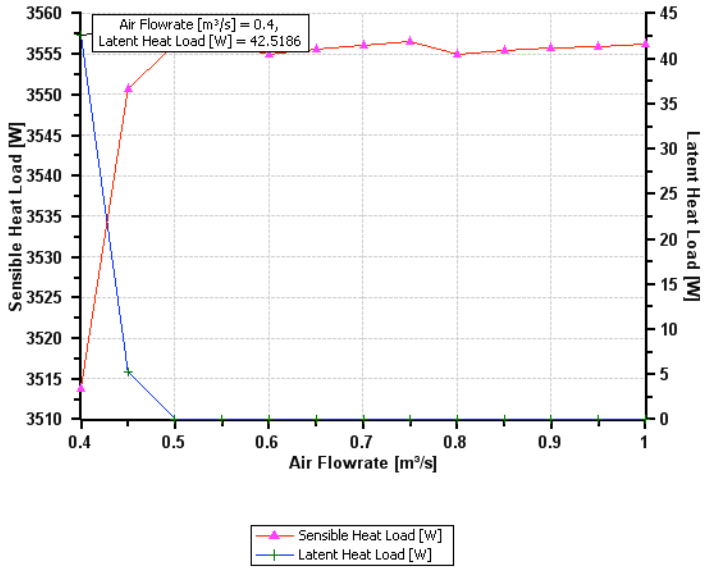

Figure 5. Air flow rate vs. evaporator capacity.

Figure 6 shows the effect of the volumetric air flow rate on the air outlet temperature. These results explain why the condensation occurs below 0.5 m^3/s. The reason is that as the flow rate is reduced, the difference between the air inlet and outlet temperature increases, for a fixed cooling capacity. Therefore, the outlet temperature reaches a value below that of the inlet condition's dew point.

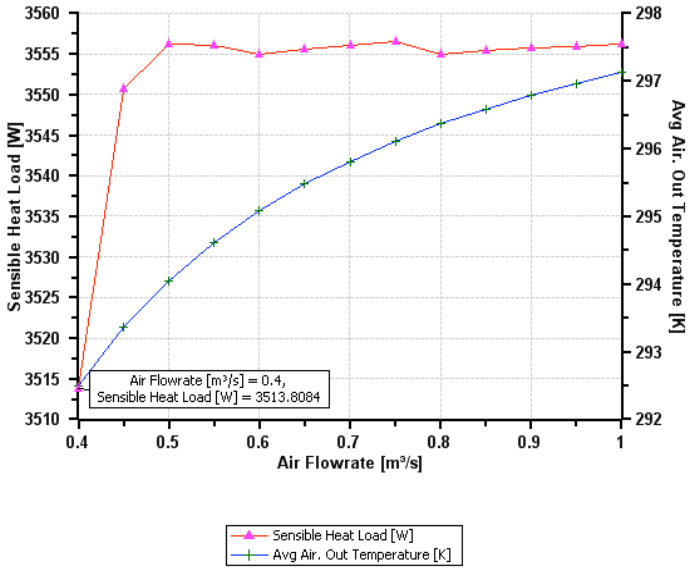

Figure 6. The effect of the air flow rate on the outlet air temperature.

4. Difficulties Encountered/Overcome

- Finding the appropriate instruments to satisfy the required accuracy

5. Planned Project Activities for the Next Quarter

The following activities are to be conducted in the next quarter:

- Continue the construction of the experiment
- Calibrate the instruments

Appendix

Key References

[1] Stine, W.B., Geyer, W.B., 2001, Power from the sun, www.powerfromthesun.net.
[2] Threlkeld,.J, Kuehn, T., Ramsy, J.,1998, Thermal Environmental Engineering, Prentice-Hall, Inc, USA
[3] http://www.nrel.gov/rredc/solar_data.html
[4] http://rredc.nrel.gov/solar/old_data/nsrdb/tmy2/State.html
[5] Notton, G., Poggi, P., Cristofari, C., 2006, Predicting hourly solar irradiations on inclined surfaces based on the horizontal measurements: Performances of the association of well-known mathematical models, *Energy Conversion and Management*, 47 1816–1829
[6] http://rredc.nrel.gov/solar/old_data/nsrdb/1991-2005/siteonthefly.cgi?id=724060
[7] ASHRAE, 1999, Applications Handbook, CH.32
[8] Kreith, F. and Kreider, J.F., 1978, Principles of solar engineering, *Hemisphere publishing corporation* Washington USA
[9] Kalogirou, S., 2004, Solar thermal collectors and applications, *Progress in Energy and Combustion Science* 30 pp. 231–295
[10] Goswami, Y., Kreith, F. and Kreider, J.F., 2000, Principles of solar engineering, *Taylor and Francis,* PA, USA,
[11] Duffie, J.A., Beckman, W.A., 1991, *Solar engineering of thermal processes*, Second edition, John Wiley & Sons, Inc., New York, ISBN: 0-471-51056-4.
[12] Pasupathy, A., Velraj, R., Seeniraj, R.V., 2008, Phase change material-based building architecture for thermal management in residential and commercial establishments, *Renewable and Sustainable Energy Reviews*, pp.39–64
[13] Dieng, A., Wang, R. , 2001 Literature Review on Solar Adsorption Technologies of Ice-making and Air Conditioning Purposes and Recent Developments in Solar Technology, *Renewable and Sustainable Energy Reviews* 5 pp.313–342
[14] Sumathy, K., Yeug, K, Yong, L., 2003, Technology Development in the Solar Adsorption Refrigeration Systems, *Progress in Energy and Combustion Science* 29 pp 301–327
[15] Roger, A. Messenger, J. V., 2005, Photovoltaic Systems Engineering, 2nd ed. Taylor & Francis
[16] http://www.nfpa.org/
[17] http://ieeexplore.ieee.org/iel5/7946/21930/01019771.pdf?arnumber=1019771
[18] TRANE, "Product Data: 4DCZ6036A through 4DCZ6060A" (2008), 22-1815-03
[19] METEONORM, "Global Meteorological Database for Engineers, Planners and Education"(2007).

Waste Heat Utilization in the Petroleum Industry

UMD Investigators: Reinhard Radermacher, Yunho Hwang
GRAs: Amir Mortazavi, Abdullah Alabdulkarem
PI Investigators: Saleh Al Hashimi, Peter Rodgers
GRAs: Sahil Popli, Alyas Ali Alshehhi
Start Date: October 2006

1. Objective/Abstract

The main objective of this project is to minimize overall energy consumption of gas or oil processing plants by utilizing waste heat and/or improving cycle design. Consideration will include the use of absorption chillers and steam cycles, among other options.

2. Deliverables for the Completed Quarter

The following were modeled using HYSYS:

- CO_2 capturing plant from a power plant
- Gas turbine steam and absorption-chiller triple combined cycle

3. Summary of Project Activities for the Completed Quarter

HYSYS was used to model a CO_2 capturing plant from a flue gas of gas-turbine-based power plant. The plant consists of an absorber column and a stripper column. The solvent used in the model is Monoethanolamine (MEA). HYSYS models of gas turbine steam and absorption chiller combined cycle were developed.

3.1 CO_2 capturing plant

The configuration of the plant is shown in Figure 1. Both of the absorber and stripper column are 20 stages, 6.1 m in height and 0.427 m in diameter with FLEXIPAC 1Y packing. The developed model uses the built-in amine property package in HYSYS, which has been validated by ASPEN Tech. The model matched the experimental data fairly well, as shown in Table 1. CO_2 removal from the flue gas was estimated to be 62.22% with 4.309 MJ/kg CO_2 energy consumption. This energy consumption will reduce the efficiency and power output of the power plant. The temperature profile in the absorber and stripper are shown in Figure 2 and Figure 3, respectively.

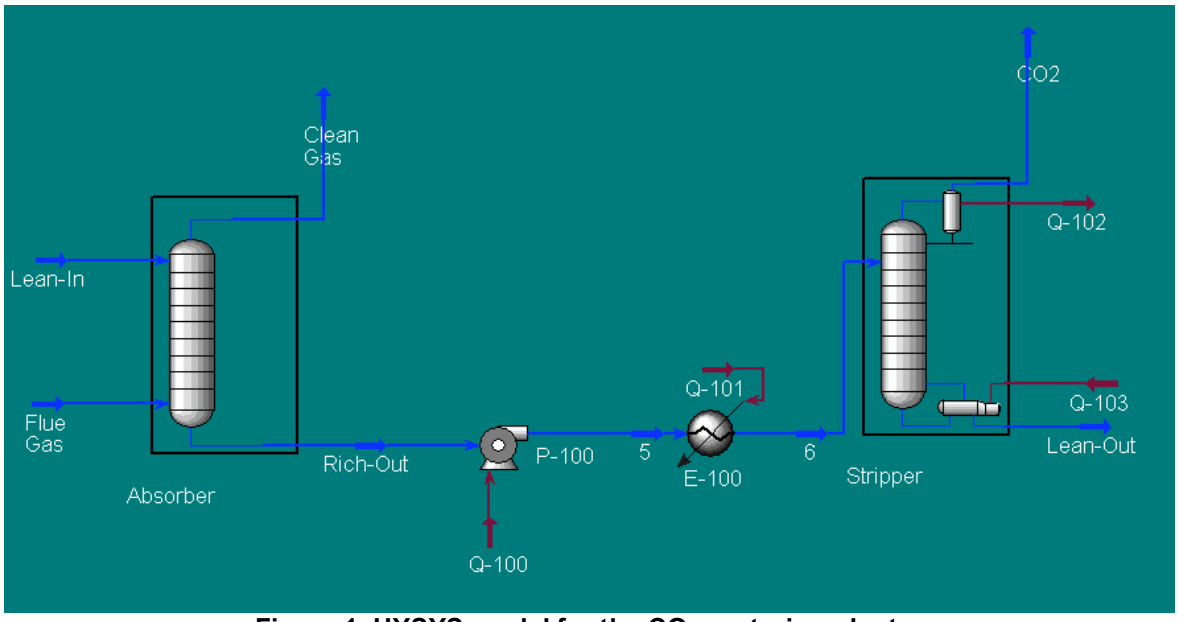

Figure 1. HYSYS model for the CO_2 capturing plant.

Table 1. Performance of the HYSYS model vs. experimental data

	HYSYS	Measurement
Richout (kg CO_2/h)	252.7	N/A
Sweetgas (kg CO_2/h)	39.4	N/A
Fluegas (kg CO_2/h)	149.5	149.5
LeanIn (kg CO_2/h)	142.69	142.69
CO_2_pure (kg/h)	93.06	92
MEA_in CO_2 (kg/h)	2.6	N/A
Qboiler(kW)	247.5	N/A
Qcond (kW)	8.13	N/A
%CO_2 Removal	62.22	69
CO_2 loading of RICHIN, MolCO_2/MolMEA	0.498	0.539
CO_2 loading of LEANIN, MolCO_2/MolMEA	0.281	0.281
Energy Consumption (MJ/kg CO_2)	4.309	4*

*estimated

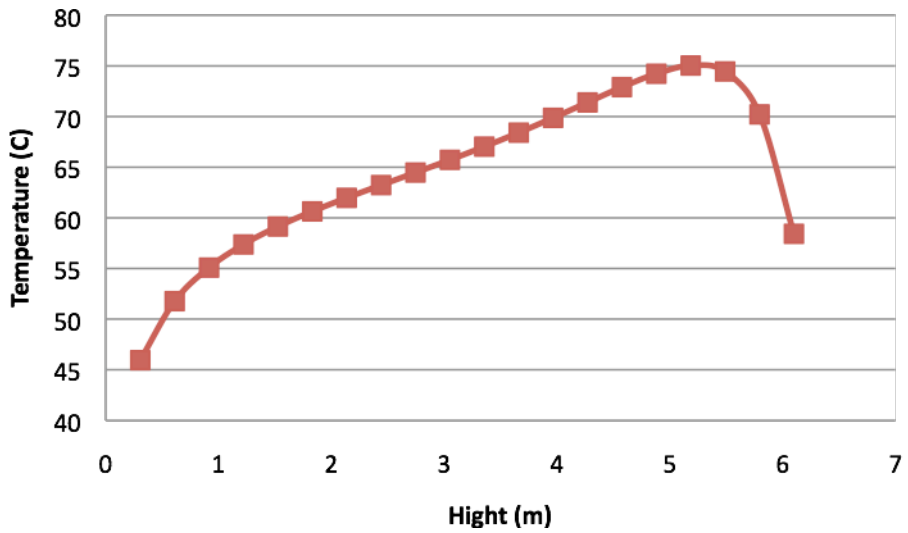

Figure 2. Temperature profile in the absorber.

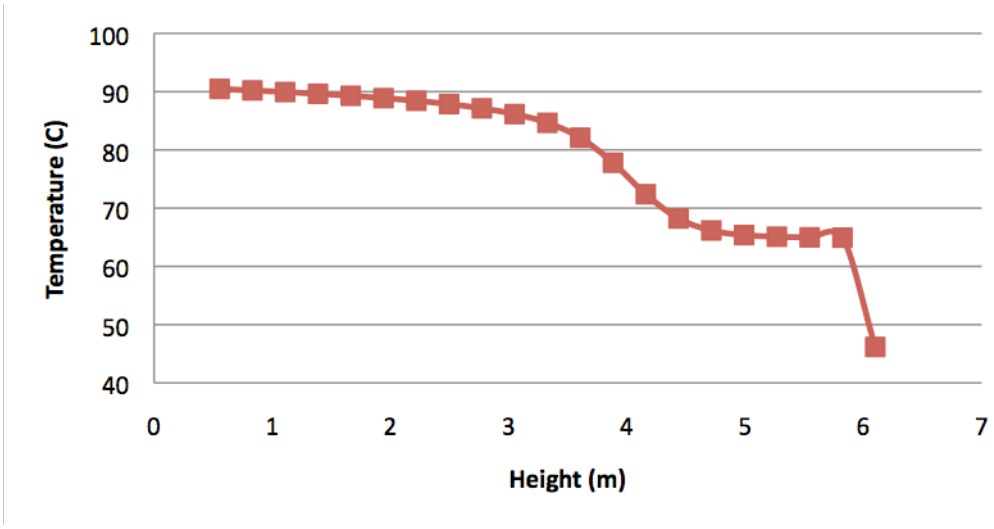

Figure 3. Temperature profile in the stripper.

3.2. Gas turbine steam absorption chiller combined cycle

The HYSYS model of the gas turbine steam absorption triple combined cycle is shown in Figure 4. The gas turbine and steam cycle power output is used to run MCR and propane cycle compressors of the APCI LNG plant. The absorption chiller cooling output will be used to replace the first stage of the propane cycle of the APCI LNG plant. However, this has not been accomplished yet.

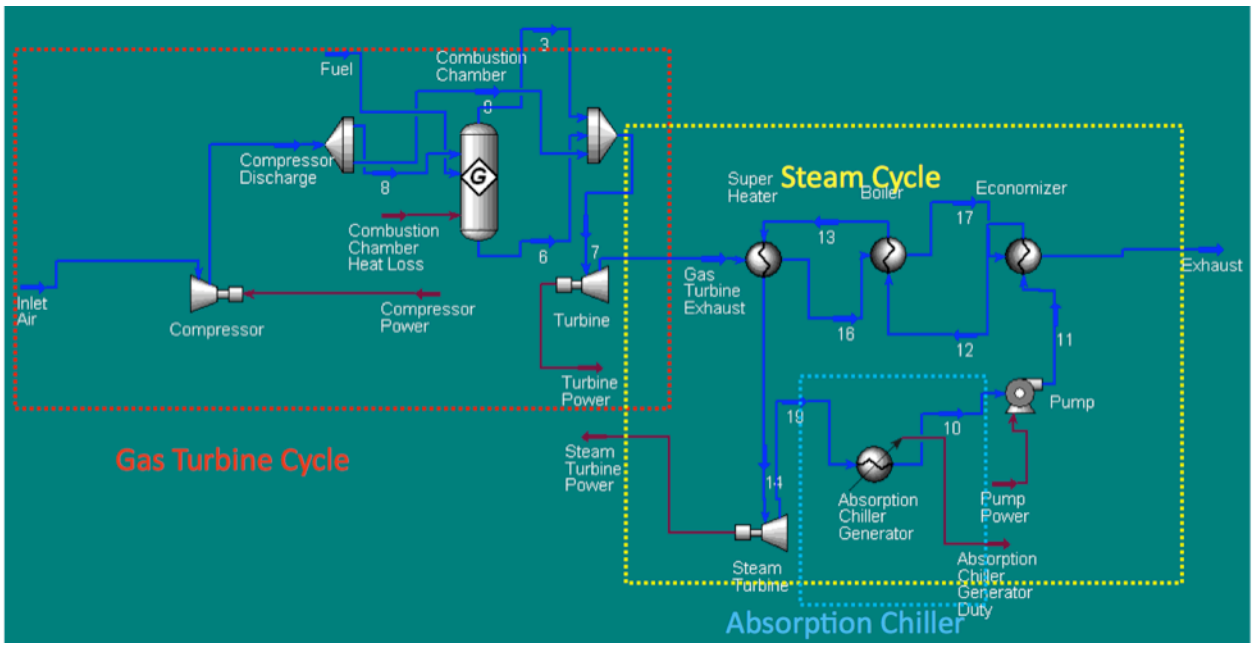

Figure 4. The HYSYS model of the gas turbine steam absorption triple combined cycle.

4. Difficulties Encountered/Overcome

None to report.

5. Planned Project Activities for the Next Quarter

The following activities are to be conducted in the next quarter:

- Design a carbon sequestration plant.
- Connect the triple combined cycle to the APCI LNG plant
- Optimize the gas turbine, steam and absorption chiller triple combined cycle as a driver of the APCI LNG plant.

Appendix

Justification and Background

Waste heat utilization opportunities are abundant in the oil and gas industry. Proper use of waste heat could result in improved cycle efficiency, reduced energy usage, reduction in CO_2 emissions, and increased production capacity.

CEEE at the University of Maryland has extensive experience in the design and implementation of integrated combined cooling, heating, and power (CCHP) projects. The faculty at PI has experience in the design and operation of petroleum processing plants. Jointly the team is well equipped to address the challenge posed by this project.

Key References

[1] Alefeld, G., Radermacher, R., 1994, "Heat conversion systems", CRC Press, Boca Raton.
[2] Al-Hamdan, Q.Z., Ebaid, M.S.Y., 2006, "Modeling and simulation of a gas turbine engine for power generation", ASME Journal of Engineering for Gas Turbines and Power, Vol. 128, pp. 302-311.
[3] LNG technology selection,
[4] http://www.fwc.com/publications/tech_papers/files/TariqLNG.pdf, Last access, June, 2008
[5] Haring, H., 2008, " Industrial Gas Processing", Wiley-VCH, Weinheim
[6] ASHRAE, 2002, "ASHRAE Refrigeration Handbook", American Society of Heating, Refrigeration and Air-Conditioning Engineers, Atlanta, GA, USA.
[7] ASHRAE, 2005, "ASHRAE Fundamentals Handbook", American Society of Heating, Refrigeration and Air-Conditioning Engineers, Atlanta, GA, USA.
[8] Brant, B., Brueske, S., Erickson, D.C., Papar, R., 1998, "New waste-heat refrigeration unit cuts flaring, reduces pollution", Oil & Gas Journal, May 18, pp.61-64.
[9] Brooks, F.,J., 2000 "GE gas turbine performance characteristics", GE Power Systems Schenectady, NY, GER-3567H.
[10] Cohen, H., Rogers, G.F.C., Saravanamuttoo, H.I.H., 1996, "Gas turbine theory", 4th edition, Longman Scientific & Technical, Singapore.
[11] Erickson, D.C., 2000 "LPG recovery from reformer treat gas", US Patent 6,158,241.
[12] Erickson, D.C., Anand, G., Papar, R.A., Tang, J., 1998, "Refinery waste heat powered absorption refrigeration – cycle specification and design", Proceeding of the ASME Advanced Energy System Division, AES-Vol. 38, pp.391-402.
[13] Erickson, D.C., Kelly, F., 1998, "LPG recovery from refinery by waste heat powered absorption refrigeration", IECEC-98-079, 33rd Intersociety Engineering Conference on Energy Conversion, Colorado Springs, CO.
[14] Giampaolo, T., 2003, "The gas turbine handbook: principles and practices", 2nd edition, The Fairmont Press, Lilburn, GA.
[15] Herold, K.E.; Radermacher, R., Klein, S, 1996, "Absorption chillers and heat pumps", CRC Press, Boca Raton.
[16] Kim, T.S., Hwang, S.H., 2006, "Part load performance analysis of recuperated gas turbine considering engine configuration and operation strategy", Energy, Vol. 31, pp., 260-277.
[17] Klein, S.A., 2005, "Engineering Equation Solver" F-Chart Software.
[18] Kurz, R., 2005, "Gas turbine performance", 44th Turbomachinery Symposium, pp.131-146.
[19] Kurzke, J., 2003, "Model based gas turbine parameter corrections", GT2003-38234, Proceedings of 2003 ASME TURBO EXPO: Power for Land, Sea, & Air, Atlanta, GA, USA.
[20] Li, Y.G., Pilidis, P., Newby, M.A., 2006, "An adaptation approach for gas turbine design-point performance simulation", Journal of Engineering for Gas Turbines and Power, Vol. 128, pp. 789-795.

[21] Orlando, J. A., 1996, “Cogeneration design guide”, American Society of Heating, Refrigeration and Air-Conditioning Engineers, Atlanta, GA.
[22] Pande, M., 1996, “Tools for fractionator design in ammonia-water absorption machines”, Master Thesis, University of Maryland, College Park.
[23] Walsh, P.P., Fletcher, P., 1998, “Gas turbine performance”, Blackwell Science, Oxford.

Thrust 2
Energy-Efficient Transport Processes

Multidisciplinary Design and Characterization of Polymer Composite Seawater Heat Exchanger Module

PI Investigator: Peter Rodgers
UMD Investigators: Avram Bar-Cohen, Satyandra K. Gupta, David Bigio, H.A. Bruck
GRAs: Juan Cevallos, F. Robinson, T. Hall, W. Pappas
Start Date: Oct 2006

1. Introduction

Heat exchangers are extensively used in all oil and gas processing operations with seawater as the preferred coolant in near-shore operations. The performance and cost effectiveness of conventional metallic heat exchangers in such environments are severely constrained by corrosion and scale deposits. Polymer heat exchangers, currently under investigation by the EERC team, offer a promising alternative to metallic heat exchangers for the fossil fuel industry. Recent advances in carbon-fiber polymer composites, yielding polymer materials with thermal conductivities equal to or higher than titanium, can be applied to the development of low-cost and low-weight compact heat exchangers for corrosive fluids. These attributes, combined with the low energy investment in the formation and fabrication of these polymer heat exchangers and their ease of manufacturing, appear to make near-term applications of seawater polymer heat exchangers viable. Numerical simulations and laboratory experiments, performed by the UMD/PI EERC team in the first phase of this research, strongly support these conclusions.

2. Milestones/Deliverables Scheduled for the Completed Quarter (related project task shown in parenthesis)

I. Hygrothermally age specimens in 25°C freshwater and saltwater to complete characterization of moisture absorption and subsequent changes in mechanical properties to differentiate between the effects of moisture diffusion and aging temperature (A5)

II. Develop ANSYS model using hygrothermally aged mechanical properties to determine if the mechanical response of polymer composite heat exchangers under typical LNG loading conditions will be feasible for replacing metallic heat exchangers at the Das Island liquefied natural gas facility (A3)

III. Design series of experiments to study mechanical properties of carbon-filled nylon polymers subjected to hygrothermal aging in dynamic stress environment at a variety of temperatures in order to investigate effect of stress applied during aging of material upon mechanical properties of material (A5)

IV. Construct dynamic chamber to conduct tensile testing of hygrothermally aged polymer samples in an aqueous saline environment (A5)

V. Design apparatus for application of tensile stress to carbon-filled nylon samples undergoing hygrothermal aging in aqueous saline environment (A5)

VI. Evaluate the thermofluid performance of different PHX concepts, using several figures of merit to understand their advantages and disadvantages (A1)

VII. Split plate-fin heat exchanger module design space to improve mold-filling model (B1)

VIII. Use model simplification techniques to develop Volume Scaling mold-filling model applicable to portions of the PHX module design space (B1)

IX. Submit a poster presentation entitled "*Saltwater Hygrothermal Aging Studies of Short Carbon Fiber Reinforced Polyamide 12*" to the ASME International Mechanical Engineering Congress & Exposition (A5)

3. Summary of Project Activities for the Completed Quarter

I. Hygrothermally age specimens in 25°C freshwater and saltwater to determine if mechanical property degradation is result of moisture diffusion or aging temperature

a. Experimental Setup

- Tensile specimens were injection-molded in accordance with American Society for Testing and Materials (ASTM) standards for testing for the tensile properties of plastics. Two commercially available materials were used: unreinforced PA12 from EMS-Grivory and short carbon fiber-reinforced PA12 (33 vol. %, 51 wt. % carbon fiber) from PolyOne.
- All specimens were injection-molded and then dried at 80°C over calcium sulfate until additional drying time did not result in moisture removal. Each specimen was then weighed on a balance with a precision of 0.1 milligrams.
- Twelve specimens of each material were placed into eight different water baths. The water baths were maintained at four temperatures (25, 40, 50 and 60 °C) and two salinity levels (freshwater, 45g/kg).
- The experimental setup is shown in Figure 1.

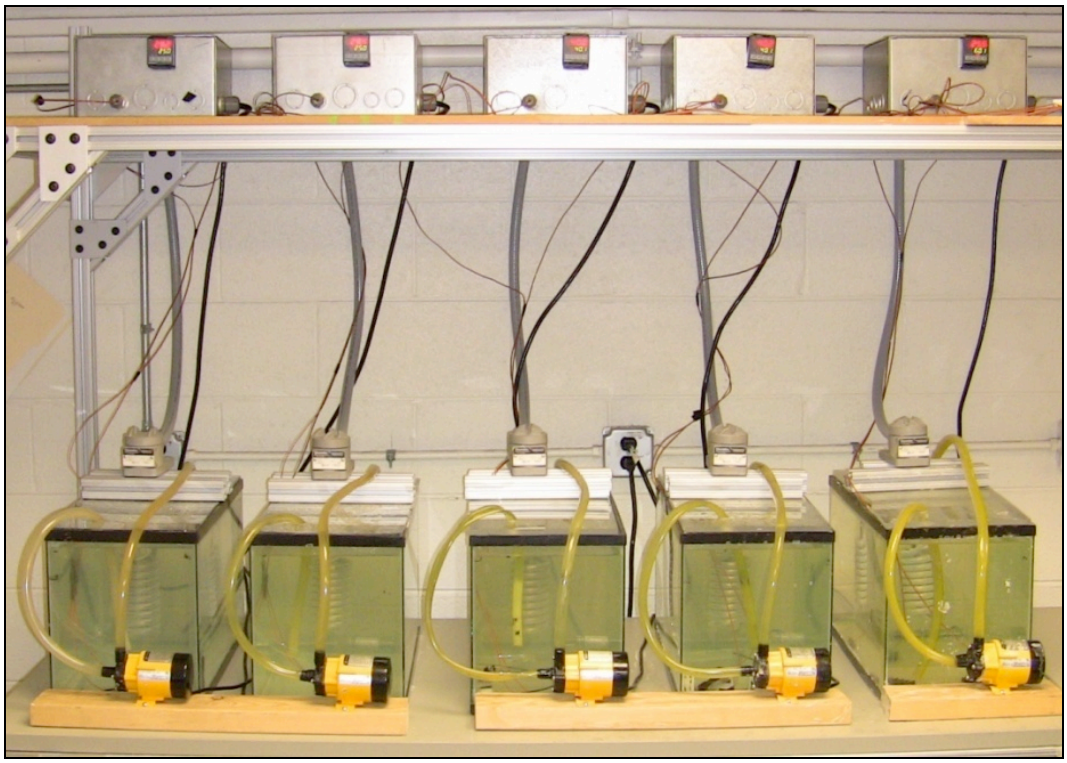

Figure 1. Experimental setup for hygrothermal aging experiment.

b.Mechanical Property Results

- The results from the tensile tests of the unreinforced specimens hygrothermally-aged at 25°C are provided in Table 1. The mechanical property results from hygrothermal aging at 40, 50 and 60°C are provided for comparison. These results have been updated from previous reports based on the testing of additional specimens.
- The results for the freshwater and saltwater tests have been combined because it was found that the presence of salt did not significantly affect the mechanical properties.
- The elastic modulus of the hygrothermally-aged, unreinforced PA12 does not vary significantly with temperature and there is no consistent trend with respect to temperature. Thus, it appears that temperature does not significantly affect the elastic modulus of the aged unreinforced PA12.
- The yield strength, elongation at yield, and ultimate strength of unreinforced PA12 appear to vary slightly with temperature. The yield strength decreases from 22.49 MPa to 19.05 MPa as the water temperature increases from 25°C to 60°C. This trend is consistent (i.e., the yield strength decreases monotonically with temperature) within the range of temperatures used for this study. Elongation at yield appears to decrease slightly with increasing temperature, decreasing from 3.65% at 25°C to 3.25% at 60°C. However, the trend is not consistent throughout the range of temperatures for this study. This variation has been attributed to statistical variation. The ultimate strength appears to decrease with increasing water temperature, from 48.63 MPa at 25°C to 37.31 MPa at 60°C. The trend of decreasing ultimate strength is consistent for the temperatures used in this study.

Table 1. Mechanical properties of hygrothermally-aged, unreinforced PA12

Temperature (°C)	Elastic Modulus (GPa)	Yield Strength (MPa)	Elongation at Yield (%)	Ultimate Strength (MPa)
25	0.66	22.49	3.65	48.63
Property Retention	45.2%	56.1%	122%	112%
40	0.68	21.21	3.30	45.84
Property Retention	46.6%	52.9%	110%	105%
50	0.65	20.98	3.59	42.79
Property Retention	44.5%	52.3%	120%	98.3%
60	0.62	19.05	3.25	37.31
Property Retention	42.5%	47.5%	108%	85.8%

- The results for the hygrothermally-aged, reinforced polyamide 12 are provided in Table 2. Mechanical properties resulting from hygrothermal aging at 40, 50 and 60°C are also shown for comparison. These results have been updated based on the testing of additional specimens.
- Measurements from the freshwater and saltwater tests have been combined because it was found that the presence of the salt did not significantly affect the mechanical properties.
- All mechanical properties tested for this study (i.e., elastic modulus, yield strength, elongation at yield, ultimate strength and elongation at failure) appear to be affected by increasing water temperature.

- Elastic modulus follows a consistent decreasing trend with increasing water temperature. At 25°C, the elastic modulus is 13.87 GPa and drops to 9.26 GPa at a water temperature of 60°C. Similarly, at 25°C, the yield strength is 77.58 MPa, whereas the yield strength drops to 60.15 MPa at a water temperature of 60°C. Elongation at yield tends to increase with increasing water temperature. The only exception occurs between water temperatures of 25 and 40°C. However, this result has been attributed to statistical variability. At 25°C, elongation at yield is 0.77% whereas elongation at yield increases to 0.88% at a water temperature of 60°C. Ultimate strength follows a fairly consistent decreasing trend with increasing water temperature. At 25°C, the ultimate strength is 94.79 MPa, whereas the ultimate strength drops to 85.99 MPa at a water temperature of 60°C. Finally, elongation at failure follows a consistent increasing trend with increasing water temperature (1.78% at 25°C and 3.06% at 60°C).

Table 2. Mechanical properties of hygrothermally-aged, reinforced PA12

Temperature (°C)	Elastic Modulus (GPa)	Yield Strength (MPa)	Elongation at Yield (%)	Ultimate Strength (MPa)	Elongation at Failure (%)
25	13.87	77.58	0.77	94.79	1.78
Property Retention	75.0%	84.8%	108%	90.3%	129%
40	11.60	60.85	0.73	85.88	2.80
Property Retention	62.7%	66.5%	103%	81.8%	203%
50	10.91	60.33	0.77	86.04	2.98
Property Retention	59.0%	65.9%	108%	81.9%	216%
60	9.26	60.15	0.88	85.99	3.06
Property Retention	50.1%	65.7%	119%	81.9%	222%

- In general, it appears that the mechanical properties are best retained at a water temperature of 25°C. Nonetheless, a degradation of mechanical properties is still seen at this lower temperature. Therefore, the combined effects of both moisture absorption and elevated temperatures lead to the change in mechanical properties seen in specimens aged in water temperatures of 40, 50 and 60°C.
- The change in mechanical properties due to hygrothermal aging are significant and must be accounted for when designing heat exchangers made from polymer composite materials. It would appear from the unreinforced PA12 that there is only an effect from the moisture on the degradation of mechanical properties, which is most likely due to a short-range reconfiguration of the molecular structure and reduction of Van der Waal's forces that makes the material 100% more flexible and half as yield resistant. However, there is no substantial change in the ultimate strength and ductility of the material that is more dependent on the long-range characteristics of the polymer. For the reinforced PA12, there is an additional effect of temperature, which is most likely due to decohesion at the particle-matrix interface that increases flexibility by 50% and decreases strength by 30% while increasing ductility by 100%. However, in general the particles do substantially improve the stiffness and strength of the aged polymer at the expense of ductility.

II. *Develop finite element analysis (FEA) model using hygrothermally aged mechanical properties to determine feasibility of replacing metallic heat exchangers at the Das Island liquefied natural gas facility with polymer composite heat exchangers*

a. Purpose

- Carbon fiber reinforced composites have lower elastic moduli, lower yield strengths, and greater ductility than their metallic counterparts. Moreover, their mechanical properties present significant anisotropy. These differences affect material behavior under loading. Before implementing polymer composite materials in heat exchangers, the behavior of these materials as they are exposed to the pressure loads exerted by the gases cooled during the liquefaction of natural gas must be understood.
- Modeling fiber reinforced polymers is more challenging than modeling metals due to the inherit anisotropy that results from fiber orientation in the matrix. Elastic modulus and yield strength are greater in the direction of the fiber orientation. Thus, structural models must account for anisotropy to provide accurate results.

b. Isotropic Model

- An isotropic 3D FEA model is being developed for a laboratory-scale heat exchanger to provide a baseline for comparison to orthotropic and anisotropic polymer composite heat exchangers. The behavior of isotropic heat exchangers under the expected loading will aid in understanding the behavior of polymer composite heat exchangers. The discretized model relies on geometric inputs to construct the heat exchanger module. These geometric inputs are gas-side fin thickness, water-side fin thickness, base thickness, fin height, module width, module depth, number of gas-side fins, and number of water-side fins. An example of a heat exchanger geometry developed as an FEA model is shown in Figure 2**Error! Reference source not found.**.

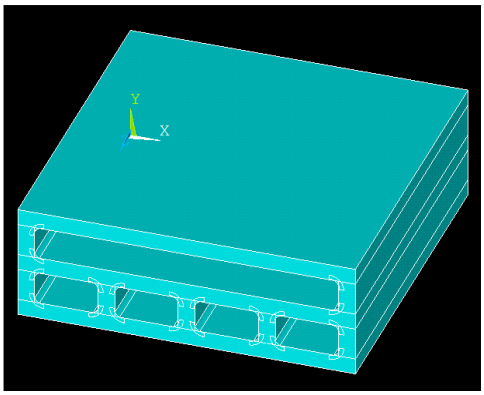

Figure 2. Sample heat exchanger geometry.

c. Orthotropic Model

- An orthotropic 3D FEA model is being developed for a laboratory-scale polymer composite heat exchanger that can serve as a vehicle for exploring the effects of gas pressure on a notional polymer composite heat exchanger. The discretized model relies on the same geometric inputs (i.e., gas-side fin thickness, water-side fin thickness, base thickness, fin height, module width, module depth, number of gas-side fins and number of water-side fins) as the isotropic model to construct the heat exchanger module. These parameters provide maximum geometric flexibility for eventual optimization of heat exchanger geometry.
- The measured 60°C properties for hygrothermally-aged reinforced PA12 will be used in this model for the mechanical properties in the fiber-aligned direction. Available analytical formulations will be used to determine the off-axis properties of the reinforced PA12, based on the fiber concentration and fiber geometry. In future models, assigned mechanical properties will also account for expected change in materials properties due to the elevated operating temperatures of Das Island heat exchangers.

d. *Anisotropic Model*

- The commercially available, injection-molding simulation software Moldflow has the capability to produce full anisotropic models for FEA. The Moldflow simulation will be based on the desired geometry and carbon fiber reinforced polyamide. Moldflow will calculate the elastic modulus along each axis and the shear modulus at each orientation (i.e. x-y, y-z and x-z) for each key point.
- Once imported into the FEA program, structural analyses can be performed with these directional properties. It is expected that the performance of this model will most closely resemble the actual performance of a fiber reinforced heat exchanger module.

III. *Design series of experiments to study mechanical properties of carbon-filled nylon polymers subjected to hygrothermal aging in dynamic stress environment at a variety of temperatures in order to investigate effect of stress applied during aging of material upon mechanical properties of material*

- The maximum hoop stresses in the heat exchangers of Das Island liquefied natural gas facility were calculated using heat exchanger geometries and pressures found in the Das Island heat exchanger data sheets. These calculated values were used to select appropriate stress levels at which to perform experiments.
- A range of temperatures (25, 40, 50 and 50ºC), salinities (freshwater, 45g/kg), and stresses (20, 40, and 60% of material yield strength) were selected for application to carbon-filled nylon tensile testing specimens. Salinities and temperatures were selected to maintain experimental parity with previous material investigation experiments conducted by Mr. Frank Robinson. The loads required to induce the desired stress levels in the carbon-filled nylon were based upon the results of the mechanical testing performed in Mr. Robinson's previous experiments.
- Aging times for each combination of the experimental variable values were calculated based on the time necessary for the carbon-filled nylon to become saturated with aqueous solution at each of the selected temperatures.

IV. *Construct dynamic chamber to conduct tensile testing of hygrothermally aged polymer samples in an aqueous saline environment*

- An acrylic plastic chamber in which to conduct tensile testing on hygrothermally aged carbon-filled nylon samples immersed in heated aqueous solution was designed and constructed. The chamber has inlet and outlet valves so that heated salt water can be pumped through the chamber during tensile testing to more accurately represent conditions expected to be present in the industrial implementation of these heat exchangers.

V. *Design apparatus for application of tensile stress to carbon-filled nylon samples undergoing hygrothermal aging in aqueous saline environment*

- The aging apparatus used by Mr. Robinson to hygrothermally age specimens was modified to apply stress to the specimens during aging.
- In the modified apparatus, six bolts will be inserted through the base of a glass aging tank and into a sheet of steel. Clevis joints connected to the bolts will constrain the testing specimens and connect them to a pulley system. A pulley system will be constructed from aluminum framing above the tank. Using the pulley system, the tensile specimens will be loaded to create the desired stresses during hygrothermal aging.
- The apparatus will be able to impose tensile loads on up to six specimens simultaneously undergoing hygrothermal aging.

VI. Evaluate the thermofluid performance of different PHX concepts, using several figures of merit to understand their advantages and disadvantages

- The thermal performance of polymer plate-coil and plate-fin heat exchanger modules was compared using equal flow rates and expended pumping power. Both modules consist of a 1m-long and 1m-wide plate. The plate-fin module has straight rectangular fins on each side of the plate, while the plate-coil has tubes embedded in it (see Figure 3).

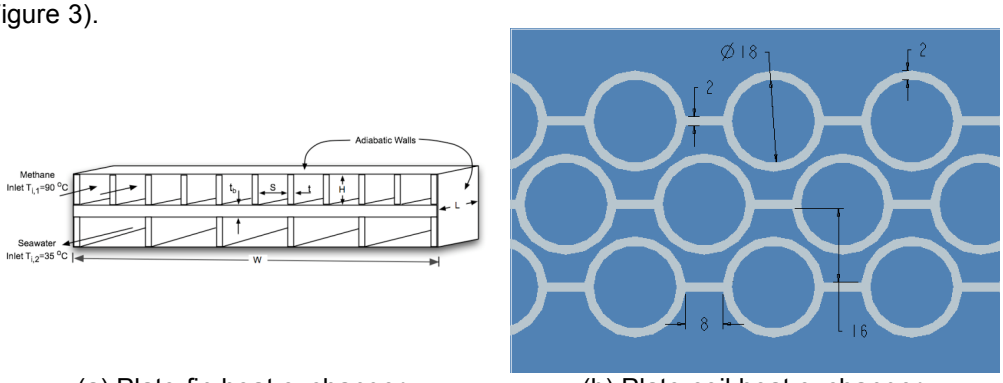

(a) Plate-fin heat exchanger (L = 1m, S = 5 mm, H = 10 mm, t = 2 mm)

(b) Plate-coil heat exchanger (dimensions in mm)

Figure 3. Heat exchanger geometries used for comparison.

- The heat transfer rate was calculated with the standard e-NTU counterflow relation, using a one-dimensional thermal resistance network. Other important metrics considered in this analysis were pumping power (calculated based on pressure drop), coefficient of performance, heat transfer per unit mass, and heat transfer per unit volume.
- Table 3 below shows that, for the stated conditions, comparable ranges of Reynolds numbers, resulting from similar hydraulic diameters and fluid velocities, resulted in similar heat transfer coefficients and pressure drops for the two designs.

Table 3. HX Parameters for plate-coil and plate-fin designs

		Plate-coil	Plate-fin
Gas-side area	**m^2**	2.76	4.298
Water-side area	**m^2**	2.02	1.446
Gas hydraulic diameter	**mm**	8.684	6.667
Water hydraulic diameter	**mm**	18	16
Gas velocity	**m/s**	3.3 - 16.7	2.8 - 14
Water velocity	**m/s**	2.2	2.1
Gas pressure drop	**Pa**	76 - 1300	77 - 1290
Water pressure drop	**Pa**	4115	4200
Gas Reynolds number	**-**	6700 - 34000	4300 - 21800
Water Reynolds number	**-**	54700	46500
Gas heat transfer coefficient	**W/m^2K**	104 - 370	90 - 340
Water heat transfer coefficient	**W/m^2K**	11000	10700

- Note that the plate-fin has more gas-side surface area than the plate-coil; however, the fin area accounts for ~66% of the total surface area in the plate-fin, and this added fin area is not as efficient in transferring heat as the base area (due to fin inefficiency). Therefore, the gas-side convective thermal resistance is modestly lower in the plate-fin design. The wall thermal resistance is lower in the plate-coil due to the additional water-side area available for conduction through the tubes. Summing the thermal resistances, the total thermal resistances are almost equal at the higher flow rates and very close to each other at the low flow rates (see Figure 4).

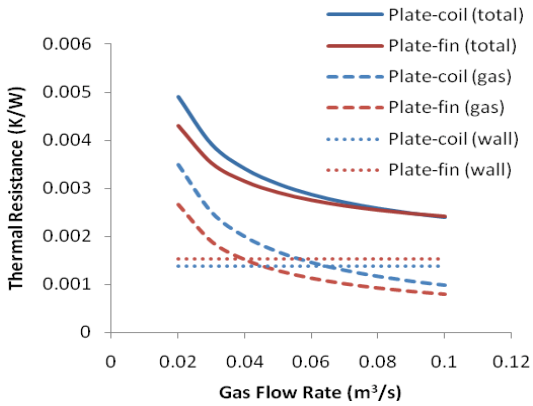

Figure 4. Thermal resistances.

- The pumping power is comparable for both designs (Figure 5a) and so is the heat transfer rate (Figure 5b), due to the thermal resistances shown in Figure 4.

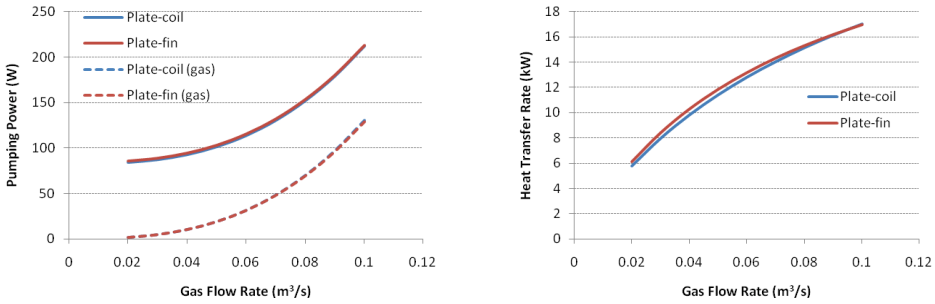

(a) Pumping power (b) Heat transfer rate

Figure 5. Heat transfer rate and pumping power as a function of gas flow rate (Water flow rate = 0.02 m^3/s, see Figure 3 and Table 3).

- However, the plate-coil design requires substantially less mass, resulting in more favorable heat transfer per unit mass values as shown in Figure 6. The plate coil heat exchanger also provides a somewhat higher value of heat transfer per unit volume. The mass and volume advantages of the plate-coil HX justify further evaluation of this promising design.

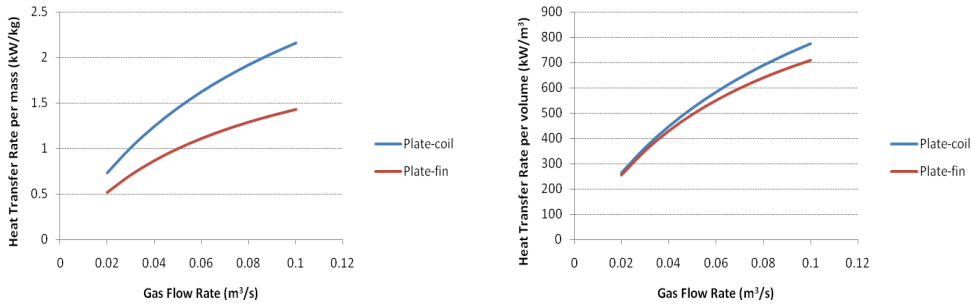

(a) Heat transfer rate per unit mass (b) Heat transfer rate per unit volume

Figure 6. Heat transfer rate per unit mass and volume as a function of gas flow rate (Water flow rate = 0.02 m^3/s, see Figure 3 and Table 3).

VII. Split plate-fin heat exchanger module design space to improve mold-filling meta model

a. ***Motivation:*** The molding process is too complex to be summarized with a single mold-filling meta-model due to competing failure and mold filling phenomena.

b. ***Action Plan:*** Split PHX module design space into design regions, determine failure modes, and apply separate meta-modeling techniques depending on failure mode.

c. ***Findings:***

- Normalized dimensions with respect to the base thickness of the geometry and developed the following 12 design regions based on normalized fin spacing, fin thickness, and fin height (Figure 6).

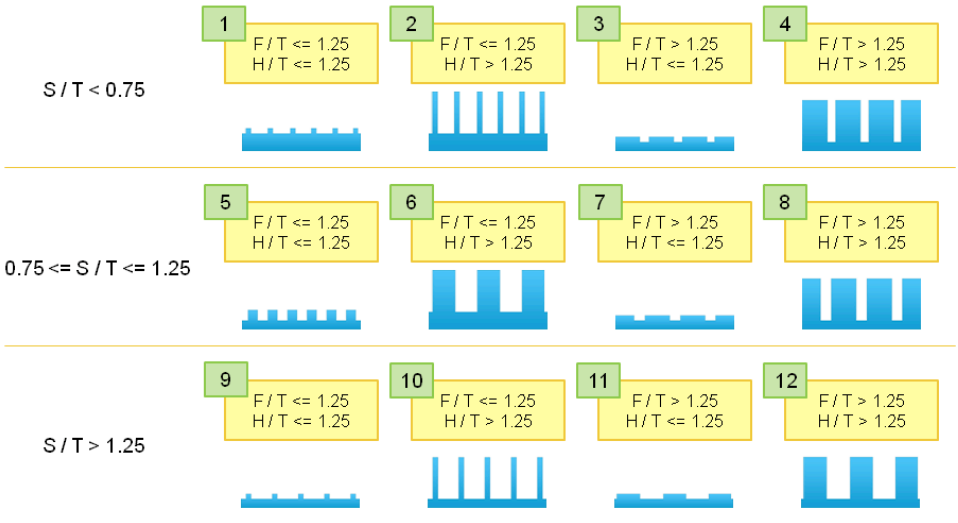

T = Base Thickness, S = Fin Spacing, F = Fin Thickness, H = Fin Height

Figure 6. PHX module design regions.

- Performed Moldflow® analyses with representative geometries from each design region to determine the failure mode of each design region.
  - Design Regions 3, 5, 7, 9, 10: Ideal Flow

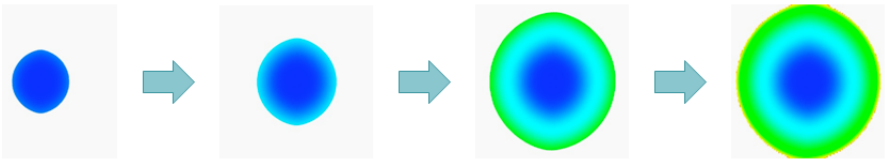

Figure 7. Ideal flow progression.

- Design Regions 1, 2: Unbalanced Base / Fin

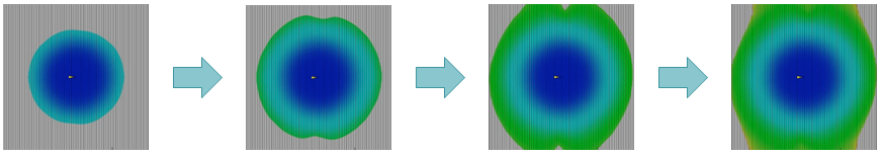

Figure 8. Unbalanced Base / Fin flow progression.

- Design Regions 4, 12: Fin Runaway

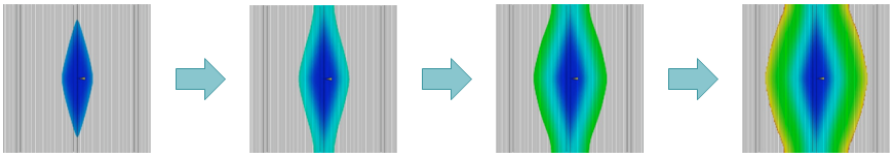

Figure 9. Fin Runaway flow progression.

VIII. Use model simplification techniques to develop a volume scaling mold-filling model applicable to portions of the PHX module design space

a. Motivation: *Utilize multiple modeling techniques to develop a hybrid mold-filling model that is accurate for all PHX module geometries and failure modes.*

b. Approach: Develop a meta or analytical model for flat-plate filling. Perform finned-plate filling Moldflow® analysis and compare to volume scaling filling. Determine which design regions volume scaling is applicable.

c. Findings:

- Divided the mold-filling model into four components: Volume Scaling model, Volume Distortion model, Combined Plate / Edge Gate model, and Full Statistical Meta-Model.

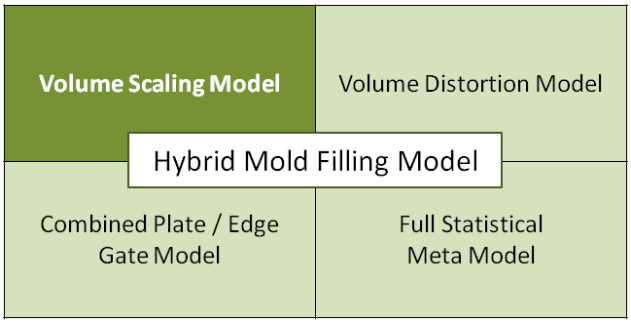

Figure 10. Components of the hybrid mold-filling model.

- Utilized technique of matching cross-sectional area of finned-plate geometry with flat-plate geometry by scaling height of flat-plate.

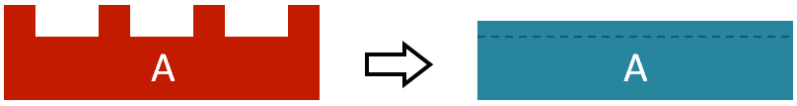

Figure 11. Method for Volume Scaling.

- Developed flat-plate filling meta-model for PolyOne, a carbon fiber filled-nylon composite
  - Plate Thickness, H: 1 - 10 mm
    Injection Pressure, P: 150 - 180 MPa
    Injection Flow Rate, F: 4500 - 5000 cm^3/s
    Melt Temperature, T: 250 - 277 °C

$$R(H,P,F,T) = \begin{cases} 5.3493 \times 10^{-7} TFPH^{1.3358} & H \geq 2 \\ 6.9813 \times 10^{-7} TFPH^{1.0156} & 2 < H \leq 5 \\ 8.8125 \times 10^{-7} TFPH^{0.8723} & H > 5 \end{cases}$$

Equation 1. Flat-plate, mold-filling meta-model.

  - The above set of equations represents the flat-plate, mold-filling meta-model developed, where R = Filled Radius. For the test points used to analyze the model, the average error was 0.05% with a range of +6.75% to -8.45%. The R^2 value for each equation is greater than 0.98.
- Performed finned-plate and volume-scaled flat-plate analyses in Moldflow® and compared the results to determine applicable design regions. Mesh convergence analyses confirmed that the meshing tolerance was suitable and the results accurate.

Table 4. Volume scaling comparison results

Case	T, mm	H, mm	F, mm	S, mm	Region	H_{scaled}, mm	% Error
1	4	2	1	9	1	4.2	50.48%
2	4	2	2	8	1	4.4	51.73%
3	4	2	3	7	1	4.6	134.68%
4	4	2	4	6	1	4.8	52.48%
5	4	2	5	5	5	5	-4.70%
6	4	2	6	4	7	5.2	2.50%
7	4	2	7	3	7	5.4	3.09%
8	4	2	8	2	3	5.6	2.44%
9	4	2	9	1	3	5.8	0.83%

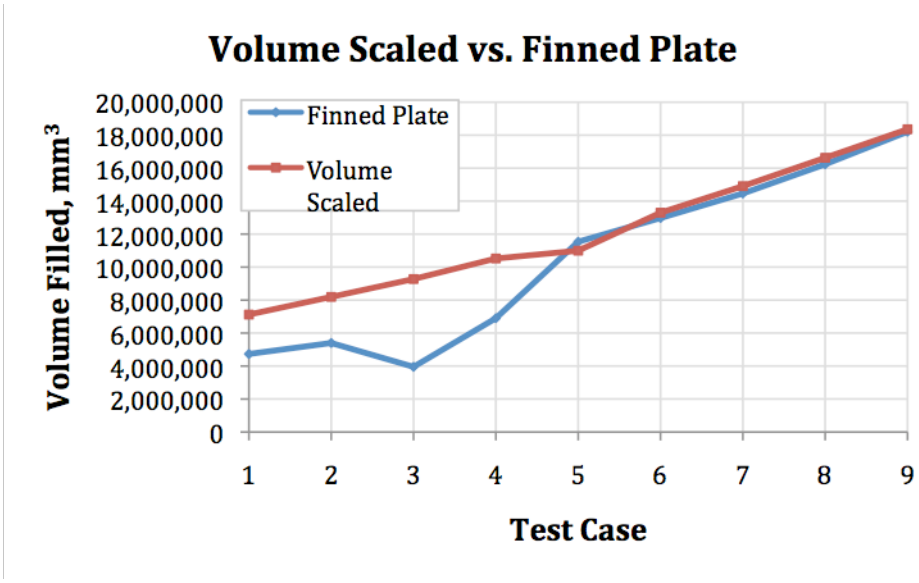

Figure 12. Volume Scaled Comparison results.

- The volume scaling method was successful at approximating filling behavior of design regions 3, 5, and 7

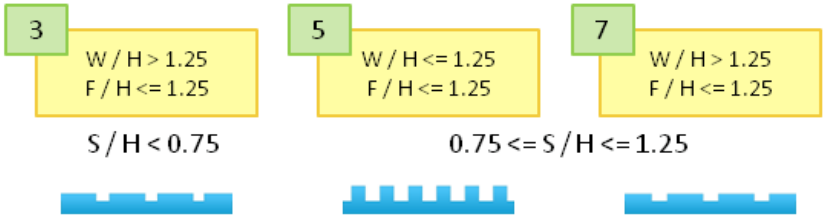

Figure 13. Applicable design regions for Volume Scaling.

- Updated mold filling modeling process to include volume scaling method

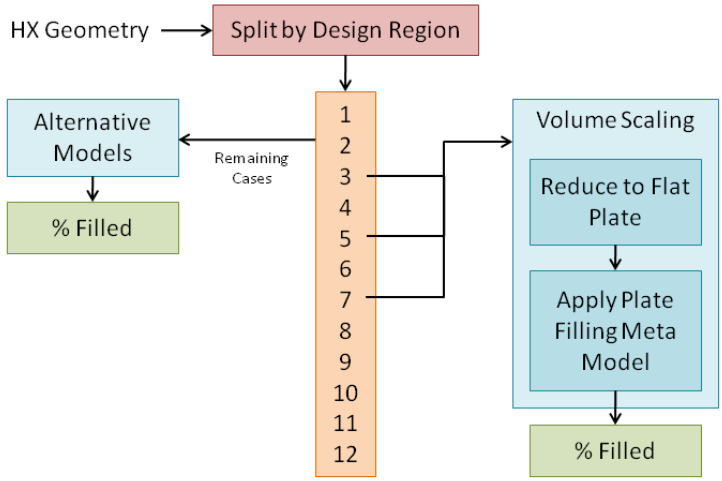

Figure 14. Mold filling model diagram.

IX. A poster presentation entitled "Saltwater Hygrothermal Aging Studies of Short Carbon Fiber Reinforced Polyamide 12," co-authored by Frank Robinson, Prof. Hugh Bruck, Prof. S.K. Gupta, and Prof. Avram Bar-Cohen, was accepted for presentation at the ASME International Mechanical Engineering Congress & Exposition

4. Difficulties Encountered/Overcome

None to report

5. Planned Project Activities for the Next Quarter

- Complete FEA models for isotropic, orthotropic and anisotropic heat exchanger modules and use structural results to optimize heat exchanger geometry
- Construct apparatus for application of tensile stress to carbon-filled nylon samples undergoing hygrothermal aging in aqueous saline environment
- Begin hygrothermally aging carbon-filled nylon testing specimens under tensile load at temperatures (25, 40, 50, and 60ºC) and salinity conditions (freshwater and 45g/kg) previously specified
- Characterize mechanical and thermal properties of polymer composites using various combinations of micro-/nanofibers
- Determine the effects of the operating conditions (Q/N vs. N) on the structure and properties of the material
- Develop volume distortion model and combined plate/edge gate model to complete hybrid mold filling model
- Conduct Moldflow® analyses and experimental investigations into the behavior of fiber orientation as a function of injection molding parameters and material properties
- Begin development of a fiber orientation meta-model
- Continue development of predictive models for anisotropic heat exchanger modules
- Continue evaluation of the thermofluid performance of different PHX concepts, using several figures of merit to understand their advantages and disadvantages

Appendix

Goals

The goal of the proposed 3-year EERC II polymer composite heat exchanger (PCHX) project is to develop the science and technology needed to underpin the systematic design of polymer-fiber composite heat exchanger modules that address the needs of the fossil fuel industry. The project team, lead by A. Bar-Cohen, brings together expertise in thermal science and technology (Bar-Cohen, Rodgers) with polymer composite molding and manufacturing (Gupta, Bigio). Design studies and molding simulations, as well as fabrication and testing of laboratory-scale polymer composite heat exchangers, during the first phase of this project, have provided the foundation for aggressive pursuit of such polymer composite heat exchangers.

Successful development of cost-effective, high-performance PCHX's will require a detailed understanding of the limitations imposed on the thermal performance, mechanical integrity, and cost of such heat exchange devices by the candidate polymer material; carbon fiber geometry, orientation, and concentration; thermal and mechanical anisotropy of the polymer-fiber composite; molding processes; thermal and structural failure mechanisms in the molded heat exchanger; and the energy investment in the fabrication and formation of the heat exchangers. The development and experimental as well as numerical validation of a multi-disciplinary computerized design methodology, along with the fabrication and testing of scaled polymer heat exchanger modules, would provide a unique knowledge-base from which low-life-cycle-cost heat exchange systems for the petroleum and gas industries could be developed.

Project Tasks

A. Thermal Design and Characterization of Polymer Composite Heat Exchanger Module (Prof. Avram Bar-Cohen - UMD, Prof. Peter Rodgers - PI)

1. ***Design and thermofluid evaluation of PHX concepts for LNG applications***, including sensitivity of thermal performance to key parameters, quantification of primary thermal and exergy figures-of-merit (metrics), comparison to conventional heat exchangers, and identification of least-mass/least-energy designs;

2. ***Detailed design, fabrication, and thermal characterization of least-energy PCHX module***, including mold fabrication for most promising design, assembly and instrumentation of laboratory prototype, analysis of thermal and structural performance under simulated LNG processing conditions;

3. ***Development of predictive models for anisotropic heat exchanger modules***, including use of molding CFD software for prediction of fiber orientation and effective thermal/ structural properties, numerical and analytical models for molded anisotropic fins, derivation of least-material anisotropic fin equations, determination of heat flow sensitivity to fiber geometry/concentration/orientation;

4. ***Evaluation of convective enhancement features in molded channels***, including identification of "best practices" in conventional heat exchangers, manufacturability analysis of candidate features with attention to mold complexity, part ejection, and warpage, polymer composite molding of 3-5 candidate enhanced channels; thermofluid characterization of candidate enhanced channels under simulated LNG processing conditions; and

5. ***Determination of seawater effects on polymer composite finned plates***, including design and molding of test samples, immersion in saltwater tanks at different temperatures and concentrations for pre-determined periods, surface/bulk imaging and mechanical characterization before and after immersion, analysis and correlation of effects.

B. Manufacturability Analysis and Mold Design for Polymer Composite Heat Exchanger Module (Prof. SK Gupta – UMD):

1. *Development of an improved meta-model for mold filling predictions*: We plan to develop an improved meta-model for predicting mold filling for typical heat exchanger geometries. This meta-model will account for multiple gates with adjustable spacing. The data for developing this meta-model will be generated using mold flow simulations. We plan to utilize radial basis function based meta-models to provide the right balance of accuracy and computational speed.

2 *Creation of a computational framework for gate placement to optimize fiber orientation*: We plan to develop a computational framework for placing gates to optimize the fiber orientation, utilizing simulated fiber orientations to select the gates. The sensitivity of the gate locations on fiber orientation will be developed. Gradient-based optimization techniques will be used to optimize the fiber orientation. The optimization problem will incorporate the constraint satisfaction formulation of the weld-line locations to ensure that the fiber orientation formulation produces acceptable weld-lines.

3. *Generation of insert molding process models to incorporate connectors at the weld-lines*: In order to ensure that the weld lines do not compromise the structural integrity, we plan to embed metal connectors at the expected weld-lines locations. In order to accurately place these metal connectors in the structures, we plan to develop process models of the insert molding process and mold design templates for performing insert molding.

C. Polymer-Fiber Interactions in Polymer Composite Heat Exchanger Modules (Prof. David Bigio):

1. ***Develop key relationships for the dependence of fiber orientation on the flow geometry of the finned-plate PCHX module,*** in commercially available polymer composites, including the effect of carbon fiber length and diameter, for high and low fiber concentrations, for both base plate and fin passages in the mold, and the effect of fiber orientation/distribution on thermo-mechanical properties, verify relationships with suitable small scale experiments;

2. ***Determine achievable thermo-mechanical property enhancement*** through control of carbon fiber orientation, in the commercially available polymer composites, with attention to flow regimes, mixing processes in the flow of the melt, and heat exchanger module design, and verify experimentally;

3. ***Explore optimization of PCHX polymer composite properties through the creation of novel polymer composite compositions***, including multi-scale filler geometries, develop the molding methods for the desired geometries, create the novel composites and experimentally verify improved thermo-mechanical polymer composite properties.

References

[1] Luckow, P., Cevallos, J.G., Bar-Cohen, A., Thermal Anisotropy in Injection Molded Polymer Composite Fins, 2009 (in progress)

[2] Cevallos, J.G., Gupta, S.K., Bar-Cohen, A., *Incorporating Moldability Considerations during the Design of Thermally Enhanced Polymer Heat Exchangers,* 2009 (submitted)

[3] Cevallos, J.G., Bar-Cohen, A., Bergles, A.E., Gupta, S.K., Rodgers, P., *Polymer Heat Exchangers – History, Opportunities, and Challenges* (in progress)

[4] Luckow, P., A. Bar-Cohen, P. Rodgers, 2009, *"Minimum Mass Polymer Seawater Heat Exchanger for LNG Applications,"* accepted for publication, ASME TSEA, January 2010.

Study on Microchannel-Based Absorber/Stripper and Electrostatic Precipitators for CO_2 Separation from Flue Gas

UMD Investigators: Serguei Dessiatoun, Amir Shooshtari
GRAs: Paul Breuninger, Toni Pfennig
PI Investigators: Michael Ohadi, Afshin Goharzadeh, Mohamed Alshehhi
Start Date: Oct 2006

1. Objective/Abstract

This project is focused on the development of a high-efficiency CO_2 separation process from flue gas flow. The project addresses three stages of the separation process: cooling down the flue gas, separating the solid particles and condensed water droplets, and separating the CO_2 using the absorption process. A microchannel-based CO_2 separator to be developed in this project will significantly increase controllability of the thermal state of the reaction and the efficiency of the separation process while decreasing the reaction time and energy consumption. Moreover, using such technology will lead to a reduction of equipment size and therefore minimize the footprint and cost of the equipment.

Flue gas also usually contains many contaminants in solid and liquid forms. The bulk of them are separated in gravity and inertia-driven feed gas separators. However, fine particles are carried on with the flow and can damage compressors, contaminate the gas absorption process, and reduce the quality of gas products. Currently, electrostatic separation is the most effective technique for separation of those particles and will be used in this project. The current stage of this study intends to address separation of droplets and particles using an EHD gas-liquid separation technique to remove conductive and nonconductive liquid particles suspended in a moving gaseous medium.

2. Milestones/Deliverables Scheduled for the Completed Quarter

- Literature review on separation techniques, the kinetics between CO_2 and alkanolamines in aqueous solutions, and investigation of their reaction rate
- Identification of the alkanolamine suitable for experimental study
- Design of test section and experimental setup
- Flow visualization of the EHD induced flow

3. Summary of Project Activities for the Completed Quarter

Literature Review

CO_2 separation methods

Various methods for separating CO_2 from flue gas have been developed and demonstrated in industrial plants. For post-combustion CO_2 separation from flue gas, there are four different approaches as listed in Table 1.

Table 1. CO_2 separation technologies (Aaron & Tsouris, 2005)

Separation Technologies	Advantages	Disadvantages
Absorption	• Well-established solvents are available • CO_2 absorbers can be regenerated • Solvent can be recycled • Proper instrumentation and surveillance can minimize labor operational costs	• Requires pre-treatment processing • Moderate to high total cost • Solvents susceptible to degradation
Adsorption	• Requires vessels capable of withstanding only small pressure changes • Sorbent can be regenerated	• System cannot easily handle large concentrations of CO_2 • Available sorbents are not selective enough for CO_2 separation
Cryogenic Distillation	• Produces liquid CO_2 with higher transportability • CO_2 recovery is very high	• The process is extremely energy intensive • High total cost • Requires pre-treatment to remove all other components
Membrane Diffusion	• No need to acquire sophisticated components • System is compact and lightweight • Does not require a separating agent	• Process is not selective enough or not very permeable to CO_2 • Requires compression of flue gas

In the current study, absorption technology will be implemented through a micro-channel based separator. The chemical absorption technique has been proven to be reliable and has found wide applications in the chemical and petrochemical industries. This is because the only commercially available process that can absorb a reasonable amount of CO_2 from dilute atmospheric pressure is chemical absorption. The other techniques are generally less energy efficient and more expensive than chemical absorption. This can be attributed, in part, to the very low CO_2 partial pressure in the flue gas (Herzog, 1999). In the flue gas, CO_2 is typically present at low concentrations (partial pressures). Without considering the presence of moisture, for a combustion with 110% of theoretical air, if coal is used, CO_2 represents about 15 mol% of the flue gas. This percentage is still lower if oil and natural gas are used as fuel, 13% and 9%, respectively (Herzog, Golomb, & Zemba, 1991).

In CO_2 absorption, a solvent is used (amine) to absorb one component (CO_2) over another depending on the chemical properties of both the solvent and CO_2. In this process, the flue gas first enters a cooler to get cooled. Then, the gas passes through a separator where the flying ash particles and water droplets are removed from the flue gas. A concentration about 100-150 mg/m^3 is normally considered the upper limit for particulate matter for typical industrial processes. Next, the flue gas enters the absorption chamber to react with amine and separate CO_2. Conventionally, the gas to be scrubbed enters the absorber at the bottom, flows up, and leaves at the top, whereas the solvent enters the top of the absorber, flows down (contacting the gas), and emerges at the bottom. Dilution of the circulating amine with water is done to reduce viscosity of the circulating fluid. The favorable conditions for such processes are low temperature and high pressure. Chemical absorption takes place in the absorber from 20 to 50° C. After absorption, the treated gas exits the absorber at the top, where the rich absorbent containing the absorbed gas exits from bottom. Due to the exothermic reaction between CO_2 and the absorbent, the

temperature will be higher than that of the incoming liquid. The rich absorbent is further heated in a liquid-liquid heat exchanger before it enters the stripper. In the stripper the absorbent is heated in order to strip off the carbon dioxide. As the temperature is close to 100 °C, a considerable amount of steam is also produced. The liberated CO_2 leaves the stripper column at the top together with the steam. The CO_2: steam ratio in this stream may be as high as 50:50. The regenerated absorbent leaves the stripper at the bottom. It is cooled in the liquid-liquid heat exchanger mentioned above. The cold regenerated absorbent is pumped back to the absorber. The hot gas leaving the stripper is cooled in a heat exchanger whereby most of the steam is condensed. The condensate is led back to the absorber (Aresta, 2003). A schematic of a typical absorption process is shown in Figure 1. Note that flue gas desulfurization stage is not included in this figure.

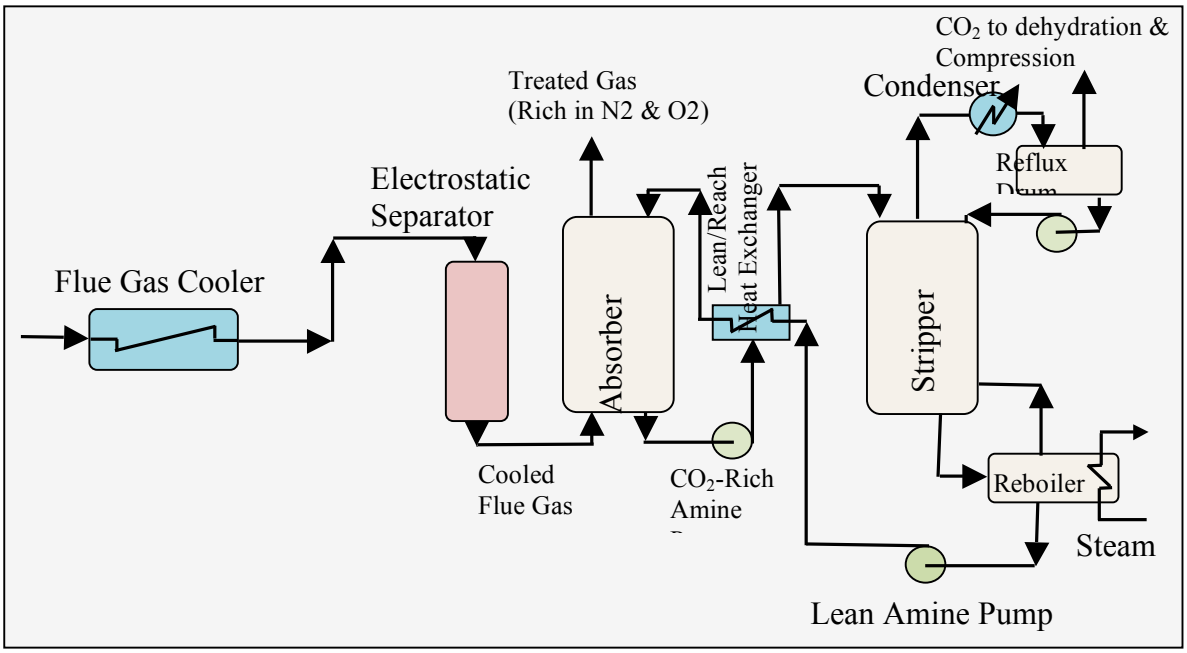

Figure 1. Typical absorption unit for CO_2 recovery from flue gas.

Mass and heat transfer are inversely proportional to the distances the chemicals must travel. A reduction of the size of absorber or stripper proportionally decreases the reaction time and increases controllability of the thermal state of the reaction. At the micro-scale, the mixing and reaction can occur in milliseconds, and the reaction zone temperature can be controlled within a few degrees. Due to the reduced length scale in the microchannel-based process equipment, the transfer length is short and well defined. Surface-to-volume ratio is very high and dominates transfer process. In most cases flow in microchannels is laminar; therefore, mixing time can be described as:

$$t = \frac{D_h^{\,2}}{2D} \qquad (1)$$

where D_h is the characteristic dimension of the channel and D is diffusion coefficient. For gases and low viscosity liquids, D ranges from 10^{-5} to 10^{-6} m^2/s and 10^{-9} to 10^{-10} m^2/s, respectively. Reduction of the mixing channel characteristic dimension to the hundred-micron range reduces the mixing time for liquids to one second, which is about one hundred times enhancement. An

order of magnitude evaluation of expected mixing and reaction time for the selected microstructure devices can be seen in Figure 2.

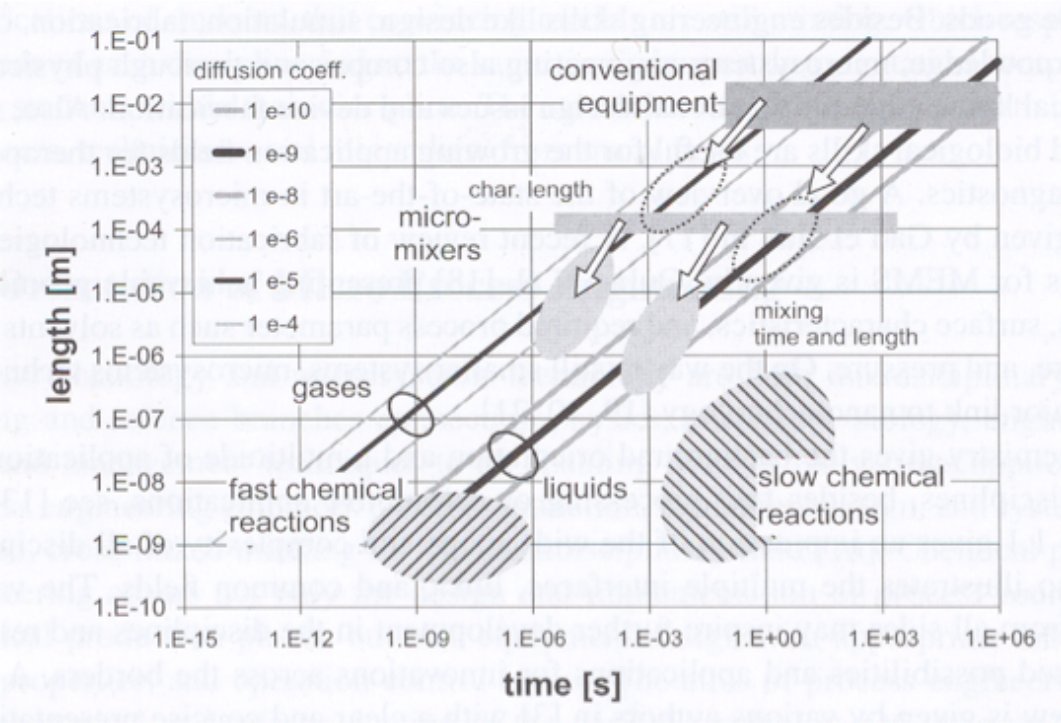

Figure 2. Characteristic length and time scale for mixing in microstructured devices together with chemical reaction (Kockmann, 2008).

Aqueous alkanolamine absorbents

Absorption of CO_2 by alkanolamines in aqueous solutions is a well-established process. Alkanolamines are amines with at least one hydroxyl group. The structural formula of selected alkanolamines is given in Figure 3.

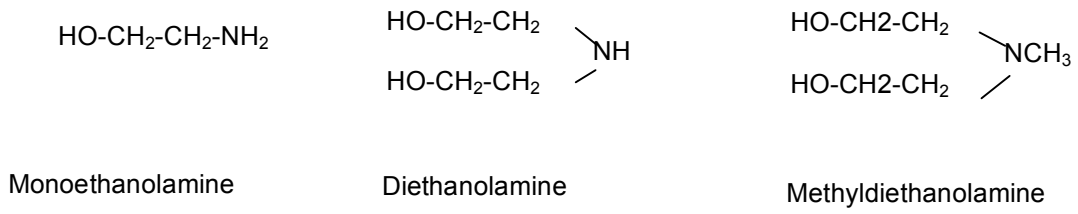

Figure 3. Structure of selected alkanolamines (Aresta 2003).

The reaction CO_2 with alkanolamine takes place at low temperatures of about 20-50 ^{o}C. To invert the reaction and regenerate CO_2, the temperature of the solution should increase to 110-130 ^{o}C. The absorption process is exothermic, while the desorption reaction is endothermic. The CO_2 absorption heat of reaction for selected alkanolamines is given in Table 2 and a comparison among physical properties of selected amines is presented in Table 3.

Table 2. Heat of reaction for absorption of CO_2 in selected alkanolamines (Aresta 2003)

Alkanolamine	Heat of Reaction (kJ/kg CO2)
Monoethanolamine (MEA)	1919
Diethanolamine (DEA)	1519
Triethanolamine (TEA)	989
Methyldiethanolamine (MDEA)	1105

Table 3. Physical propoerties of selected alkanolamines (Kohl and Nielsen 1985)

Physical Properties of Alkanolamines

Property	MEA*	DEA*	TEA*	MDEA*	DIPA*	DGA**
Mol. weight	61.09	105.14	149.19	119.17	133.19	105.14
Specific gravity,	1.0179	1.0919	1.1258	1.0418	0.9890	1.0550
20/20°C	—	(30/20°C)	—	—	(45/20°C)	—
Boiling point, °C						
760 mmHg	171	decomp.	360	247.2	248.7	221
50 mmHg	100	187	244	164	167	—
10 mmHg	69	150	208	128	133	—
Vapor pressure,						
mmHg at 20°C	0.36	0.01	0.01	0.01	0.01	0.01
Freezing point, °C	10.5	28.0	21.2	–21.0	42	–9.5
Solubility in water,						
% by weight at 20°C	Complete	96.4	Complete	Complete	87	Complete
Absolute viscosity,						
cps at 20°C	24.1	380(30°C)	1,013	101	198(45°C)	26(24°C)
Heat of vaporization,						
Btu/lb at 1 atm	355	288(23 mm) (168.5°C)	230	223	184.5	219.1
Approximate cost,						
$/lb***	0.59	0.60	0.61	1.40	—	0.93

Notes:

**Data of Union Carbide Chemicals Company (1957) except for pricing.*

***Data of Jefferson Chemical Company, Inc. (1969) except for pricing.*

****Kenney (1995). Prices are for bulk sales. Add $0.10 per pound for drum sales.*

Compared to other amines, MEA has higher absorption rate because of its higher capacity and reactivity with acid gases. Moreover, it is chemically stable. However, MEA creates heat stable salts and needs a high amount of heat for desorption. It is also very corrosive. On the other hand, DEA has a lower corrosivity of absorption products compared to MEA, lower heat of reaction, lower heat of regeneration, lower vapor pressure, and better desorption than MEA, and also it exhibits high stability in presence of carbonyl sulfide. Moreover, its reaction products with species such as COS and CS_2 can be conveniently regenerated, and it also is less toxic than methylethanolamine. DEA does not create irremovable heat stable salts. Given the above advantages, DEA has been selected for use in further experimental studies.

Reaction kinetics

The reaction mechanism of CO_2 with primary and secondary alkanolamine, proposed by Caplow (Caplow 1968) and reintroduced by Danckwerts (Danckwerts 1979), is generally accepted as the reaction mechanism.

$$CO_2 + R_2NH \underset{k_{-1}}{\overset{k_2}{\rightleftarrows}} R_2NH^+COO^- \tag{2}$$

$$R_2NH^+COO^- + B \underset{k_{-b}}{\overset{k_b}{\rightleftarrows}} R_2NCOO^- + BH^+ \tag{3}$$

The first step of the reaction is the reaction of CO_2 with amine to form a zwitterion intermediate. The second step of the reaction is the base-catalyzed deprotonation of this zwitterion. Theoretically, any base present in the solution may contribute to the deprotonation of the zwitterion. The contribution of each base to the overall reaction rate depends on its concentration as well as its basicity. Hence, the main contributions to the deprotonation of the zwitterion in an aqueous solution of a primary or a secondary alkanolamine are from the amine, hydroxide, and water (Rinker, Ashour and Sandall 1996). According to Rinker et al, there are two limiting cases in the zwitterion mechanism. When the zwitterion formation reaction is rate limiting, the reaction rate appears to be first-order in both the amine and CO_2 concentrations. In the case of monoethanolamine (MEA), a primary alkanolamine, the formation of the zwitterion has been shown to be the rate-determining step (Danckwerts 1979, Sada, et al. 1985, Versteeg and van Swaaij 1988, Littel, Versteeg and van Swaaij 1992) On the other hand, when the zwitterion deprotonation reactions are rate limiting, the overall reaction rate appears to have a fractional order between 1 and 2 in the amine concentration. Several authors have reported rate coefficients for this limiting case of the zwitterion mechanism for DEA and DIPA (Blauwhoff, Versteeg and van Swaaij 1984, Versteeg and van Swaaij, 1988, Glasscock, Critchfield and Rochelle 1991). Similarly, if neither reaction in the zwitterion mechanism is rate limiting, the reaction rate exhibits a fractional order between 1 and 2 with respect to the amine concentration; however, the rate expression is more complicated than in the limiting cases. Blauwhoff et al. (Blauwhoff, Versteeg and van Swaaij 1984) summarized some of the previous work on the reaction between CO_2 and aqueous DEA as shown in Table 4. In this table k_1 is the rate constant. Under pseudo first-order assumption with respect to CO_2 we have:

$$r = k_1[CO_2] = k_{app}[CO_2] \tag{4}$$

where r is the reaction rate and $[CO_2]$ is the concentration of CO_2.

Table 4. Literature data on the reaction beween CO2 and aqueous DEA (Blauwhoff, Versteeg and van Swaaij 1984)

reference	temperature (range) °C	DEA mole/l	$k_1 = \frac{r}{[CO_2]}$ s^{-1}	E_{act} kJ/mole	Experimental technique
Blanc and Demarais [5]	20-60	0.05-4.0	$10^{(\frac{-2274.5}{T} + 10.4493)} *[DEA]$	-	Wetted-wall column
Hikita et.al[19]	5.8-40.3	0.174-0.719	$10^{(12.41 - \frac{2775}{T})} *[DEA]^2$	53.1	Rapid mixing method
Van Krevelen and Hoftijzer [28]	19-56	0.05-3	260 $[DEA]^2$	-	Packed column
Nunge and Gill [34]	29.4,35,40.6	~10 - ~12	$C*[DEA]^2$	54.4	Agitated vessel
Jørgensen [26]	0	0.1,0.2,0.3	$(730+4910*[OH^-])[DEA]$ $(692+3380[OH^-]+ 1056 [DEA])*[DEA][16]$	-	Competitive reaction with 0.1,0.2,0.3 M NaOH
Laddha and Danckwerts [31]	11	0.5-2.0	$\frac{[DEA]}{\frac{1}{890} + \frac{1}{560[DEA]}}$	-	Stirred cell
Jensen et.al[22]	18	0.1,0.2	5080 [DEA]	-	Competitive reaction with 0.1,0.2 M NaOH
Jørgensen [26]	18	0.1,0.2,0.3	$(3990+13950[OH^-])[DEA]$	-	Competitive reaction with 0.2,0.3 M NaOH
Sharma [47]	18	1.0	1000 [DEA]	~41.8	Laminar jet
Coldrey and Harris [13]	19	0.1-1.0	$430 [DEA] + 1000[OH^-]^{\frac{1}{2}} - \frac{60([DEAH^+]+[Product])}{[DEA][CO_2]}$		Rapid mixing method with 0.002-0.005 M NaOH
Alvarez-Fuster et.al.[1]	20	0.25-0.82	840 $[DEA]^2$	-	Wetted-wall column
Ratkovics and Horvath [39]	20	0.108-0.964	$k_2 [DEA]^a$	-	Packed column
Donaldson and Nguyen [17]	25	0.031-0.088	1400 [DEA] for [DEA]→0		Facilitated transport in aqueous amine membranes
Groothuis [18]	25	2.0	1300 [DEA] 830 [DEA]*	-	Stirred cell
Laddha and Danckwerts [30]	25	0.46-2.88	$\frac{[DEA]}{\frac{1}{1410} + \frac{1}{1200[DEA]}}$	-	Stirred cell
Sada et.al.[43]	25	0.249-1.922	1340 [DEA]	-	Laminar jet
Sharma [47] Danckwerts and Sharma [15]	25	1.0	1500 [DEA] 1240 [DEA]*	41.8	Laminar jet
Sharma [47] Danckwerts and Sharma [15]	35	1.0	2500 [DEA]	41.8	Laminar jet
Leder [32]	80	-	$1.78*10^3$[DEA]	43.9	Stirred cell

*: corrected for $m_{CO_2}\sqrt{D_{CO_2}}$ in table 2

Rinker et al. (Rinker, Ashour and Sandall 1996) estimated the reaction rate between CO_2 and aqueous DEA from absorption data obtained in a laminar-liquid jet absorber. A comparison of their estimated apparent rate coefficient at 298 K to the estimated reported by other investigators is presented in Figure 4.

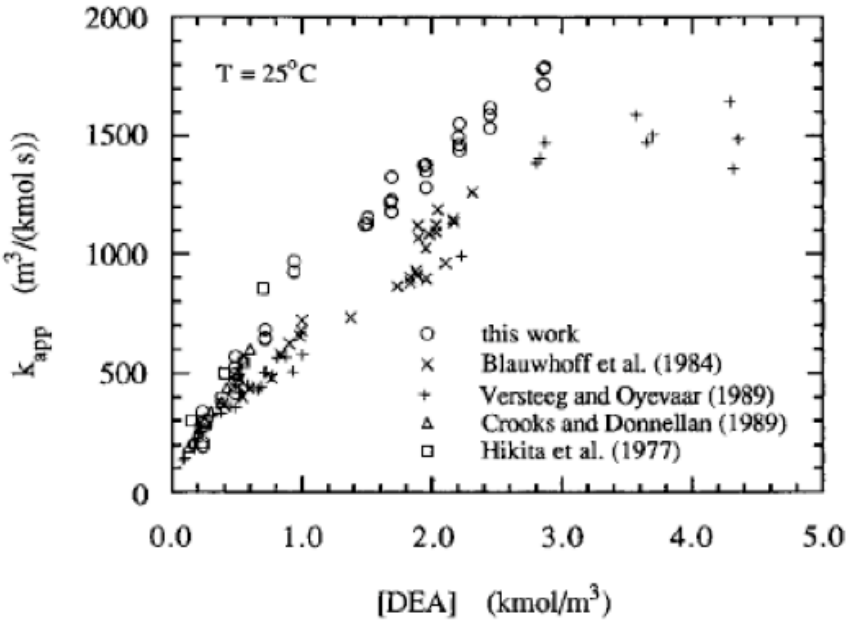

Figure 4. Comparison of the apparent rate coefficeint estimated by Rinker et al. with those reported by other investigators (Rinker, Ashour and Sandall 1996).

According to Versteeg and Oyevaar (1989), the reaction of CO_2 with DEA can be assumed as a pseudo-steady state forward reaction and reaction rate can be calculated as

$$r_{CO_2} = \frac{[R_1R_2NH][CO_2]}{\frac{1}{k_2} + \frac{1}{k_{H2O}[H_2O] + k_{[R_1R_2NH]}[R_1R_2NH]}} = k_{app}[CO_2] \quad (5)$$

where

$$k_{H2O} = \frac{k_2 k_{b,H2O}}{k_{-1}} \quad (6)$$

$$k_{[R_1R_2NH]} = \frac{k_2 k_{b,[R_1R_2NH]}}{k_{-1}} \quad (7)$$

Values for k_2, , $k_{b,[R_1R_2NH]}$, $k_{b,H2O}$, and k_{-1} are reported by Versteeg and Oyevaar (1989). To calculate k_{app} , we have the following equation:

$$k_{app} = \frac{[DEA]}{\frac{1}{k_2} + \frac{k_{-1}}{k_{H_2O}[H_2O] + k_{DEA}[DEA]}} \quad (8)$$

The variation of the apparent rate constant, K_{app}, versus DEA concentration for the temperature 298K and the concentration between 0.1 mol/l and 4.0 mol/l based on Equation (8) is presented in Figure 5.

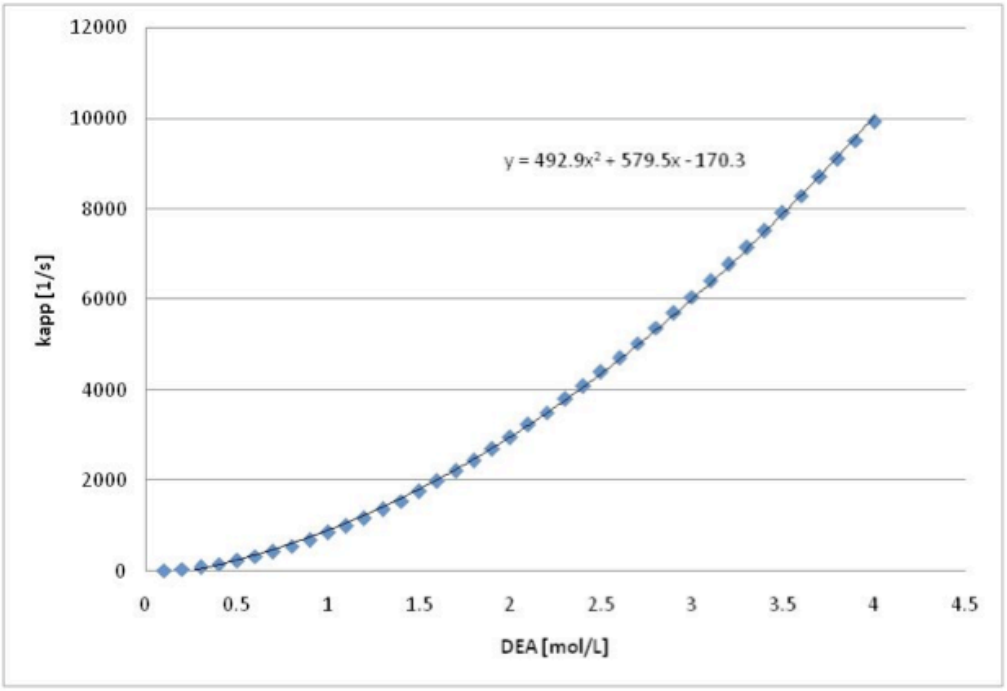

Figure 5. The variation of the apparent rate constant, Kapp, verses DEA concentration for the temperature 298K.

Solubility of CO_2 in aqueous DEA solutions

In the design of absorption process it is essential to estimate the solubility of CO_2 in amine solutions. An important constant to describe the solubility of a gas into solution is the Henry's law constant. The Henry's law constant can be expressed with the following equation:

$$H = \frac{p}{c} \tag{9}$$

where p is the partial pressure of the solute gas above the solution, c is the concentration of the solute and *H* is the constant with the dimension of pressure divided by concentration. Due to reactivity with alkanolamine solutions, the direct measurement of CO_2 solubility is impractical. However, the N_2O analogy has been frequently used to estimate the solubility of CO_2 in amine solutions (Yaghi and Houache 2008). The solubility of CO_2 in amine solutions based on this analogy can be calculated as follows:

$$H_{CO_2} = H_{N_2O}\left(\frac{H_{CO_2}}{H_{N_2O}}\right)_{in\ water} \tag{10}$$

where H_{CO_2} and H_{N_2O} are solubility of CO_2 and N_2O in amine solutions, respectively. Therefore, in order to calculate the solubility of CO_2 in DEA, three parameters must be determined: the physical solubility of CO_2 and N_2O in water, and the solubility of N_2O in DEA. The solubility of N_2O in water is given by Yaghi et al. as follows:

(11)

$$H_{N_2O,W} = 10.86 \times 10^6 \exp\left(\frac{-2372}{T}\right)$$

where $H_{N_2O,W}$ is the Henry's constant in Pa. $m^3.mol^{-1}$ and *T* is the absolute temperature.

The solubility of N_2O in pure DEA can be calculated as follows (Yaghi and Houache 2008):

$$H_{N_2O,pure\ DEA} = a + bT + CT^2 \quad (12)$$

where $H_{N_2O,pure\ DEA}$ is Henry's constant in Pa.m^3.mol^{-1} and T is the absolute temperature. Parameters a, b, and c for DEA are tabulated in Table 5.

Table 5. Coefficient in Equation 12 for solubility of N_2O in pure DEA

	a	b	c	%Error
N_2O-DEA	**47103**	**-305**	**0.5337**	**0.4**

For aqueous solutions Yaghi et al. compared their calculated values for Henry's constant with other available data for a range of DEA concentrations as shown in Figure 6.

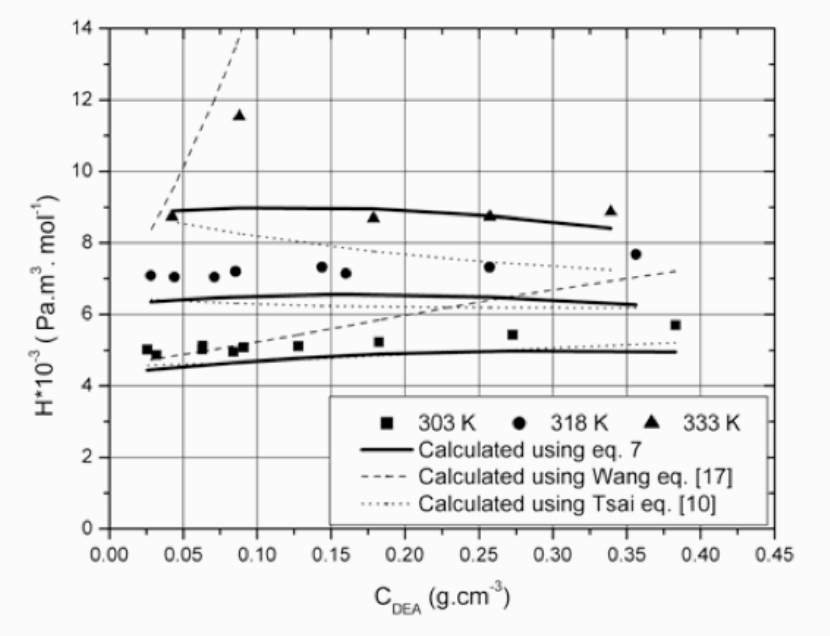

Figure 6. Solubility of N_2O in aqueous DEA solutions (Yaghi and Houache 2008).

In order to use Equation (10), the solubility of CO_2 in water must also be known. The solubility of CO_2 and many other gases can be found from Figure 7 (Seader and Henley 2006).

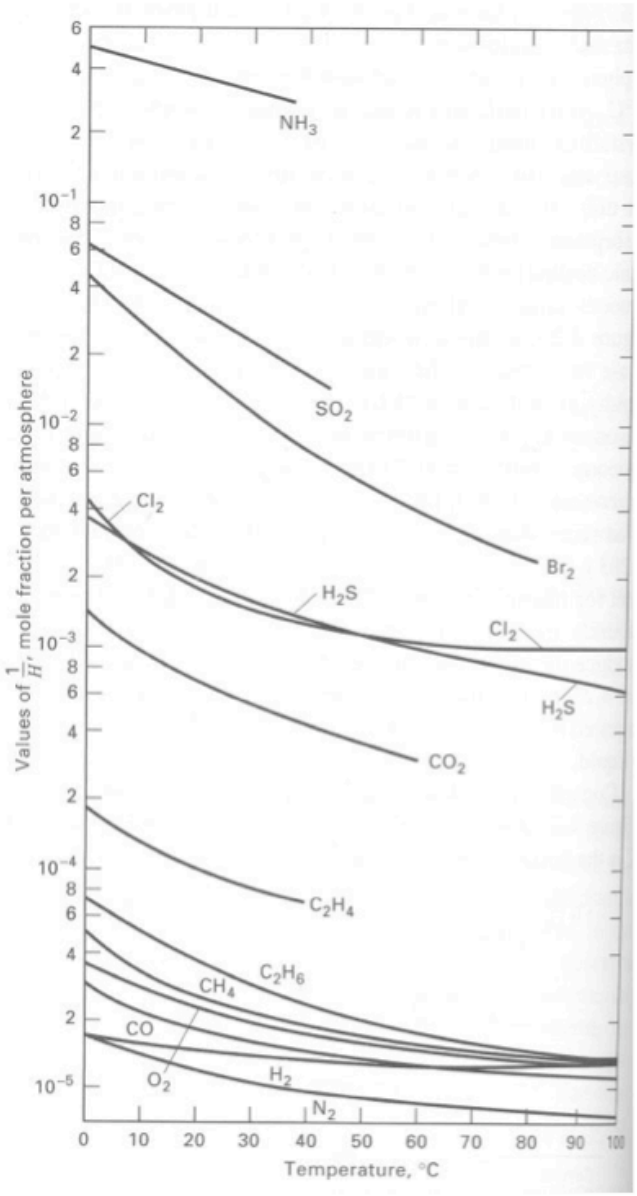

Figure 7. Henry's law constant for solubility of CO_2 and many other gases in water (Seader and Henley 2006).

Design and Fabrication of Experimental Test Section

In order to study the CO_2 absorption process in DEA using microchannels, an experimental setup was designed. The schematic drawing of the experimental setup is shown in Figure 8. The CO_2 gas flows from a gas cylinder into the microchannel absorber. A schematic of microchanel absorber is shown in Figure 9. A scale is used to monitor the amount of mass of gas flowing into the microchannel absorber. The gas flow rate is controlled by a regulator valve. Diethanolamine is driven from a container to the microchannel absorber using a gear pump. A chiller is used to control the temperature of the absorption process in the microchannel absorber. The CO_2-rich DEA stream leaves the absorber and enters the separator. If there is any non-absorbed gas mixed with the liquid, it will be separated in the separator and the CO_2-rich DEA is collected. The flow rate of liquid product is measured by a Coriolis mass flowmeter (not shown in Figure 8). A scale is used to measure the difference between the weights of fresh DEA and collected CO_2-rich

DEA. This difference corresponds to the amount of CO_2 absorbed during the experiment. A high-speed camera is used for visualization study of the absorption process.

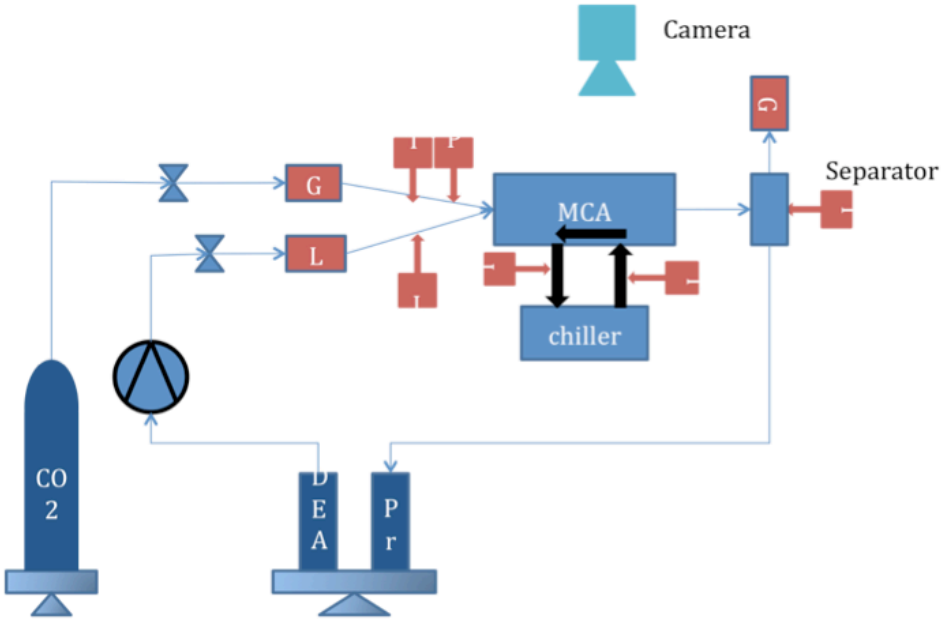

Figure 8. Experimental setup for study of CO_2 absorption in microchannel absorber.

A detailed drawing of the microchannels is shown in Figure 9. On both sides of the plate there are two sets of microchannels: one for absorption process and another for cooling water. There are 10 microchannels for the absorption process, each with 39.6 mm length, 1.264 mm height and 0.5 mm width.

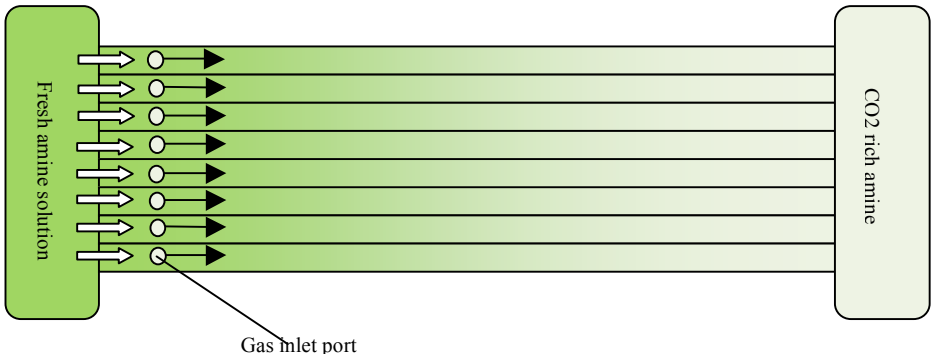

Figure 9. Microchannel absorber schematic drawing.

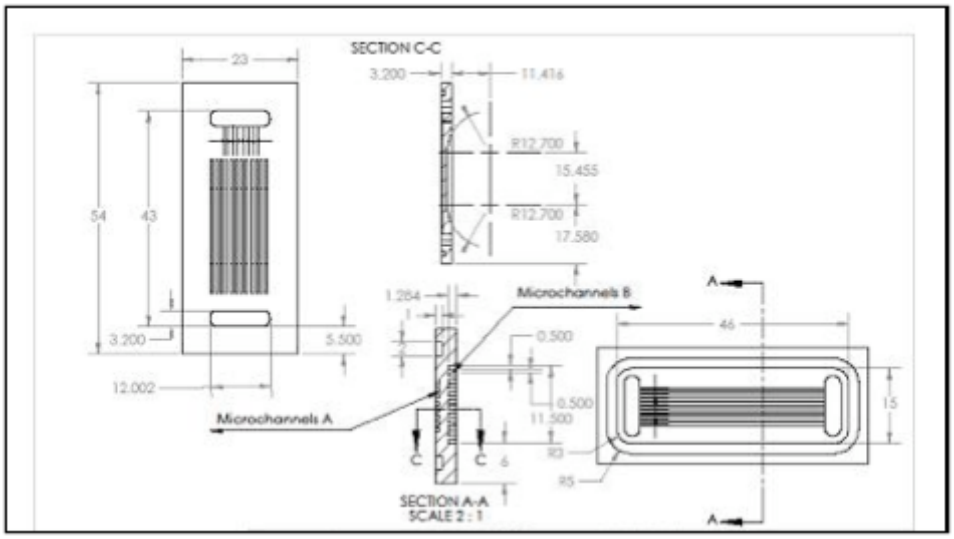

Figure 10. Microchannel base (all dimensions are in mm).

The test section components and assembly are shown in Figure 10 and Figures 11 and 12, respectively.

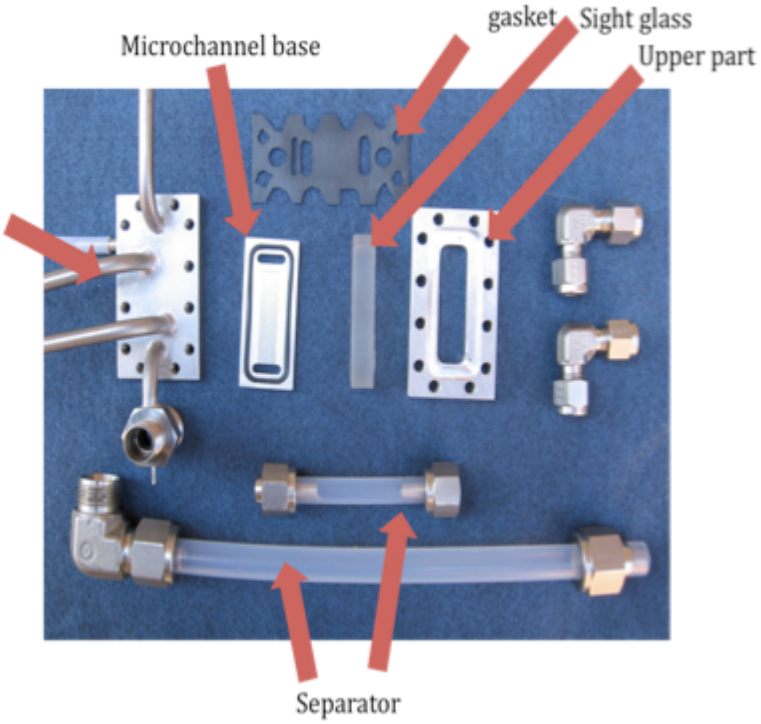

Figure 11. Test section components.

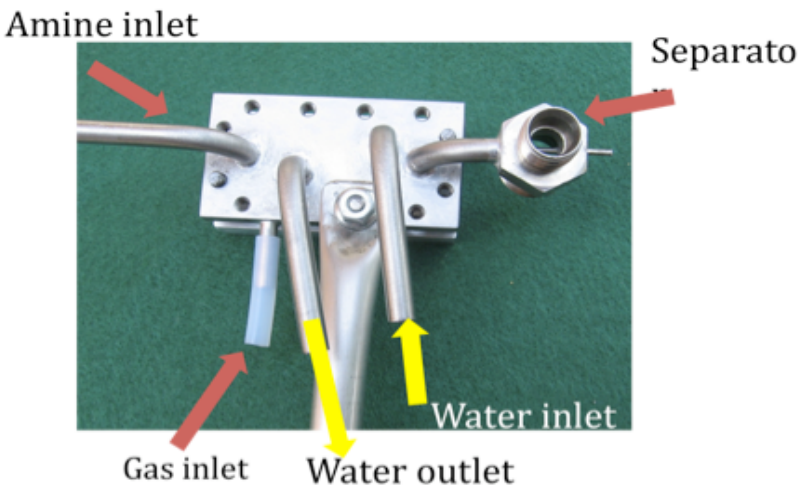

Figure 12. Test section assembly.

Flow visualization of the EHD induced flow

Background and motivation

The motion of and precipitation of particles in air flow of an electrostatic precipitation (ESP) depend on many factors, such as particle properties, electric field, space charge, and gas flow field. It has been shown by many publications that a significant interaction between these factors exists, resulting in considerable turbulent flow structures (known as EHD secondary) in the volume between wire and collecting electrode. However, it is not yet clear whether these turbulent flow structures advance or deteriorate the fine particle precipitation process. To elucidate the influence of the electrically generated flow disturbances in ESPs, more experimental investigation are needed. Recently, the method of particle image velocimetry (PIV) was introduced for instantaneous measurement of the flow velocity field including the turbulence. In particular, the PIV technique has been used for investigating the structure of electrohydrodynamically induced secondary flow in ESPs. Our current experimental work is a visualization study of the EHD secondary with a high-speed camera, which will benefit our further velocity distribution measurement using PIV.

Objectives

- Measure the flow patterns under different operations
- Check the influence of applied voltage, gas flow velocity on the electrostatic separator
- Visualization study of EHD increasing flow turbulence (EHD secondary flow and reversal flow)

Experiment setup

The apparatus used in this experiment consists of an ESP module (Figure 13), a high voltage power supply (range 0-40KV), an atomizer (generating average oil droplet size of 2μm), a laser, a high-speed camera and a PC computer. The testing setup is shown in Figure 14.

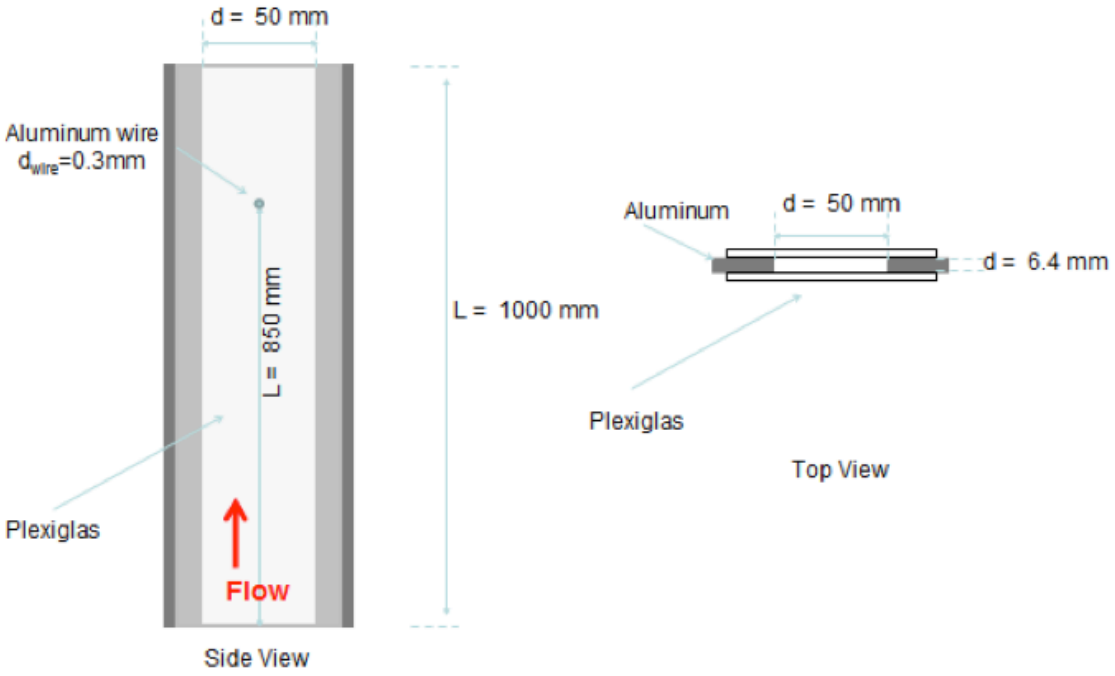

Figure 13. Geometry of testing ESP module.

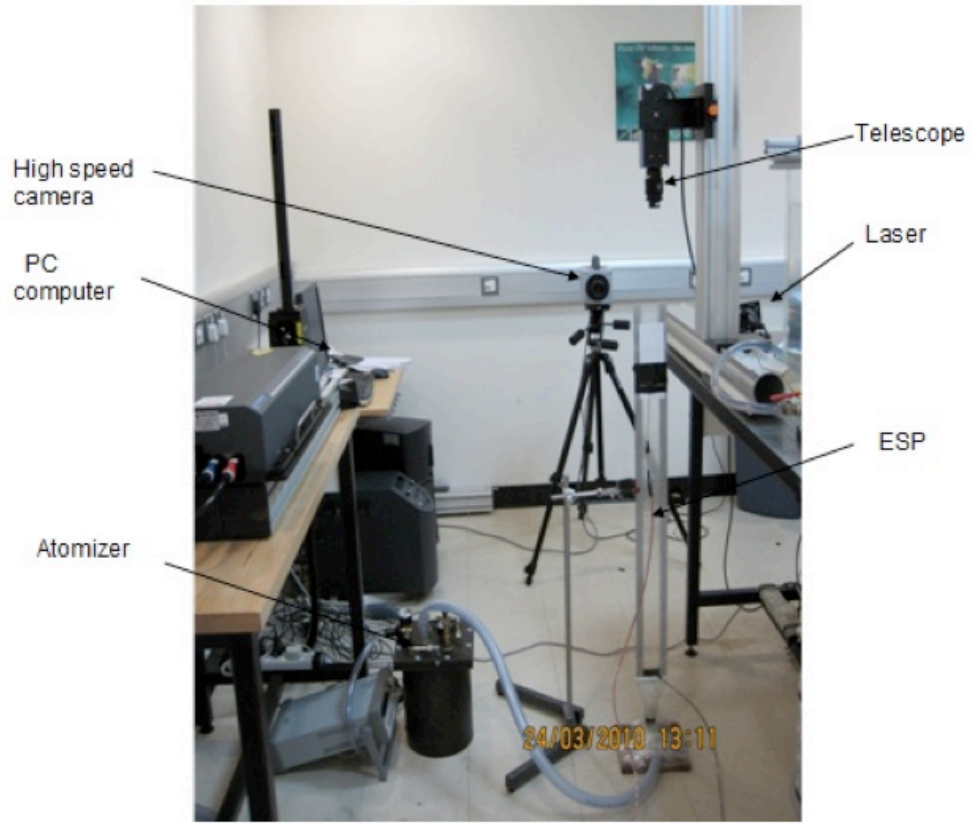

Figure 14. Experimental setup for the EHD flow measurement in the ESP.

Results

The results of the visualization study are shown in Figures 15-20 below.

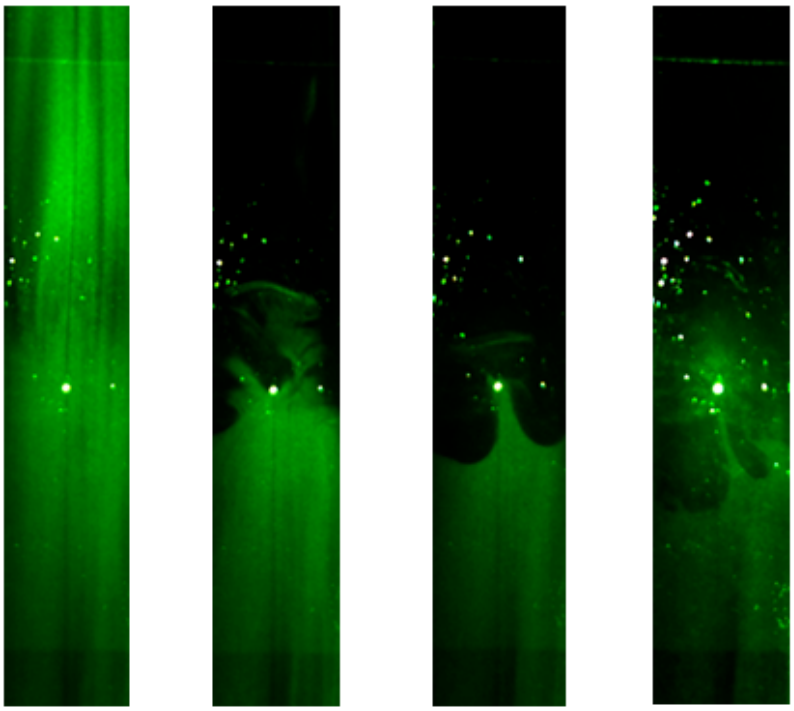

Figure 15. Measurement at Q=0.6L/min.

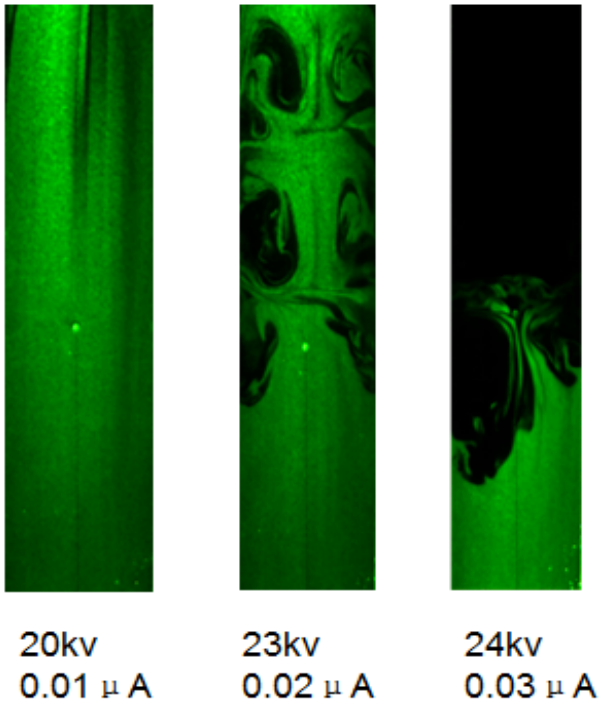

Figure 16. Measurement at Q=1.0L/min.

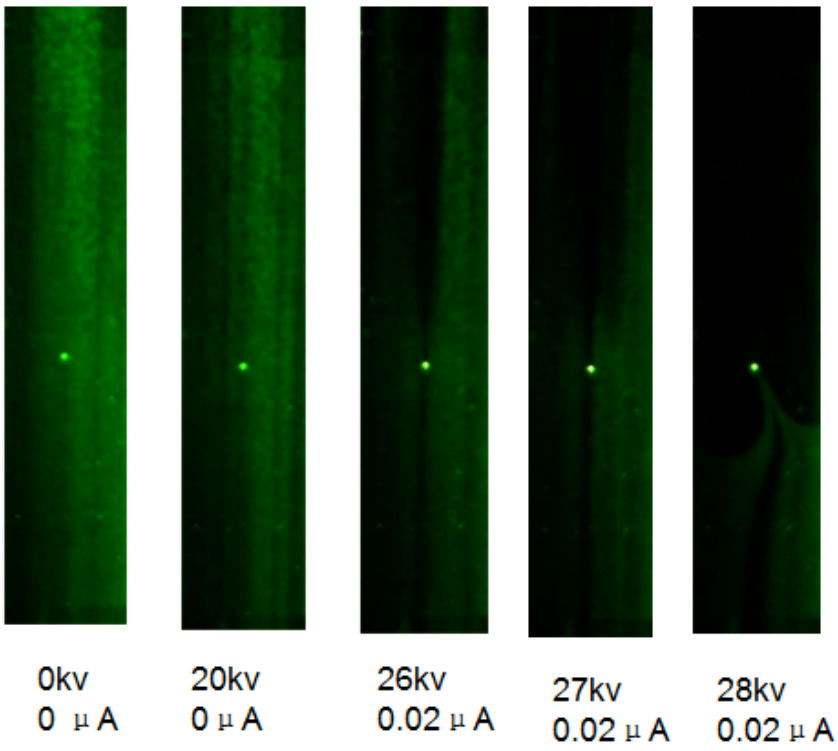

Figure 17. Measurement at Q=1.2L/min.

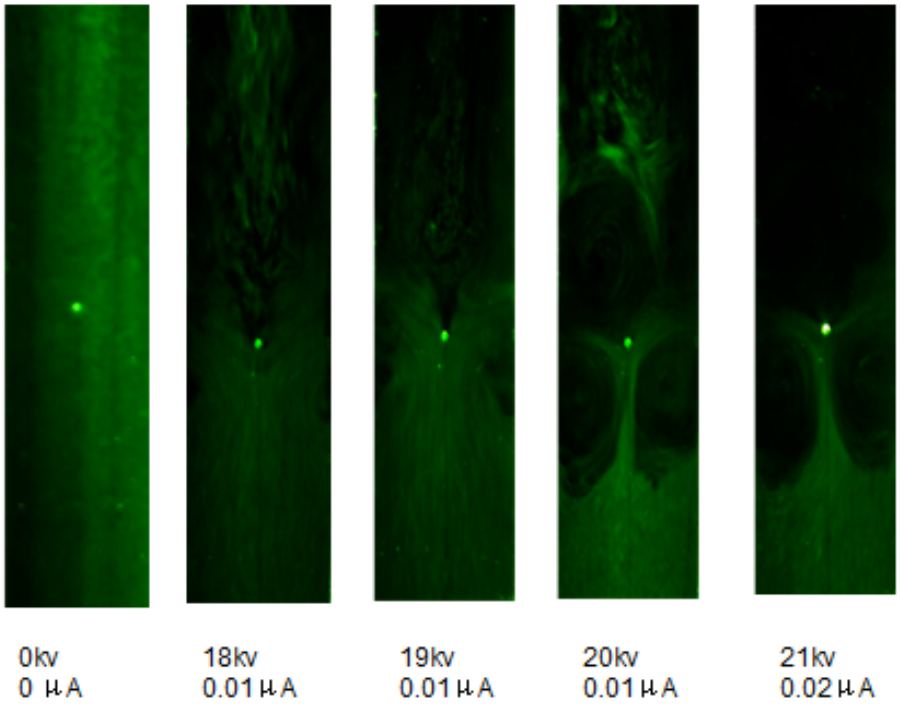

Figure 18. Measurement at 3L/min.

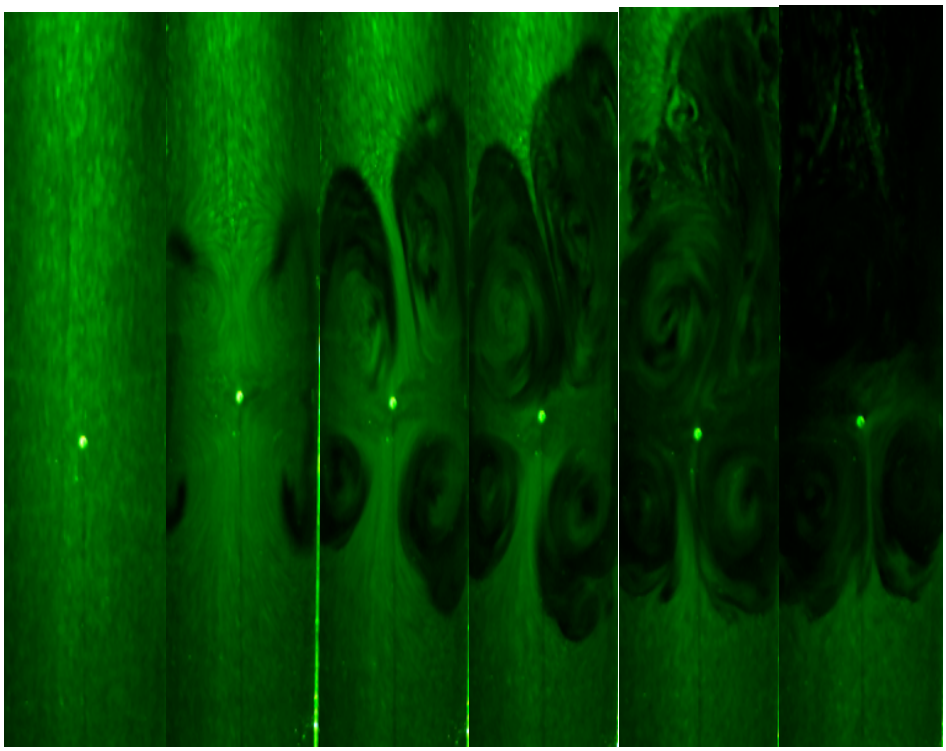

Figure 19. One full process of EHD flow from onset to steady state under 3L/min-20KV-0.01uA.

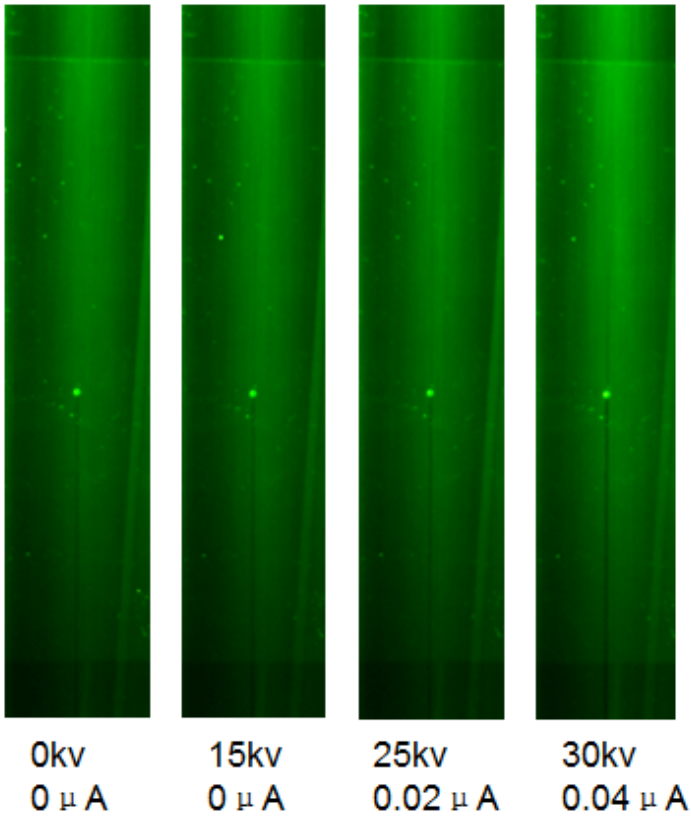

Figure 20. Measurement at 25L/min.

Flow pattern summary

Based on the above measurements, we summarized the following EHD flow patterns inside ESP:

Pattern 1. Laminar flow for very low Re and without corona discharge.

Pattern 2. The streamlines upstream are mostly parallel to the wall, and a very narrow oscillating jet is generated behind the wire and expands slightly towards the channel.

Pattern 3. A wider oscillating jet appears downstream, while two large vortices are generated close to the plate upstream.

Pattern 4. Large oscillations occupy almost all of the downstream, while two large vortices upstream become even larger and close to the wire.

Pattern 5. Four fully developed large vortices are formed around the wire with two located on the downstream side stretching the main flow direction.

Pattern 6. Only two symmetrical large vortices upstream; we can see nothing downstream because of the very low concentration.

Future work

The above measurements need to be further investigated because of the limitation of the atomizer. The concentration of the oil droplets cannot reach a steady-state under such a low flow rate; instead they decrease quickly during the test. And with the high-speed camera, we cannot determine the velocity distribution and, furthermore, we cannot see the flow when the concentration is very low. We were only able to prepare for the preparation for future PIV test.

4. Difficulties Encountered/Overcome

None to report.

5. Planned Project Activities for the Next Quarter

- Conduct preliminary tests on CO2 absorption
- Investigate the possibility of development of a numerical model for absorption process
- Conduct PIV measurements
- Continue on collaboration work with the PI partners to compare PIV measurements with numerical modeling results for the electrostatic separation process
- Prepare manuscripts for publication based on the collected data

Appendix

Justification and Background

Separation comprises a significant part of the oil and natural gas production process. In many stages of this process, electrostatic separation significantly increases the efficiency and often decreases the cost of production. Most of the oil producers, including ADNOC, operate where the climate is hot and therefore use refrigeration and air-conditioning equipment. The efficiency and reliability of this equipment appreciably suffers due to mal-distribution of lubricant oil in the system. Electrostatic separation can correct this mal-distribution and improve the efficiency of this refrigeration and air-conditioning equipment. Similarly, vapor compression equipment with lubricant circulation is also used in oil refinery processes. This circulation can be significantly improved using EHD separators to increase heat-pumping efficiency. UMD has already developed a working prototype for gas-and-non-conductive droplet separation. However, the fundamentals of this separation mechanism must be better understood to enable optimization of the working design. There is also a need to explore the feasibility of separation of gas-and-conductive liquid mixtures, which poses additional challenges.

Conventional gas/liquid separators are based on inertial and gravitational forces. They have poor efficiency when separating micron-size particles in the flow due to low gravitational and inertial forces acting on small particles. In contrast, electro-hydrodynamic (EHD) forces strongly affect particles of such size. The combination of a conventional separator with EHD allows us to create the most effective and lowest pressure-drop particle separator, with potential applications to separation of electrically conductive and non-conductive liquid particles. The separation of electrically conductive particles like water-air mixtures (fog) imposes significant design constraints on separator electrode design and high-voltage power supply selection.

Approach

Detailed analysis and identification of the phenomena and the design challenges involved in effective implementation of the mechanism. Parametric study of existing and improved separators. Design iterations, including numerical flow and field simulations, fabrication, and testing. Creation of database and engineering design correlations.

Three-Year Schedule

Year 1:

- Conduct literature review to understand the basic of mass transfer in micrreactor and separation of flue gas with microreactor;
- Evaluate existing technologies and assess their applicability to CO_2 separation of flue gas;
- Repeat and implement some previous classical examples of microchannel separation to get familiarized with fundamentals and basic challenge;
- Analyze heat transfer and particles fouling of flue gas cooling equipment;
- Analyze mixing in microchannels and possibility to use it in CO_2 separation;
- Continue improving efficiency of EHD separator for the fine liquid and solid particles;
- Evaluate and optimize current designs of UMD EHD separators for non-conductive liquid particles in gas flow;
- Conduct visualization study of liquid and solid particles migration in the electrical field.

Year 2:

- Simulate mixing and separation phenomena in microreactor via modeling and analytical means;

- Develop laboratory scale microchannel absorber and desorber for CO_2 separation;
- Conduct parametric study on microreactor separation;
- Conduct optimization study.

Year 3:
- Conduct visualization study on absorption and desorption in microchannels;
- Design iterations and implementation.
- Experiment on different designs.
- Present the best design to ADNOC group of companies.
- Develop design correlation.
- Prepare report.

References

[1] Aaron, Douglas, and Costas Tsouris. "Separation of CO2 from Flue Gas: A Review." *Separation Science and Technology* 40 (2005): 321-348.

[2] Aresta, Michael, ed. *Carbon Dioxide Recovery and Utilization.* Kluwer Academic Publishers, 2003.

[3] Blauwhoff, P. M. M., G. F. Versteeg, and W. P. M. van Swaaij. "A study on the reaction between CO2 and alkanolamines in aqueous solutions." *Chem. Eng. Sci.* 39 (1984): 207-225.

[4] Caplow, Michael. "Kinetics of Carbamate Formation and Breakdown." *J. Am. Chem. Soc* 90, no. 24 (1968): 6795–6803.

[5] Danckwerts, P. V. "The Reaction of CO2 with Ethanolamines." *Chemical Engineering Science* 34, no. 4 (1979): 443-446 .

[6] Glasscock, D. A., J. E. Critchfield, and G. T. Rochelle. "CO2 absorption/desorption in mixtures of methyldiethanolamine with monoethanolamine or diethanolamine." *Chem. Eng. Sci* 46 (1991): 2829-2845.

[7] Herzog, H., D. Golomb, and S. Zemba. "Feasibility, modeling and economics of sequestering power plant CO2 emissions in the deep ocean." *Environmental Progress* 10 , no. 1 (1991): 64-74.

[8] Herzog, Howard. "An Introduction to CO2 Separation and Capture Technologies." MIT Energy Laboratory, 1999.

[9] Kockmann, N. *Transport Phenomena in Micro Process Engineering.* Berlin: Springer-Verlag, 2008.

[10] Kohl, Arthur L., and Richard B. Nielsen. *Gas purification.* Houston, Texas: Gulf Publishing Company, 1985.

[11] Littel, R. J., G. F. Versteeg, and W. P. M. van Swaaij. "Kinetics of CO2 with primary and secondary amines in aqueous solutions-II.Influence of temperature on zwitterion formation and deprotonation rates." *Chem. Eng. Sci.* 47 (1992): 2037-2045.

[12] Rinker, Edward B., Sami S. Ashour, and Orville C. Sandall. "Kinetics and Modeling of Carbon Dioxide Absorption into Aqueous Solutions of Diethanolamine." *Ind. Eng. Chem. Res.* 35 , no. 4 (1996): 1107–1114.

[13] Sada, E., H. Kumazawa, Q. Han, and H. Matsuyama. "Chemical kinetics of the reaction of carbon dioxide with ethanolamines in nonaqueous solvents." *AIChE J.* 31 (1985): 1297-1303.

[14] Seader, J. d., and Ernest J. Henley. *Separation Process Principles.* Edited by Ernest J. Henley. Wiley, 2006.

[15] Versteeg, G. F., and M. H. Oyevaar. "The reaction between CO2 and diethanolamine at 298 K." *Chem. Eng. Sci* 44 (1989): 1264-1268.

[16] Versteeg, G. F., and W. P. M. van Swaaij. "On the kinetics between CO2 and alkanolamines both in aqueous and nonaqueous solutions-I. Primary and secondary amines." *Chem. Eng. Sci.* 43 (1988): 573-585.

[17] Versteeg, G. F., and W. P. M. van Swaaij. "On the kinetics between CO2 and alkanolamines both in aqueous and nonaqueous solutions-II. Tertiary amines." *Chem. Eng. Sci* 43 (1988): 587-591.
[18] Yaghi, Basma, and Omar Houache. "Solubility of Nitrous Oxide in Amine Aqueous Solutions." *Journal of Engineering, Computing and Architecture* 2, no. 1 (2008).

Microreactors for Oil and Gas Processes Using Microchannel Technologies

UMD Investigators: Serguei Dessiatoun, Amir Shooshtari
GRA: Pradeep Kumar Singh
PI Investigators: Michael Ohadi, Afshin Goharzadeh, Ebrahim Al-Hajri (Returning ADNOC Scholar)
Start Date: Oct 2006

1. Objective/Abstract

Microfabrication techniques are increasingly used in gas and petrochemical engineering to realize structures with capabilities exceeding those of conventional macroscopic systems. In addition to already-demonstrated chemical analysis applications, microfabricated chemical systems are expected to have a number of advantages for chemical synthesis, chemical kinetics studies, and process development. Chemical processing advantages from increased heat and mass transfer in small dimensions are demonstrated with model gas, liquid and multiphase reaction systems.

Evaluation of different applications of microreactors and their impact on UAE industry economic has been conducted in this quarter. The application of microreactors in the polymerization of ethylene and propylene is feasible and may provide significant economical benefits, therefore will be considered for further investigation in the current project

2. Milestones/Deliverables Scheduled for the Completed Quarter

- Identifying target reaction.

3. Summary of Project Activities for the Completed Quarter

Identifying target reaction

Methane and oxygen production

In order to determine reactions suitable for the petrochemical industry, an extensive literature survey was done. The initial literature review focused on microreactor technologies and their working principles. KP Brooks et al. [1] discussed adsorption, absorption, the Sabatier Reaction (SR), Reverse Water Gas Shift (RWGS) and separation reactions in microreactors.

The Sabatier reaction is given as

$$2H_2O \rightarrow O_2 + 2H_2 \rightarrow \text{(respiration)} \rightarrow CO_2 + 2H_2 + 2H_2 \text{ (added)} \rightarrow 2H_2O + CH_4 \text{ (discarded)}$$

The RWGS reaction is given by:

$$CO + H_2O \rightarrow CO_2 + H_2$$

In absorption reactions it was found that the overall mass transfer coefficient was as much as 2.6 times greater than that for a conventional packed column for thinnest microwick [1].

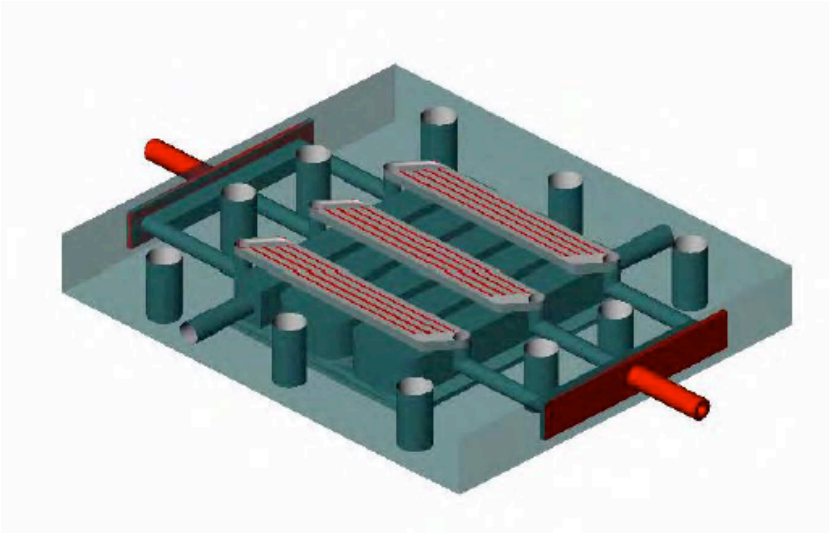

Figure 1. A semi-transparent rendering of one section of a three-parallel microchannel membrane contactor absorber. The red-lines are membrane support ribs, the red tubes on the ends of the unit are headers feeding the 3-parallel channels, and the gray tubes on the sides of the structure are fluid ports for the serpentine heat-exchange channel.

Brooks et al. [1] performed experimental work in a single channel adsorber to assess an adsorber system based on microchannels. A temperature cycle between 12 and 77°C could be achieved in less than two minutes with greater than 90% of theoretical working capacity. It was found a diurnal cycle thermal-swing adsorption system requires more than 100-times more adsorbent than a microchannel sorption pump operating on 2-minute cycles.

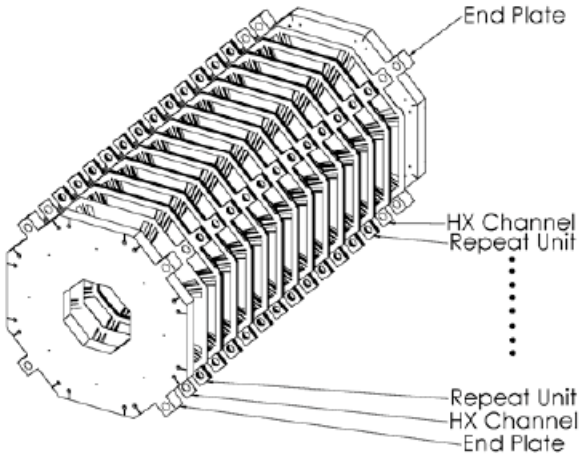

Figure 2. An exploded view of multiple repeat units, capping heat-exchange shims, and endplates arranged for bonding.

Their testing with the RWGS and SR units was encouraging. Overall 60% conversion was achieved using a two-stage RWGS reactor in which water was removed between two stages [1].

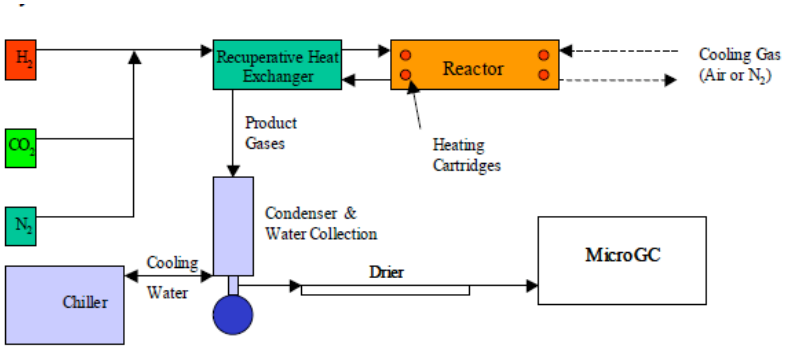

Figure 3. Generic equipment layout for RWGS & SR reactor testing.

This paper provided us with the perspective of the nature of reactions that can be performed in microreactors.

Evaluation:

- **Feasibility: high**
- **Impact: moderate**.

Hydrogen peroxide synthesis

H_2O_2 can be produced in two ways:

1) Direct conversion of H_2 and O_2 into H_2O_2
2) Auto oxidation of anthraquinone.

The process of direct conversion of H_2 and O_2 into H_2O_2 is shown below. This process is known as the Riedl-Pfleiderer process, having been first discovered by them in 1936. The overall equation for the process is deceptively simple:

$$H_2 + O_2 \rightarrow H_2O_2$$

Initially, synthesis of hydrogen peroxide in a microreactor was considered for as a possible candidate for research. Hydrogen peroxide, being the strongest oxidant, could be used in the petrochemical industry for oxidation of carbohydrates. Catalytic synthesis of hydrogen peroxide by direct conversion was looked at by S. Maehara et al. [2]. In the study it was found that the concentration of hydrogen peroxide was very low, 0.204 g/kg. In another similar study by Voloshin et al. [3], they tried to obtain a higher hydrogen peroxide concentration by adding 1% (w/w) H_2SO_4 and 10 ppm NaBr. The addition of 1% (w/w) H_2SO_4 and 10 ppm NaBr stabilizes H_2O_2 from further decomposition. They also tried to increase the H_2O_2 concentration by increasing selectivity of H_2O_2 by maintaining the H_2 conversion rate as low 2%. However, they still were unable to produce hydrogen peroxide with high concentrations. So the production of

H_2O_2 by direct conversion is not a feasible method for industries where H_2O_2 concentration required is very high.

The auto-oxidation process is given shown by the reaction below.

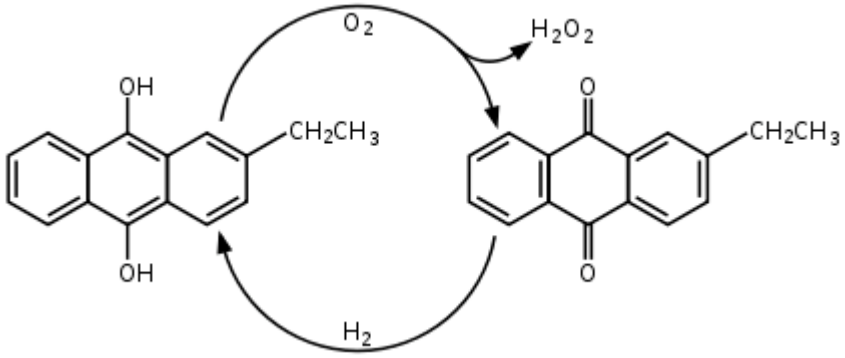

Auto-oxidation (AO) of anthraquinone is another method currently in use in the industry for H_2O_2 synthesis. Conventional methods require very high inventory of reagent, as has been discussed by [4,5]. Additionally, the conventional method results in degradation of hydrogenated anthraquinone due to overt reduction reactions [4,5] and formation of epoxides due to excessive oxidation [4,5]. This results in loss of expensive anthraquinone [4,5]. Also the residence time for reactants is very high for the conventional method and require more expensive material to design the entire process [4,5]. Auto-oxidation being a well-tested method for the synthesis of H_2O_2, if performed in microreactors, would result in higher efficiency, high conversion rate and low residence time [4,5].

Evaluation:

- **Feasibility: high;**
- **Impact: moderate.**

Steam methane reforming

Steam reforming reactions are endothermic in nature and involve five species in two reversible reactions.

$$CH_4 + H_2O \Leftrightarrow CO + 3H_2 \qquad \Delta H298 = 206 \text{ kJ/ mol}$$
$$CO + H_2O \Leftrightarrow CO_2 + H_2 \qquad \Delta H298 = -41 \text{ kJ /mol}$$

Overall reaction:

$$CH_4 + 2H_2O \Leftrightarrow CO_2 + 4H_2 \qquad \Delta H298 = 165 \text{ kJ /mol}$$

Multiple reactors are connected in parallel to achieve plant-scale capacity, as shown in Figure 4 below, where a full-scale unit (3.9m × 5.8m × 3.9m*)* produces $10m^3$ of hydrogen per second by manifolding 30 commercial-scale microchannel reactors housed evenly between six reactor assemblies [20].

Microchannel process technology advantages are based on the use of small diameter channels to improve both heat and mass transfer rates by one to two orders of magnitude. Critical channel dimensions typically range from 50 to 5000 micro-m and flow regimes are usually laminar. Transport rates are inversely proportional to channel diameters. Further, microchannels allow for an increase in the amount of surface area per unit volume—thus also increasing the overall productivity per unit volume [20].

Conventional methane steam reforming catalysts based on extruded pellets have reaction times on the order of seconds. Inserted engineered structures described in this paper are based on catalyst-coated FeCrAlY felts that are adjacent to the heat transfer wall and facilitate reaction rates on the order of milliseconds.

One particular technical challenge addressed in this paper surrounds the stable operation of combined reforming and combustion with low excess air in adjacent reaction microchannels.

In this study the combustion of methane/natural gas was carried out in parallel to the SMR reaction. Shown below is the experimental setup:

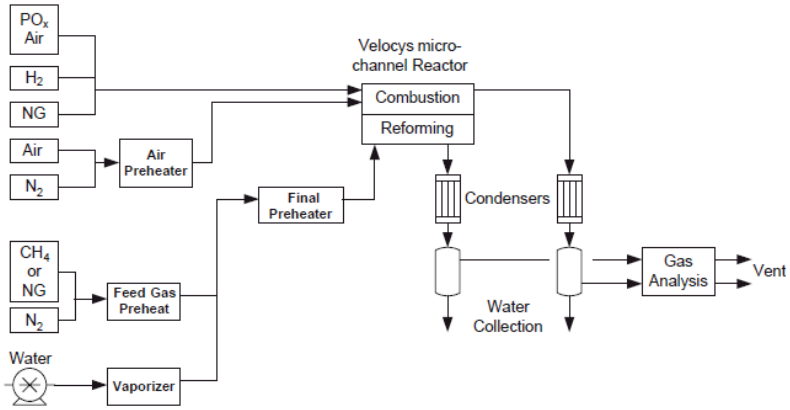

Figure 4: Experimental set-up for microchannel reformer.

Water was vaporized at pressure in a resistance-heated microchannel heat exchanger and mixed with preheated methane or natural gas. The resulting mixture was then preheated to the desired reactor inlet temperature (280–310 °C) with the aid of an electrical microchannel preheater. An external resistance-heated microchannel heat exchanger was also used to preheat the inlet combustion air to 150–160 °C.

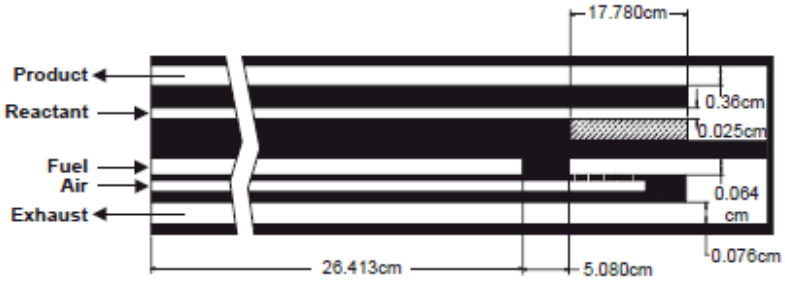

Figure 5. Microchannel steam reforming reactor with integrated partial oxidation.

The catalyst was washcoated on the walls of the combustion chamber, while for the SMR reaction the catalyst was solution-coated on a porous metal, 40-pore/cm foam and inserted in the reactor. The reforming catalyst was prepared as a powder, which was then made into slurry and deposited on a FeCrAlY felt substrate (0.25 mm nominal thickness, 75% porosity). The SMR catalyst was 10% Rh on a gamma alumina support modified with 4.5% MgO (w/w).

Methane conversion of >90% was achieved at >150kPa pressure and 850 ^{o} C with contact time as low as 6 ms. Internal heat transfer flux was 17 W/cm^2. Volumetric heat transfer flux was more than 65 W/cm^3, which is very high compared to conventional SMR reactor volumetric heat transfer value of 1 W/cm^3.

For these tests, combustion of methane or natural gas was conducted with low rates of excess air (25%), an important requirement for plant scale-up to reduce the cost of blowers or compressors. Heat was transferred as it was generated to drive the endothermic reforming reaction. The average area heat flux exceeded 17 W/cm^2 while maintaining acceptable metal wall temperatures (< 900 ◦C), an important consideration for mechanical integrity.

Mathematical modeling of the steam methane reforming reaction:
The reaction system considered in this work is the endothermic steam reforming of methane and methane catalytic combustion taking place in alternate channels of a microreactor. The main chemical processes involved in the process are:

- Methane steam reforming:

$$CH4 + H2O \Leftrightarrow CO + 3H2 \qquad \Delta H = +206 \text{ kJ/mol},$$

- Water gas-shift:

$$CO + H2O \Leftrightarrow CO2 + H2 \qquad \Delta H = -41 \text{ kJ/mol},$$

- Reverse methanation:

$$CH4 + 2H2O \Leftrightarrow CO2 + 4H2 \qquad \Delta H = +164 \text{ kJ/mol},$$

The net reaction rates for the above reactions are given by:

$$r_1 = \frac{\frac{k_1}{p_{H_2}^{2.5}}\left(p_{CH_4}\,p_{H_2O} - \frac{p_{H_2}^3\,p_{CO}}{K_{e,1}}\right)}{(\mathrm{Den})^2}, \quad \mathrm{kmol/kg_{cat}/h},$$

$$r_2 = \frac{\frac{k_2}{p_{H_2}}\left(p_{CO}\,p_{H_2O} - \frac{p_{H_2}\,p_{CO_2}}{K_{e,2}}\right)}{(\mathrm{Den})^2}, \quad \mathrm{kmol/kg_{cat}/h},$$

$$r_3 = \frac{\frac{k_3}{p_{H_2}^{3.5}}\left(p_{CH_4}\,p_{H_2O}^2 - \frac{p_{H_2}^4\,p_{CO_2}}{K_{e,3}}\right)}{(\mathrm{Den})^2}, \quad \mathrm{kmol/kg_{cat}/h},$$

$$\text{where Den} = 1 + K_{CO}\,p_{CO} + K_{H_2}\,p_{H_2} + K_{CH_4}\,p_{CH_4} + K_{H_2O}\,p_{H_2O}/p_{H_2}.$$

The values of pre-exponential factors, activation energies, heat of absorption, and equilibrium constants are given below:

Table 1. Pre-exponential factors for reaction rates, heats of adsorption and corresponding activation energies

Constant	Pre-exponential factor $A(k_k)$; $A(K_i)$	Activation energy, E_k (kJ/mol) Heat of adsorption $(-\Delta H)_k$ (kJ/mol)
k_1 (kmol bar$^{0.5}$/(kg$_{cat}$ h))	4.225×10^{15}	240.1
k_2 (kmol/(kg$_{cat}$ h bar))	1.955×10^{6}	67.13
k_3 (kmol bar$^{0.5}$/(kg$_{cat}$ h))	1.020×10^{15}	243.9
K_{CO} (bar^{-1})	8.23×10^{-5}	70.65
K_{CH_4} (bar^{-1})	6.65×10^{-4}	38.28
K_{H_2O} -	1.77×10^{5}	−88.68
K_{H_2} (bar^{-1})	6.12×10^{-9}	82.9
	$K_{e,1} = \exp(-26830/T + 30.114)$, bar^2	
	$K_{e,2} = \exp(4400/T - 4.036)$, -	
	$K_{e,3} = \exp(-22430/T + 26.078)$, bar^2	

The reaction rate constant is independent of concentration and is given by:

$$k = A(T/T_0)^n e^{-E_a/RT}$$

where n is temperature exponent and Ea is activation energy.

The rate of reaction terms determine the generation/consumption of a particular species, which appear in transport equations for species.

$$\frac{\partial c}{\partial t} + u_i \frac{\partial c}{\partial x_i} = \frac{\partial}{\partial x_i}\left(D \frac{\partial c}{\partial x_i}\right) - r,$$

where c is the concentration of solute in units of mol/volume, ui the flow velocity, D the molecular diffusivity and r the source term due to chemical reactions.

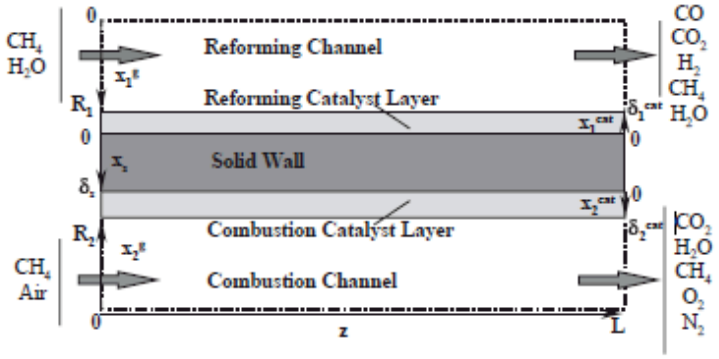

Figure 6. Single-plate geometry within the CPR depicting the modeling domains.

The dependence of the physical properties of chemical species on temperature is accounted for via the following expressions:

$$heat\ capacity: c_p = a + bT + cT^2 + dT^3,$$

$$thermal\ conductivity: k = k_0 \left(\frac{T}{T^0}\right)^{0.75},$$

$$diffusion\ coefficient: D_G = D_{G0} \left(\frac{T}{T^0}\right)^{1.75}.$$

The diffusion coefficients have been calculated for a binary mixture between component i and H_2O (reforming channel) or air (combustion channel). The heat capacity and thermal conductivity of the reaction mixtures are calculated based on local composition. The effective diffusion coefficient for the catalyst layer is calculated from

$$D_{\text{eff}_{i,j}} = \frac{\varepsilon}{\tau}\left(\frac{1}{D_{K_{i,j}}} + \frac{1}{D_{G_{i,j}}}\right)^{-1}$$

where $DG_{i,j}$ is molecular diffusion coefficient is calculated by Fuller's method and the Knudsen diffusion coefficient, $DK_{i,j}$ is calculated from

$$D_{K_{i,j}} = 97R_p\sqrt{\frac{T_j^{\text{cat}}}{M_{i,j}}}$$

The simulation of the reaction can be done using the above unique characteristics and continuity, momentum and energy equations.

Evaluation:

- **Feasibility: high;**
- **Impact: moderate.**

H_2S decomposition

Introduction: Given below are the methods to decompose H_2S into hydrogen and sulfur:

1. Catalytic or noncatalytic thermal decomposition.
2. Thermochemical decomposition.
3. Electrochemical decomposition.
4. Photochemical decomposition.
5. Plasma method of decomposition.

Thermal decomposition:
Hydrogen sulfide breaks down into hydrogen and sulfur on the application of heat. The thermal decomposition reaction can be considered to follow the stoichiometric equation below:

$$2H_2S \leftrightarrow 2H_2 + S_2$$

Thermal decomposition studies in tubular reactors: The following table summarizes the experimental tests done in a tubular reactor:

Table 2. Experimental results in a tubular reactor

Reactor Type	Operating variables	Results	References
Flow tubular reactor	Temp: 750-1350. Pressure: 1 atm. Catalysts: Silica beads, cobalt molybdate and 1% pre-sulfided platinum	Below 1250K the influence of catalyst was found to be very significant. Cobalt-molybdate catalyst was most active of the three.	Raymont [15,16,20,21]
Non-isothermal flow reactor Fused alumina tube with crushed alumina pieces filled	Temp: 873-1133K. Pressure: 131-303 kPa. Flow rate: 3.4-36 mol/m^2s	The flow rates used satisfied the plug flow. Reactor material did not act as a catalyst. Activation energies of 196 and 105 J/mol were obtained for the forward and reverse reactions. Decomposition rate was of second order.	Kaloidas and Papayannakos [22]
Flow tubular reactor	Catalyst: molybdenum disulfide	The activation energy of reaction rate determining H_2S cleavage step was 217 kJ/mol. The catalytic activity of MoS_2 decreased with time, stabilizing at 65% of the initial value after about 15-25 h of operation.	Kaloidas and Papayannakos [25]
Quartz circular reactor	Temp 1090-1230 K. Pressure 13-51 kPa. Catalyst: Alumina, Cr_2S_3, WS_2 and MoS_2. Flow rate: 0.03-0.10 Nm^3/h Reaction products	Sulfur was removed by condensation at heat exchanger. Swing adsorption was used to separate H_2 and H_2S. MoS_2 was superior catalyst.	Bandermann and Harder [26], Chivers et al. [27]

	were cooled down to 700K to hinder the recombination		

Thermal decomposition studies by equilibrium shift: The equilibrium reaction is:

$$2H_2S \leftrightarrow 2H_2 + S_2$$

By removing S_2 the reaction is shifted in the forward direction. This can be easily understood from the below rate of reaction equation for H_2S:

$$r_{H2S} = k_1 P_{H2S} - k2 P_{H2} (P_{S2})^{1/2}$$

To hinder recombination, the reaction products are quickly cooled down to 700 K or lower temperature after leaving the reactor. The sulfur is removed by condensation in a heat exchanger followed by an electro-filter. A pressure swing adsorption system is used to separate the gas containing 25-30% hydrogen and 75-70% hydrogen sulfide. Hydrogen sulfide is recirculated to the reaction chamber.

The research is summarized in the table below:

Table 3. Summary of research on thermal decomposition by equilibrium shift

Reactor Type	Operating variables	Results	References
Pyrex glass re-circulating system	Temp: 773-1073K Pressure: 5-20 kPa Catalyst: MoS_2| Cold trap to remove sulfur	It was possible to convert more than 95% of H_2S.	Fukuda et al. [28]
Pyrex glass re-circulating system	Temp: 773 K Pressure: 6kPa Catalyst: MoS_2 reduced in H_2 and MoS_2|evacuated at high temperature H_2S was frozen at 77K.	Direct thermal decomposition in the absence of catalyst was shown to be negligible. Catalytic activity of MoS_2 was enhanced if the MoS_2 was reduced by hydrogen at higher temperatures. - The activity of the catalyst did not increase considerably when the catalyst was evacuated at high temperature instead of being reduced.	Sugioka and Aomura [29-31]

Other thermal decomposition methods such as product removal by membrane, product removal by thermal diffusion and thermal methods by solar energy have been tested. But because they are in initial stages of development they are not very promising in the present context.

Processes based on membrane reactors are not technologically available today. A high-temperature solar furnace on a large scale is not a reality yet; the problem of material of construction is not trivial. The thermal diffusion column reactors have not been developed as practical devices and the system has been found to be energetically inefficient.

The product removal scheme of Fukuda et al. [28] is unworkable on a large scale because of the large heating/cooling load. The scheme suggested by Bandermann and Harder [26] is based on today's technology and has been claimed to be commercially feasible.

Thermochemical Methods of Decomposition:

A thermochemical method of decomposition is represented by following equation.

$$(M \text{ or } M_xS_y) + zH_2S \rightarrow (MS_z \text{ or } M_xS_{y+z}) + zH_2$$
$$(MS_z \text{ or } M_xS_{y+z}) \rightarrow (M \text{ or } M_xS_y) + zS^*$$

Overall,

$$zH_2S \rightarrow zH_2 + zS^*$$

Table 4. Summary of research on thermochemical methods of decomposition

Sulfide	Higher sulfide	Sulfiding temperature	Decomposition temperature	Comments	References
FeS	$FeS_{1,2}$	823 (reduced pressure) 873 (normal pressure)	1023 (reduced pressure)	H2 evolution was only 30% of the theoretical value. FeS is not recovered to original form	[59-62]
Ni_3S_2	NiS	823 (reduced pressure)	1023 (reduced pressure)	H_2 evolution worsens cycle by cycle.	[59-62]
Ni_3S_2, MoS_2	NiS	673-773	1073 (reduced pressure0	Excellent results cycle by cycle. Double sulfide of Ni and Mo not observed	[59-62]
Pb (Molten)	PbS	873	750-800	H_2S either soft blown over molten lead or bubbled into it. Ni for bubbling method and Cu for the soft blowing methods were found to be catalytic. Regeneration was carried out at low oxygen pressure.	[59,60]

Other reactions are carried out by replacing metal with CO or I_2. But there are uncontrollable side reactions that render this method unattractive. The reaction with I_2 has a problem with the isolation of pure sulfur. There is still a wide gap that needs to be bridged before these methods become commercially viable.

Electrochemical Methods of Decomposition:
The methods of electrolysis of water can be adapted to the electrolysis of H_2S. The passivation of the electrodes by sulfur, however, poses a problem not encountered in water electrolysis. There are three methods of electrolysis:

1. Direct electrolysis
2. Indirect electrolysis
3. High temperature electrolysis

There are various problems associated with the electrochemical method. The electrolysis of hydrogen sulfide presents difficulties because of its low solubility and low electrical conductance as a liquid. Due to these reasons this method of H_2S decomposition is not yet a preferred method of decomposition.

Photochemical Methods of Decomposition:
The photochemical decomposition method utilizes photocatalysts such as powdered semiconductor particles, semiconductor electrodes, colored redox species such as dyes and metal complexes, or colored redox species adsorbed on semiconductor electrodes.

Again, photochemical methods are in the development stage, but they have a long way to go before they will be commercially viable.

Plasma Methods of Decomposition:

Chemical processes can be operated at temperatures up to 20,000 K and pressures from 10 to 109 Pa. using low temperature plasma. The high temperature generated by the plasmas allows very high conversions for thermodynamically limited endothermic reactions. The ability to attain high conversions in practice depends on the effectiveness of the quenching system.

To bring the temperature from 20000 K to 700K is a challenge in the plasma method of decomposition.

Evaluation:

- **Feasibility: moderate;**
- **Impact: high.**

Polyethylene and polypropylene production

UAE industrial development shifted naturally to the polymer production. Large gas reserves in the country resulted in the low raw material and transportation costs and therefore competitively low polymer costs. This, combined with high quality provided by Borstar technology, makes polymer production in the UAE potentially very profitable. Borouge – a business venture of ADNOC and Borealis, has the potential to become the world's largest producer of the most common polymers, polyethylene (PE) and polypropylene (PP).

Polyethylene and polypropylene are typically produced with Ziegler–Natta catalyst systems [21–23], but how the Ziegler–Natta system really works is not entirely clear. Better understanding of the behavior would offer significant support to catalyst design and development. Catalyst polymerization and fragmentation behaviors greatly depend on the type of catalyst and the nature of the catalyst support [24]. It is widely believed that the catalyst needs to be highly porous so that the monomer can diffuse into the particle. The mechanical strength of the catalyst structure must be high enough to withstand handling of the catalyst, but at the same time low enough to break up in polymerization. Fragmentation of catalyst particles affords higher polymer yields and ensures absence of big catalyst fragments in the final product. The active sites should also be well distributed over the catalyst particle so that the polymer is evenly formed within the catalyst [24–26].

The growth and the fragmentation of catalyst particles in olefin polymerization have been studied by several research groups, and at least three different models for particle morphology in polymer growth have been presented. In the core–shell model, also known as the layer-by-layer model, the catalyst particle does not break up at the beginning of the polymerization process. The

polymerization reaction occurs on the surface of the particle, which acts as a core, and the polymer grows in the form of a shell around the core. The monomer diffuses through the accumulated polymer to the catalyst surface, where it reacts. According to some investigations [28,29], this kind of polymer growth proceeds in the slurry phase of propylene polymerization if the porosity of the catalyst is low (monomer diffusion is limited). In the case of a highly porous catalyst the monomer diffusion is less limited; the monomer can penetrate into the pores of the catalyst more easily, and the polymer grows throughout the particle. The result is an immediate fragmentation of the catalyst particle [28,29].

The particle morphology model, known as the multigrain model, is one of the most popular and simple models for the particle growth in olefin polymerization [31]. According to the multigrain model, immediately when the polymerization starts the catalyst particles break up into small fragments (microparticles), and the polymerization reaction occurs on the surface of these microparticles following the core–shell model. The microparticles together form porous macroparticles [30,31].

The third model is the polymeric flow model. According to this model it is also assumed that the catalyst particles break up at the beginning of the polymerization [30]. Polymer and catalyst fragments are considered as one phase, and the polymerization reaction occurs at active sites which are embedded in the polymer and are moving radially outward with the forming polymer [30]. The multigrain and polymeric flow models are the models most commonly used to explain the replication phenomena [27].

This complex polymerization process affects polymer molecular weight, density and mechanical properties. Bostar® polymerization technology allows variation of polymerization conditions at a different stage of the process, and as result, production of the polymers with the desirable properties. The Bostar® process includes at least two reactors working in series. It also may include pre-polymerization reactor (Figure 7) that adds significant flexibility in manipulating the polymer morphology. The feed to the reactor consists of ethylene, comonomer, hydrogen, inerts, and catalyst. A stream of unreacted gases flows from the top of the reactor and is cooled by passing through a heat exchanger in counter-current flow with cooling water. Cooling rates in the heat exchanger are adjusted by instantaneously blending cold and warm water streams while maintaining a constant total cooling water flow rate through the heat exchanger. Change in the feed product temperature usually results in the fluctuation of the reactor temperature that can reach a few C° and may take a few hours to stabilize as shown on Figure 8, even using best control strategies [32].

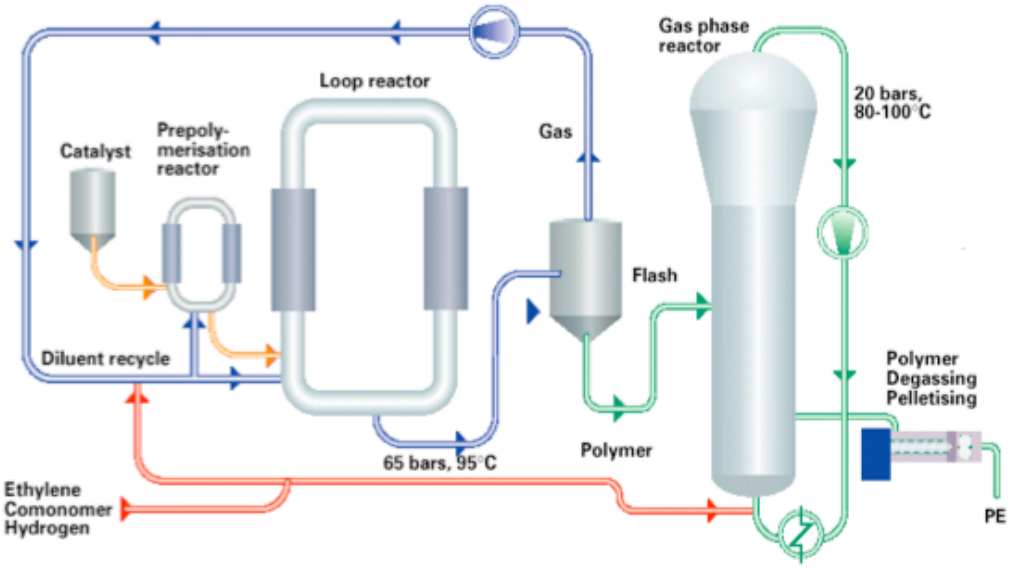

Figure 7. Bostar® process diagram.

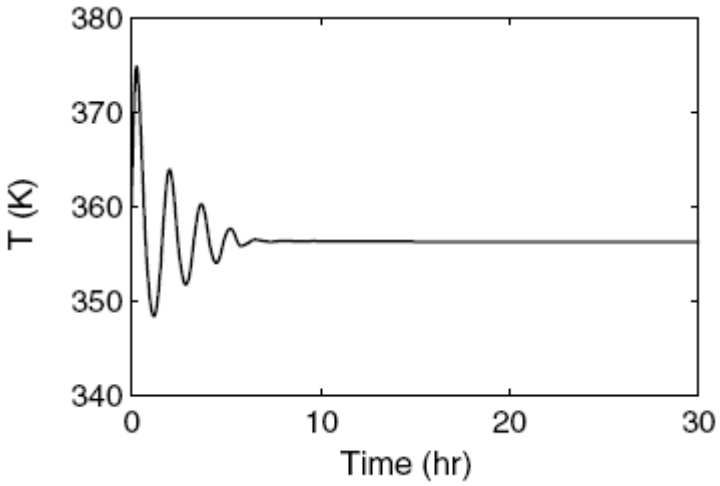

Figure 8. Reactor temperature variations.

The flexibility provided by the multi-reactor arrangement of the Bostar® process is significantly diminished with an increase in the reaction temperature variations, which are generally proportional to the reactor size. Figure 9 demonstrates temperature influence on the polypropylene particle morphology. The increase in the scale of polymer production of Borouge reactors inevitably increases the complexity of temperature control in the reactors and may result in the decrease in polymer quality. Application of microreactors on the other hand, provides the most flexibility of the temperature and composition control and would be extremely beneficial to the polymer quality, particularly if it is used on the initial stage of polymerization or on the pre-polymerization stage. Its effect on polymer production at UAE and their quality could be significant. The application of microreactor technology in polymerization could have a greater economical effect on UAE industry than other evaluated applications and should be explored in this project.

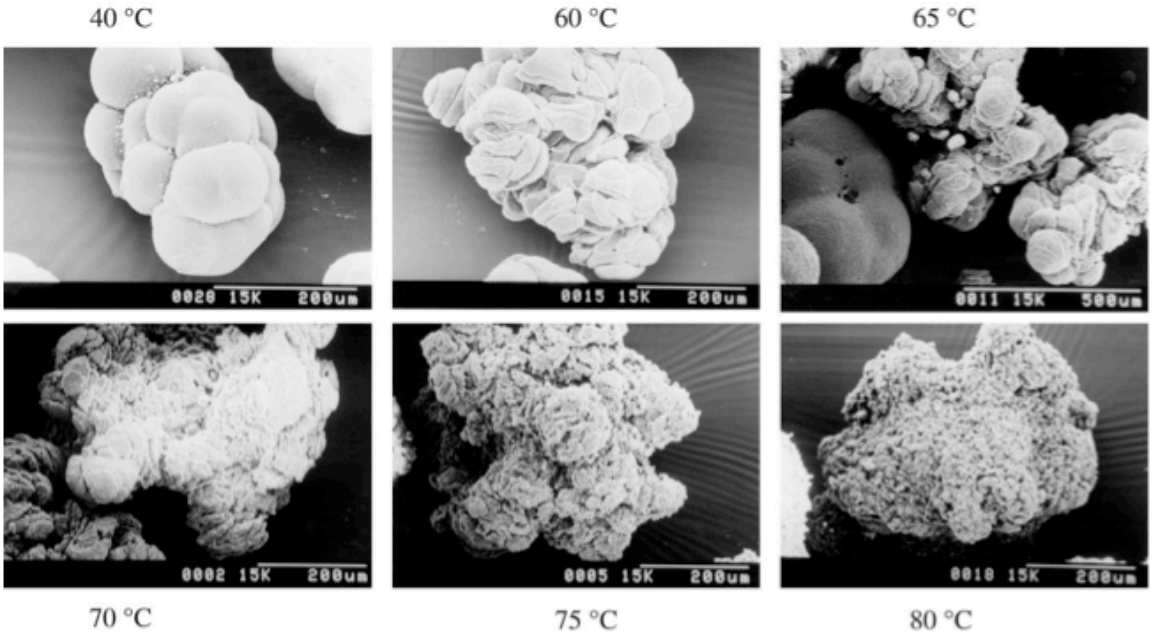

Figure 9. Temperature influence on morphology; Ziegler-Natta polymerization of propylene.

Evaluation:

- **Feasibility: high;**
- **Impact: high.**

4. Difficulties Encountered/Overcome

- Identifying a reaction that is of an interest to ADNOC which also can be experimented with in the lab.

5. Planned Project Activities for the Next Quarter

- Continuing the work on literature survey to examine other's work.
- Further evaluations of potential reaction and reactors fabrication technologies.

Appendix

Justification and Background

Microreactors form a basis for the potential future downscaling of existing chemical processes, allowing tremendous reductions in capital and operating cost. They provide finer control of conditions, allow for faster process times, and improve safety in operation. Also, they should not encounter a significant problem in scaling from laboratory-sized systems to commercial-sized systems, since their operating principle will simply allow them to be stacked together modularly.

Of critical importance to the microreactors' capability to make the jump into industrial applications is the mixing efficiency, which controls the reaction rates and the yield expected from a reactor. Due to the scale of the systems, laminar flow is almost always encountered, which means that the vortices typically associated with turbulent flow are often missing. Instilling vortices into the flows to encourage mixing is accordingly a matter of construction of mixer channels.

Correct design parameters of microreactor influence the process yield. Designing microreactor for appropriate reaction conditions is very important for the reactions to be fast. Microreactors can be energy efficient too by appropriately designing and visualizing heat transfer. The channel dimensions have direct impact on diffusive mixing of reactants.

Approach

- Literature survey of the microreactor technologies as well as microchannel fabrication technologies.
- Selection of the target process for realization in microreactors with maximum benefit.
- Selection of microchannel fabrication technology suitable for microchannel mass production.
- Design and fabrication of a microreactor using microchannel fabricating technology suitable for mass production.
- Microreactor demonstration.
- Prepare experimental set-up and conduct the experiments.

Two-Year Schedule

Year 1:

- Conduct literature review to study current technologies for micoreactors, micromixers, and incorporation of catalysts into microreaction technology.
- Evaluate existing microchannel formation techniques and their applications to microreactor construction.
- Selection of the target process for realization in microreactors with maximum benefit to ADNOC.
- Selection of microchannel manufacturing process most suitable for mass production.
- Preparation of a microreactor testing facility.
- Visualization study of mixing in microchannels.

Year 2:

- Continue selection of the target process for realization in microreactors with maximum benefit to ADNOC.
- Continue selection of microchannel manufacturing process most suitable for mass production.

- Continue visualization study of mixing in microchannels.
- Continue preparation of a microreactor testing facility.
- Design and fabricate microreactors using microchannel fabricating technology selected.

References

[1] Development of a Microchannel In Situ Propellant Production System- September 2005 Prepared for the National Aeronautics and Space Administration Lyndon B. Johnson pace Center by KP Brooks, SD Rassat and WE TeGrotenhuis

[2] Catalytic synthesis of hydrogen peroxide in microreactors, Chemical Engineering Research and Design, volume 86, Issue 4, April 2008, Pages 410-415. S. Maehara, M. Taneda, K. Kusakabe

[3] Kinetics of hydrogen peroxide synthesis by direct combination of H2 and O2 in a microreactor, Catalysis Today, Volume 125, Issues 1-2, 15 July 2007, Pages 40-47 Yury Voloshin, Raghunath Halder, Adeniyi Lawal

[4] Auto-oxidation production of hydrogen peroxide via oxidation in a microreactor United States Patent 7416718, Sethi, Dalbir S. (Cranbury, NJ, US), Dada, Emmanuel A. (Bensalem, PA, US), Hammack, Kevin (League City, TX, US), Zhou, Xinliang (Sugar Land, TX, US)

[5] Experimental studies on hydrogenation of anthraquinone derivative in a microreactor Catalysis Today, Volume 125, Issues 1-2, 15 July 2007, Pages 48-55 Raghunath Halder, Adeniyi Lawal

[6] Chinese Journal of Chemical Engineering, 16(4) 503-516 (2008), “A State-of-the-Art Review of Mixing in Microfluidic Mixers” , Elmabruk A. Mansur, YE Mingxing , WANG Yundong and DAI Youyuan, The State Key Laboratory of Chemical Engineering, Department of Chemical Engineering, Tsinghua University,Beijing 100084, China.

[7] Morini, G.L., “Viscous heating in liquid flows in micro-channels”, Int. J. Heat Mass Transfer, 48, 3637-3647 (2005).

[8] Judy, J., Maynes, D., Webb, B.W., “Characterization of frictional pressure drop for liquid flows through microchannels”, Int. J. Heat Mass Transfer, 45, 3477-3489 (2002).

[9] Glasgow, I., Batton, J., Aubry, N., “Electroosmotic mixing in microchannels”,Lab Chip, 4, 558-562 (2004).

[10] Engler, M., Kockmann, N., Kiefer, T., Woias, P., “Numerical and experimental investigations on liquid mixing in static micromixers”,Chem. Eng. J., 101, 315-322 (2004).

[11] Yu, H.Y., Xiao, S.S., Chen, H., Fan, S.F., “Influence of flow velocity profile on mixing in micromixer”, Nanotechnology and Precision Engineering (China), 3 (4), 290-294 (2005). (in Chinese).

[12] Bothe, D., Stemichb, C., Warnecke, H., “Fluid mixing in a T-shaped micro-mixer”, Chem. Eng. Sci., 61, 2950-2958 (2006).

[13] Zhao, Y.C, Ying, Y., Chen, G.W., Yuan, Q., “Characterization of micro-mixing in T-shaped micro-mixer”, J. Chem. Ind. Eng. (China),57, 1884-1890 (2006). (in Chinese).

[14] Goullet, A., Glasgow, I., Aubry, N., “Effects of microchannel geometry on pulsed flow mixing”, Mech. Res. Commun., 33, 39-746 (2006).

[15] Johnson, T., Ross, D., Locascio, L., “Rapid microfluidic mixing”,Anal. Chem., 74, 45-51 (2002).

[16] Seok Woo Lee, Dong Sung Kim2, Seung S. Lee, and Tai Hun Kwon, “SPLIT AND RECOMBINATION MICROMIXER BASED ON PDMS THREE-DIMENSIONAL MICRO STRUCTURE”, Korea Advanced Institute of Science and Technology, Pohang University of Science and Technology.

[17] The Engineering ToolBox, “Thermal Conductivity of some common Materials”, Online Resources, Tools and Basic Information for Engineering and Design of Technical Applications, Available at: http://www.engineeringtoolbox.com/thermal-conductivity-d_429.html Lass accessed on July 17, 2009

[18] DuPont Teflon fluoropolymer manufacturer, Fluoropolymer Typical Properties, available online at: http://www2.dupont.com/Teflon_Industrial/en_US/tech_info/techinfo_compare.html last accessed on July 17, 2009

[19] Rodgers P, 2009, “MEEG376 Core measurements Uncertainty analysis”, The Petroleum Institute, spring 2009

[20] A.Y. Tonkovich, S. Perry, D. Qiu, T. LaPlante, W.A. Rogers, Microchannel process technology for compact methane steam reforming. Velocys, Inc., Technology Development, 7950 Corporate Drive, Plain City, OH 43064, USA. Y.Wang (Battelle, Pacific Northwest National Laboratory, Richland, WA 99352, USA)

[21] “The discovery and progress of MgCl2-supported TiCl4 catalysts”. N. Kashiwa, J. Polym. Sci. A: Polym. Chem. 42 (1–8) (2004) 1.

[22] J.J.A. Dusseault, C.C. Hsu, J. Macromol. Sci. Rev. Macromol. Chem. Phys. C 33 (2) (1993) 103.

[23] S. Kojoh, T. Fujita, N. Kashiwa, Recent Res. Dev. Polym. Sci. 5 (2001) 43.

[24] J.T.M. Pater, G. Weickert, J. Loos, W.P.M. van Swaaij, Chem. Eng. Sci. 56 (2001) 4107.

[25] J.T.M. Pater, G.Weickert,W.P.M. van Swaaij, J. Appl. Polym. Sci. 87 (2003) 1421.

[26] G.Weickert, G.B. Meier, J.T.M. Pater, K.R.Westerterp, Chem. Eng. Sci. 54 (1999) 3291.

[27] L. Noristi, E. Marchetti, G. Baruzzi, P. Sgarzi, J. Polym. Sci. A: Polym. Chem. 32 (1994) 3047.

[28] X. Zheng, J. Loos, Morphology evolution in the early stages of olefin polymerization, Macromol. Symp., 236, 249-258, (2006).

[29] X. Zheng, M.S. Pimplapure, G. Weickert, J. Loos, Influence of porosity on the fragmentation of Ziegler-Natta catalysts in the early stages of propylene polymerization, e-Polym., 028, 1-10, (2006).

[30] M. Bartke, in: J.R. Severn, J.C. Chadwick (Eds.), Tailor-Made Polymers. Via Immobilization of Alpha-Olefin Polymerization Catalyst, Wiley–VCH Verlag GmbH & Co. KGaA,Weinheim, 2008.

[31] G. Cecchin, E. Marchetti, G. Baruzzi, Macromol. Chem. Phys. 202 (2001) 1987.

[32] Adiwinata G., Prashant M., Panagiotis D. C., Fault-tolerant control of a polyethylene reactor, Journal of Process Control 17 (2007) 439–451

Thrust 3
Energy System Management

Integration of Engineering and Business Decisions for Robust Optimization of Petrochemical Systems

UMD Investigators: Shapour Azarm, P.K. Kannan
PI Investigators: Ali Almansoori, Saleh Al Hashimi
UMD GRA: Weiwei Hu
PI GRA: Naveen Al Qasas
Start Date: Oct 2006

1. Objective/Abstract

The overall objective of this project is to develop a framework for integrating engineering and business decisions. Towards that objective, a robust decision support system is being developed that can be used for multi-objective and multi-disciplinary optimization under uncertainty of oil, gas and petrochemical systems. In this quarter, we continued refining the case study model and developing efficient robust optimization techniques for integrating business and engineering decisions. Since our last quarterly report, we have obtained some preliminary results in optimizing business and engineering decisions using an Approximation Assisted Multi-Objective Robust Optimization (AA-MORO) approach. In the last research quarter, we proposed to extend AA-MORO to a multi-objective multi-disciplinary system. The proposed approach is based on a Multi-objective collaborative Robust Optimization (McRO) and it is called Approximation Assisted McRO (AA-McRO). AA-McRO can be used to optimize the integrated business and engineering decisions in a decomposed fashion. The proposed AA-McRO allows, for example, the petrochemical decision makers in each subsystem to optimize their decision variables and a system level optimizer to coordinate between subsystem optimal decisions. A significant advantage of the proposed AA-McRO approach is that it requires considerably less function calls than a previous McRO approach. Finally, our work on dashboard development is continuing, and we will show in this report some results on the role of dashboard in coordinating the decisions from different disciplines, e.g., in a chemical process plant, in fulfilling an integrated business-engineering decision approach using the proposed AA-MORO approach.

2. Deliverables for the Completed Quarter

- Continued the research on the integration of business and engineering decisions based on an oil refinery case study:
  - Developed the business and engineering analysis models in the integrated framework.
  - Obtained optimized decisions under uncertainty for the integrated framework using a multi-objective robust optimization approach.
  - Planned to use a multi-objective multi-disciplinary optimization approach to solve the robust optimization problem in the integrated framework.

- Proposed an Approximation Assisted Multi-objective collaborative Robust Optimization (AA-McRO) approach for the integration framework:
  - A literature review on approximation assisted optimization approaches, particularly in the area of multi-disciplinary applications, has been completed.
  - Preliminary problem formulation and framework of the AA-McRO approach has been established.

- A numerical test problem with two fully coupled subsystems was developed to test the proposed AA-McRO, and some preliminary results have been obtained.

- Continued our research on the dashboard development for the integration framework:
  - The dashboard's main user interface has been successfully connected with the simulation programs in NetLogo and Matlab for petrochemical process applications.
  - Decisions made on the basis of the dashboard are to be implemented directly into the business and engineering simulation models

- Progress on recent joint publications:
  - Hu, W., M. Li, S. Azarm, A. Almansoori, "On Improving Multi-Objective Robust Optimization Under Interval Uncertainty Using Worst Possible Point Constraint Cuts," *Journal of Mechanical Design* (to be submitted).
  - W. Hu, A. Almansoori, S. Al Hashimi, P.K. Kannan and S. Azarm, Kamaha, P., "Corporate Dashboards for Multi-Unit Firms: An Agent-Based Approach for Supply Chain Optimization" (to be submitted).
  - An extended abstract based on AA-McRO was submitted to AIAA/ISSMO 2010 in Feb 2010 (submitted and under review)

3. Summary of Project Activities for the Completed Quarter

- Teleconference meetings (via MSN's Windows Live Messenger) were held between UMD and PI project collaborators on March 02 and April 06. A summary of the highlights from these meetings is given below:

  - During the meeting on March 02, the UMD research team reported its latest work on the joint publications, including an extended abstract that was submitted to the AIAA MAO/ATIO 2010 conference. The other two journal papers were under final review and prepared for submission.
  - During the meeting on April 06, the UMD research team gave a presentation on their research progress on the approximation assisted optimization approaches. The progress on the joint publications was updated. The schedule of Weiwei Hu's Ph.D. proposal defense was determined, with Prof. Almansoori to serve on the committee through a video conference on April 28.

- Business and Engineering Analysis Models for a Chemical Separation Process

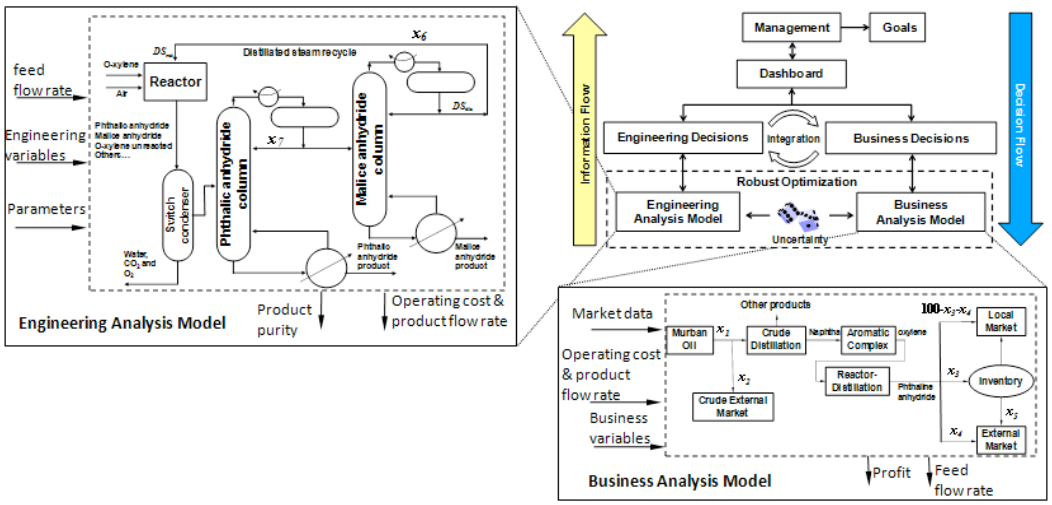

Figure 1. Engineering and business analysis models in the case study.

The business and engineering analysis models in the integrated decision framework are shown in Figure 1. In the business analysis model, the crude oil is separated into the fractions such as kerosene, gas oil, naphtha, and residue in the CDU. Naphtha is fed to the aromatic complex and converted into oxylene. Following the aromatic complex, the reactor distillation process produces phthalic anhydride from oxylene. In the engineering analysis model, two distillation subsystems are used to separate phthalic anhydride and maleic anhydride from un-reacted oxylene after catalytic reaction in the reactor subsystem. It should be noted that the oil refining process contains a large number of engineering processes. However, in this case study, the engineering process is only focused on one such process for expositional purposes. However, the integration framework and the DSS proposed in this case study can be easily extended to consider more processes.

- Integrated Decision Support Framework-Based Robust Optimization

The analysis models for business and engineering domain are connected through an interface as shown in Figure 2. The business analysis model is simulated using the agent-based simulation software NetLogo. Based on the multi-agent modeling environment, the business analysis model characterizes the crude oil and end-product markets by simulating the customer purchasing activities. According to the interactions between the markets and the oil refinery, the profit from end-product sales can be obtained as output from the business analysis model. On the other hand, the engineering analysis model is focused on the reactor-distillation process for producing phthalic anhydride from naphtha, which is simulated in a Matlab environment. The purity of phthalic anhydride is calculated through a series of Matlab functions according to the operational variables and parameters such as the feed flow rate of naphtha, pressure and temperature in the distillation tower, and so on. The objective of the robust optimization is to obtain the optimal business and engineering decisions to maximize profit and maximize purity based on the integrated business and engineering analysis model.

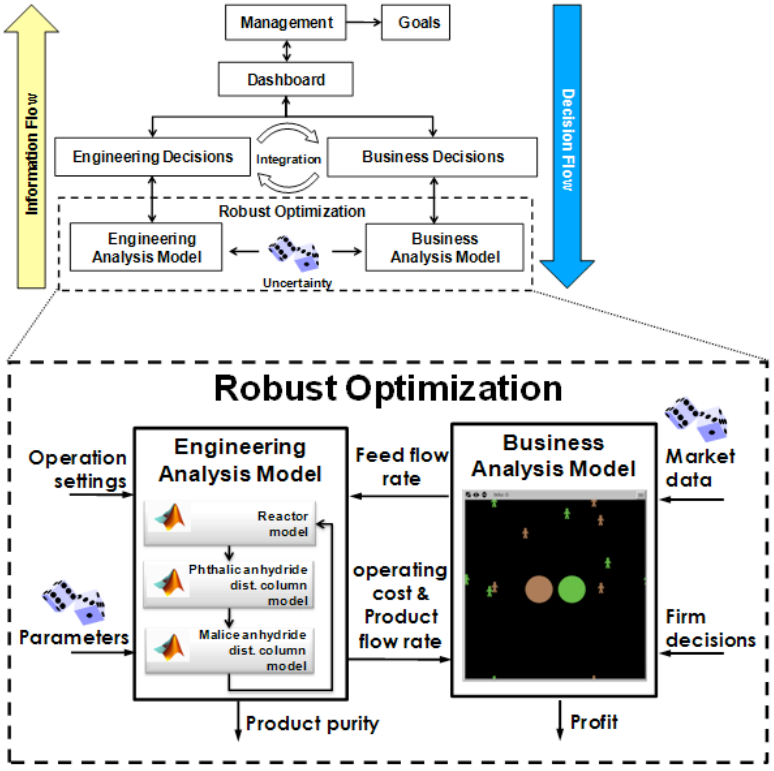

Figure 2. Robust optimization in engineering-business models.

- Robust Decisions Using Approximation Assisted McRO (AA-McRO)

  We propose AA-McRO for the robust optimization in the integrated decision framework. The problem definition is a general multi-objective, multi-disciplinary system, which can represent, for example, a multi-disciplinary chemical process plant, as shown in Figure 3 where the dashed rectangle contains the system problem. Without the loss of generality, we assume the system contains three subsystems. However, this framework can be extended to account for more than three subsystems. The objective is to minimize the system level objectives $\mathbf{f}_{sys}$ subject to system constraints $\mathbf{g}_{sys}$ (a bold symbol, such as $\mathbf{f}_{sys}$, represents a row vector). In Figure 3, the system input includes, among others, the shared variables $\mathbf{x}_{sh}$ and parameters $\mathbf{p}_{sh}$. The shared variables and parameters are input to all subsystems within the system domain. For each subsystem, however, the input also includes some local design variables and parameters. For example, $\mathbf{x}_1$ and $\mathbf{p}_1$ are input only to subsystem 1. The three subsystems in Figure 3 are fully interconnected through the coupling variables $\mathbf{y}$. The subscript of y indicates the start and end of the corresponding coupling variables. For example, $\mathbf{y}_{12}$ implies the coupling variables are output from subsystem 1 and input to subsystem 2.

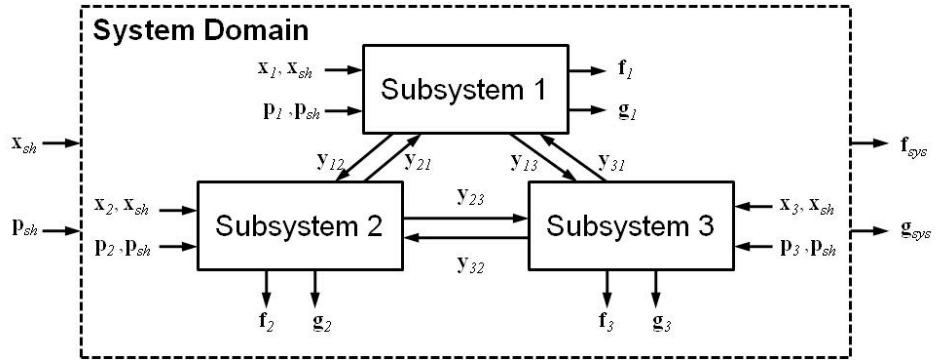

Figure 3. A multi-objective system with three coupled subsystems.

The proposed AA-McRO approach is based on a McRO framework with the added metamodel blocks as shown in Figure 4.

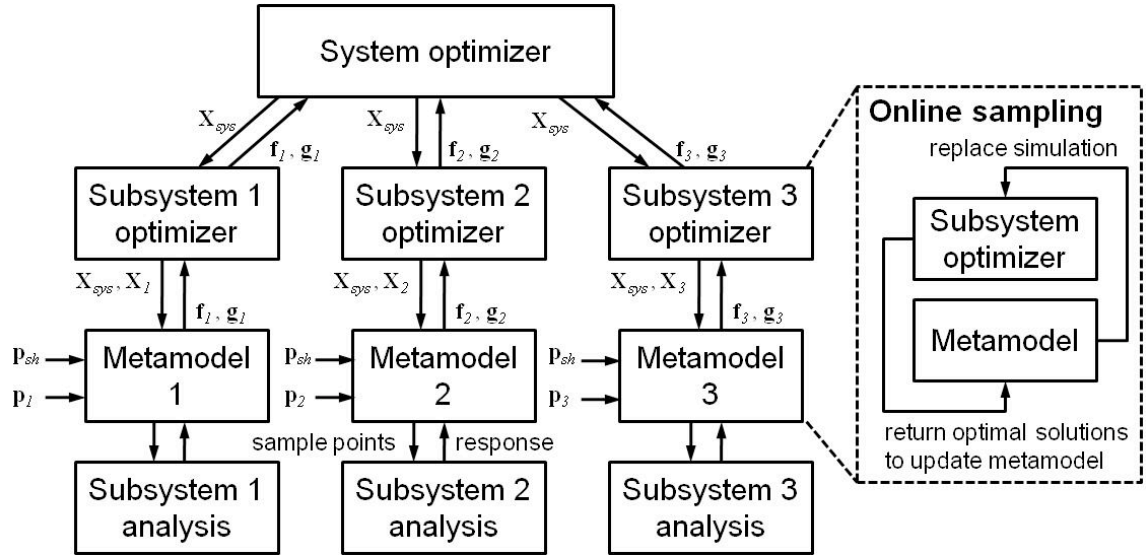

Figure 4. Approximation-assisted multi-objective collaborative robust optimization framework.

To reduce the computational costs, we propose to replace the computationally expensive subsystem analysis with a metamodel. As shown in Figure 4, a subsystem optimizer does not communicate directly with its subsystem analysis model. Instead, it is connected with a metamodel (or a compact model) built specially for that subsystem. In identifying robust optimal solutions, the proposed AA-McRO incorporates a robustness evaluation scheme as a part of the system level optimization. If a system level design solution satisfies all subsystems' "consistency conditions," a robustness evaluation scheme is then invoked to check whether the current design is robust (i.e., relatively insensitive to uncertainty). The robustness evaluation is essentially based on a worst case analysis. For instance, we have devised a systematic approach that can be used to determine whether for the worst amount of uncertainty the constraints are violated.

At the moment, and as an initial feasibility study, we have implemented and verified the proposed AA-McRO approach using a simple numerical example. The optimal solutions obtained from AA-McRO are compared with those from an existing McRO approach and

shown in Figure 5. Due to the interval uncertainty considered, solutions by AA-McRO and the McRO only covers a portion of the deterministic optimal solutions. The computational effort in terms of the number of function calls by the McRO and AA-McRO approaches are also shown in Figure 5. The number of function calls (the number below each bar in Figure 5 shows the number of function calls) by AA-McRO is comparable to the deterministic approach, while the McRO is almost three orders of magnitude higher than the proposed AA-McRO.

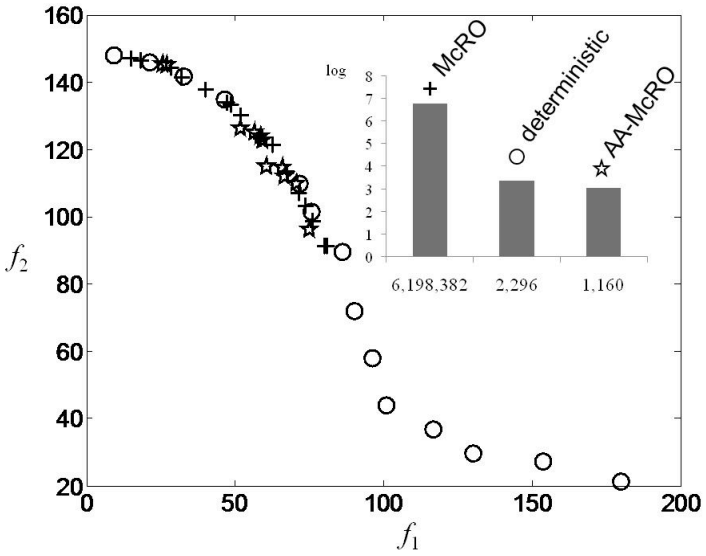

Figure 5. Optimal solutions for the numerical example.

- Integration of Dashboard with Simulation

The dashboard in the proposed integration framework is a computer interface that facilitates efficient decision-making in the enterprise. The screenshots of a preliminary dashboard based on the integrated business and engineering decisions are shown in Figure 6. The dashboard shown is developed using the Graphical User Interface capability in Matlab. Since operation and control of the dashboard is an iterative and dynamic process, we use a simple case study scenario to demonstrate the working of the dashboard.

Initially, the decision variables are determined according to previously determined settings, as shown in the "Control Panel" of Figure 6 (a). Next, these decision variables are sent to the corresponding department in the refinery for determination. Three sliders are designed at the bottom of the dashboard for decision makers to obtain the expected and current plant performance and make real-time decisions accordingly. When the "Real Data" button is pressed, the current performance data are obtained and shown under the "Firm Performance" panel on the dashboard. The decision maker can then press the "Simulation" button to start the business and engineering analysis models, which are developed beforehand to represent the actual business and engineering systems in the refinery, as an example, based on the current setting of decision variables. The simulated performance values from the analysis models are returned and shown in the "Simulation Result" panel. At this time, the real-time firm performance data can be compared against the simulated performance. If the simulation results resemble the actual firm performance, such as the case example shown in Figure 6 (a), or the decision-maker tends to trust the analysis model, the decision-maker can then press the "Optimization" button. As a result, the "all-at-once" robust optimization is run in the background. Based on the business and engineering analysis models, the optimization problem is solved until

the business and engineering analysis models are converged. Since the business and engineering analysis models are connected though the coupled variables in the optimization problem, as the optimization searches for the optimal decisions, it automatically ensures the optimal solutions are consistent between businesses and engineering domains. In reality, this is essentially how decisions from different departments are coordinated through dashboards. The optimal decisions are obtained and shown in the "Recommended Decisions" panel on the dashboard. The reason that these optimal decisions can only denoted as recommended decisions is that the agent-based business analysis model in Netlogo may be different from the reality due to market fluctuation and uncertainty.

In general, the decision-maker should follow the "Recommended Decisions" and change the values of decision variables under the "Control Panel," as shown in Figure 6 (b). Although not shown in these figures, the real-time and simulated performance may be significantly different. In that case, the decision-maker should make adjustments considering both the recommended decisions and the actual firm's performances. In Figure 6 (b) the plant performance and simulation result after implementing the recommended decisions are shown where the simulated and actual performance are very close. In this case, the decision-maker is not required to make any adjustment unless some disagreements between the firm and simulated performances are observed.

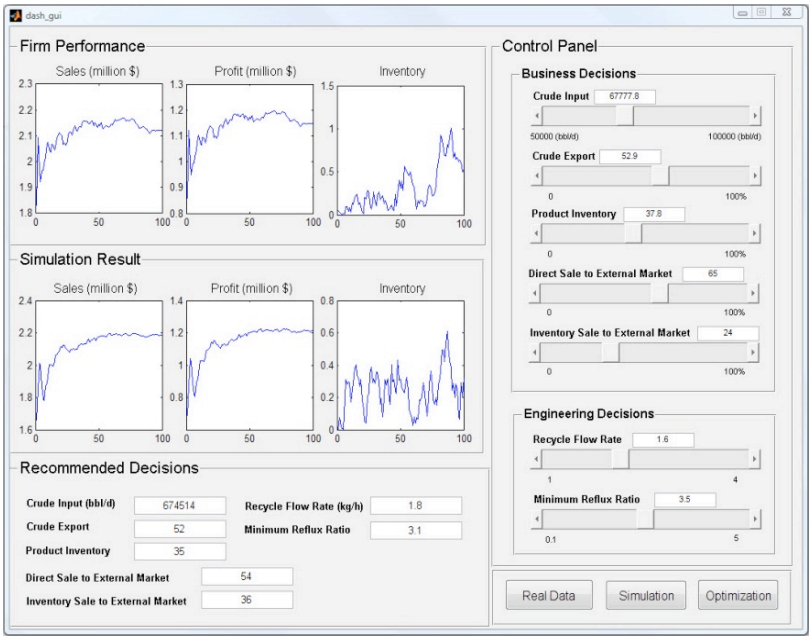

(a)

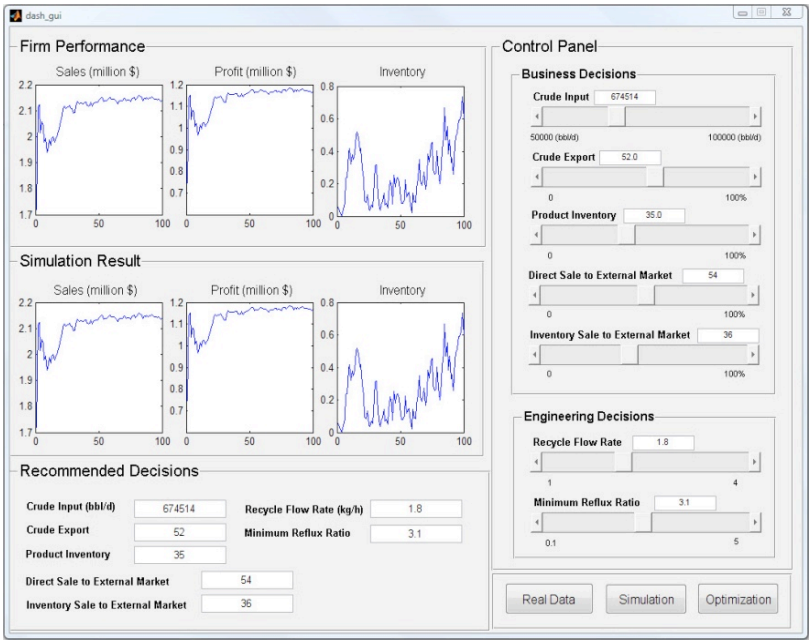

(b)

Figure 6. Preliminary dashboard for the proposed integration framework: (a) before recommended decisions are implemented; (b) after recommended decisions are implemented.

4. Difficulties Encountered/Overcome

The proposed AA-McRO approach has been implemented with a fully coupled multi-disciplinary numerical, though a simple example as shown in this report. However, more test problems are required to test the proposed AA-McRO approach. We plan to develop and test several more test problems with different levels of difficulty using AA-McRO in the next research quarter. On the other hand, the integrated business and engineering decision case study for a chemical process was solved using the proposed AA-MORO approach in an "all-at-once" fashion. We are planning to reformulate the problem as a McRO problem and solve it using the proposed AA-McRO approach. In the McRO formulation of the integrated decision problem, both the business and engineering domains are allowed to have multiple objectives.

Another challenge in applying the AA-McRO approach is that it introduces another source of uncertainty through approximation to the optimization problem. This uncertainty could propagate through the coupling variables and make convergence of the optimization problem more difficult to achieve. We are planning to explore these and other challenges in upcoming quarters.

5. Planned Project Activities for the Next Quarter

- Include an online validation procedure in the proposed AA-MORO and AA-McRO approach to improve the approximation process.
- Test additional examples using the proposed AA-MORO and AA-McRO.
- Reformulate the integrated business and engineering decision framework as a multi-objective multi-disciplinary optimization problem.

- Use the proposed AA-McRO approach to solve the integrated chemical process decision problem and compare its optimal solutions with the ones obtained from AA-MORO.
- Continue improving the functionality and usability of the integrated engineering-business process by way of dashboard.

Appendix

Justification and Background

Many oil, gas and petrochemical systems involve numerous coupled subsystems. These systems and their subsystems usually have uncertain inputs and thus it can be difficult to make the "best" engineering and business decisions in terms of independent operations of these complex systems. It becomes even more difficult to make those decisions when the system consists of many units or plants producing different products. This difficulty presents an opportunity taken on in this project; a review of mainstream literature has revealed that previous models in management of petrochemical systems have been in majority based on either engineering or business decisions but not both. There is a significant gap in the literature as to how these two types of decisions should be devised and integrated. To address this important gap, the focus of this investigation is to develop an integrated robust decision support framework considering both engineering and business models under uncertain conditions. Our overall objective has several underlying research issues or objectives, including: (i) how to develop business models that include management decisions in a multi-unit organization and at the same time account for engineering aspects; (ii) how to determine the relative importance and effects of uncertain system and/or subsystem input parameters on subsystem and/or system outputs (e.g., system performance); (iii) defining a set of metrics, a dashboard, that will serve as a visualization tool to keep track of the company's financial status and provide for easy communication between various levels in the company, and (iii) how to extend our current single-level robust optimization method to multi-subsystem problems and maintain reasonable computational complexity for the method. These underlying objectives will be organized into tasks throughout the time frame allocated to the project. The details of the tasks are explained in the next section.

Approach

There are two main tasks in this investigation as detailed in the following.

Task 1 (PI):
Develop and implement engineering analysis models, in a Matlab (or Matlab compatible) environment, for a crude distillation unit case study model.

- Task 1.1: Develop a multi-input multi-output analysis model for a representative petrochemical system with corresponding subsystem analysis models.
- Task 1.2: Extend the analysis model in Task 1.1 to include: (i) additional complexity, (ii) subsystem details and uncertainty to include reasonable representation of engineering side of a plant. The ultimate goal is to develop an integrated multi-subsystem petrochemical analysis model for a plant or a group of units in a plant.

Task 2 (UMD):
Develop and implement a Robust Decision Support System (RDSS).

Engineering Tasks

- Task 2.1: Develop a single level (all-at-once) approximation-assisted robust optimization technique that is able to significantly reduce the computational efforts of making robust decisions.
- Task 2.2: Demonstrate an application of the approach from Task 2.1 with a case study in petrochemical systems, which will be developed by PI as a part of Task 1.
- Task 2.3: Develop an approximation assisted multi-objective multi-disciplinary robust optimization approach, which is an extension to Task 2.1.
- Task 2.4: Demonstrate an application of the approach from Task 2.3 with a case study in petrochemical systems which will be developed by PI as part of Task 1.

Business Tasks

- Task 2.5: Develop business models in Netlogo and solve a simplified refinery supply chain optimization problem with Matlab.
- Task 2.6: Develop a Dashboard and test the robustness and sensitivity of the Dashboard's elements for the model in Task 2.5.

Integration Tasks

- Task 2.7: Inspect engineering and business problems to determine coupling variables between two problems.
- Task 2.8: Integrate Tasks 2.1 to 2.4 with Tasks 2.5 to 2.6 to formulate a refinery optimization problem that considers both engineering and business objectives and constraints.
- Task 2.9: make the supply chain management problem more realistic by considering more decision levels, more finished products and a wider market, and by increasing the size of the refinery's internal network and then repeat Task 2.8.
- Task 2.10: Verify and validate the integrated model.

References

[1] Douglas, J.M., 1988, "Conceptual Design of Chemical Processes", McGraw-Hill, New York, USA.

[2] Forbes, R.J., 1948, "Short History of the Art of Distillation", Brill, Leiden, Holland.

[3] Gargeya, V., 2005, "Plant Level Performance Measurement: An Exploratory Case Study of a Pharmaceutical Encapsulation Company", Technovation, 25(12), 1457-1467.

[4] Gattu, G., Palavajjhala, S., and Robertson, D. 2003, "Are Oil Refineries Ready for Non-Linear Control and Optimization?" International Symposium on Process Systems Engineering and Control, Mumbai, India.

[5] Grossmann, I. E., 2005, "Enterprise-Wide Optimization: A New Frontier in Process Systems Engineering," AIChE Journal, 51(7), p. 1846-1857.

[6] Halemane K. P., Grossmann I. E., 1983, "Optimal Process Design under Uncertainty," AIChE Journal, 29(3), 425-433.

[7] Jackson, J., Hofmann, J., Wassick, J. and Grossmann, I., 2003, "A nonlinear multi-period process optimization model for production planning in multi-plant facilities", Proceedings FOCAPO2003, 281-284..

[8] Janak, L., Lin, X. and Floudas, C. A., 2007, "A New Robust Optimization Approach for Scheduling Under Uncertainty: II. Uncertainty with Known Probability Distribution," Computers and Chemical Engineering, 31(3), 171-195.

[9] Kaplan, R. and Norton, D., 1996, "Using the Balanced Scorecard As a Strategic Management System", Harvard Business Review, 74(1), 75-85.

[10] Kleijnen, J. and Smits, M., 2003, "Performance metrics in supply chain management". Journal of the Operational Research Society, 54(5), 507–514.

[11] Kroo, I., and Manning, V., 2000, "Collaborative Optimization: Status and Directions," Proceedings of the 8th AIAA/NASA/ISSMO Symposium on Multidisciplinary Analysis and Optimization, Long Beach, CA, pp. AIAA 2000-4721.

[12] Lin, X., Janak, S. L. and Floudas, C. A., 2004, "A New Robust Optimization Approach for Scheduling Under Uncertainty: I. Bounded Uncertainty," Computers and Chemical Engineering, 28(6-7), 1069-1085.

[13] Li, M., Azarm, S., and Boyars, A., 2006, "A New Deterministic Approach Using Sensitivity Region Measures for Multi-Objective Robust and Feasibility Robust Design Optimization," Journal of Mechanical Design, 128(4), pp. 874-883.

[14] Li, M., and Azarm, S., 2008, "Multiobjective Collaborative Robust Optimization with Interval Uncertainty and Interdisciplinary Uncertainty Propagation," Journal of Mechanical Design,

130(8), pp. 081402-11.
[15] Micheletto, S. R., Carvalho, M. C. A. and Pinto, J. M., 2008, “Operational Optimization of the Utility System of an Oil Refinery,” Computers and Chemical Engineering, 32(1-2), 170-185.
[16] Netlogo, http://ccl.northwestern.edu/netlogo/
[17] Pinto, J., Joly, M. and Moro, L., 2000, “Planning and scheduling models for refinery operations”, Computers and Chemical Engineering, 24(9), 2259–2276.
[18] Sahdev, M., Jain, K., Srivastava, P., “Petroleum Refinery Planning and optimization Using Linear Programming”, The Chemical Engineers' Resource Page, http://www.cheresources.com/refinery_planning_optimization.shtml
[19] Simpson, T. W., and Mistree, F., 2001, "Kriging Models for Global Approximation in Simulation-Based Multidisciplinary Design Optimization," AIAA Journal, 39(12), pp. 2233-2241.
[20] Suresh, S. Pitty, Li, W., Adhitya, A., Srinivasan, R., Karimi, A., 2008, “Decision support for integrated refinery supply chains”, Computer and Chemical Engineering, 32, 2767–2786.
[21] Hu, W., M. Li, S. Azarm, S. Al Hashimi, A. Almansoori, and N. Al Qasas, “On Improving Multi-Objective Robust Optimization Under Interval Uncertainty Using Worst Possible Point Constraint Cuts,” *CD-ROM Proceedings of the ASME 2009 International Design Engineering Technical Conferences*, Aug. 30 – Sep. 2, 2009, San Diego, CA, USA.

Dynamics and Control of Drill Strings

UMD Investigator: Balakumar Balachandran
PI Investigators: Hamad Karki and Youssef Abdelmagid
GRA: Chien-Min Liao (started in Spring 2007)
Start Date: Oct 2006

1. Objective/Abstract

Drill-string dynamics need to be better understood to understand drill-string failures, control drill-string motions, and steer them to their appropriate locations in oil wells. Although a considerable amount of work has been carried out on understanding drill-string vibrations (for example, Leine and van Campen, 2002; Melakhessou *et al*., 2003; Spanos *et al*., 2003), the nonlinear dynamics of this system are only partially understood given that the drill strings can undergo axial, torsional, and lateral vibrations, and operational difficulties include sticking, buckling, and fatiguing of strings. In addition, the prior models focus on either bending or torsional or axial motions. Hence, it is important to consider coupled axial-bending-torsional vibrations and contact instability in oil and gas well drilling.

The overall goal of the proposed research is to understand the nonlinear dynamics of the drill string and develop a control-theoretic framework for its stabilization, enabling energy efficient drilling with longer life spans for the equipment. Specific research objectives of this project are the following: i) building on Phase I efforts, to develop and study control-oriented models for the drill strings through analytical and numerical methods, ii) investigate the control of an under-actuated nonlinear system (drill string) with complex interactions with the environment, and iii) use the drill-string test-beds constructed at the Petroleum Institute (PI) & the University of Maryland (UMD) to validate the analytical findings and suggest possible strategies to mitigate drill-string failures in fixed and floating platform environments.

2. Summary of Results

The rotor trajectory can be used as a window to monitor the system behavior of a drill-string system. As reported previously, the friction coefficient associated with the contact between the rotor and the outer shell plays an important role in determining the nature of the motions of the drill string. An ideal situation would be one in which the drill string motions keep it close to the center of the outer shell or bore well. This is further considered here in this quarter. To investigate how mass imbalance, which is common in curved drill strings, affects the drill string motions, parametric studies are conducted to understand the role of mass imbalance and the associated torsion motions.

This section is broken up into three subsections, with Section 2.1 containing a summary of the experimental investigations conducted in this quarter along with the associated results, Section 2.2 containing numerical results obtained through simulations conducted with the reduced-order model reported previously, and Section 2.3 including comparisons between numerical results and previously published experimental results.

2.1 Experimental Investigations into Torsion Vibrations

With the primary aim of understanding the role of mass imbalance on torsion motions, different experiments were conducted. As noted above, the curvature of a drill string could result in a mass imbalance. Related experimental investigations and results are reported here.

2.1.1 Description of Experiment System

The drill string system is shown in Figure 1. This system is mainly composed of a 88.900 cm (35 inches) long aluminum rod with a diameter of 0.635 cm (quarter inch) and two discs with one attached to the bottom of the rod and another to the top of the rod. The disc at the top end has a diameter of 20.320 cm (8 inches) and 1.270 cm (half inch) thickness, and this disc is fixed to the driving motor and allowed to undergo pure rotational motions. The bottom disc (rotor) has a diameter of 15.240 cm (6 inches) and 1.270 cm (half inch) thickness, and this disc is designed to be free and to enable attachments such as a braking disc. However, in the current experiments, a braking disc is not used. The bottom rotor is enclosed within a cylindrical shell whose diameter is 19.050 cm (7.5 inches); this shell is referred to as the "outer shell" in this report. This shell encloses the rotor and the contact between the shell and the rotor is of interest to this work. From an energy standpoint, the system energy is expected to be conserved before and after contact; however, energy dissipation is expected whenever there is contact between the shell and the rotor.

An unbalanced mass is attached on the top plane of the rotor at a distance of 6.350 cm (2.5 inches) from the center of the disc. A rotating disc with a mass imbalance is expected to result in excitations of the lateral motions of the disc, and these lateral motions are expected to cause bending motions of the drill string and also create possibilities for contact between the rotor and the outer shell. In the current experiments, two different masses are used, with one being 40 grams and another being 70 grams. These will be referred to as "small" and "large" unbalance mass, respectively, in this report. A driving motor is controlled to generate different rotation speeds, and four different speeds are considered. These are 70 rpm (revolutions per second), 300 rpm, 850 rpm, and 1350 rpm. Due to experimental limitations, the actual rotation speeds are found to vary from the set values. In this report, only the data pertaining to the speeds of 70 rpm and 300 rpm are presented.

The experiments have been grouped into three categories, labeled as T1, T2, and T3. The group T1 pertains to experiments with no unbalanced mass, the group T2 corresponds to the experiments with the 40 gram mass or the "small" unbalanced mass, and the group T3 corresponds to the experiments with the 70 gram mass or the "large" unbalanced mass. The label R2 is used for experiments pertaining to a speed of 300 rpm, and the label R5 is used for experiments pertaining to a speed of 70 rpm.

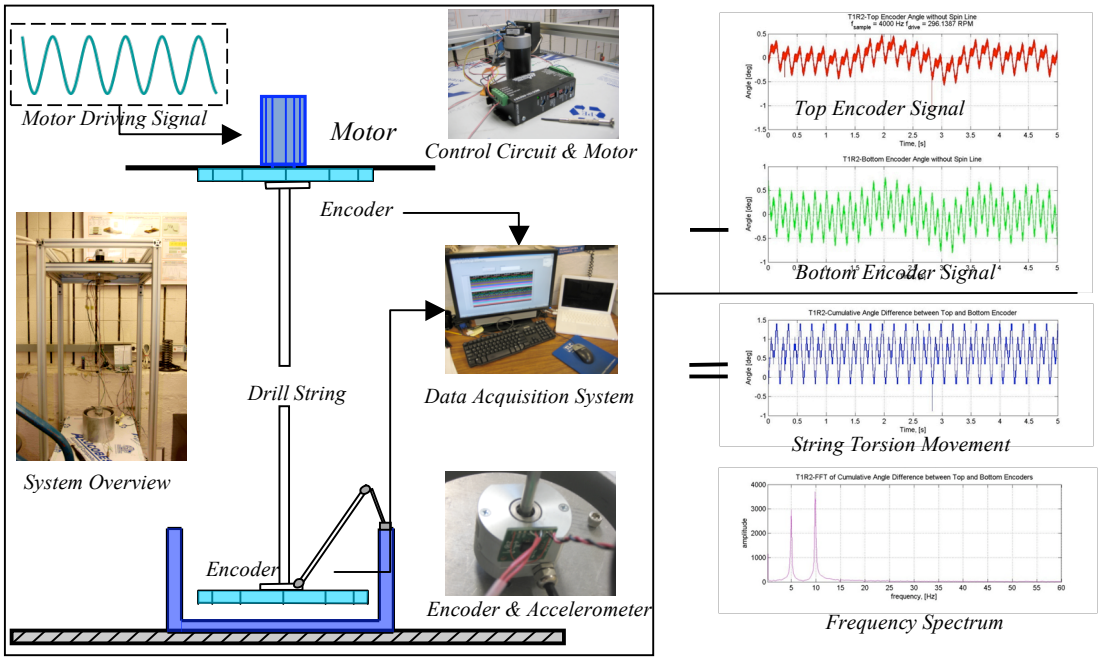

Figure 1. Experimental arrangement and representative measurements.

2.1.3 Experimental Results

In Figures 2 and 3, the results obtained for operation speeds of 70 rpm and 300 rpm are shown, respectively. At this driving speed, the rotor makes contact with the shell. The plots in the left column show the time histories of the angular difference between the angular motions measured at the top and bottom of the drill string by using two absolute encoders, and the plots in the right column show the associated frequency spectra. While the results of Figure 2a correspond to the case with no unbalanced mass, the results of Figures 2b and 2c correspond to the cases with "small" and "large" unbalanced masses, respectively. Two distinct frequencies are noticeable in the response, with one (the low frequency component) corresponding to the lateral motion of the rotor and the other (the high frequency component) corresponding to the torsion motion. As the mass imbalance increases, the amplitude of torsion vibrations also increases. When the system is excited at the higher rotation speed of 300 rpm, the rotor does not make contact with the shell and stays closer to the center of the shell; that is, the lateral motions are not pronounced as in the 70 rpm case and the associated low-frequency component has a small magnitude. With increase in the mass imbalance, the lateral motions are seen to increase in magnitude while the torsion motion is seen to decrease in amplitude. These studies point to how the unbalanced mass can influence the system dynamics in contact and no-contact situations.

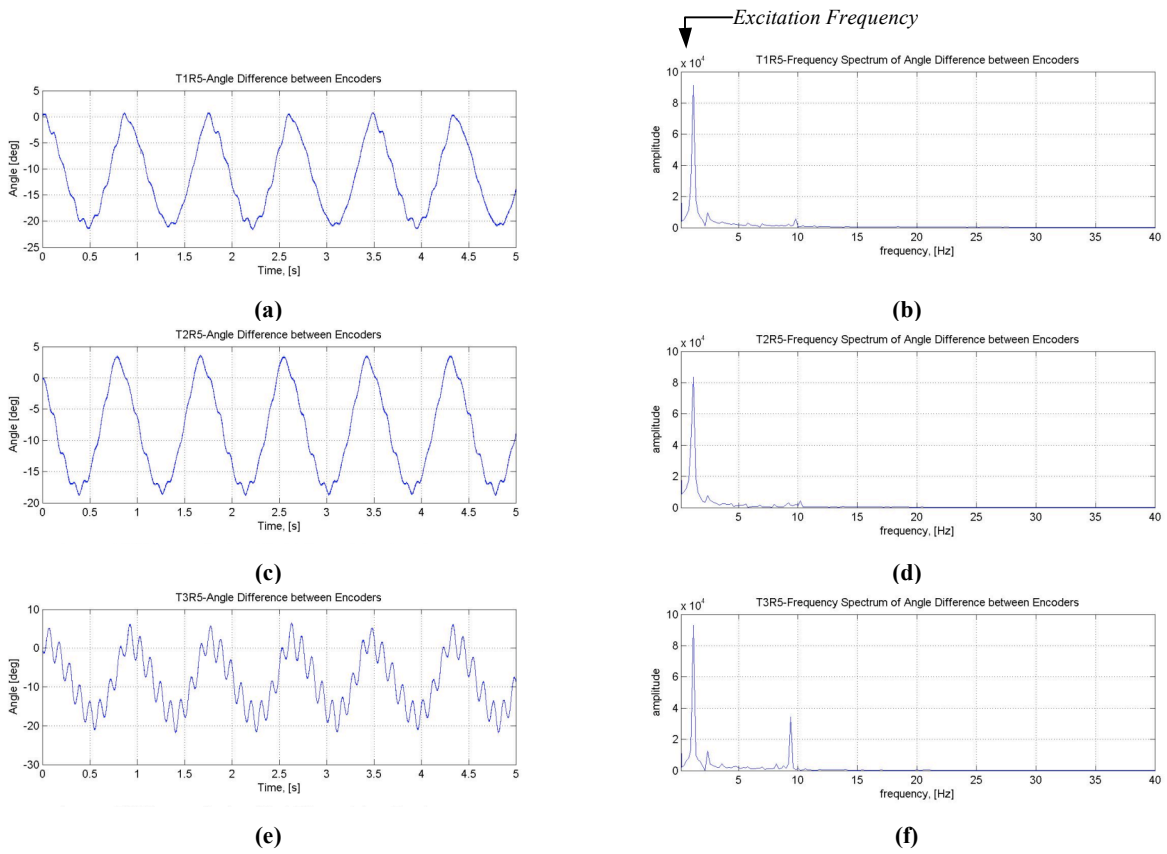

Figure 2. Rotor response for different levels of mass imbalance and 70 rpm rotation speed: a) and b) no mass; c) and d) case with small unbalance; and e) and f) case with large unbalance.

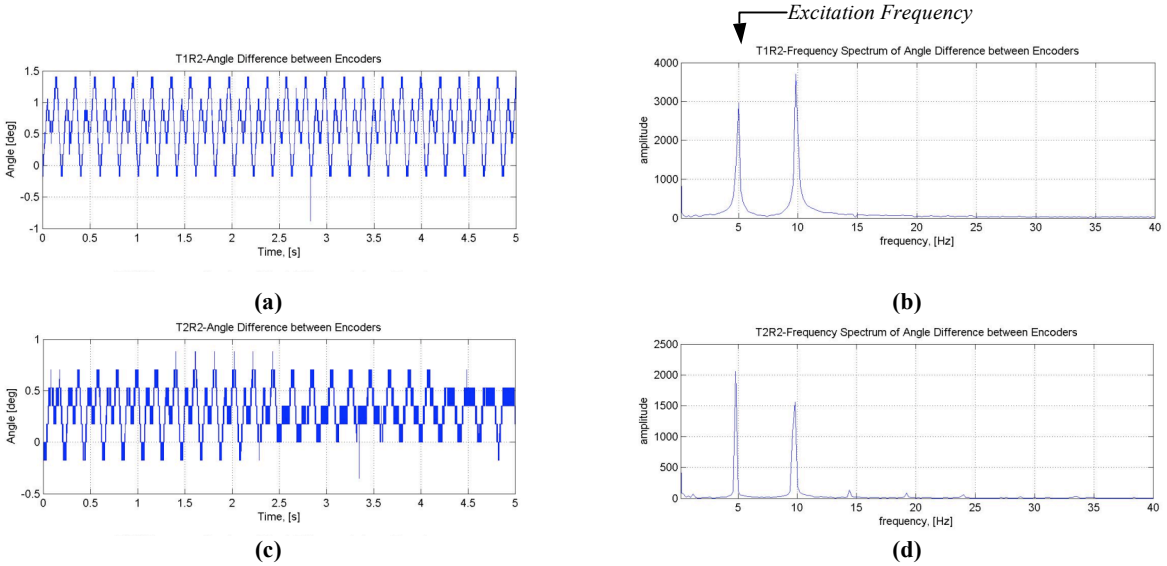

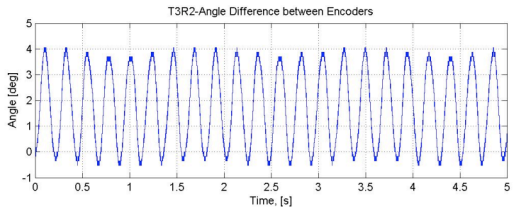

(e)

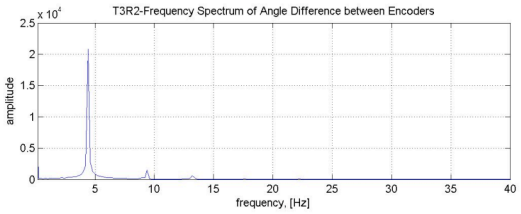

(f)

Figure 3. Rotor with different levels of mass imbalance and 300 rpm rotation speed. a) and b) no mass; c) and d) case with small unbalance; and e) and f) case with large unbalance.

2.2 Numerical Investigations into Torsion Vibration

In the previous section, experimental results were presented and the influence of unbalanced mass was examined. To generate the corresponding numerical results, the reduced-order models discussed in previous reports were used. Different levels of mass imbalance are considered, and the time histories of torsion motions and the corresponding frequency spectra are examined. The results obtained for the low rotation speed are shown in Figure 4, and the results obtained for the high rotation speed are shown in Figure 5. The numerical results indicate a higher level of torsion vibrations than those observed in the experiments. However, overall, the numerical results are in agreement with the experimental observation of the increase in the torsion vibration level with the increase in mass imbalance at the low rotation speed. The model is currently being examined to improve the correspondence between the experimental and numerical results.

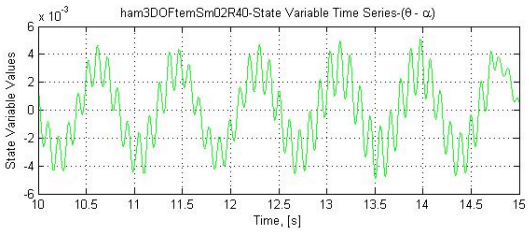

(a)

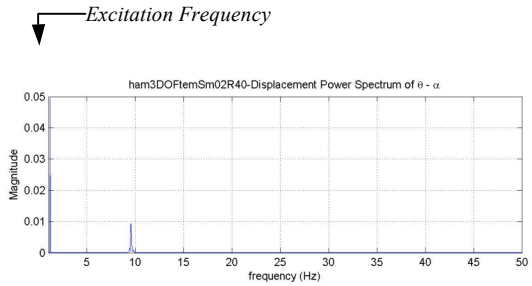

(b)

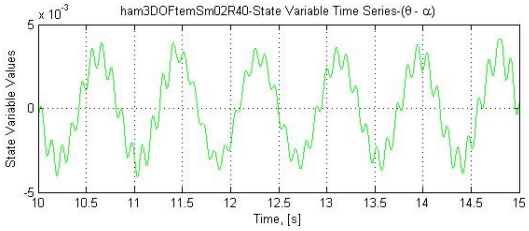

(c)

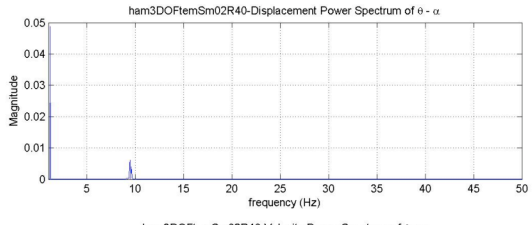

(d)

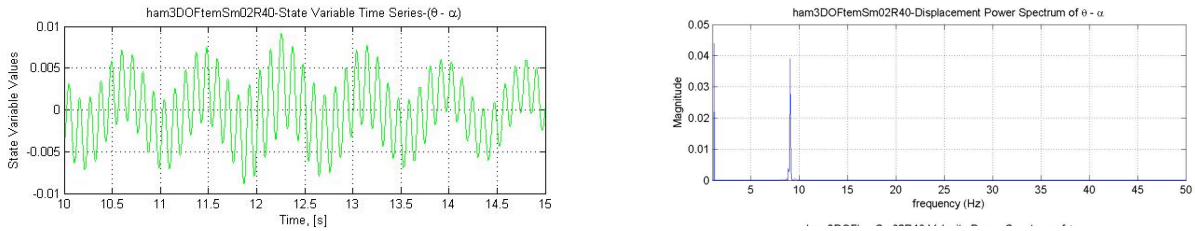

(e) (f)

Figure 4. Rotor with different levels of mass imbalance and low rotation speed. a) and b) no mass; c) and d) case with small unbalance; and e) and f) case with large unbalance.

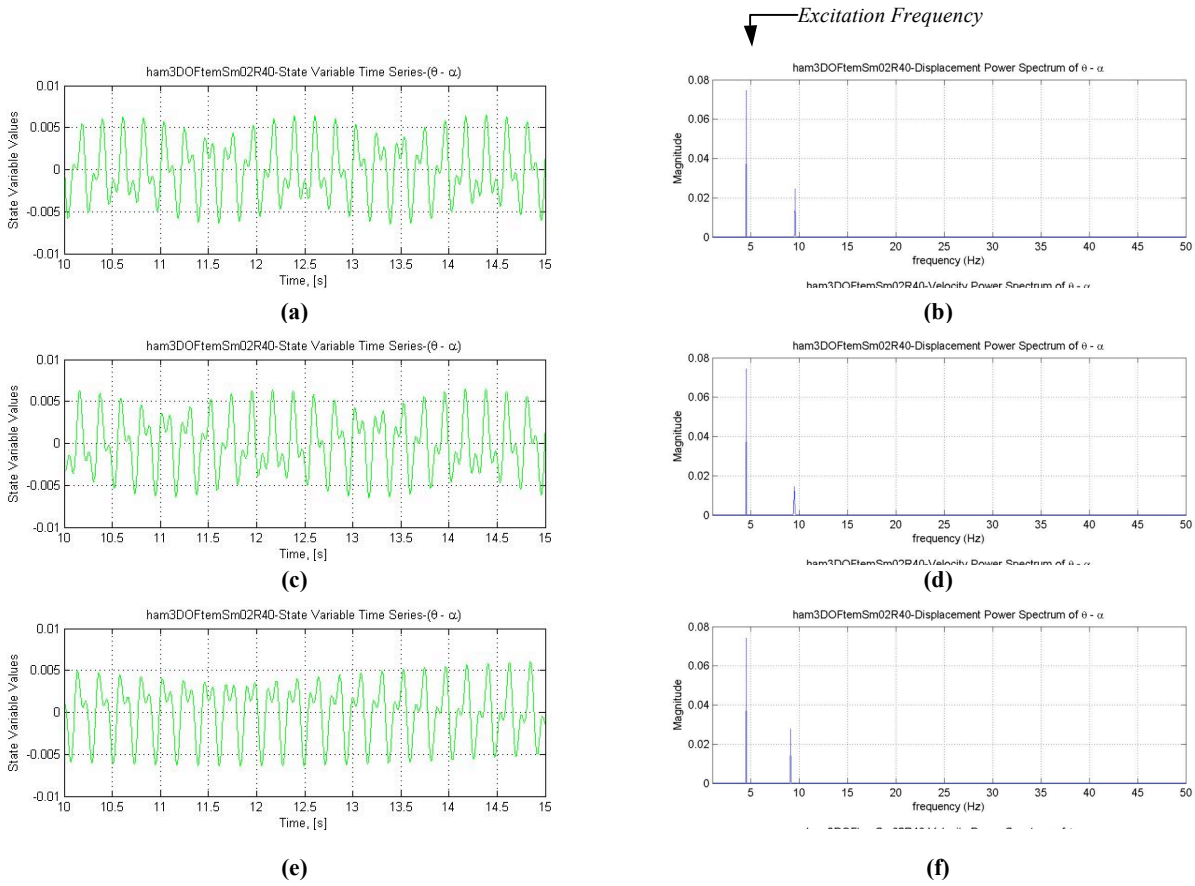

(a) (b)

(c) (d)

(e) (f)

Figure 5. Rotor with different levels of mass imbalance and high rotation speed. a) and b) no mass; c) and d) case with small unbalance; and e) and f) case with large unbalance.

2.3 Comparison of Rotor Trajectories

The reduced-order models described in previous reports can be used for different types of rotor motions including bumping and sticking motions at different rotation speeds. To illustrate the predictive capabilities of these models, in Figure 6, the predicted rotor trajectories for the experimental configuration of Melakhessou et al. (2003) are shown. While the model used by Melakhessou et al. (2003) does not capture the observed experimental motions correctly, the present model does well.

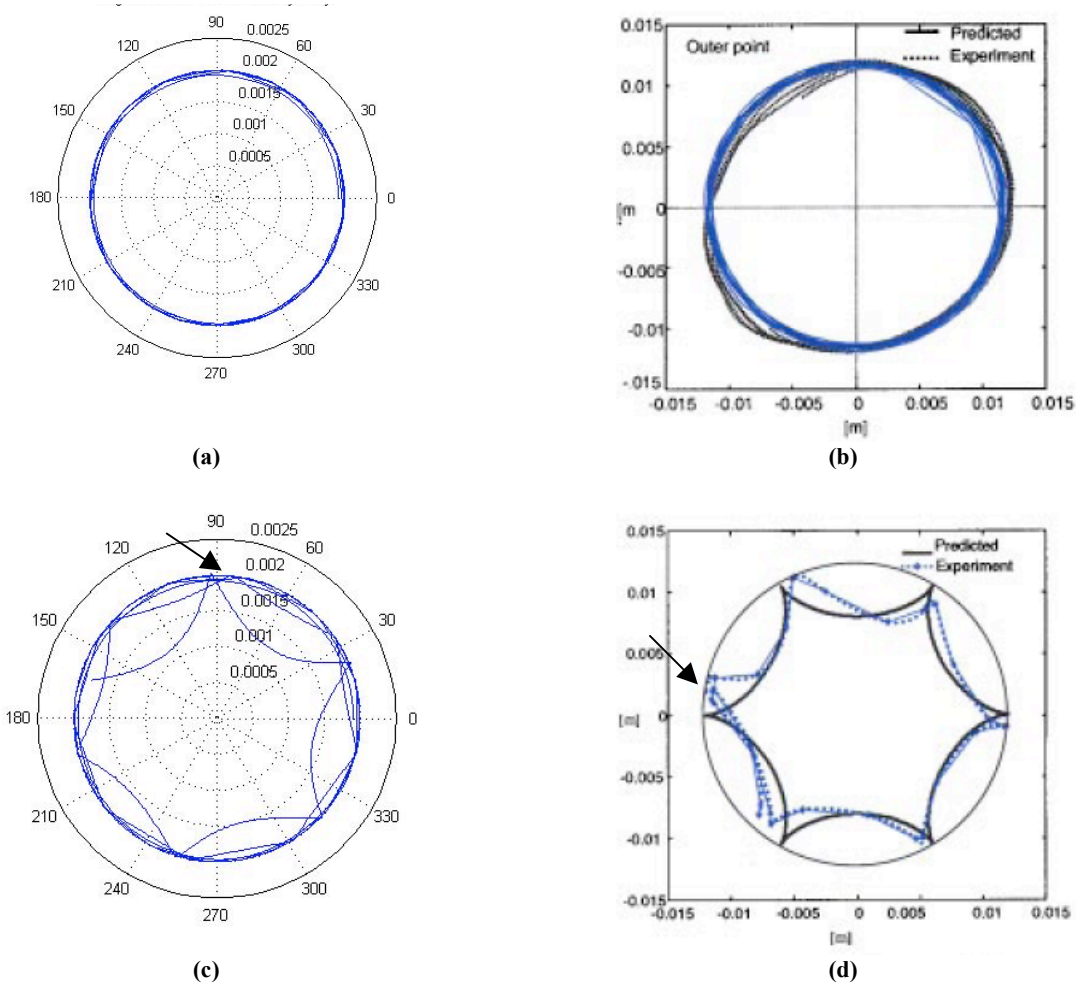

Figure 6. Comparison of rotor trajectories predicted by current work and those presented in earlier literature. a) predicted rolling motion, b) rolling motion studied in previous work, c) predicted bumping motion, and c) bumping motion studied in previous work. The arrows used in the figure point to features that are captured by the current model.

3. Concluding Remarks and Future Work

In this phase, the authors focused on torsion vibration of the drill string and studied the effects of mass imbalance for different rotation speeds. It was shown that the current model captures the different features of the contact and non-contact dynamics better than those reported in the literature. In future work, these efforts are to be continued in accordance with the stated objectives.

Appendix

Approach

A combined analytical, numerical, and experimental approach is being pursued at the University of Maryland and the Petroleum Institute. Specifically, the drill string is being modeled as a reduced-order nonlinear dynamical system. Appropriate attention is also to be paid to the interactions with the environment. The experiments at UMD and PI are tailored to address specific aspects of the drill-string dynamics as well as complement each other. Actuator and sensor choices are also to be explored to determine how best to control the system dynamics. The studies will be initiated with drill strings located on fixed platforms, and later extended to systems located on floating platforms.

Three-Year Schedule

Phase II:

January 1, 2009 to December 31, 2009: Carry out quantitative comparisons between experimental results and predictions of reduced-order models for open-loop studies; understand stick-slip interactions and explore continuum mechanics based drill-string models for fixed platform environments and experimental results; examine different configurations including horizontal drilling

January 1, 2010 to December 31, 2010: Construct control schemes; carry out experimental, analytical, and numerical studies; and identify appropriate schemes; study horizontal drilling configurations through experiments and analysis; initiate drill-string models for off-shore environments including floating platforms

January 1, 2011 to December 31, 2011: Carry out experiments, analysis, and numerical efforts with a focus on drill-string operations in off-shore environments.

References

[1] Akgun, F. 2004, "A Finite Element Model for Analyzing Horizontal Well BHA Behavior," J. of Petrol. Sci & Eng., Vol. 42, pp. 121-132.

[2] Bednarz, S., 2004, "Design and Exploitation Problems of Drill Strings in Directional Drilling," Acta Montanistica Slovaca, Vol. 9, pp. 152-155.

[3] Downtown, G., 2009, "*New Directions in Rotary Steerable Drilling*", Oilfield Review, pp. 18-29.

[4] Leine, R. I., van Campen, D. H., and Keultjes, W. J. G. (2002). "Stick-Slip Whirl Interaction in Drill String Dynamics," *ASME Journal of Vibration and Acoustics*, Vol. 124 (2), pp. 209-220.

[5] Liao, C.-M., Balachandran, B., and Karkoub, M., (2009). "Drill-String Dynamics: Reduced Order Models," To appear in Proceedings of ASME IMECE 2009, Nov. 13-19 Lake Buena Vista, FL, USA, 2009; Paper No. IMECE2009-10339.

[6] Melakhessou, H., Berlioz, A., and Ferraris, G. (2003). "A Nonlinear Well-Drillstring Interaction Model," *ASME Journal of Vibration and Acoustics*, Vol. 125, pp. 46-52.

[7] Mihajlović, N., van Veggel, A. A., van de Wouw, N., and Nijmeijer, H. (2004) "Analysis of Friction-Induced Limit Cycling in an Experimental Drill-String System," *ASME Journal of Dynamic Systems, Measurement, and Control*, Vol. 126(4), pp. 709-720.

[8] Mihajlović, N., van de Wouw, N., Rosielle, P.C.J.N., and Nijmeijer, H. (2007) "Interaction between torsionalal and lateral vibrations in flexible rotor systems with discontinuous friction," *Nonlinear Dynamics*, Vol. 50, pp. 679-699.

[9] Nayfeh, A. H. and Balachandran, B. (1995). *Applied Nonlinear Dynamics: Analytical, Computational, and Experimental Methods*, Wiley, New York.

[10] Spanos, P. D., Chevallier, A. M., Politis, N. P., and Payne, M. L. (2003). "Oil and Gas Well Drilling: A Vibrations Perspective," *Shock and Vibration Digest* Vol. 35(2), pp. 85-103.

[11] Short, J. A. "Introduction to Directional and Horizontal Drilling," Pennwell Pub, 1993.

[12] Singh, S. P. and Balachandran, B. (2009). "Rolling Rub Translations of a Flexibility Connected Disk," preprint.

Studies on Mobile Sensor Platforms

UMD Investigators: Balakumar Balachandran, Nikil Chopra
GRAs: Rubyca Jaai
PI Investigator: Hamad Karki, Sai Cheong Fok
GRAs: Hesham Ishmail (ADNOC Fellow)
Start Date: April 2009

1. Objective/Abstract

Mobile sensor platforms can be employed in a variety of operations including environmental and structural health monitoring operations in harsh and remote environments. The overall objective of this project is to carry out a combined analytical, numerical, and experimental effort to develop mobile sensor platforms and appropriate simultaneous localization and mapping (SLAM) algorithms for cooperative sensor platforms to operate in a harsh environment. Research objectives are the following: i) develop SLAM algorithms based platforms taking into account system constraints such as constrained communication, the type of sensors considered, allowable dynamics, and factors such as sensor failures and reliability of the considered sensors and ii) carry out experimental and supporting simulation studies by using mobile platform test platforms at the University of Maryland and the Petroleum Institute.

Motivated by inspection problems, such as external and/or internal inspection of oil storage tanks, inspection inside oil pipes, and monitoring of the exterior of offshore platforms, the authors study the localization problem associated with mobile sensor platforms. In the localization problem, an agent or a mobile sensor platform uses relative sensing information between the agent and the source to be localized to determine the location of the source. To this end, localization of a static source by using a mobile sensor platform was studied over the past quarter. With appropriate assumptions on the system dynamics, the noise robustness of a previously proposed localization algorithm (Dandach et al., 2009) was examined. By using Lyapunov analysis, it is demonstrated here that if the noise uncertainty is constant and bounded, the adaptive localization algorithm results in bounded localization errors. The analytical results are validated through numerical simulations. Another approach to localization with the use multiple agents is also presented. This approach is based on trajectory planning for the inspection of the oil tank base. Adaptive control techniques were used to make certain that the mobile agents track the desired trajectory and drive the tracking error to zero. Simulation results for this approach are also presented for two agents. Preliminary experimental work carried out to build a mobile agent that is to be used for verifying the algorithms is discussed in this report.

2. Approach

The approach used for the analysis of the boundedness of the source localization algorithm in the presence of noise is presented in Section 2.1. In Section 2.2, the approach used for the multi-agent trajectory planning and control algorithm is discussed.

2.1. Source localization

In the localization problem, an agent or a mobile sensor platform makes use of relative sensing information between the agent and the source to be localized for determining the source location. Here, the authors study the localization problem where distance measurements between the agent and the source are used to estimate the position of the source.

The problem of source localization has appealed to researchers in different fields including robotics (e.g., Fox et al., 2000; Roumeliotis and Bekey, 2002), wireless networking, (e.g., Patwari

et al., 2005; Pathirana et al., 2005) and adaptive control analysis (e.g., Dandach et al., 2009; Cao et al., 2006).

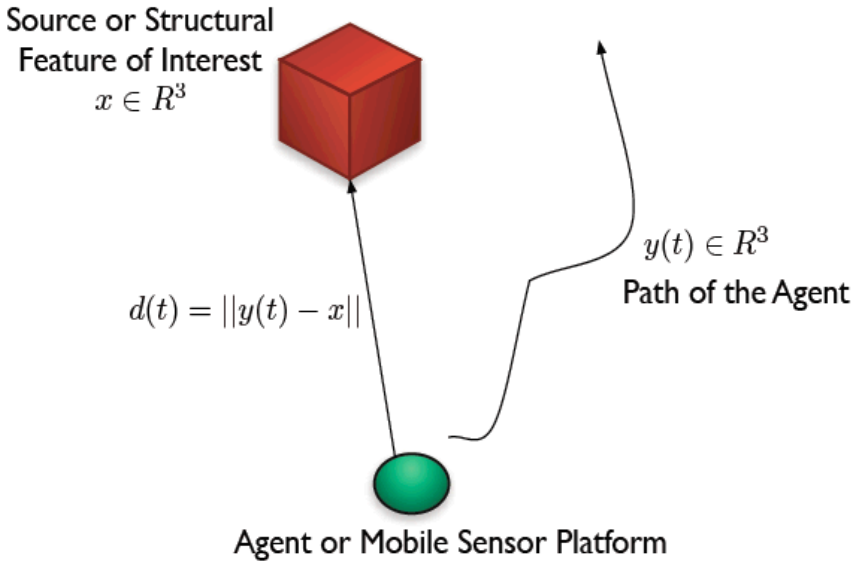

Figure 1. The goal is to estimate the location of x of the source given the measurements d(t) and y(t).

While the localization problem in the ideal noise-free case can be solved relatively easily, noise in sensor measurements is a primary impediment to robust localization. To address this, in this effort, the algorithm proposed by Dandach et al. (2009), was analyzed by using Lyapunov techniques (Khalil, 2002), and the robustness of the adaptive algorithm to noise in sensor measurements was studied. Following the earlier approach (Dandach et al., 2009), and by using a Lyapunov formulation of their localization algorithm, it is demonstrated that in the case of a static source and constant, bounded noise in the distance measurements, the localization errors are ultimately bounded. The problem setting is provided in Figure 1, where $y(t) \in R^3$ is the trajectory of the sensor platform, $x \in R^3$ is the location of the source, and $d(t)$ is the distance measurement obtained by the sensor platform. Then, the problem is to use the signals $d(t)$ and $y(t)$ to estimate the location x of the source.

2.2. Trajectory planning and control

As shown in Figure 2, the approach is divided into four parts, i) localization, ii) trajectory planning, iii) measurement (data gathering), and iv) mapping. These parts are discussed next.

Figure 2. Flow chart of different stages in trajectory planning and control approach.

i) Localization: In this part, the locations of the mobile agents are to be determined by using different types of sensors such as ultrasonic sensors or digital compass.

ii) Trajectory: In order to simulate the dynamics of the mobile agent, the mobile vehicle dynamics are assumed to be similar to the dynamics derived in Pourboghrat and Karlsson (2002). By using two mobile agents, the goal is to maximize mobile vehicle movement efficiencies. In order to accomplish this, an adaptive control law will be used for each agent to ensure that the tracking error converges to zero. The area to be inspected is divided into grids as illustrated in Figure 2.3, with measurements to be carried out at each node as shown. Further, the approach will allow for peer-to-peer communication between the mobile agents to make sure that each node in the grid is visited by one of the agents to maximize efficiency.

iii) Data Gathering (Measurements)*:* The mobile agents will visit each of the nodes shown in Figure 3, and they will be used to measure the thickness of the oil tank floor. For the simulations, the thickness values will be randomly generated numbers in the range of 0-9 with the assumption that thickness values equal to seven or above are acceptable. If a thickness reading is below the acceptable value, say 5, as shown in Figure 2.3, four additional nodes will be introduced around it. The four new nodes will be additionally inspected by one of the mobile agents.

iv) Mapping: Finally, after all the data are gathered, a three-dimensional plot will be presented. The positions will be shown in the X-Y plane, and the Z direction data show the thickness readings.

The rest of this report is organized as follows. The results on source localization and Lyapunov analysis are presented in Section 4.1 and the associated numerical results are given in Section 4.2. Simulation results obtained for the trajectory planning are discussed in Section 4.3. The development of a mobile agent for experimental studies is discussed in Section 4.4. Concluding remarks are presented along with directions for future work in Section 5.

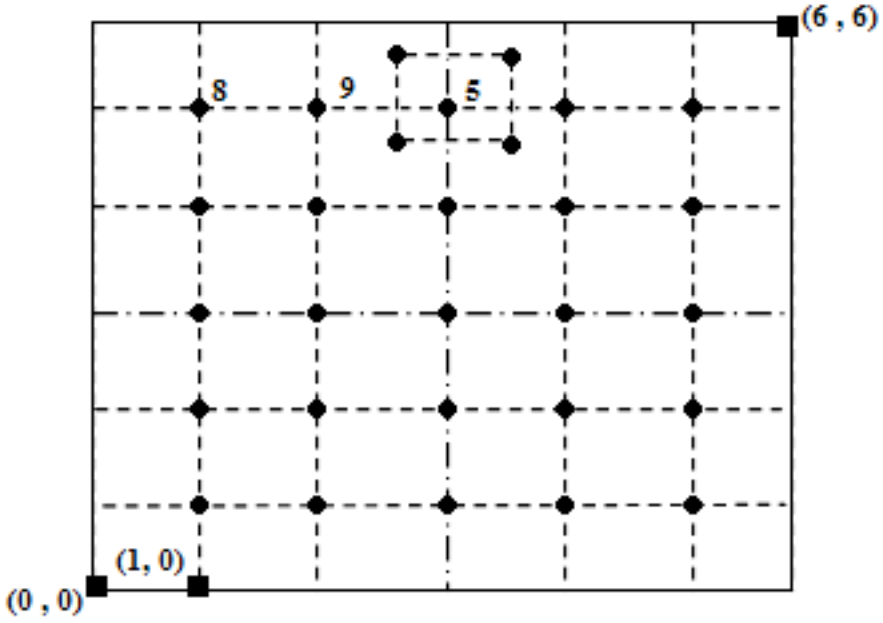

Figure 3. Illustration of the grid and measurement nodes.

3. Summary of Results

The results on source localization and the corresponding Lyapunov analysis are presented in Section 3.1 and the associated numerical results are given in Section 3.2. Simulation results for the trajectory planning and control approach are presented in Section 3.3. The development of a mobile agent for experimental work is discussed in Section 3.4.

3.1. Source localization and Lyapunov analysis

It is assumed in this report that the distance measurement obtained by the mobile sensor platform is affected by noise so that

$$d(t) = \| y(t) - x + w \| \tag{1}$$

where w is the constant disturbance in the distance measurement. The following assumptions are made on the mobile sensor platform trajectory *y*(*t*) and the noise *w* for the subsequent analysis.

Assumption A1: The agent trajectory $y : R \rightarrow R^3 \in C^2$. Furthermore, there exists a constant B_0 such that

$$\| y(t) \| + \| \dot{y}(t) \| + \| \ddot{y}(t) \| \leq B_0 \tag{2}$$

Assumption A2: The constant noise $w \in R^3$ is bounded and there exists $n_b > 0$ such that $\| w \| \leq n_b$. By using (1) and (2), it can be shown that

$$\frac{d}{dt}\{d^2(t)\} = 2\dot{y}^T(t)(y(t) - x + w \tag{3}$$

The assumption A1 ensures that finite power is needed to force or actuate the mobile sensor platform. As noted in an earlier work (Dandach *et al*., 2009), if the derivatives of the distance measurement *d*(.) and the mobile sensor platform trajectory *y*(.) are available over a time interval $[0,T]$, and if the signal $\dot{y}(\cdot)$ spans R^3 over $[0,T]$, then the constant vector x can be estimated from the above equation. However, in a practical setting, the distance measurements are inherently noisy, and hence, an alternative mechanism for estimating the source vector x needs to be developed. The authors demonstrate in what follows that the formulation proposed in the earlier work (Dandach *et al*., 2009) can be modified to include a constant noise that enters the distance measurement as given by (1). Following the earlier work (Dandach *et al*., 2009), for a given $\alpha > 0$,the authors define the signals $\eta(\cdot), m(\cdot)$ and $P(\cdot)$ according to

$$\begin{aligned}
\dot{z}_1(t) &= -\alpha z_1(t) + \frac{1}{2}d^2(t) \quad z_1(0) = 0 \\
\eta(t) &= -\alpha z_1(t) + \frac{1}{2}d^2(t), \\
\dot{z}_2(t) &= -\alpha z_2(t) + \frac{1}{2}y^T(t)y(t) \quad z_2(0) = 0 \\
m(t) &= -\alpha z_2(t) + \frac{1}{2}y^T(t)y(t), \\
\dot{z}_3(t) &= -\alpha z_3(t) + y(t) \quad z_3(0) = 0 \\
P(t) &= -\alpha z_3(t) + y(t)
\end{aligned} \tag{4}$$

The signals $\eta(t), m(t)$, and $P(t)$ are a filtered version of the signals $\frac{1}{2}d^2(t), \frac{1}{2}y^T(t)y(t)$, and $y(t)$, respectively. These state variable filtered signals are used subsequently in the estimation process. If p is denoted as the derivative operator, then

$$\frac{1}{p+\alpha}\{\frac{1}{2}d^2(\cdot)\} = \int_0^{\cdot} e^{-\alpha(\cdot-\tau)}\,\frac{1}{2}d^2(\tau)d\tau$$

$$\frac{p}{p+\alpha}\{\frac{1}{2}d^2(\cdot)\} = \int_0^{\cdot} e^{-\alpha(\cdot-\tau)}\,\frac{d}{d\tau}\{\frac{1}{2}d^2(\tau)\}d\tau$$

Additionally, for two vectors $a(t), b(t)$ by $a \approx b$, the authors imply that there exists $\lambda, M > 0$ such that $\forall t \geq 0, \| a(t) - b(t) \| \leq Me^{-\lambda t}$. Then, the next lemma follows

Lemma 1. Suppose that assumption A1 holds, $x \in R^3$ is a constant, the noise enters the distance measurement as described by (1), and the signals $\eta(t), m(t)$ and $P(t)$ are described by (4). Then,

$$\eta(\cdot) \approx m(\cdot) - P^T(\cdot)(x - w)$$

Proof. It can be shown by using (4), that as $\alpha > 0$,

$$\eta(\cdot) \approx \frac{p}{p+\alpha}\{\frac{1}{2}d^2(\cdot)\}$$

$$m(\cdot) \approx \frac{p}{p+\alpha}\{\frac{1}{2}y^T(\cdot)y(\cdot)\}$$

$$P(\cdot) \approx \frac{p}{p+\alpha}\{y(\cdot)\}$$

Then, by using the above equations, (1) and the fact that x is a constant, it can be shown that

$$\eta(\cdot) \approx \frac{p}{p+\alpha}\{\frac{1}{2}d^2(\cdot)\} \approx \frac{1}{p+\alpha}\{\dot{y}^T(\cdot)(y(\cdot) - x + w)\}$$

$$\approx \frac{p}{p+\alpha}\{\frac{1}{2}y^T(\cdot)y(\cdot)\} - (\frac{p}{p+\alpha}\{y^T(\cdot)\})(x - w)$$

$$\approx m(\cdot) - P^T(\cdot)(x - w)$$

Let the adaptive estimation process for the source position be given as

$$\dot{\hat{x}}(t) = -\gamma P(t)(\eta(t) - m(t) + P^T(t)\hat{x}(t)) \tag{5}$$

where $\gamma > 0$ is a constant. Define the estimation error as

$$\tilde{x}(t) = \hat{x}(t) - x \tag{6}$$

The next result demonstrates that the estimation error (6) is ultimately bounded.

Theorem 1. Consider the dynamical system described by (1), (4), and (5). Suppose that assumptions A1, A2 hold and $x \in R^3$ is a constant. If there exist constants $k_1 > 0, k_2 > 0$ and $T > 0$ such that for $\forall t \geq 0$

$$k_1 I \leq \int_t^{t+T} P(\tau)P^T(\tau)d\tau \leq k_2 I \tag{7}$$

then the estimation error defined by (5) is ultimately bounded.

Proof. Consider the differential equation

$$\dot{\hat{x}}(t) = \dot{\tilde{x}}(t) = -\gamma P(t)P^T(t)\tilde{x}(t)) \tag{8}$$

If (7) is satisfied, then it is well known (Anderson, 1977) that the dynamics (8) are exponentially stable; that is, the equilibrium point of the dynamical system is asymptotically stable. By using the converse Lyapunov function result (Theorem 4.14, Khalil, 2002), it can be shown that there exist positive constants c_1, c_2, c_3, and c_4 and $V : [0, \infty) \times R^3 \to R$ such that

$$c_1 \| \tilde{x} \|^2 \leq V(t, \tilde{x}) \leq c_2 \| \tilde{x} \|^2 \tag{9}$$

$$\frac{\partial V}{\partial t}+\frac{\partial V}{\partial \tilde{x}}(-\gamma P(t)P^T(t)\tilde{x}(t)) \le -c_3 \| \tilde{x} \|^2 \quad (10)$$

$$\| \frac{\partial V}{\partial \tilde{x}} \| \le c_4 \| \tilde{x} \| \quad (11)$$

The estimation dynamics (5) can be rewritten as

$$\begin{aligned}\dot{\hat{x}}(t) &= -\gamma P(t)(\eta(t)-m(t)+P^T(t)\hat{x}(t)) \\ &= -\gamma P(t)(\eta(t)-m(t)+P^T(t)(x(t)-w)-P^T(t)(x(t)-w)+P^T(t)\hat{x}(t)) \\ &= -\gamma P(t)P^T(t)\tilde{x}-\gamma P(t)(\eta(t)-m(t)+P^T(t)(x(t)-w))-\gamma P(t)P^T(t)w = f(\tilde{x},t) \quad (12)\end{aligned}$$

and from Lemma 1, it is known that

$$\eta(\cdot) \approx m(\cdot)-P^T(\cdot)(x-w)$$

Hence, there exists $\lambda > 0, M > 0$ such that

$$\| \eta(t)-m(t)+P^T(t)(x-w) \| \le Me^{-\lambda t} \quad (13)$$

Let $V(\tilde{x},t)$ be a candidate Lyapunov function for the dynamical system (12). Then, the derivative along system trajectories is given by

$$\begin{aligned}\dot{V}(\tilde{x},t) &= \frac{\partial V}{\partial t}+\frac{\partial V}{\partial \tilde{x}} f(\tilde{x},t) \\ &= \frac{\partial V}{\partial t}+\frac{\partial V}{\partial \tilde{x}}(-\gamma P(t)P^T(t)\tilde{x}-\gamma P(t)(\eta(t)-m(t)+P^T(t)(x(t)-w))-\gamma P(t)P^T(t)w)\end{aligned}$$

After using (10), (11), the derivative can be rewritten as

$$\begin{aligned}\dot{V}(\tilde{x},t) &\le -c_3 \| \tilde{x} \|^2 + \frac{\partial V}{\partial \tilde{x}}(-\gamma P(t)(\eta(t)-m(t)+P^T(t)(x(t)-w))-\gamma P(t)P^T(t)w) \\ &\le -c_3 \| \tilde{x} \|^2 + c_4 \| \tilde{x} \| \| -\gamma P(t)(\eta(t)-m(t)+P^T(t)(x(t)-w))-\gamma P(t)P^T(t)w \| \\ &\le -c_3 \| \tilde{x} \|^2 + c_4\gamma \| P(t) \| \| \eta(t)-m(t)+P^T(t)(x(t)-w) \| \| \tilde{x} \| + c_4\gamma \| P(t)P^T(t)w \| \| \tilde{x} \| \\ &\le -c_3 \| \tilde{x} \|^2 + c_4\gamma M e^{-\lambda t} \| P(t) \| \| \tilde{x} \| + c_4\gamma \| P(t)P^T(t)w \| \| \tilde{x} \| \quad (14)\end{aligned}$$

From assumptions A1 and A2, it follows that there exists $n_t > 0$ such that

$$c_4\gamma M e^{-\lambda t} \| P(t) \| + c_4\gamma \| P(t)P^T(t)w \| \le n_t \quad (15)$$

After substituting in (14), the result is

$$\begin{aligned}\dot{V}(\tilde{x},t) &\le -c_3 \| \tilde{x} \|^2 + n_t \| \tilde{x} \| \\ &\le -(c_3-\theta) \| \tilde{x} \|^2 - \theta \| \tilde{x} \|^2 + n_t \| \tilde{x} \| \\ &\le -(c_3-\theta) \| \tilde{x} \|^2 - \theta \| \tilde{x} \| (\| \tilde{x} \| - \frac{n_t}{\theta})\end{aligned}$$

for $0 < \theta < c_3$. Consequently, for $\| \tilde{x} \| > \frac{n_t}{\theta}$,

$$\dot{V}(\tilde{x},t) \le -(c_3 - \theta) \| \tilde{x} \|^2 \tag{16}$$

By using the above inequality, the bounds on the Lyapunov function (9), and by invoking Theorem 4.18 (Khalil, 2002), it is shown that the estimation error is ultimately bounded. This result is contingent on the persistency of excitation (p.e.) (7) condition. It can be seen that this condition imposes certain constraints on admissible sensor platform trajectories. This subject will be treated in the future research.

3.2. Numerical studies

The results developed in the previous section have been validated for a source located at $x = [2\ 3\ 2]^T m$ and a trajectory of the mobile sensor platform prescribed according to $y(t) = [2 + 2\sin(t)\ 2\cos(2t)\ 2\sin(0.5t)]^T m$. The system dynamics as described by (4) and (5) were first simulated for the case with no noise in the distance measurement. As seen in Figure 4, in the absence of noise, the tracking errors approach the origin in an asymptotic fashion. Subsequently, noise $w = [0.05\ 0.3\ 0.02]^T$ was added to the distance measurement as described by (1). As shown in Figure 5, and as predicted by Theorem 1, the estimation errors are bounded.

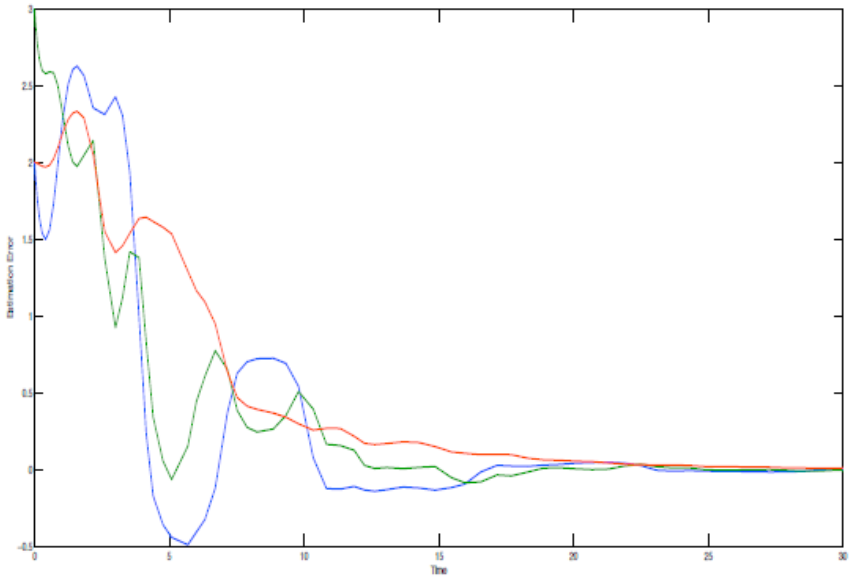

Figure 4. In the absence of noise, the estimation errors are exponentially stable.

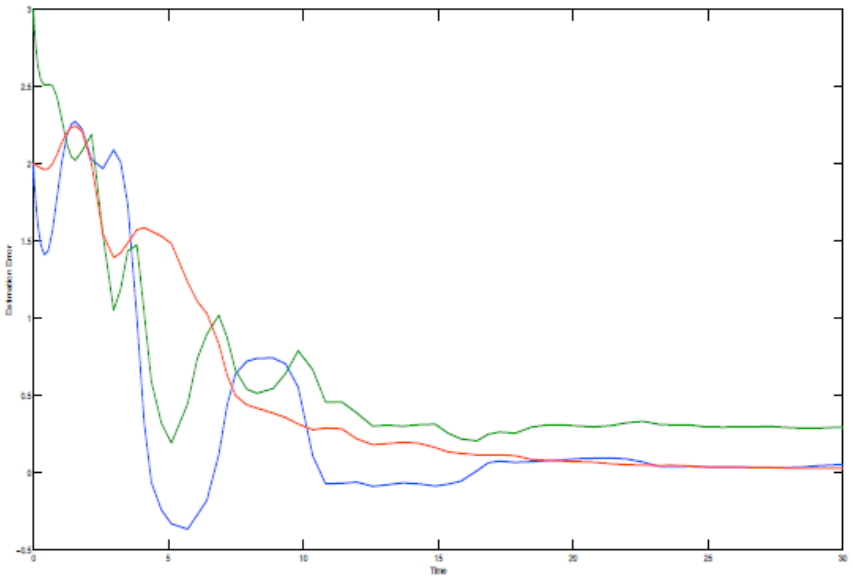

Figure 5. In the presence of bounded noise, the estimation errors are bounded.

3.3 Simulation results for trajectory planning and control algorithm

An algorithm was developed in order to define the location of the mobile agents inside an above-ground oil storage tank. The above-ground oil storage tank is cylindrical in shape with a base diameter ranging from 6.096 to 103.632 meters. The algorithm requires two inputs. The first input is the orientation of the mobile vehicle, which can be determined by using a digital compass with the angle being measured from the north direction. The second input is distance that can be measured by using ultrasonic range sensors to measure the distance from the mobile agent to the tank wall. The algorithm is to be tested, first, by using two ultrasonic sensors, and then, by using three ultrasonic sensors.

First, let us assume that the ultrasonic range sensor is perfect, meaning that the cone angle and distance measurements do not have any uncertainty. In addition, let us also assume the digital compass reading is perfect without uncertainty. The input values and expected answers are exact values generated by using SolidWorks software. Finally, the algorithm is tested by running a Matlab script, which is used to calculate ρ and Θ based on Φ_1 and distances 1 and 2. The obtained results are presented graphically. Two ultrasonic sensors are tested in 4 different quadrants. The orientation of the second sensor is 60^o with respect to the first sensor ($\Phi_2 = \Phi_1 + 60^o$). In Table 1, the given and expected values in 4 different quadrants generated by using the SolidWorks program are shown. In Table 2, the results obtained after running the Matlab script are shown. In Figure 6, the location of the mobile vehicle is shown. This location is determined by the intersection of sensor 1 and 2 information.

Table 1. Given and expected values generated using SolidWorks program

Quadrant	Φ (Orientation w.r.t N) degrees	Distance 1 m	Distance 2 m	Expected ρ m	Expected Θ degrees
1	27.96	17.47	23.75	32.57	32.43
2	27.96	41.66	18.26	34.38	126.34
3	27.96	85.59	63.64	36.25	-143.67
4	27.96	22.52	75.74	41.62	-54.05

Table 2. Calculated ρ and Θ based on Φ_1 and distances 1 and 2.

Quadrant	Calculated ρ m	Calculated Θ degrees
1	32.57	32.43
2	34.38	126.34
3	36.25	-143.67
4	41.62	-54.05

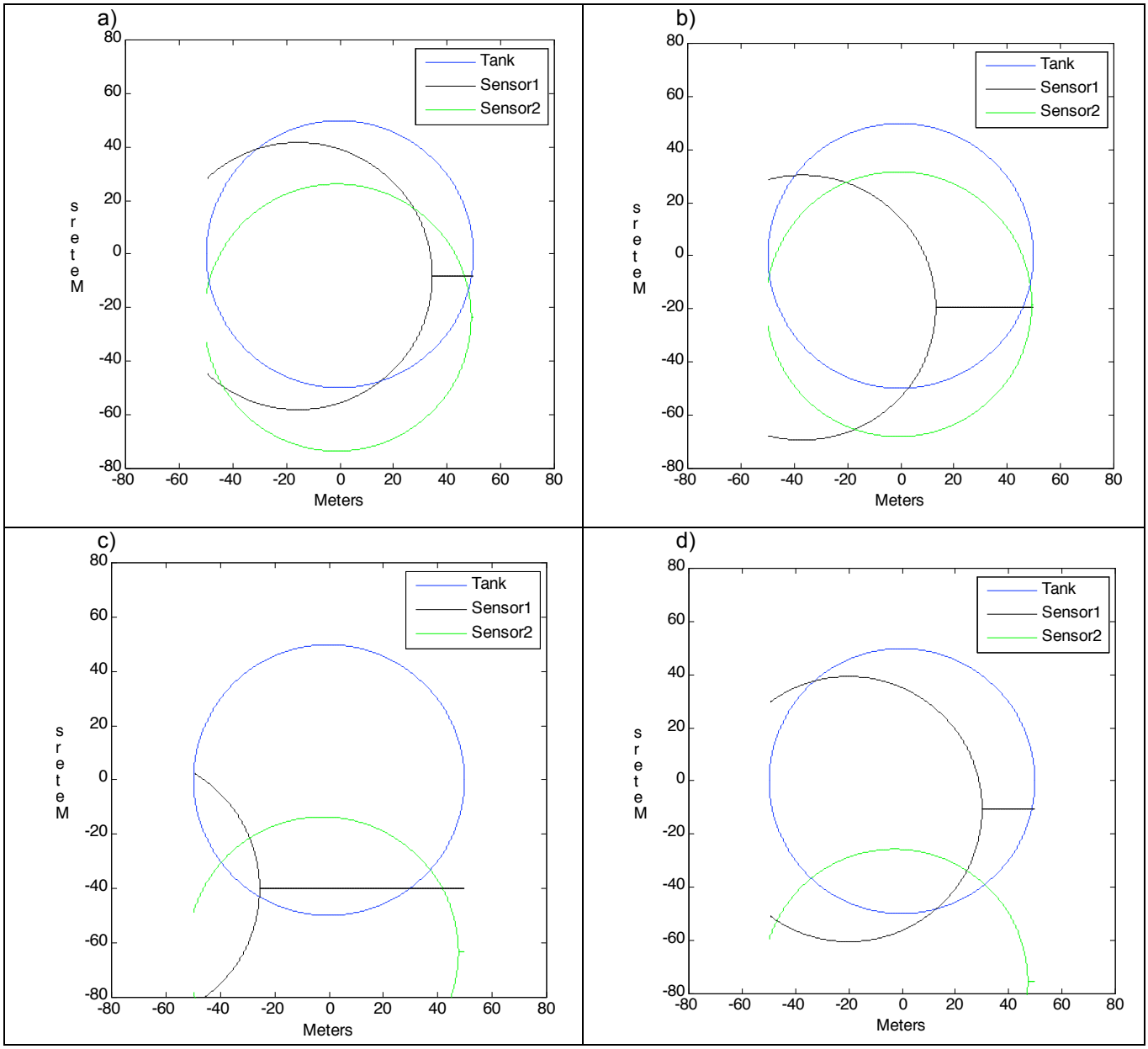

Figure 6. Location of mobile agent with respect to different quadrants.

Next, uncertainty is introduced in the ultrasonic sensor. As shown in Table 3, the cone angle is 25°. When uncertainty is introduced, the location of the mobile vehicle becomes uncertain, as shown in Figure 7.

Table 3. Values generated using Solidworks program.

Quadrant	Φ(Orientation angle measured w.r.t N) degrees	Distance 1 m	Distance 2 m	Cone angle degrees
1	39.9	38.29, 45.20, 52.87	72.79, 77.40, 79.95	25°
2	39.90	45.20	77.40	25°

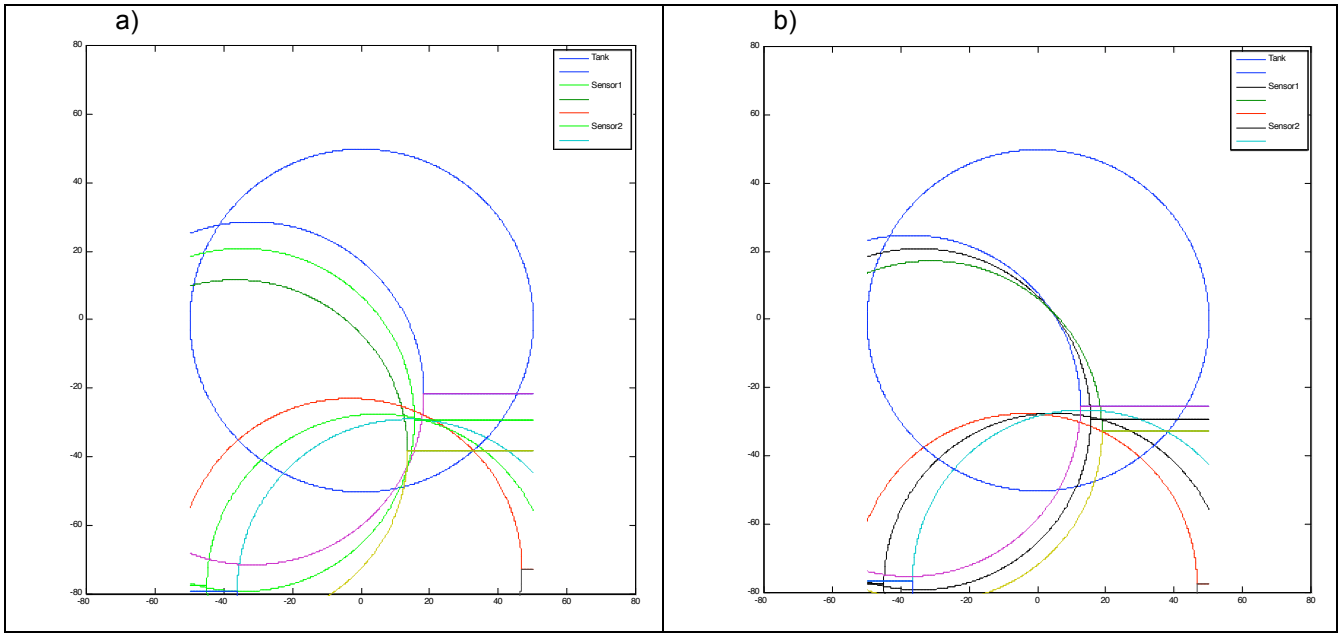

Figure 7. Location of mobile agent with respect to different quadrants in the presence of uncertainty in measurements.

3.4. Experimental work

In order to experimentally test the localization algorithms such as the one presented above, it is necessary to build a mobile platform that will house the sensors to be used for the localization and mapping. A ground-based mobile agent to carry out the experimental measurements necessary for simultaneous localization and mapping has been built. The ground-based agent houses a microcontroller, two accelerometers, and three ultrasonic sensors with the following specifications:

- Arduino Duemilanove microcontroller with 16MHz speed and 512KB memory (EEPROM)
- Devantech Ultrasonic Range Finder SRF05 with a range of 4m and resolution of 3cm to 4cm
- Dimension Engineering Buffered ±3g triple axis accelerometer for motion sensing

The agent is a tracked platform that is actuated by using two DC gear motors (see Figure 8). The microcontroller and the motors are battery powered.

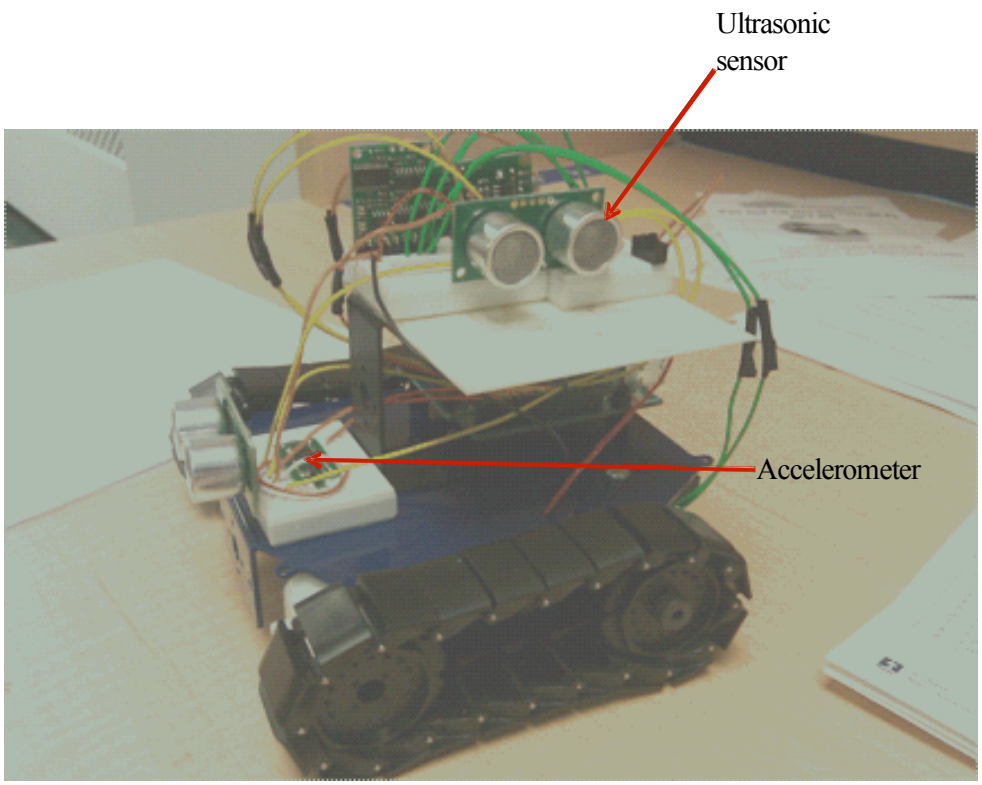

Figure 8. Mobile rover to be used in SLAM experiments.

The ultrasonic sensors are placed on the front and the two sides of the agent in order to provide scans from multiple directions at the same time. The sensors have been set up for obstacle avoidance in order to allow the mobile agent to navigate without collisions. Further, the ultrasonic sensors are to be used for measurements to carry out localization by using range finder scans (e.g., Weiss et al., 1994). Accelerometers have been added to the platform for use in future experiments on SLAM in order to monitor the agent's motions. SLAM algorithms require vehicle motion models as well as measurement models that will provide the locations of the different landmarks in the environment. The accelerometer data are to be used for developing the vehicle motion models.

4. Planned Project Activities for the Next Quarter

As a first step, the source localization algorithm will be used with the rover sensor measurements to implement localization to determine the positions of landmarks (source localization presented in this report) with respect to the agent. A ground arrangement will first be implemented with landmarks in pre-defined locations, and the rover will be used to take measurements in this arrangement, and source localization studies will be carried out.

Future steps to be taken in the trajectory planning and control studies include the formulation of a simulation model for the mobile agent trajectory. Adaptive control laws will be added to ensure that the tracking error goes to zero and the mobile vehicle follows the trajectory. Decision-making between the mobile agents will be developed to maximize movement efficiency.

Further numerical and experimental studies will be conducted to develop and verify SLAM algorithms for multiple mobile platforms. After initial studies in the ground based set-ups, a scaled experimental arrangement to test the algorithms in a fluid environment will also be developed at the University of Maryland. Once the scaling laws have been established, suitable underwater sensor platforms will be acquired and a scaled tank will be constructed.

Appendix

Three-year schedule

Phase II:

April 1, 2009 to December 31, 2009: Carry out analytical and numerical investigations into SLAM algorithm based mobile platforms for representative geometrical profile measurements, construction of experimental test platforms, and preliminary experimental findings

January 1, 2010 to December 31, 2010: Continuation of analytical, experimental, and numerical efforts, with one of the focus areas to be development of appropriate communication and motion planning protocols for operations in harsh environments

January 1, 2011 to December 31, 2011: Continuation of experimental and numerical studies and formulation of recommendations for appropriate sensor and mobile platform configurations for use in oil tanks.

References

[1] Anderson, B., 1977 “Exponential stability of linear equations arising in adaptive identification," IEEE Transactions on Automatic Control, Vol. 22(1), pp. 83-88.

[2] Cao, M., Anderson, B. D., and Morse, A. S., 2006, “Sensor network localization with imprecise distances," Systems Control Letters, Vol. 55(11), pp. 887-893.

[3] Dandach, S., Fidan, B., Dasgupta, S., and Anderson, B. D., 2009, “A continuous time linear adaptive source localization algorithm, robust to persistent drift," Systems Control Letters Vol. 58 (1), pp. 7-16.

[4] Fox, D., Burgard, W., Kruppa, H., and Thrun, S., 2000, “A probabilistic approach to collaborative multi-robot localization," Autonomous Robots, Vol. 8 (3), pp. 325-344.

[5] Khalil, H., 2002, “Nonlinear Systems”, Prentice Hall, New Jersey.

[6] Pathirana, P., Bulusu, N., Savkin, A., and Jha, S., 2005 “Node localization using mobile robots in delay-tolerant sensor networks," IEEE Transactions on Mobile Computing, Vol. 4 (3), pp. 285-296.

[7] Patwari, N., Ash, J., Kyperountas, S., Hero, A.O., I., Moses, R., and Correal, N., 2005, “Locating the nodes: cooperative localization in wireless sensor networks," IEEE Signal Processing Magazine, Vol. 22 (4), pp. 54-69.

[8] Pourboghrat, F., Karlsson, M.P., 2002, “Adaptive control of dynamic mobile robot with nonholonomic constraints,” Computers & Electrical Engineering, Vol. 28 (4) pp. 241-253.

[9] Roumeliotis, S. and Bekey, G., 2002, “Distributed multirobot localization," IEEE Transactions on Robotics and Automation, Vol. 18 (5), pp. 781-795.

[10] Weiss, G., Wetzler, C., and von Puttkamer, E., 1994, “Keeping track of position and orientation of moving indoor systems by correlation of range-finder scans,” Proceedings of the IEEE International Conference on Intelligent Robots and Systems, pp.595-601 Vol.1, 12-16 September.

Development of a Probabilistic Model for Degradation Effects of Corrosion-Fatigue Cracking in Oil and Gas Pipelines

UMD Investigator: Mohammad Modarres
PI Investigators: Abdennour Seibi
GRA: Mohammad Nuhi
Start Date: Oct 2006

1. Objectives/Abstract

This research continues phase-I mechanistic modeling of the *corrosion-fatigue* phenomenon for applications to pipeline health, risk and reliability management. The objective of this study is to perform additional mechanistic-based probabilistic models derived from physics of failure studies and validate them using the state-of-the-art experimental laboratory being developed at the PI as part of the phase I of this study. Where possible, observed field data from ADNOC operating facilities will be used to supplement observations from the laboratory experiments based on the well-established Bayesian approach to mechanistic model updating and validation developed in Phase I. Uncertainties about the structure of the mechanistic models as well as their parameters will also be characterized and accounted for when such models are applied. The proposed models will allow the end users (e.g., maintenance analysts and Inspection crew) to integrate observed performance data from a wide range of pipelines and selected refinery equipment, such as pumps, compressors and motor-operated valves. Admitting the fact that modeling all degradation mechanisms would be a challenging undertaking, the proposed research will additionally address the following degradation phenomena related to the petroleum industry: pitting corrosion, stress cracking corrosion (SCC), and creep-fatigue.

2. Deliverables for the Completed Quarter

- Literature review on creep deformation model
- Development of mechanistic model for creep deformation
- Preparation of samples for experimental work: aluminum 7075 dog-bone and X70 carbon steel (ASTM-standardized)

3. Summary of Project Activities for the Completed Quarter

Background

A number of deterministic models have been proposed to assess reliability and life-remaining assessment of pipelines. Among these models is the ASME B31G code, which is most widely used for the assessment of corroded pipelines. However, these models are highly conservative and lack the ability to estimate the true life of the pipelines and other equipment used in the oil industry. To address this shortcoming one needs to develop a best-estimate assessment of the life of these structures and equipment (to assess their reliability and risk imposed) and to assess the uncertainties surrounding such estimates. The proposed probabilistic mechanistic models, when fully developed, would integrate the physics of failure of the leading failure degradation phenomena in the oil industry into the formal risk and reliability assessments. Such physical models will be validated using a state-of-the-art reliability assessment laboratory at UMD and at PI (being developed). Uncertainties about the model structures and parameters will also be quantified. Such models will incorporate inspection data (characterizing limited and uncertain evidences). The rate of degradation is influenced by many factors such as pipeline materials, process conditions, geometry and location. Based on these factors, a best estimate of the

structure (pipeline) or equipment (primarily valves, pumps and compressors) service life (reliability and remaining life) is to be calculated and uncertainties associated with the service life quantified. This estimate would serve as a basis that guides decisions regarding maintenance and replacement practices.

Phase I of this research focused on developing a corrosion-fatigue model. It successfully proposed such a model and developed an advanced laboratory for testing this phenomenon at PI. The current research continues in the same line of research by investigating and developing additional degradation phenomena (SCC, pitting corrosion, and creep-fatigue) and integrates these phenomena with reliability and risk assessment through four different tasks. The long-term objective of this research is to develop a comprehensive library of probabilistic mechanistic models for all degradation phenomena pertinent to structures (piping, and pressure vessels) used in the oil industry.

Summary of Results

The following tasks have been completed in the last three months:

Literature Review

According to the American Standard for Testing Materials (ASTM), creep deformation is any strain that occurs when a material is subjected to a sustained stress. The rate at which this deformation occurs depends not only on the magnitude of the applied stress, but also on time and temperature. According to this definition, creep is a kinetic process and is usually written as an appropriate rate law [1-2]. In crystalline solids creep is of concern when the service temperature is greater than or equal to approximately $0.5T_m$, where T_m is the absolute melting temperature given in degrees Kelvin. Creep of materials is a serious problem for thermal power plants and oil/gas refineries where components such as steam generators, distillation towers, and valves are subjected to elevated temperatures. More details will be discussed as part of the model development task.

Mechanistic Model Development

1. Phenomenological Descriptions of Creep

Although there are different theories describing creep, current studies are focused on finding a correlation between experimental results and micromechanical models. The early models—the Norton and Norton–Baily models [1-2]—of creep describe this mechanism by a phenomenological rate relation:

$$\dot{\varepsilon} = A \quad \sigma^n \exp\left(\frac{-Q_c}{kT}\right)$$

where A and n are material parameters, Q_c is the activation energy of the creep process, and k is the Boltzman's constant. The key external variables are temperature, T (in degree Kelvin), and stress, σ, while specific values for n and Q_c are associated with specific creep mechanisms. Monkman and Grant [1, 3] found an empirical relation that indicates that the minimum strain rate is inversely proportional to the time to rupture of aluminum and steel materials. So for a given material at a given stress and temperature, the product of the rupture time (t_r) and the minimum creep rate ($\dot{\varepsilon}_m$) is constant:

$$t_r \times \dot{\varepsilon}_m = Const.$$

By substituting the creep rate in the Monkman-Grant relation, one can find the rupture time as a function of stress and temperature:

$$t_r = A'\sigma^{-n}\exp(\frac{Q_c}{RT})$$

where A' and n are material parameters, and R is the gas constant.
By taking logarithm from both sides of the above equation, one can find a practical "Relative Miller parameter," which relates the rupture time to the temperature:

$$P_{Larson-Miller} = T(C + \ln t_r) = \frac{Q_c}{R}$$

where C is approximately equal to 20-23 for different materials[1] 20.

2. Creep Properties

The behavior of creep is given by plotting strain (e) (or strain rate $\dot{\varepsilon}$) versus time (t). The shape of the creep curve is determined by several competing mechanisms, including strain-hardening, softening processes (such as recovery, re-crystallization, and precipitation) and damaging processes (such as cavitation, cracking in grains and grain boundaries, and specimen necking) [1-7]. Strain-hardening tends to decrease the strain rate, while the other processes tend to increase the creep rate. The balance among these factors determines the shape of the creep curve.

During primary creep, (See Figure 1 for a description of phases of creep) the decreasing slope of the creep curve is related to strain-hardening. Secondary-stage creep is explained in terms of a balance between strain-hardening and the softening and damaging processes, which results in an almost constant creep rate. As strain continues, micro-structural damages continue to accumulate and the creep rate continues to increase. This final stage, or tertiary creep, will result in final failure of the material (gradual or abrupt rupture of the specimen) [11]. Figure 1 illustrates a typical creep curve.

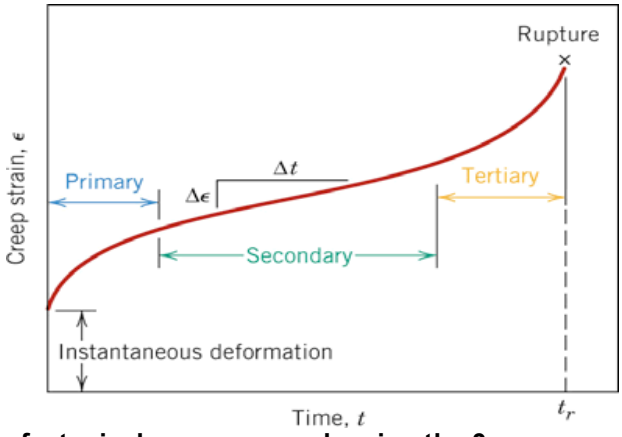

Figure 1. Illustration of a typical creep curve showing the 3 common regions of creep [12].

Stress and temperature are key stress factors that affect creep. Figure 2 illustrates mechanical tensile stress and temperature dependencies for a given creep curve.

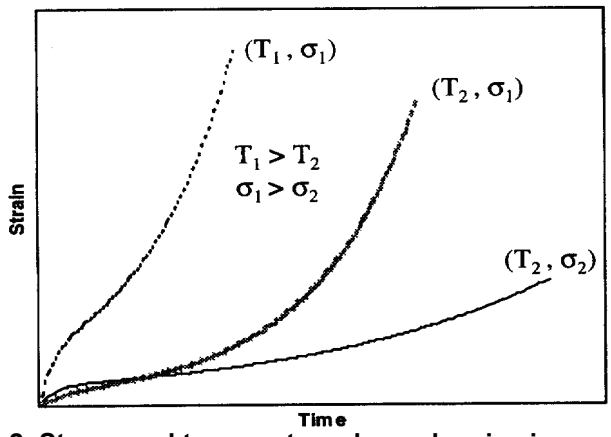

Figure 2. Stress and temperature dependencies in creep [13].

3. Creep Models Covering the Three Stages of Creep Curve

Creep behavior has been known for more than a century. More than twenty-five models have been proposed to explain different parts of creep curve for different materials. Only a few of these models cover all the three stages of the creep curve [1, 3, 6].
In the following, we refer to those models that can cover some parts of the creep curve accurately and also give a physical explanation for the underlying stage:

- The theta projection (Evans-Wilshire) model [5,6,14] takes the creep curve as a composition of decaying primary and accelerating tertiary stages. Then, the creep strain is considered to increased with time:

$$\varepsilon = \theta_1[(1-\exp(-\theta_2 t)] + \theta_3[\exp(\theta_4 t) - 1]$$

where θ_i (with i=1, 2, 3, and 4) are material parameters and their values vary with temperature (T) and stress (σ) as follows:

$$\log\theta_i = A_i + B_i\sigma + C_i T + D_i\sigma T$$

where A_i, B_i, and C_i and D_i are constants. The four θ parameters are determined by a non-linear least square fitting (NLSF) analyses.
The theta projection creep equation has two terms: the first term describes the hardening process, and the second term deals with the softening process. The primary advantage of the theta projection model is its ability to model the stress and temperature changes accurately. Moreover, since there is a relation between q values and yield stress at the appropriate creep temperature, on one hand, and q values and minimum creep rate at a given time, on the other hand, the model can give a physical description of the creep mechanism.
However, in order to assess a reliable creep behavior at any stress and temperature, one needs to estimate sixteen constants; the large number of parameters requires large amounts of data to achieve reasonable confidence on the estimation of the sixteen parameters. The other disadvantage of this model is that it underestimates rupture life for some of the materials [14].

- The Maruyama model (modified θ-model) [19, 20] reduces the numbers of q values in the theta projection model to one rate constant, a; the form of the model is given by:

$$\varepsilon = A[(1-\exp(-\alpha t)] + B[\exp(\alpha t) - 1]$$

where A and B are parameters related to strain hardening and softening, respectively, and α is the rate constant of creep deformation. The creep rate is given by:

$$\dot{\varepsilon} = \alpha[A\exp(-\alpha t) + B\exp(\alpha t)]$$

While the theta projection model takes hardening and softening independently during the creep processes, the modified theta model takes them simultaneously.
The advantage of this model over the theta projection is the reduced number of parameters to deal with. Because the equation has only one rate constant, determining the parameters is somewhat easier than the original theta-projection method.
The disadvantage of this model is its inability to describe the creep curve near the rupture point [38].

- The Graham-Walles model [39] uses a polynomial series for describing the three-stage creep curve:

$$\varepsilon = at^{1/3} + bt + ct^3$$

where a, b, and c are stress dependent parameters. Each term of this polynomial is obeying Norton-Bailley law [1, 17], which is given by:

$$\varepsilon = K\sigma^n t^m$$

where n and m are material related parameters and K is a constant.
Although the Graham-Walles model provides a mathematical tool to capture the three stages of creep curve, it does not explicitly express the temperature dependency.
Moreover, determining all parameters requires effort. In addition, the fixed exponents of time reduce the flexibility of this model [17].
Figure 3 shows the superposition of three individual terms in the Graham-Walles model.

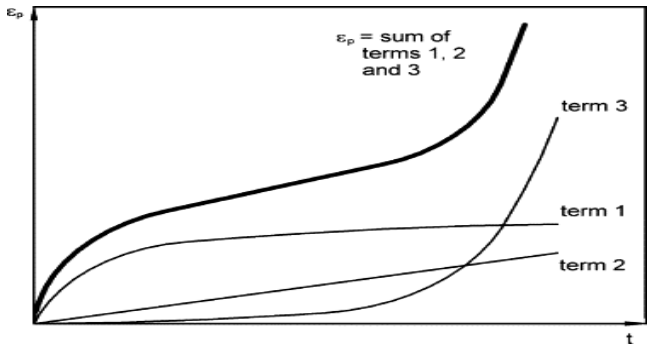

Figure 3. The Graham–Walles approach is the superposition of three individual terms, schematically [3].

- The Kachannov-Rabotnov-Constitutive-Damage model [3, 39] represents continuum damage (CDM) as an effective damage of a cross section of materials because of internal voids. The internal stress increases with time as a function of damage. This damage is represented by the ratio of the remaining effective area A, to the original area A_0. This area loss or damage is shown schematically in figure 4.

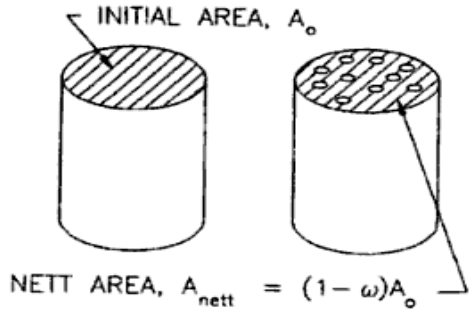

Figure 4. Kachanov's damage model

As damages accumulate, the internal stress increases from σ_0 to σ value:

$$\sigma = \sigma_0 A_0/A$$

Rabotnov [1, 39] replaced this relation with a damage parameter ω using transformation:

$$\omega = (1- A/A_0)$$

The creep rate and damage rate obey the secondary creep law of the Norton form:

$$\dot{\varepsilon} = K\sigma^n \quad , \quad \dot{\varepsilon}_0 = K\sigma_0^{\ n}$$

After some time t, under the load (P= σ A), the original length L_0 increases to L, and area A_0 decreases to an area A. As a result, the true stress at time t, for constant volume $A_0 L_0 = A L$ is:

$$\sigma = \sigma_0 A_0/A = \sigma_0 L/L_0$$

Substituting this stress in the Norton creep law gives:

$$\frac{\dot{\varepsilon}}{\dot{\varepsilon}_0} = \left(\frac{\sigma}{\sigma_0}\right)^n = \left(\frac{A_0}{A}\right)^n = \frac{1}{(1-\omega)^n}$$

Then the creep rate is given by:

$$\dot{\varepsilon} = \frac{k\sigma_0^n}{(1-\omega)^p}$$

where n and p are material parameters. At time zero, ω =0 (no damage), but as damage increases, the creep rate increases. Finally, when ω reaches some critical value ω_f =1, the strain rate tends to infinity and damage occurs. Kachanov made a simple assumption that the damage rate should be a function of the σ_0:

$$\frac{d\omega}{dt} = \dot{\omega} = \frac{B\sigma_0^k}{(1-\omega)^r}$$

By solving these two rate equations together, one can find the strain as function of rupture time: we can estimate the continuity relation:

$$\frac{\varepsilon}{\varepsilon_r} = [1 - (1 - \frac{t}{t_r})^{1/\lambda}]$$

where t_r is the rupture time and ε_r is the rupture strain and l is the material parameter. The rupture strain is given by the following relation:

$$\varepsilon_r = \lambda \varepsilon^* \quad and \quad \varepsilon^* = \dot{\varepsilon}_0 t_r$$

Figure 5 shows Kachanov's strain-time curve.

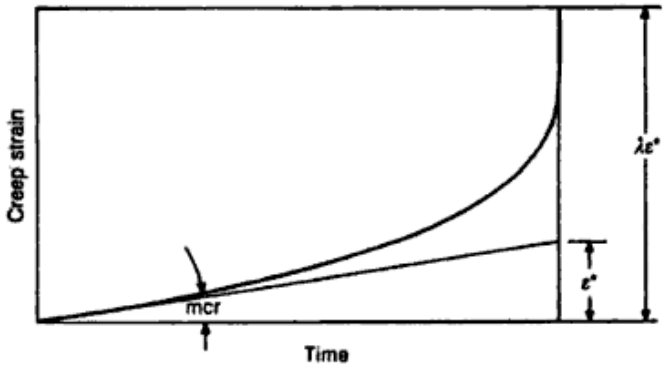

Figure 5. Kachanov's strain-time relation [3].

Kachanov's model uses a simple physical explanation to describe the tertiary part of creep curve. Although it almost gives a good approximation for some materials, it is a model which considers only characteristics of the third stage.

4. Development of a New Model

The proposed model in this research has been inspired by Sawada et al. [7], in which the long-term creep curve behavior has been described up to the secondary stage (time >10^5 hr) for different types of steels. Sawada et al. showed that among the generally accepted creep curves:

Power Law: $\varepsilon = \varepsilon_i + at^b + \dot{\varepsilon}_m t$

Exponential Law: $\varepsilon = \varepsilon_i + a[1 - \exp(-bt)] + \dot{\varepsilon}_m t$

Logarithmic Law: $\varepsilon = \varepsilon_i + a\ln(1 + bt) + \dot{\varepsilon}_m t$

Blackburn's Equation: $\varepsilon = \varepsilon_i + [a(1 - \exp(-bt)] + c[1 - \exp(dt)] + \dot{\varepsilon}_m t$

where t is the time, ε_i is the initial strain and the coefficients a,b,c, and d are material parameters. The power law fits the long creep curves, while the exponential and logarithmic laws and Blackburn's equation cannot represent the primary stage of creep curve during long-term testing.

We propose to use a power law model for the primary part of the creep curve; additionally, we use a combination of power law and exponential law to cover the secondary and tertiary parts of creep. The proposed combined part can be written as:

$$\varepsilon = \varepsilon_{primary} + \varepsilon_{\sec ondary/tertiary} = At^n + Bt^m \exp(pt)$$

where the variables A and B contain the stress and temperature dependencies like the Norton equations and n, *m* and *p* are constants. Moreover, we suggest the creep rate with the following form:

$$\frac{d\varepsilon}{dt} = nAt^{n-1} + B(m + pt)t^{m-1}\exp(pt)$$

4-1. Comparison of the New Empirical Probabilistic Model with the Theta-Projection Model and Kachanov's Model

In this section, we compare our proposed model with the theta-projection model. We use the data related to polycrystalline Cu with the following parameters in 700K and 20 MPa. The q values are given in Table 1.

Table 1. Values of q extrapolation coefficient in 700K and 20 MPa for Cu polycrystal

$\theta_1 = 2.408\text{x}10^{-3}$
$\theta_2 = 2.306\text{x}10^{-5}$
$\theta_3 = 1.08\text{x}10^{-3}$
$\theta_4 = 1.706\text{x}10^{-5}$

Using these parameters, the resulting strain-time expression for theta-projection model is as follows:

$$\varepsilon = (0.002408)(1 - \exp(-2.306\times10^{-5}t) + (0.00108)(\exp(1.706\times10^{-5}t - 1))$$

The resulting strain rate-time expression has the following form in the theta-projection model:

$$d\varepsilon/dt = (5.6\times10^{-8})\exp(-0.0020408t) + (1.8\times10^{-8})(\exp(1.706\times10^{-5}t))$$

Using the proposed empirical model yields similar expression for strain-time and strain rate-time as the ones developed by the theta-projection model:

$\varepsilon_c = 5\text{x}10^{-7}\ t^{0.745} + 3.86\text{x}10^{-6}\ t^{0.469}\ \exp(1.612\text{x}10^{-5}\ t)$

$\dot{\varepsilon} = 3.725\text{x}10^{-7}\ t^{-0.255} + 1.81034\text{x}10^{-6}\ t^{-0.531}\ \exp(1.612\text{x}10^{-5}\ t)\ [1+3.4371\text{x}10^{-5}\ t]$

Next the resulting expressions for both models are compared by plotting all four expressions with respect to time. Figure 9 shows the strain vs. time comparison for the two models, while Figure 10 shows the strain rate vs. time for the two models.

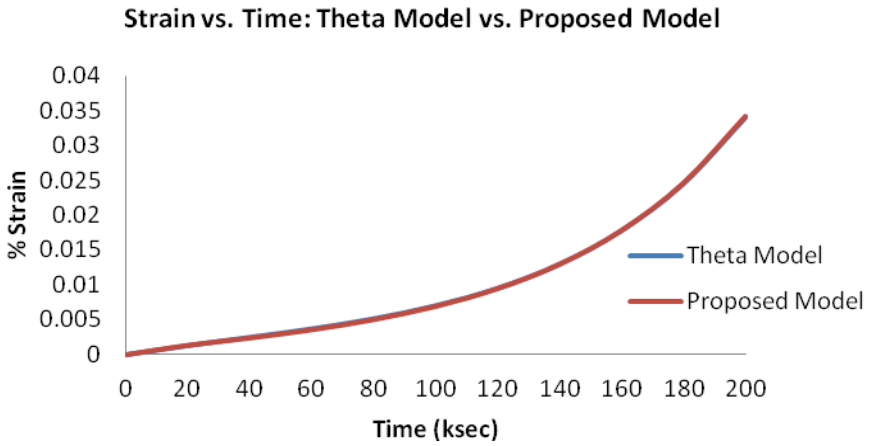

Figure 9. Strain vs. time comparison of the theta and proposed models.

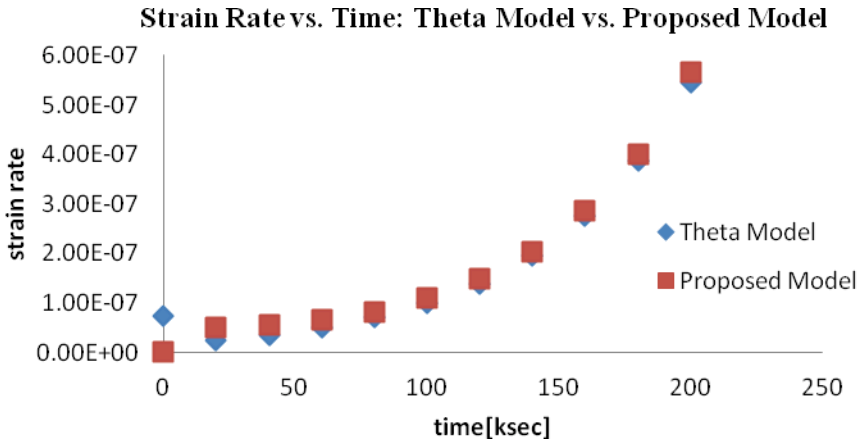

Figure 10. Strain rate vs. time comparison of the theta and proposed models.

As seen in Figure 9, the two models produce nearly identical strain vs. time curves. The difference between the corresponding values between the two curves is approximately 2.5×10^{-5}. Additionally, as seen in Figure 10, the two models produce nearly identical strain rate vs. time curves.

Figure 11 compares the proposed empirical relation with Kachanov's model and shows that the empirical model is capable of fitting such an abrupt model (by giving the appropriate coefficient) very well.

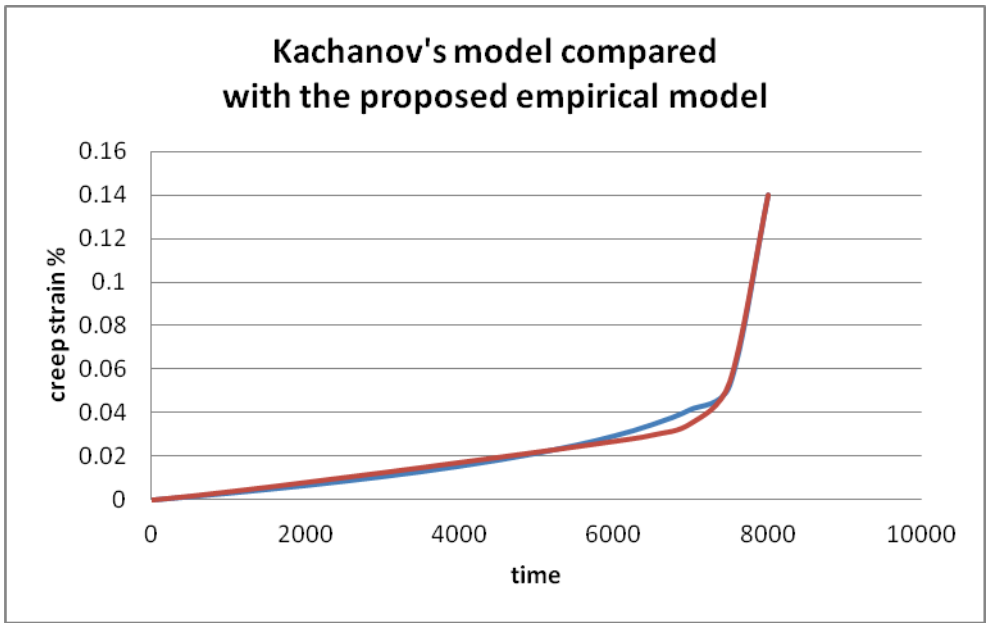

Figure 11. Kachanov's strain-time model (blue) compared with the proposed empirical model.

Kachanov's creep equation is given by:

$$\varepsilon_c = 0.14*[1-(1-t/8000)^{0.17}]$$

while the proposed empirical model gives:

$$\varepsilon_c = 2.025x10^{-6}*t^{1.091} + 3.6638x10^{-84}*t^{20.55}*\exp(0.000645*t)$$

As seen from Figure 11, the proposed empirical model fits the Kachanov's damage model well and can be used as an abrupt damage model, where damages (like voids formation at the grain boundaries) are proposed.

By determining the uncertainty of the very model together with the uncertainty of model parameters and the experimental data, our model will uniquely consider the source and effect of the errors.

- **Experimental Effort in Support of Model Development**

In order to do the creep experiment, aluminum 7075 dog-bone and X70 carbon steel (ASTM-standardized) samples were prepared. Figure 12 shows these specimens with their appropriate stainless holders for fixing them in the furnace; the holders are installed in the grips of the MTS machine.

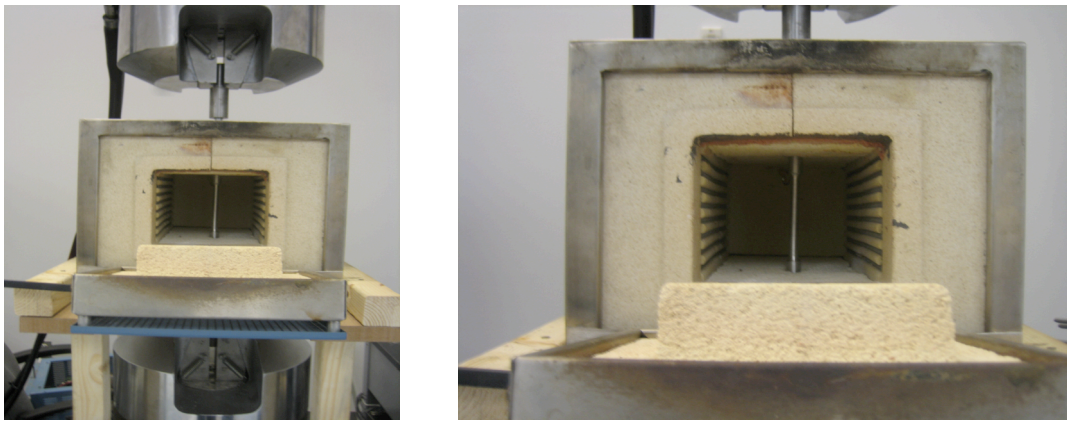

Figure 12. Al-sample fixed in the threaded holders (left) and into the grips of MTS machine (right).

Figure 13 shows the Al sample with the top and bottom holders.

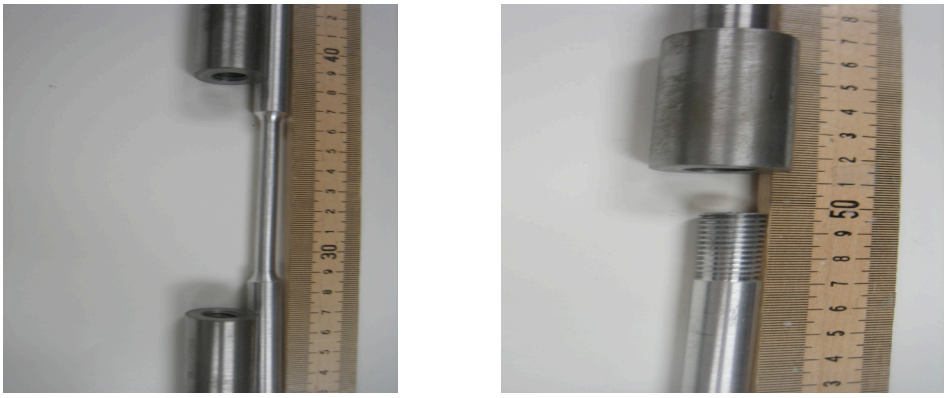

Figure 13. Al-sample with two threaded holders (left), in top or bottom view (right).

X70 carbon steel specimens needed special long stainless steel holders, which are specially threaded at the top and can be fixed to the CT specimens. Figure 14 shows these special grips, a CT specimen, and the form that they are fixed in the MTS machine (figure 15).

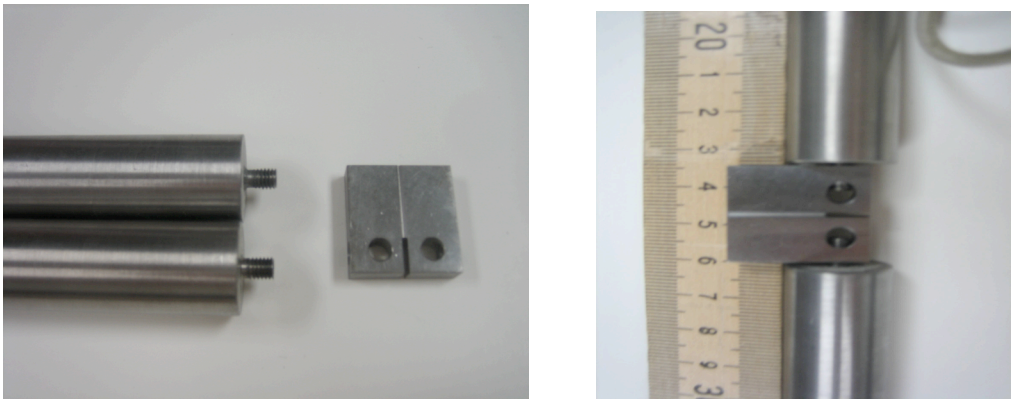

Figure 14. X70 carbon steel with top and bottom threaded grips.

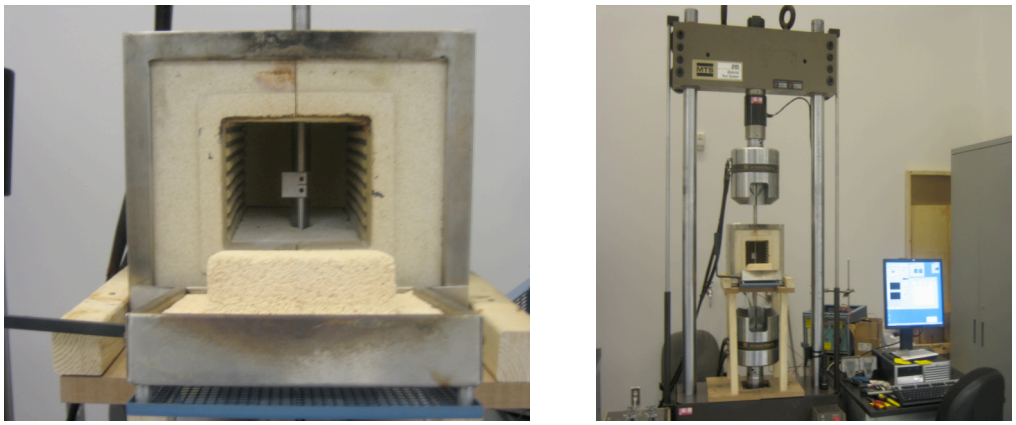

Figure 15. X70 carbon steel fixed in the furnace (left) and connected to the MTS macine (right).

A long-scaled creep- (SCC)-corrosion-fatigue (all-purpose chamber) for Dog-bone and CT specimens has been designed, made and tested. In order to test its workability, several experiments have been performed on carbon-reinforced polymer, aluminum and steel prototype samples. Figure 16 shows the long, medium- and small-sized chambers with the prototype dog-bone polymer specimen.

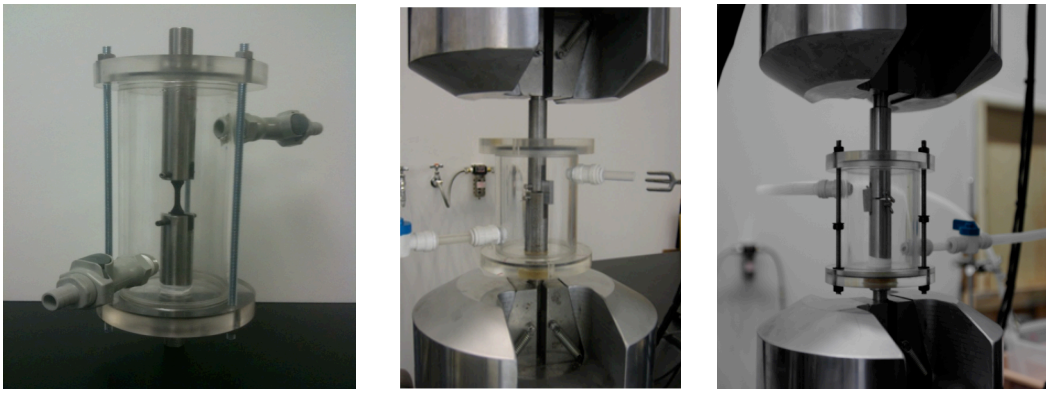

Figure 16. Long (left), medium-sized (middle) and small-sized (right) all-purposechambers for different sample sizes.

Figure 17 shows the furnace together with the CT and dog-bone samples installed in the MTS machine.

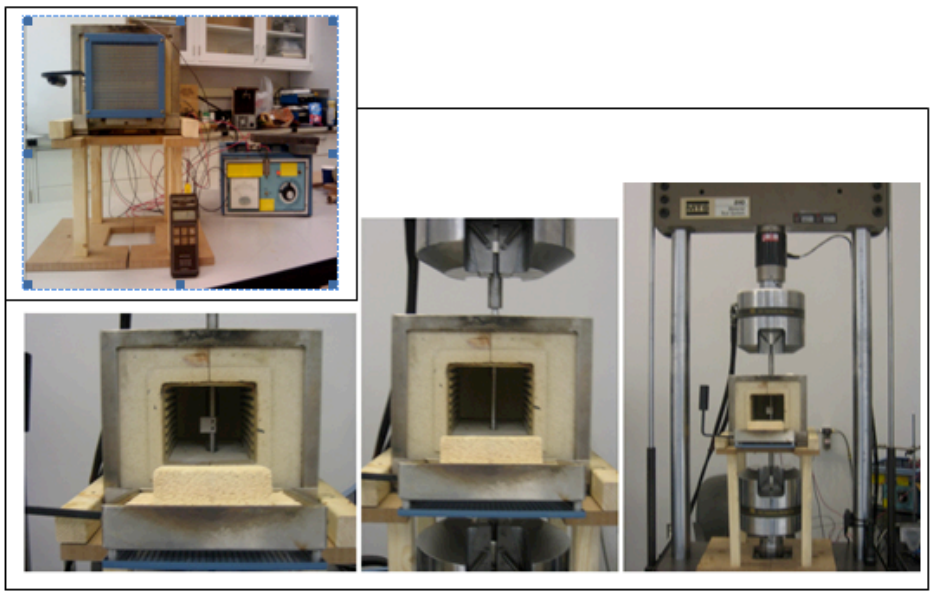

Figure 17. Furnace with CT and dog-bone samples on the MTS machine.

4. Difficulties Encountered/Overcome

None to report. Project is on schedule.

5. Planned Project Activities for the Next Quarter

1. Simulation and refinement of the mechanistic models (PoF models) for creep will be performed. The related report will be submitted.
2. The corresponding simulation tool to help both model development and field applications will be developed.
3. The UMD PoF-based laboratory will be expanded to include strain rate estimation with strain gauge capabilities. Grain gauge measuring equipment have already been ordered from National Instrument Corporation and will be installed in the near future.
4. A long Plexiglas chambers designed (outside of this project) by Mr. Nuhi and Dr. Modarres will be installed on the MTS machines of the PoF-laboratory.
5. A stainless steel chamber is now planned to expand the measurements capabilities of the laboratory for measuring different samples under different gas atmospheres. The creep experiments should be performed according to an acceptable time schedule. These experiments would test the validity of stress and temperature dependencies of Norton, Monkman and Grant empirical equations. Then additional experiments can be performed to determine the complete stress and temperature dependencies of different empirical parameters; the results will be compared with Evans, Murayami and Graham-Wallis generic models.

6. Papers published and being prepared for publication by the Team

1- M. Chookah, M. Nuhi, and M. Modarres, “Assessment of Integrity of Oil Pipelines Subject to Corrosion-Fatigue and Pitting Corrosion”, presented by Prof. Modarres at the International Conference of Integrity- Reliability-Failure (IRF) in Porto, Portugal, July 20-24 2009. (The cost of the conference and associated travels was not covered by EERC)

2- M. Chookah, M. Nuhi, and M. Modarres, A. Seibi “A Probabilistic Physics of Failure Model for Prognostic Health Monitoring of Piping Subject to Pitting and Corrosion –Fatigue” is sent for publication to the “Journal of Reliability Engineering and System Safety”.
3- A paper on “Development of a Database of Mechanistic Models of Failure for Application to Pipeline and Equipment Risk, Reliability and Health Management (Pitting Corrosion- Pit Depth and Density), prepared for publication at a conference. We are studying the possibility that the PI interns present the paper.

Appendix

Approach

The test rig, which is currently installed at UMD and is expected to be installed at PI later, will be used along with two new facilities for testing creep stress corrosion cracking (SCC) to conduct the necessary experimental studies reflecting field conditions for model validation developed in EERC phase I & II of this project. The equipment needed includes corrosion test cells, autoclaves, heating oven, multiphase flow loops, and testing machines for slow strain rate and crack growth testing. This activity also requires a complete line of monitoring equipment for evaluation of corrosion, scaling, and chemical treatment for field and laboratory. This test rig will be a useful tool for teaching, research, and possibly training field engineers from operating companies.

Two-Year Schedule

This project involves three distinct tasks. The first task is the development of the mechanistic models, development of a corresponding simulation tool to help both model development and field applications. The second task focuses on experimental activities to generate relevant data to validate the proposed models of Task 1. Finally, the third task involves the actual validation of the models proposed in Task 1 with the experimental results obtained in Task 2, including Bayesian estimation of the model parameters.

Task 1: Develop the best estimate mechanistic (physics of failure) empirical models for pitting corrosion, SCC, and fatigue-creep. The model development involves the following activities.

Task1.1: Gather, review and select most promising physics of failure based methods and algorithms proposed in the literature.

- Literature surveys for creep and stress corrosion cracking (SCC) degradation mechanisms are almost completed and will be classified for finding the relevant models (100% done).

Task1.2: Select, develop or adopt a detailed mechanistic model (one deterministic model for each phenomenon) that properly describes the degradation process.

- Development of the mechanistic models and of a corresponding simulation tool to help both model development and field applications after classifying the models and choosing the appropriate one should be done in the next future (50% complete).

Task 1.3: Develop a Monte-Carlo based mathematical simulation routine on Matlab depicting the detailed mechanistic model of each degradation phenomenon (far faster than real-time).

- This part was completed for the empirical model developed based on the works of the PI interns for pitting corrosion. After proposing the similar models for SCC and creep-fatigue, it will be repeated (50% completed).

Task 1.4: Based on the results of the simulation a simplified empirical model that best describes the results of simulation will be proposed. Such a model relates the degradation (e.g., depth of the pit or the crack growth rate) to applied loads such as pipeline internal pressure and chemical composition of the product inside the pipeline, as a function of time or cycle of load application.

- This part is completed for the pitting corrosion and corrosion-fatigue, but further work will be done for the other failure mechanisms (50% complete).

Task 2: A PoF reliability analysis laboratory has been designed and being developed at PI. Currently, the advanced corrosion-fatigue purchased by the PI was installed at the University of Maryland (the Cortest Rig) has already been sent to Cortest to ship to PI.

Task 2.1: Completing the remaining corrosion-fatigue tests being conducted by Mr. Nuhi and Chookah. (100% Completed)

Task 2.2: Pitting Corrosion Experiments (develop test plan, prepare samples and the facility, perform the test, and evaluate the test results) (100% Completed).

Task 2.3 SCC Experiments (develop test plan, prepare samples and the facility, perform the test, and evaluate the test results). (Not started yet)

- This task will be done in the next future but SCC specimen holders have already designed and made according to the recent patents and ASTM-Standard.

Task 2.4 Creep-Fatigue Experiments: The equipments and samples are completely ready (100% completed); the tests will be performed in future and the results will be evaluated.

- A small-scaled corrosion-fatigue (or creep) chamber has been designed (not as part of this project), made and tested for dog-bone specimens and checked its workability on the UMD MTS machines using an Aluminum alloy sample. Another more sophisticated one has been already designed and tested for CT-specimens and is tested. Moreover, another chamber has been made for long specimens.
- A heating chamber has been designed and tested for creep experiments.

Task 3: This task involves modification, advancement and use of the WinBugs' Bayesian formalism for model validation using experimental data and integration of the field data and information including sensor-based data (acoustics and/or optical) to update the empirical models and estimate the remaining life of oil pipelines and structures. (50% Complete)

- The WinBugs' Bayesian formalism for model estimation and validation was developed as part of Dr. Chookah's work. This formalism is being updated and new applications of the formalism have been performed using past experimental data and new data of corrosion-fatigue obtained since departure of Dr. Chookah. Further work with this software for integration the experimental data has already be done..

Schedule/Milestones/Deliverables

Tasks 1.1-1.3 (5/1/09-12/15/09); Task 1.4 (12/15/09-3/1/10); Task 2.1 (completed 7/1/09); Task2.2 (7/1/09-12/15/09); Task 2.3 (12/15/09 – 6/1/10); Task 2.4 (6/1/10-2/1/11); Task 3 (12/15/09-3/15/11).

The Cortest rig was boxed and shipped to the Cortest Corporation to test and sent to PI.

The project is on schedule and there is no issue or delay at this point.

Dr. Seibi was appointed as a Co-Advisor of Mr. Nuhi.

Visits

- Dr. A.Seibi visited UMD in July 2009
- Two PI students Abdullah Al Tamimi, and Mohammad Abu Daghah took parts at summer internship (2009).
- Prof. Modarres attended the 1st Annual PI Partner Schools Research Workshop. The Petroleum Institute, Abu Dhabi, U.A.E. January 6-7, 2010.

References on creep for evaluation of a new empirical model

[1] Metal Handbook,(ASTM), Jeffery C. Gibeling "Creep deformation of Metals, polymers, ceramics, and composites".vol.8, Metal testing and evaluation p363-382, 2000

[2] Metal Handbook,(ASTM),Howard R. Voohees, "Assessment and use of Creep-Rupture properties", vol. 8, Metal testing and evaluation p383-397, 2000

[3] R-.K.Penny and D.L.Marriott, Design for Creep, Chapman & Hall,London. 1971

[4] T.H.Hyde, "Creep of materials and structures,Mechanical Engineering Publications, London,1994

[5] R.W.Evans and B. Wlishire," Introduction to creep", The institute of materials,1993

[6] S.R.Holdsworth ,et al." Factors influencing creep model equation selection, International journal of pressure vessels and piping 85 (2008) 80-88

[7] K. Sawadw,et al.; "Analysis of long-term creep curves by constitutive equations"; Material science and engineering A 510-511(2009),190-194

[8] V. Srivastava,et al. "Low stress creep behavior of 7075 high strength aluminium alloy. Material science and engineering A 382 (2004),50-56

[9] B. Wilshire and H.Burt, "A unified theoretical and practical approach to creep and creep fracture", Materials science and engineering,p. 3-12.2005

[10] S.Chaudhuri and R.N.Ghosh, "Creep behavior of 2.2Cr1Mo steel-Effects of thermal ageing and pre-strain, Material science and engineering A 510-511 (2009),136-141

[11] B.F.Dyson ISI J International, Vol. 30 (1990), No, lO, pp. 802-81

[12] www.ami.ac.uk/courses/topics/0124_seom/index.html

[13] M. Law et al. International journal of pressure vessels and piping 75 (1998) 437-442

[14] Woo-Gon et al.; "Creep Characterization of a Ni-Based Hastelloy-X Alloy by Using Theta Projection Method"; Engineering Fracture Mechanics 75 (2008) 4985-4995.

[15] SR. Holdsworth, "Developments in the assessment of creep strain and ductility data". Material High Temperature 2004;21(1):125-132

[16] R. W. Swindeman, M. J. Swindeman, "A comparison of creep models for nickel based alloys for advanced energy systems", International journal of pressure vessels and piping 85 (2008) 72-79

[17] A. Feher et al.; "An Interactive Application for Assessment of Creep Equations"; FVW/FVHT; 31. Vortragsveranstaltung am 28, November 2008.

[18] R.W. Evans and B. Wilshire, *Creep of Metals and Alloys* (London: The Institute of Metals, 1985), pp. 203–243.

[19] K. Maruyama and H. Oikawa, *Trans. ASME, J. Press. Vess.Technol.* 109, 142 (1990)

[20] K. Maruyama and H. Oikawa, *J. Jpn. Inst. Met.* 55, 189 (1991).

[21]"Creep and stress rupture" www.materialsengineer.com/CA-Creep-Stress-Rupture.htm

[22] Xiao-Chi Nin et.al." Creep damage prediction of the steam pipelines with high temperature and high pressure. International Journal of Pressure Vessels and Piping 86 (2009) 593–598ure".

[23] T.H. Hyde, A. Yaghi and M. Proctor, Use of the reference stress method in estimating the life of pipe bends under creep conditions, *Int J Press Vessels and Piping* **75** (2) (1998), pp. 161-169.

[24] W. Sun, T.H. Hyde, A.A. Becker and J.A. Williams, Comparison of the creep and damage failure prediction of the new, service-aged and repaired thick-walled circumferential CrMoV pipe welds using material properties at 640 °C, *Int J Press Vessels and Piping* **77** (7) (2000), pp. 389–398.

[25] W. Sun, T.H. Hyde, A.A. Becker and J.A. Williams, Steady-state creep reference rupture stresses for internally pressurised pipes for use in life prediction, *Int J Press Vessels and Piping* **79** (2) (2002), pp. 135–143.
[26] S.-T. Tu, R. Wu and R. Sandstrom, Design against creep failure for weldments in 0.5 Cr 0 Mo 0.25 V pipe, *Int J Press Vessels and Piping* **58** (3) (1994), pp. 345 – 354.
[27] J.M. Gong, S.T. Tu and X. Ling, Research of welding effect on creep damage of high temperature furnace tubes, *Key Eng Mat* **171–174** (2000), pp. 189–196.
[28] Chen JJ. Investigation of design criterion and welding repair principle of high temperature components using continuum damage mechanics based finite element method. Ms. D thesis. Nanjing University of Technology: Nanjing; 2002 [in Chinese].
[29] T.H. Hyde, W. Sun and J.A. Williams, Prediction of creep failure life of internally pressurized thick walled CrMoV pipes, *Int J Press Vessels and Piping* **76** (14–15) (1999), pp. 925–933.
[30] S.T. Tu, P. Segle and J.M. Gong, Creep damage and fracture of weldments at high temperature, *Int J Press Vessels and Piping* **81** (2) (2004), pp. 199–209.
[31] S.T. Tu, P. Segle and J.M. Gong, Strength design and life assessment of welded structures subjected to high temperature creep, *Int J Press Vessels and Piping* **66** (1–3) (1996), pp. 171–186.
[32] D.R. Hayhurst, P.R. Dimmer and C.J. Morrison, Development of continuum damage in the creep rupture of notched bars [J], *Philos Trans R Soc Lond* **A311** (1984), pp. 103–129.
[33] W. Blume, P. Eisenlohr, "Understanding Creep—a Review", Metallurgical and Materials Transactions A Vol. 33A, 2002—291.
[34] Yongsun Yi et al.; "Stress and Temperature Dependence of Creep in Alloy 600 in Primary Water", Metallurgical and Materials Transactions A Vol. 32A, OCTOBER 2001—2553.
[35] J M Brear, C J Middleton, " The applicability of weld failure prediction maps to new and service-exposed repair welds", in www.seseurope.com
[36] M. Aghaie-Khafri1 , S. Farahany, " Creep Degradation of Thermally Exposed IN738C Superalloy", Journal of Engineering for Gas Turbines and Power, MAY 2009, Vol. 131 / 034501-1
[37] R. F. Miller R. L. Sindelar. "Analysis for Materials Test Reactor (MTR Fuel Assemblies in Dry Storage)", WSRC-TR-95-OI 21
[38] Yoshiharu Kariya et al.; "The Constitutive Creep Equation fr a Eutectic Sn-Ag Alloy Using the Modified Theta Projection Concept"; Journal of Electronic Materials; Vol. 32, No. 12; 2003
[39] Stefan Holmstroem, "Engineering Tools for Robust Creep Modeling", VIT Pubications 728.
[40] T. Hullstein et al., "Fracture Mechanics characterization of crack growth under creep conditions." The Journal of Strain Analysis for Engineering Design, Vol. 23. No 2. 1988
[41] S.H Ryu et al. "Quasi steady state creep crack growth in a 3.5 NiCrMoV Steel." Metallurgical & Material Transactions A. Vol. 28. No 3 1997.
[42] A. Conte. "Experimental and numerical investigations on the creep crack growth in IM 718." www.icf11.com/proceeding/Extended/5428.pdf